


Title	Development and reliability of a direct access sensor using flip chip on flex technology with anisotropic conductive adhesive
Author(s)	Jesudoss, Pio
Publication date	2011
Original citation	Jesudoss, P. 2011. Development and reliability of a direct access sensor using flip chip on flex technology with anisotropic conductive adhesive. PhD Thesis, University College Cork.
Type of publication	Doctoral thesis
Rights	© 2011, Pio Jesudoss. http://creativecommons.org/licenses/by-nc-nd/3.0/ 
Embargo information	No embargo required
Item downloaded from	http://hdl.handle.net/10468/3079

Downloaded on 2017-02-12T08:24:39Z



UCC

University College Cork, Ireland
Coláiste na hOllscoile Corcaigh



UCC
Coláiste na hOllscoile Corcaigh, Éire
University College Cork, Ireland



Development and Reliability of a Direct Access Sensor using Flip Chip on Flex Technology with Anisotropic Conductive Adhesive

A Thesis Presented to University College Cork

For the Degree of Doctor of Philosophy

Pio Jesudoss, MSc

Supervisors

Dr Alan Mathewson

Mr Frank Stam

Dr William M.D. Wright

April 2011.

To My beloved wife Cathy Brown.

Abstract

Technological developments in biomedical microsystems are opening up new opportunities to improve healthcare procedures. Swallowable diagnostic sensing capsules are an example of these. In none of the diagnostic sensing capsules, is the first level packaging of the sensor achieved by the Flip Chip Over Hole (FCOH) method using Anisotropic Conductive Adhesive (ACA). ACA's relatively simple process steps make it suitable for bonding a Direct Access Sensor (DAS). This PhD work was undertaken to develop a novel sensor attachment method on foldable circuitry to be used in a capsule environment.

In a direct access sensor, ACA not only provides the electrical interconnection but simultaneously seals the interconnect area and the underlying electronics from the sensor area in a capsule application. This work characterized the ACA joint used in the DAS in terms of development qualification, mechanical reliability during integration, electrical characterization, hygrothermal reliability and reliability when exposed to fluid conditions representative of those found in the human gut.

The development and characterization showed that the ACA FCOH was a viable option for the DAS interconnection and sealing in a capsule environment. Parameter optimization showed that an ACA deposit dot diameter of $280\mu\text{m}$ and a height of $60\mu\text{m}$ provided reliable flip chip alignment and bonding. It was found that sufficient adhesive supported shear stresses of at least $120\text{N}/\text{mm}^2$, providing good adhesion and good interconnection, all indicating good reliability. The mechanical characterization of a specific assembly showed that a 23mm diameter capsule would be the smallest suitable capsule for insertion without any deleterious consequences on the joint. It also showed that ACA contacts formed a strong joint and withstood the -6N required to secure the final sensor assembly in place before encapsulation. Electrical characterization of the ACA joint in a fluid environment showed that after 1hr soak, the leakage current was in the range of $100\text{nA}/\text{mm}$. The $77\mu\text{m}$ thick ACA was saturated with moisture in the first hour of soak. During the first 4hr soak, the study showed that the ions in the solution actively contribute to the leakage current and was characterized by the varying rate of change of conductance. A long term reliability study of the ACA joint showed that in constant humidity, the offline test measurements showed a thermal strain of 0.004 and a hygroscopic strain of 0.0052 and resulted in a fatigue like process. It also showed that shear stress was the dominant stress during hygrothermal aging. *In-vitro* tests showed that high temperature and acidity had a deleterious effect of the ACA and its joint. It also showed that the ACA contact joints positioned at around or over 1mm would survive the gastrointestinal (GI) fluids and would be able to provide a reliable contact during the entire 72hr of the GI transit time.

A final capsule demonstrator was achieved by successfully integrating the DAS, the battery and the final foldable circuitry into a glycerine capsule. Final capsule soak tests suggested that the silicone encapsulated system could survive the 72hr gut transition.

Acknowledgement

This thesis work was undertaken at Tyndall National Institute and University College Cork in Cork Ireland between June 2006 – April 2011.

I would like to express my sincere gratitude to Dr Alan Mathewson for offering me the great opportunity to undertake the thesis work in his research group. I will always be grateful for his help and assistance. I would especially like to thank both my supervisors Mr Frank Stam, and Dr Alan Mathewson for their guidance, help, sincerity, encouragement and their valuable assistance during my thesis and my dissertation. I also would like to thank my academic Supervisor Dr William M.D. Wright for his guidance, assistance, concern, and consideration regarding my academic requirements.

I would like to acknowledge Enterprise Ireland CFTD /05 / 122 and HEA PRTLI-IV project NEMBES for providing the opportunity to carry out the work presented in this thesis.

I would also like to thank:

Dr Karen Twomey, Principal Investigator of the DIACAPS project, for her valuable support and advice on the sensors and electrochemical system, Dr Olivier Chevalerias, for helping me get on my feet at Tyndall at my arrival, Mr Kenneth Rodgers, for training me in the lab and answering all the technical related questions, Dr Kevin McCarthy, for his help and letting me use his lab for electrical measurements, Tony Compagno, Don Lynch, Alan Murphy, Ethel Noonan, Dr Liam Lewis, Nicolas Sassiati, Aidan Daly, and all my fellow students.

Colm Mc Caffery and Eva Alvarez, fellow students in the DIACAPS project working on the circuitry and electrochemical sides of the project. They were very helpful in helping me build up my knowledge in their respective fields.

Catherine Brown, for proof reading and providing full support during my thesis, to the entire Packaging Lab staff for their kindness and their assistance, to all other research staff and postgraduates who had contributed directly or indirectly to this work.

To my fellow students, just to mention the few: Sanjay, Nick, Nicolas, Pierre, Micki, Karen, Aidan, Tamjid, Colm, Eva, Susie, Amélie, Ethel, Aidan, Vimal, Andreas, Vanessa, Santosh, Ethel, Jean-Michel, Andrea, Ronan, Pdraig, Brian, Wen Wu, and all my other lunch colleagues.

To all my family, and I am sure to all the people that I must have forgot to mention.

List of Publications

Journal Publications

P. Jesudoss, A. Mathewson, W. M. D. Wright, F. Stam, “Mechanical assessment of an anisotropic conductive adhesive joint of a direct access sensor on a flexible substrate for a swallowable capsule application”, *Microelectronics Reliability*, vol. 53, no. 3, pp. 452-462, 2013.

Conference Proceedings

P. Jesudoss, A. Mathewson, W. M. D. Wright, K. Twomey, F. Stam, “A Swallowable Diagnostic Capsule with a Direct Access Sensor Using Anisotropic Conductive Adhesive”, *IEEE IRPS*, 2011, pp. 1 – 4.

P. Jesudoss, W. Chen, A. Mathewson, W. M. D. Wright, K. McCarthy, F. Stam, “Electrical characterization of Anisotropic conductive adhesive based flip chip for a direct access sensor”, *60th Proceedings of Electronic Components and Technology Conference (ECTC)*, 2010, pp. 369 – 374.

P. Jesudoss, A. Mathewson, W. M.D. Wright, C. McCaffrey, V. Ogurtsov, K. Twomey, F. Stam, “System packaging & integration for a swallowable capsule using a direct access sensor”, *Microelectronics and Packaging Conference, EMPC*, 2009, pp. 1 – 4.

P. Jesudoss, A. Mathewson, B. O’Flynn, W. M.D. Wright, F. Stam, “Effect of Solder Volume on joint shape with variable chip-to-board contact pad ratio”, *XXXII International Microelectronics and Packaging Poland Conference. IEEE Components, Packaging and Manufacturing Technology (CPMT) Society. IEEE*, 2008

P. Jesudoss, A. Mathewson, W. M.D. Wright, F. Stam, “Evaluation of chip-to-board interconnection using variable aspect ratio contact pad areas”, *IEEE, 26th International Conference on Microelectronics, 2008. MIEL 2008*, 11-14 May 2008, pp. 565 – 568.

Table of Contents

ABSTRACT.....	I
ACKNOWLEDGEMENT	II
LIST OF PUBLICATIONS.....	III
TABLE OF CONTENTS.....	IV
LIST OF FIGURES.....	IX
LIST OF TABLES	XV
NOMENCLATURE LIST OF ABBREVIATIONS.....	XVII
CHAPTER 1 INTRODUCTION	1
1.1. General overview of the digestive system.....	1
1.2. Inflammatory bowel disease	4
1.2.1. Crohn’s disease	5
1.2.2. Ulcerative Colitis.....	5
1.3. Diagnostic pills	6
1.4. Thesis outline	9
CHAPTER 2 BACKGROUND TO THE PROJECT	12
2.1. Background to the project	12

2.2. Sensor interconnection methods	13
2.2.1. Wirebonding.....	13
2.2.1.1. Sensor interconnection methods used in diagnostic sensing pills.....	15
2.2.2. Introduction to Flip Chip (FC) and Flip Chip Over Hole (FCOH) technology	18
2.2.2.1. Flip Chip interconnection process.....	20
2.2.2.2. Flip Chip Over Hole (FCOH) or Direct Access Sensor (DAS).....	30
2.3. Choice of interconnect scheme for the swallowable capsule project	32
2.3.1. Microelectronic sensor chip – pad metallization scheme	32
2.4. Conclusions	35
 CHAPTER 3 DEVELOPMENT OF THE DAS.....	 38
3.1 Introduction.....	38
3.2. Experimental details	39
3.2.1. Materials	40
3.2.1.1. Sensor chip.....	40
3.2.1.2. Test substrate	41
3.2.1.3. Anisotropic Conductive Adhesive paste (ACA).....	41
3.2.2. Bonding process	42
3.2.3. Estimating the number of conducting particles	44
3.3. Design of Experiments (DOE)	45
3.3.1. Dot diameter qualification through DOE to achieve the smallest footprint.....	45
3.3.2. Hypothesis testing.....	47
3.3.2.1. Statistical inference for a single sample on the mean of a population, σ unknown.....	49
3.4. Dispense pattern qualification	55
3.4.1. ACA spread	55
3.4.2. Shear test	57

3.4.2.1. Test method	57
3.4.2.2. Shear test results	59
3.4.2.3. Fractographical analysis.....	61
3.5. Electrochemistry - Direct Access Sensor testing	64
3.6. DAS capsule placement	67
3.6.1. Sensor placement option	67
3.6.2. Preliminary DAS packaging.....	68
3.7. Conclusion	70
CHAPTER 4 MECHANICAL CHARACTERIZATION OF THE ACA JOINT FOR A DAS	73
4.1. Introduction.....	73
4.2. Mechanical testing.....	76
4.2.1. Preliminary capsule insertion.....	76
4.2.2. Mechanical testing of the ACA joints during capsule insertion.....	78
4.2.2.1. Material and methods	78
4.2.2.2. Results and discussion	85
4.3. Conclusion	101
CHAPTER 5 ELECTRICAL CHARACTERIZATION OF ACA IN A DAS	104
5.1. Introduction.....	104
5.2. Leakage testing	105
5.2.1. Preliminary gross gravimetric analysis	105
5.2.1.1. Fick's law	107
5.2.2. ACA leakage current in a DAS.....	111
5.2.2.1. Materials and methods.....	111

5.2.2.2. Testing solutions	116
5.2.2.3. Results and discussion.....	116
5.2.2.3.1 Measured leakage current.....	116
5.2.2.3.2. Discussion of the measured leakage current result	122
5.2.2.3.3. Rate of change of conductance over time.....	135
5.3. Conclusion	139
CHAPTER 6 LONG TERM RELIABILITY OF THE ACA INTERCONNECT IN A DAS.....	142
6.1. Introduction.....	142
6.2. Constant humidity testing.....	142
6.2.1. Materials and methods	143
6.2.1.1. Further encapsulation process	143
6.2.1.2. Electrical measurement	143
6.2.2. Results	144
6.2.3. Discussion.....	146
6.2.4. Failure analysis	149
6.3. In-vitro testing	153
6.3.1. Materials and methods	154
6.3.1.1. Encapsulation process.....	154
6.3.1.2. Electrical measurement	155
6.3.2. Results and discussion.....	157
6.3.3. Failure analysis	167
6.4. Conclusion	172
CHAPTER 7 CAPSULE INTEGRATION	175
7.1. Introduction.....	175

7.2. DAS in the modular flexible prototype.....	175
7.2.1. Modular flexible prototype board.....	175
7.2.2. Sensor attachment modular flexible board.....	177
7.2.3. Electrochemistry – modular flex board DAS testing	178
7.3. Battery integration	184
7.4. Capsule integration	186
7.4.1. Battery test - dry environment.....	190
7.4.2. Encapsulated assembly with battery - fluid environment test	193
7.5. Conclusion	197
 CHAPTER 8 CONCLUSION AND FUTURE WORK	 199
8.1. Conclusion	199
8.2. Future work	203
 APPENDIX A1: INITIAL CAPSULE PACKAGING SOLUTION - DESIGN SELECTION.....	 206
 APPENDIX A2: WINDOW SELECTION.....	 209
 REFERENCES.....	 211

List of Figures

FIGURE 1.1. THE HUMAN DIGESTIVE SYSTEM [4].	2
FIGURE 2.1. SCHEMATIC OF THE COMPONENTS OF A SWALLOWABLE CAPSULE.	12
FIGURE 2.2. SENSORS ELECTRICALLY CONNECTED TO THE SUBSTRATE VIA (A) BALL BONDING; (B) WEDGE BONDING [30].	14
FIGURE 2.3. SMARTPILL [34].	16
FIGURE 2.4. IPILL BY PHILIPS (A) MECHANICAL DESIGN SHOWING THE WIRE BONDED PH SENSOR; (B) PICTURE OF THE WIRE BONDED SENSOR WITH THE WIRE BOND COVERED BY EPOXY [21].	16
FIGURE 2.5. SCHEMATIC OF FIRST VERSION OF IDEAS [37].	17
FIGURE 2.6. SCHEMATIC OF FC PROCESS.	19
FIGURE 2.7. DIFFERENT FC INTERCONNECTION PROCESSES.	20
FIGURE 2.8. SCHEMATIC OF SENSOR PLACED FACE UP ON THE SAME SIDE AS THE BOND PAD FOR FC INTERCONNECTION.	29
FIGURE 2.9. SCHEMATIC OF SENSOR FACE DOWN.	30
FIGURE 2.10. EXPANDED SCHEMATIC OF FCOH PROCESS.	31
FIGURE 2.11. SCHEMATIC OF DEPOSITED STACK LAYER OF THE MICROELECTRONICS SENSOR.	32
FIGURE 2.12. DISSOLUTION RATE OF GOLD.	33
FIGURE 3.1. THE DIRECT ACCESS SENSOR CHIP.	40
FIGURE 3.2. FLEXIBLE SUBSTRATE WITH WINDOW OPENING FOR SENSOR ACCESS.	41
FIGURE 3.3. SEM IMAGE OF: (A) A GOLD STUD BUMP; (B) A COINED STUD BUMP.	43
FIGURE 3.4. ACA REFLOW PROFILE.	43
FIGURE 3.5. IMAGES OF ACA PARTICLES: (A) COMPOSITE IMAGE OF 300MM SQUARE PAD WITH ACA PARTICLES IN GRAY SCALE; (B) PROCESSED IMAGE VIA IMAGE J SOFTWARE SHOWING JUST THE CONDUCTIVE PARTICLES ON THE RIGHT SIDE.	44
FIGURE 3.6. SAMPLING DISTRIBUTION OF THE SAMPLE MEAN.	49
FIGURE 3.7. THE DISTRIBUTION OF T , WHERE $H_0: M = M_0$ IS TRUE, WITH CRITICAL REGION FOR $H_1: M \neq M_0$.	51
FIGURE 3.8. THE DISTRIBUTION OF T , P -VALUE NULL HYPOTHESIS TEST.	51
FIGURE 3.9. INTERACTION PLOT FOR DOT DIAMETER.	54

FIGURE 3.10. MICROGRAPH SHOWING THE SHAPE OF THE DOT: (A) TOP VIEW; (B) THE PROFILE VIEW AND (C) SCHEMATIC OF A SIDE VIEW OF THE DOT.	55
FIGURE 3.11. PICTURE SHOWING A SPREAD OF DOT.	56
FIGURE 3.12. THE DISPENSE PATTERN; (A) MICROGRAPH OF THE DISPENSE PATTERN; (B) SAM IMAGE OF THE DISPENSE PATTERN AND; (C) CROSS-SECTION SHOWING THE FILET FOR THE DISPENSE PATTERN.....	57
FIGURE 3.13. SCHEMATIC SHOWING THE SHEAR TESTING OF THE SENSOR CHIP.	58
FIGURE 3.14. PLOT OF SHEAR STRESS OF DISPENSE PATTERN THAT FAILED AFTER HYGROTHERMAL AGING. ...	61
FIGURE 3.15. SCHEMATICS OF TYPES OF FAILURE IN ADHESIVE-ADHERENT SYSTEM: (I) INTERFACIAL FAILURE; (II) COHESIVE FAILURE AND (III) MIXED FAILURE.	61
FIGURE 3.16. SEM IMAGES OF THE FAILED SAMPLES: (A) AFTER 24HR; (B) 168HR AND; (C) 336HR.	63
FIGURE 3.17. SCHEMATIC OF CYCLIC VOLTAMMETRY SETUP.	64
FIGURE 3.18. CYCLIC CURRENT-VOLTAGE CURVE OF THE AU WE WITH: (A) AN EXTERNAL RE. ELECTRODE AND (B) WITH PSEUDO PT RE.....	66
FIGURE 3.19. SCHEMATIC OF DIFFERENT VIABLE SENSOR PLACEMENT OPTIONS.	68
FIGURE 3.20. PROCESS FLOW OF THE SENSOR ENCAPSULATION METHOD.....	69
FIGURE 3.21. VOLTAMMETRIC RESPONSES OF AN UNENCAPSULATED SENSOR AND AN ENCAPSULATED SENSOR.	70
FIGURE 4.1. SCHEMATIC OF: (A) THREE POINT; AND (B) FOUR POINT BENDING.	73
FIGURE 4.2. SCHEMATIC OF THREE POINT INWARD BENDING.	74
FIGURE 4.3. MECHANICAL SETUP FOR PRELIMINARY CAPSULE INSERTION.....	76
FIGURE 4.4. PLOT OF FORCE REQUIRED TO PUSH THROUGH GELATINE CAPSULE AND TO FIX THE DAS.	77
FIGURE 4.5. MICROGRAPH OF TEST CHIP WITH COINED GOLD STUD BUMPS.	78
FIGURE 4.6. FLEXIBLE SUBSTRATE: (A) PROTEL LAYOUT, (B) MICROGRAPH OF THE ENTIRE SUBSTRATE AND (C) MICROGRAPH SHOWING CONDUCTIVE LINES FOR DAISY CHAIN MEASUREMENT.....	80
FIGURE 4.7. SCHEMATIC OF COVERLAY ISSUE.	80
FIGURE 4.8. SCHEMATIC SHOWING: (A) THE TOP VIEW, AND (B) THE CROSS-SECTIONAL VIEW OF THE SILICON COMPRESSION TEST.....	81
FIGURE 4.9. POLYCARBONATE BLOCK WITH DIFFERENT DIAMETER HOLES.	82
FIGURE 4.10. INSTRON MECHANICAL TEST SETUP AND ELECTRICAL TEST SETUP FOR TESTING ACA JOINTS.....	83

FIGURE 4.11. SCHEMATIC OF THE FOUR POINT MEASUREMENT TEST SETUP DURING MECHANICAL TEST.	84
FIGURE 4.12. PLOT SHOWING THE FORCE VARIATION DURING SILICON COMPRESSION TEST.	85
FIGURE 4.13. PLOT SHOWING THE VARIATION OF THE FORCE AND THE MEASURED VOLTAGE AS A FUNCTION OF DISTANCE.....	87
FIGURE 4.14. IMAGES OF THE CORRESPONDING POSITIONS DEPICTED IN THE FORCE PLOT IN DIFFERENT REGIONS.....	88
FIGURE 4.15. PLOT SHOWING THE LINEAR PART OF THE FORCE CURVE IN A 23MM DIAMETER HOLE UNTIL POSITION A.	88
FIGURE 4.16. LINEAR PART SPRING CONSTANT AS A FUNCTION OF THE DIAMETER.....	89
FIGURE 4.17. SCHEMATIC SHOWING RESISTANCE PATH BETWEEN A AND B.	91
FIGURE 4.18. SLAB GEOMETRY TO ESTIMATE CHIP AND SUBSTRATE BOND PAD RESISTANCE.	92
FIGURE 4.19. NI PARTICLE CONTACT: (A) CONTACT CYLINDRICAL APPROXIMATION AND (B) CROSS-SECTION SHOWING THE 1 μ M CONTACT.....	93
FIGURE 4.20. FIGURE SHOWING THE VARIATION OF THE MEASURED VOLTAGE AS A FUNCTION OF THE DISTANCE TRAVELLED IN A 23MM DIAMETER HOLE.	96
FIGURE 4.21. SCHEMATIC SHOWING THE REGIONS OF STRESS IN THE ASSEMBLY DURING INSERTION.....	97
FIGURE 4.22. PLOT SHOWING VARIATION OF VOLTAGE IN INDIVIDUAL DAISY CHAIN AS A FUNCTION OF DISTANCE TRAVELLED IN 21MM, 19MM, 17MM, AND 15MM DIAMETER HOLES.	98
FIGURE 4.23. MICROGRAPH SHOWING THE CRACKED DIES AFTER MECHANICAL TEST.	100
FIGURE 4.24. CRACK PROPAGATION IN THE ACA ASSEMBLY: (A) CROSS SECTIONAL MICROGRAPH OF THE ASSEMBLY AND (B) SCHEMATIC OF THE CROSS SECTION SHOWING FORCE AND DIRECTION OF PROPAGATION.	100
FIGURE 4.25. SCHEMATIC SHOWING THE POSITION OF THE CROSS-SECTION MICROGRAPH.....	101
FIGURE 5.1. VARIATION OF ACA WEIGHT GAIN VERSUS THE DURATION OF THE SOAK.	106
FIGURE 5.2. SCHEMATIC SHOWING MOISTURE PENETRATION IN THE CHOSEN SETUP.	107
FIGURE 5.3. PLOT (A) ANALYTICALLY CALCULATED MOISTURE CONCENTRATION FOR THIN ACA AND (B) RELATIONSHIP BETWEEN THICKNESS AND TIME.....	110
FIGURE 5.4. MICROGRAPH OF TEST SUBSTRATE.	112
FIGURE 5.5. ACA BONDED DAS ON FLEX SUBSTRATE.	113

FIGURE 5.6. MICROGRAPH OF STENCIL	114
FIGURE 5.7. MICROGRAPH SHOWING ACA BONDLINE AROUND THE SUBSTRATE BOND PAD	114
FIGURE 5.8. THE EXPERIMENTAL SET UP FOR LEAKAGE CURRENT MEASUREMENT.....	115
FIGURE 5.9. POLYMER MATRIX WITH NANO PORE NETWORK SHOWING: (A) WATER IN UNBOUND STATE AND (B) IN BOUND STATE DIFFUSION [140].	117
FIGURE 5.10. INITIAL I-V CHARACTERISTICS OF THE LEAKAGE CURRENT MEASURED ON A DRY SAMPLE.....	119
FIGURE 5.11. I-V CHARACTERISTICS OF THE LEAKAGE CURRENT MEASURED AFTER 1HR SOAK.	120
FIGURE 5.12. I-V CHARACTERISTICS OF THE LEAKAGE CURRENT MEASURED AFTER (A) 2HR, (B) 3HR AND (C) 4HR SOAK.	121
FIGURE 5.13. PLOT OF ANALYTICALLY CALCULATED ION CONCENTRATION IN THIN ACA IN (A) PH1.2, (B) PH6.8 AND (C) BUFFER SOLUTION.	127
FIGURE 5.14. BOND PADS WITH CONDUCTION PATH THROUGH ACA (A) PLAN VIEW OF BOND PADS, (B) SIDE VIEW OF BOND PADS.	129
FIGURE 5.15. PLOTS OF ANALYTICALLY CALCULATED LEAKAGE CURRENT FOR 1HR SOAK IN PH1.2.	130
FIGURE 5.16. PLOTS OF ANALYTICALLY CALCULATED LEAKAGE CURRENT FOR 1HR SOAK IN PH6.8.	132
FIGURE 5.17. PLOTS OF ANALYTICALLY CALCULATED LEAKAGE CURRENT AFTER 1HR SOAK IN BUFFER.....	133
FIGURE 5.18. PLOTS OF ANALYTICALLY CALCULATED TOTAL LEAKAGE CURRENT (CONTRIBUTION OF ALL IONS) IN ALL SOLUTION DURING 1HR SOAK.	134
FIGURE 5.19. MEASURED RATE OF CHANGE OF CONDUCTANCE OF THE DEVICE OVER TIME.....	136
FIGURE 5.20. CALCULATED RATE OF CHANGE OF CONDUCTANCE OF THE DEVICE OVER TIME.	137
FIGURE 5.21. COMPARING CALCULATED VS MEASURED RATE OF CHANGE OF CONDUCTANCE OF THE DEVICE OVER TIME IN DIFFERENT SOLUTION.	139
FIGURE 6.1. SECOND ENCAPSULATION PROCESS: (A) CROSS-SECTIONAL SCHEMATIC OF THE MOULD AND (B) PICTURE OF ENCAPSULATED SAMPLE FOR RELIABILITY TESTING.....	143
FIGURE 6.2. PLOT OF ACA CONTACT RESISTANCE VS. THE TIME IN HUMIDITY AGING OF ALL THE ELECTRODES IN ONE SAMPLE.....	145
FIGURE 6.3. PLOT OF ACA CONTACT RESISTANCE VS. THE TIME IN HUMIDITY AGING CORRESPONDING TO THE SAME ELECTRODE IN ALL NINE SAMPLES.	146

FIGURE 6.4. SAM IMAGES: (A) BEFORE AND (B) AFTER HYGROTHERMAL TESTING OF ONE THE SAMPLES THAT SURVIVED.....	150
FIGURE 6.5. SAM IMAGES: (A) BEFORE AND (B) AFTER HYGROTHERMAL TESTING OF ONE THE SAMPLES THAT FAILED.	150
FIGURE 6.6. CROSS-SECTION OF SAMPLES AFTER HUMIDITY TESTING (A) FAILURE BY CRACK PROPAGATION AND (B) NON FAILED SAMPLE.....	153
FIGURE 6.7. EXPERIMENTAL TEST SETUP.	155
FIGURE 6.8. CIRCUIT DIAGRAM FOR PARALLEL CIRCUITS USED TESTING.	157
FIGURE 6.9. SAM IMAGE OF THE ASSEMBLY BEFORE <i>IN-VITRO</i> TESTING.	158
FIGURE 6.10. PLOT SHOWING THE MEASURED VOLTAGE VARIATION VS. THE DURATION OF THE TEST FOR TOTAL DAISY CHAIN OF ONE OF THE SAMPLES IMMERSERD AT: (A) 80°C AND (B) 37°C.....	159
FIGURE 6.11. PLOT SHOWING THE MEASURED VOLTAGE VARIATION VS. THE DURATION OF THE TEST OF THE PARTIAL DAISY CHAINS OF ONE OF THE SAMPLE IMMERSERD IN: (A) 80°C AND (B) 37°C.....	163
FIGURE 6.12. SAM IMAGE OF SAMPLE AGED AT 80°C, AFTER TESTING.	164
FIGURE 6.13. PLOT SHOWING THE TIME OF FAILURE FOR INDIVIDUAL PARTIAL DAISY CHAINS IN DIFFERENT ARTIFICIAL GUT AND CONTROL SOLUTION AT 80°C AND AT 37°C RESPECTIVELY.....	165
FIGURE 6.14. COMPARISON OF TIME OF FAILURE OF INDIVIDUAL PARTIAL DAISY CHAIN Y IN DIFFERENT ARTIFICIAL GUT AT 80°C AND AT 37°C RESPECTIVELY.	166
FIGURE 6.15. PICTURE SHOWING THE MOVEMENT OF THE EPOXY DEGRADATION IN A DAS.....	167
FIGURE 6.16. SEM SURFACE STUDY OF SAMPLES BEFORE AND AFTER EXPOSURE TO GUT FLUIDS DURING <i>IN-VITRO</i> TEST AT 80°C.	168
FIGURE 6.17. SEM SURFACE STUDY OF SAMPLES BEFORE AND AFTER EXPOSURE TO GUT FLUIDS DURING <i>IN-VITRO</i> TEST AT 37°C.	170
FIGURE 6.18. CROSS-SECTIONAL ANALYSIS OF THE SAMPLES AFTER <i>IN-VITRO</i> TEST.....	171
FIGURE 7.1. MODULAR FLEXIBLE BOARD.	176
FIGURE 7.2. SCHEMATIC SHOWING: (A) THE FOLDING IN THE MODULAR FLEX BOARD; AND (B) THE THIRTEEN LAYER STRUCTURE USED IN FABRICATION OF THE MODULAR FLEXIBLE BOARD.	176
FIGURE 7.3. PROTEL DESIGN OF THE BATTERY SECTION SHOWING THE PROTRUDED SECTION WITH ENABLE AND V_{IN}	177

FIGURE 7.4. BENCHTOP ELECTROCHEMISTRY SETUP FOR TESTING	178
FIGURE 7.5. ELECTROCHEMICAL TEST RESULTS OF A SAMPLE BEFORE AND AFTER STORAGE.....	180
FIGURE 7.6. MICROGRAPHS SHOWING THE PEELING, BLISTERS AND PASSIVATION LAYER CRACK ON THE SURFACE OF THE AU WE AND THE PT CE.....	181
FIGURE 7.7. SEM IMAGE OF THE DELAMINATION BETWEEN THE PASSIVATION LAYER AND THE AU WE.....	182
FIGURE 7.8. EDX PICTURE OF PT CE.....	182
FIGURE 7.9. EDX ANALYSIS OF THE AU WE.....	183
FIGURE 7.10. SENSOR PROTECTION.	185
FIGURE 7.11. BATTERY INTEGRATION PROCESS.....	186
FIGURE 7.12. SOLID WORKS TECHNICAL DRAWING OF THE TEFLON MOULD.	188
FIGURE 7.13. PHOTOGRAPHS SHOWING: (A) THE ENTIRE GLYCERINE CAPSULE, (B) BOTTOM PART OF THE GLYCERINE CAPSULE WITH THE HOLE AT APPROXIMATELY 28MM FOR THE BATTERY WIRES AND (C) 1MM DIAMETER DRILL HOLE PLACED AT THE CENTRE OF THE DOME.....	189
FIGURE 7.14. CAPSULE INTEGRATION PROCESS.....	190
FIGURE 7.15. SCHEMATIC OF THE CIRCUITRY USED IN THE BATTERY TEST.	191
FIGURE 7.16. BATTERY VOLTAGE VARIATION OVER ONE CYCLE.....	192
FIGURE 7.17. BATTERY PERFORMANCE OVER 72HR – 320 CYCLES.....	193
FIGURE 7.18. SCHEMATIC OF THE SECOND SUBSTRATE WITH SILICONE IN THE BATTERY COMPARTMENT.....	194
FIGURE 7.19. TEST SETUP TO TEST THE BATTERY IN A LIQUID ENVIRONMENT.....	195
FIGURE 7.20. PLOT SHOWING THE VARIATION OF THE BATTERY VOLTAGE AS A FUNCTION OF TIME.....	196
FIGURE 7.21. MICROGRAPHS OF: (A) THE SOAKED ENCAPSULATED ELECTRONIC ASSEMBLY FROM CAPSULE 2, (B) ONE OF THE ELECTRONIC COMPONENTS ENLARGED AND (C) THE BATTERY FROM CAPSULE 1 AFTER THE SOAK TEST.....	197
FIGURE 8.1. SCHEMATIC OF IMPROVED MODULAR TEST BOARD.....	205
FIGURE 8.2. SCHEMATIC OF CAPSULE FOR COMMERCIALIZATION ROUTE.....	206

List of Tables

TABLE 1.1. MAJOR DIGESTIVE FUNCTIONS AND LOCATIONS, COLLECTED FROM [7,8].....	3
TABLE 1.2. DIFFERENT SWALLOWABLE CAPSULES CLASSIFIED INTO DIFFERENT FAMILIES, COLLECTED FROM [2,3,9,18,20-28].....	7
TABLE 2.1. COMPARISON OF THREE WIREBONDING METHODS [30].....	14
TABLE 2.2. DIFFERENT UBM USED IN DIFFERENT BUMPING PROCESS [46].	24
TABLE 3.1. MATERIAL SPECIFICATION FOR THE CONDUCTIVE ADHESIVE.	42
TABLE 3.2. LEVELS OF EACH FACTOR.	46
TABLE 3.3. P-VALUES FOR SIGNIFICANT TERMS.	53
TABLE 4.1. CHIP AND SUBSTRATE PAD RESISTANCE.....	93
TABLE 4.2. MATERIAL PARAMETERS OF THE MATERIALS USED IN THE MECHANICAL TEST, COLLECTED FROM [121, 122].	94
TABLE 5.1. TABLE OF PARAMETERS, COLLECTED FROM [88,130,135-137].	111
TABLE 5.2. TABLE OF DIFFUSION COEFFICIENTS OF IONS, COLLECTED FROM [147,148].....	125
TABLE 5.3. SUMMARY OF IONS AND THEIR CORRESPONDING CALCULATED CONCENTRATIONS THAT IS PRESENT IN EACH SOLUTION AFTER 4HR SOAK.....	128
TABLE 5.4. TABLE OF PARAMETERS, COLLECTED FROM [149,150].	129
TABLE 5.5. CALCULATED HOURLY ION CONCENTRATIONS.....	130
TABLE 5.6. SUMMARY OF THE CALCULATED LEAKAGE CURRENT OF EACH IONS IN PH1.2.	131
TABLE 5.7. SUMMARY OF THE CALCULATED LEAKAGE CURRENT OF EACH IONS IN PH6.8.	132
TABLE 5.8. SUMMARY OF THE CALCULATED LEAKAGE CURRENT OF EACH IONS IN BUFFER.	134
TABLE 5.9. TABLE SHOWING THE MEASURED RATE OF CHANGE OF CONDUCTANCE.	136
TABLE 5.10. TABLE OF OVERALL DIFFUSION COEFFICIENTS AND CONCENTRATIONS OF IONS IN EACH SOLUTION.	137
TABLE 6.1. MATERIAL PARAMETERS, COLLECTED FROM [121,129,135,152].	147
TABLE 6.2. TEMPERATURE, RELATIVE HUMIDITY, AND WATER CONCENTRATION IN THE AIR [155].	148
TABLE 6.3. TEST MATRIX.....	156

TABLE 7.1. CTE OF THE METAL AND THE PASSIVATION LAYER USED IN THE MICROELECTRONIC SENSOR CHIP

[170]..... 181

Nomenclature list of abbreviations

α	Significance level
a	Base radius
ϵ_0	Vacuum permittivity
ϵ_r	Dielectric constant of the epoxy
ϑ	Saturation time
κ_i	Ionic conductivity
ρ	Resistivity
ρ_w	Densities of water
ρ_e	Densities of epoxy
σ	Standard deviation
μ	Population mean
A	Area of the slab
ACA	Anisotropic Conductive Adhesive
ALT	Accelerated life time
Au	Gold
C	Moisture concentration
C_0	Initial moisture concentration
C_s	Saturated moisture concentration
CE	Counter Electrode
COF	Chip-on-Flex
CD	Crohn's disease
CTE	Coefficient of thermal expansion
d	Distance
D	Moisture diffusion coefficient

D_0	Pre-exponential factor
DAS	Direct Access Sensor
DC	Direct current
DOE	Design of Experiment
E_D	Activation energy
E_H	Activation energy
EDX	Energy Dispersion X-ray analysis
F	Faraday's constant
$F1$	Force
FC	Flip Chip
FCOH	Flip Chip Over Hole
G	Conductance
GI	Gastrointestinal
H	Henry's law coefficient
H_0	Pre-exponential factors
$H1$	Needle height
h	Spherical dome height
h_2	Thickness of the sample
I/O	Input/output
IBDs	Inflammatory bowel diseases
ICA	Isotropic conductive adhesive
K	Spring constant
l	Length
LCD	Liquid crystal display
LOC	Lab-on-a-chip
NCA	Non-conductive adhesive

Ni	Nickel
M_e	Masse of dry epoxy
M_t	Relative mass gain
M_w	Masse of water
MEMS	Micromechanical systems
Ox	Oxidation
p	Smallest value of α
$P1$	Pressure
P_{sv}	Saturated vapour pressure
Pt	Platinum
PBS	Phosphate buffer saline
PCB	Printed circuit board
$R1$	Universal gas constant
R	Resistance
RE	Reference electrode
RH	Relative humidity
Red	Reduction
S	Conductivity of the materials
$S1$	Shot time
SAM	Scanning acoustic microscopy
SEM	Scanning Electron Microscopy
SOC	System-on-a-chip
t	Time
T	Temperature in Kelvin
TC	Thermocompression bonding
TS	Thermosonic bonding

UC	Ulcerative colitis
US	Ultrasonic bonding
UBM	Under bump metallurgy
V	Voltage
V_{cap}	Volume
W_0	Weight of the dry specimen
W_t	Weight of the wet specimen
WE	Working Electrode
x	Distance
\bar{x}	Mean
x_1	Partial daisy chains in the x direction further away from the window
x_2	Middle daisy chain
x_3	Close to the window
y	Partial daisy chain in the y direction
z	Total daisy chain
z_i	Charge number on the species

Chapter 1 Introduction

The human gut is a complex and dynamic ecosystem which is composed of different microbial communities that are either permanently present in the gut or introduced from the environment [1]. There are around 100 trillion bacterial cells that have colonised the human gastrointestinal (GI) tract where they live in perfect mutual harmony with the human host. These bacteria play an essential role in the metabolic activities of breaking down food that is required by the human body. Until recently there was not enough information on the exact functioning of the GI tract [2]. This is due to the current limitations in the techniques used to collect data from the gut. These limitations could be overcome if a miniature system could move through the gut non-invasively and collect tissue samples, liquids or perform in situ measurements. This miniature system can be considered feasible due to the recent developments in microelectronics and wireless technology. These electronic systems can normally be found in the form of a capsule [3]. These capsule systems could help doctors study, understand and get more information about GI diseases and the state of the gut. The following sections will provide an overview of the human digestive system and inflammatory bowel diseases (IBDs) – the intended area of application for these capsules. An overview of the capsules that have been published in research or are reported commercial ventures will also be provided.

1.1. General overview of the digestive system

The human digestive system is a complex system that processes food to provide energy to the body. Put more precisely, the process involves ingestion, mechanical breakdown via mastication, deglutination which is swallowing of foods, digestion where enzymes and chemicals break down the food into absorbable molecules, absorption which is the passage of the absorbable molecules (nutrients) into the blood, and expulsion of waste material.

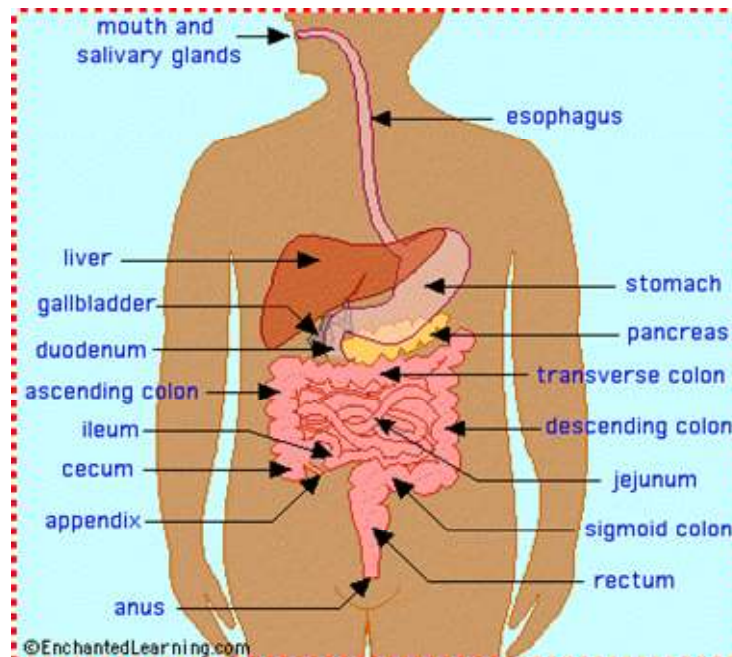


Figure 1.1. The Human digestive system [4].

The digestive system is made up of the digestive tract or Gastrointestinal (GI) tract and accessory organs. The GI tract is approximately 9m long and extends from mouth to anus. The GI tract consists of oral cavity, pharynx, oesophagus, stomach, small intestine and large intestine. The accessory digestive organs include teeth, tongue, salivary glands, liver, gallbladder and pancreas. Figure 1.1 shows the full digestive system with its GI tract and the organs involved in the digestion process [5,6].

Table 1.1 provides a summary of the digestive system organs and their function with the characteristic intestinal fluids and pH involved in the system [7,8]. As shown in Table 1.1, food starts to be digested as soon it enters the mouth. Mastication and saliva help break down the carbohydrates. It then passes through the oesophagus into the stomach.

Structure	Major digestive secretion	pH	Major digestive functions
Mouth – Lips, tongue, salivary gland	Saliva – salivary amylase, mucus, water, various salts	6-8	Mechanical Processing and start of carbohydrates break down. Moistening
Pharynx		6-8	Propulses bolus (food) from mouth into esophagus
Esophagus	Mucous	6-7	Lubricates. Propels food from pharynx into stomach
Stomach	Hydrochloric acid, pepsin, mucus, some lipase, gastrin	1-3	Stores, mixes, digests food, especially protein. Regulates even flow of food into small intestine. Acid kills bacteria
Small Intestine	Enzymes: enterokinase, amylase, lipase, nuclease, trypsin, lactase, maltase, peptidase, sucrase; salt water, mucus, hormones: cholecystokinin, gastric inhibitory peptide, secretin	6-7	Site for most chemical digestion and absorption of most water and nutrients into bloodstream
Pancreas	Enzymes: trypsin, chymotrypsin, carboxypeptidase, pancreatic amylase, pancreatic lipase, nuclease, bicarbonate	6-7	Secretes many digestive enzymes. Neutralizes stomach acid with alkaline bicarbonate secretion
Liver	Bile, bicarbonate	7-9	Secretes bile. Detoxifies harmful substances. Converts nutrients into usable forms and stores them for later use. Neutralizes stomach acid with alkaline bicarbonate solution
Gallbladder	Mucin		Stores and concentrates bile from liver and releases it when needed
Large intestine	Mucous	7.5-8	Absorbs salt and water from undigested food. Releases feces through anus. Aids synthesis of vitamins B ₁₂ and K
Rectum	None	7.5-8	Removes solid waste by process of defecation

Table 1.1. Major digestive functions and locations, collected from [7,8].

The function of the stomach is to store food, to initiate the digestion of proteins and kill microorganisms. Food stays in the stomach for approximately 4-5hr. In the stomach the food is

turned into a pasty material called the chyme which is then passed on to the small intestine. The small intestine is the primary site for the digestion of all the nutrients in the food. This is done with bile from the liver and pancreatic juices from the pancreas. The small intestine is divided into three sections called duodenum where most of the digestion takes place, jejunum, and ileum where the nutrients such as water, vitamins, and minerals are absorbed. The transition time through the small intestine is around 4-6hr. The chyme then passes through the large intestine. The large intestine is also divided into three sections: cecum, colon (ascending colon, transverse colon, descending colon, sigmoid colon, and rectum) and anal canal. The progression of the chyme through the large intestine is relatively slow (12-18hr). With the exception of water and salt, little digestion occurs in the colon. This is followed by the expulsion of the waste through the anus. In a healthy individual the whole digestion process takes between 24-48hr. The whole GI tract is prone to various distressing and fatal disorders, just to list some of them: oesophageal cancer, colorectal (colon and rectum) cancer, gastroesophageal reflux disease (GERD) which happens when the stomach acid flows back into the oesophagus attacking the lining of the oesophagus which can lead to Barrett's oesophagus disease, Crohn's disease and ulcerative colitis [9].

1.2. Inflammatory bowel disease

This project concentrates on one of the significant pathologies called inflammatory bowel diseases (IBDs). In medicine, IBD is a group of inflammatory conditions that affect the GI tract [10]. Although IBD can be divided into several categories, the two major forms of IBD are Crohn's disease (CD) and ulcerative colitis (UC) [11]. There has been a rapid growth of IBD in Europe and North America during the second half of the twentieth century and it is becoming more prevalent in the rest of the world as they adopt the western lifestyle [12]. CD and UC are chronic diseases which can lead to long-term and sometime irreversible impairment of the GI tract [10]. Despite the fact that there are no exact

known causes for CD or UC disease, several theories are put forward to explain their origins. It is believed that both CD and UC result from the interactions of genetic, immunologic, microbial and environmental factors [10,12,13]. It is also suggested that many features of UC could be bacteria driven.

1.2.1. Crohn's disease

Crohn's disease (CD) [10,11,14-17] is a chronic disease that can affect any part of the GI tract, but most commonly the terminal ileum, cecum, peri-anal area and colon. Inflammation extends through all layers of the gut wall and is characterized by patchy distribution, i.e. lesions with areas of normal tissue between them. The symptoms of Crohn's disease may vary, depending on the site and severity. The most common symptoms are diarrhoea, abdominal pain and tenderness over the intestine (often in the lower right area), weight loss, rectal bleeding, fever, tiredness and arthritis. The diagnostic methods for CD include blood and stool sampling, upper GI series, visual exam performed via sigmoidoscopy, colonoscopy and biopsy which is the collection of tissue samples from the intestinal wall. Treatment includes drug therapy, nutrition supplements, surgery or a combination of these options. However, there is no definite cure and there is a possibility that the disease could reoccur after long periods of remission.

1.2.2. Ulcerative Colitis

Ulcerative Colitis (UC) [10,11,14-17] is also a chronic disease in which the inflammatory process is limited to the rectum and the colon. The inflammation may extend in a continuous pattern throughout this whole region. The inflammation affects superficial (mucosal) layers with penetration of the white blood cell like lymphocytes and causes damage to the lining of the digestive tract. This is

characterized by deep ulcers and scarring to the intestinal wall. Ulcerative colitis is characterized by diarrhoea, anemia, fatigue, weight loss, loss of appetite, skin lesions, loss of body fluids and rectal bleeding. As in Crohn's disease UC is diagnosed by taking blood and stool samples, performing a colonoscopy, sigmoidoscopy and biopsy. Once again the treatment includes drug therapy, nutrition supplements, surgery or a combination of these options. There is no definite cure for UC and once again there is a possibility of reoccurrence of the disease after long periods of remission.

1.3. Diagnostic pills

As mentioned in the previous sections, one of the conventional methods used to investigate any suspected pathology is to use an endoscope which is inserted through the patient's mouth, nose or anus. These procedures provide some information: gastroscopy provides information about the oesophagus and the stomach while colonoscopy helps investigate the large intestine. These procedures are not only unpleasant for the patients, but are also unable to provide information from the small intestine.

With recent advances in microelectronics, wireless communication and sensor development, the limitations of endoscopy can be overcome in the format of a biomedical swallowable capsule [3]. The swallowable electronic capsule is an autonomous system which contains a sensor, the associated electronics for signal conditioning and amplifying and a radio transmitter all encapsulated in a biocompatible material. The swallowable capsule involves a non-invasive technique which can provide information about the whole GI tract. The concept of the first radio telemetry ingestible capsule was first put forward by R. Stuart Mackay and Bertil Jacobson in 1957 [3,18]. The swallowable capsules can be classified into families of imaging (PillCam, Olympus Optical) [2,18-20],

drug delivery systems [2,18,21] and sensing capsules [2,3,9,18,20-28]. Table 1.2 gives a detailed description of the different capsules that are available with their functions.

Type of capsules		Dimension	sensors	Developed by	other
Imaging	Pillcam	11x26mm	CMOS (Complimentary Metal Oxide Semiconductor)	Given Imaging	Optical dome, lens holder, lens, illuminating LEDs, battery, ASIC and antenna
	Olympus Optical	11x31mm	CCD camera	Olympus	Optical dome, LED lighting, battery life for 8 continuous hour, wireless transmission technology
Drug delivery system	Enterion capsule	11x32mm	Nil	Phaeton Research	Radio tracer, heater, electronics, RF antenna, actuating spring, piston and drug reservoir. Delivers any type of drug
	Intelisite	10x35mm	Nil	Innovative devices	Radio-frequency, shape memory alloy, one version delivers solutions and another powder
	iPill	11x26mm	pH sensor, temperature sensor	Philips	Microprocessor, sensors, fluid pump, wireless transceiver and silver oxide battery that lasts 48 hours
Diagnostic sensing capsule	Smart Pill	13x26mm	pH sensor, pressure sensor and temperature sensor	Smartpill Corp	16 bit analog to digital convertor, microprocessor, transmitter and 1.5V of silver oxide battery
	ipill	11x26mm	pH sensor, temperature sensor	Philips	Microprocessor, sensors, fluid pump, wireless transceiver and silver oxide battery that lasts 48 hours
	IDEAS (Integrated Diagnostics for Environmental and Analytical Systems)	12x36mm	pH sensor, temperature sensor, a conductivity sensor, electrochemical oxygen sensor, and NiCr resistance thermometer	University of Glasgow	The batteries, electronics and the magnet (to enable the tracking of the device in the GI tract) are protected by a hard chemical resistant epoxy resin

Table 1.2. Different swallowable capsules classified into different families, collected from [2,3,9,18,20-28].

Unlike the imaging and the drug delivery capsules where none of the parts are exposed (all the sensors and the electrical parts are sealed under a glass dome or hard plastic), the chemical sensing capsules have one or more sensors that measure biochemical variables related to the gut ecosystem through exposed sensors.

In a similar way to the chemical sensing capsules that are available in the market and in research, the project DIACAPS (Enterprise Ireland CFTD / 05/ 122) that partially supported this thesis work aims to use an electronic tongue (e-tongue) technology [29] that has been demonstrated to work in the food industry and apply it to the human gut environment. This sensor uses an electrochemistry technique to provide information on the solution under investigation. In order to use the e-tongue in a diagnostic sensing environment, it has to be integrated into a capsule format. This requires three areas of work which are: sensor integration, the development of the electronics body part to fit a capsule environment and performing analysis of the faecal fluids to identify the signature of healthy and non healthy individuals. In this project parallel work was carried out in all three areas. The work reported in this thesis concentrates on the development of a sensor interconnection method to enable the sensor to be in direct contact with the faecal fluids. There are different ways of interconnecting a sensor on to the printed circuit board (PCB) of the electronics in the capsule. The challenges involved in this are:

- Choosing the appropriate interconnection material;
- Picking the correct sealing material for the interconnection so that it will not only protect the interconnection but will also seal the underlying electronics;
- That the sealing material withstands the gut fluids;
- Making sure that the sensor interconnection withstands the capsule integration and that it does not affect the sensor functionality.

So the main aims of the thesis are to:

- Develop a method for sensor interconnection that has not been achieved for any of the other diagnostic sensing capsules;
- Characterize the sensor interconnection mechanically for sensor integration into the capsule;
- To test the reliability of the interconnection and the seal in the final environment and to build a first prototype e-tongue capsule.

1.4. Thesis outline

The thesis is organized into the following chapters:

Chapter 2 gives an overview of the sensor interconnection technology with the choice of interconnect technology that was chosen for the development of the technological demonstrator. It begins with a brief introduction into wire bonding technology and its application to sensor interconnection in the existing diagnostic sensing capsules. This will be followed by the alternative interconnection methods that are available, with a review of the different interconnection processes. In the final section, the chip's bond pad stack structure will be presented along with the reasoning behind choosing the interconnection that will be used to achieve the technological demonstrator.

Chapter 3 explores the development of the direct access sensor (DAS). This experimental part uses a Design of Experiment (DOE) approach to develop a sensor interconnection process, which is then tested in an electrochemical environment to establish the functionality of the sensor as well as the

joint. A preliminary sensor packaging method will also be described in this chapter. An assessment of the effect of encapsulation on the sensors and the interconnection's response is provided.

Chapter 4 describes the mechanical characterisation of the ACA joints during the capsule insertion process and identifies the smallest capsule diameter that could be used in the DAS integration process for a specific assembly.

Chapter 5 describes the electrical characterization of the ACA in a DAS. In particular the effect of moisture and ions on the leakage current of ACA will be described.

Chapter 6 depicts the reliability of the ACA in terms of contact resistance with accelerated life time (ALT) testing. ALT was used to accelerate the degradation mechanism of the ACA joint and to identify the dominant failure mechanism. Two distinct phases of testing were undertaken: firstly, a constant humidity aging of the ACA joint was carried out and this was followed by *in-vitro* testing.

Chapter 7 describes the integration of the capsule. In this chapter the integration of the DAC into the final electronic prototype is explained.

Chapter 8 discusses the novelty of the work carried out, the achievements of the research completed for the thesis and provides an outline for the future requirements of the final product and need for new technological development.

This thesis addresses some of the challenges faced in achieving a new highly reliable DAS that could be accommodated into a swallowable sensing capsule for measuring gut fluids. To provide a solution to this problem the process, a variation of flip chip, was developed on a flexible substrate which was then transferred onto the final prototype substrate for capsule integration. The influence of the mechanical pressure on the DAS joint in relation to the force applied when fixing it to the capsule was also characterized. The electrical characterization of the joint in response to moisture and its reliability in humid and *in-vitro* environments were verified. Finally, the sensor and battery integration into a folded serpentine form for the capsule was achieved.

Chapter 2 Background to the project

2.1. Background to the project

As mentioned in the introduction, the overall aim of the project was to develop a swallowable sensing capsule system that could take real-time measurements of the gut in the human body. As depicted in Figure 2.1, a swallowable capsule has all the parts placed in a small oval form so that it can easily be swallowed and moved through the GI tract via the segmental contraction and peristaltic movement [5]. In this sensing capsule, the sensor interfaces with the external environment through the opening provided for the sensor. The sensor measurements are communicated to the signal conditioning part via the interconnection. Different interconnection technologies such as wirebond technology or the flip chip technology that is used in other mainstream applications such as computer assembly could be used for the swallowable capsule.

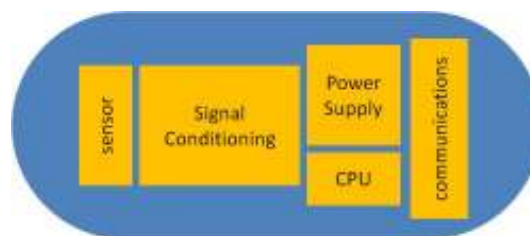


Figure 2.1. Schematic of the components of a swallowable capsule.

The aim of this chapter is to provide an insight into sensor interconnection technology used in diagnostic sensing capsules by reviewing wirebond and flip chip technology. The review of these different technologies with their different interconnection processes will provide some understanding of their issues and their advantages in order to choose a feasible interconnection that can be implemented for the DAS developed in the overall project.

2.2. Sensor interconnection methods

The following sections give an overview of the most common interconnect methods used for sensor interconnection.

2.2.1. Wirebonding

Wirebonding is the most common method used for sensor interconnection. It consists of using thin gold or aluminium wires to make connections between the bonding pads on the chips and the metallization on the substrates with a combination of heat, pressure and/or ultrasonic (US) energy [30]. First the chip is attached to the substrate face up with the help of a die attach. This is then followed by the wire bonding process. Depending on the bonding tool used (capillary or wedge) the wirebonding process could be classified as ball bonding or wedge bonding.

In a ball bonding process, the wire is passed through a hollow capillary and a small ball is formed by electrical discharge. As the wire solidifies, the surface tension of the molten metal forms a spherical shape which is then pressed to the bonding pad on the chip with sufficient force to cause plastic deformation and atomic interdiffusion between the wire and the underlying metallization. This guarantees the intimate contact between the two metal surfaces; see Figure 2.2(a). The capillary is then raised and moved to the substrate side.

In wedge bonding, the wire is fed at an angle of 30-60° through a hole in the back of a bonding wedge. Firstly the wedge is carried out on the chip bond pad by pinning the wire on to the bond pad, see Figure 2.2(b). It is then moved to the substrate side where the wire is torn off while the bonding force is maintained.

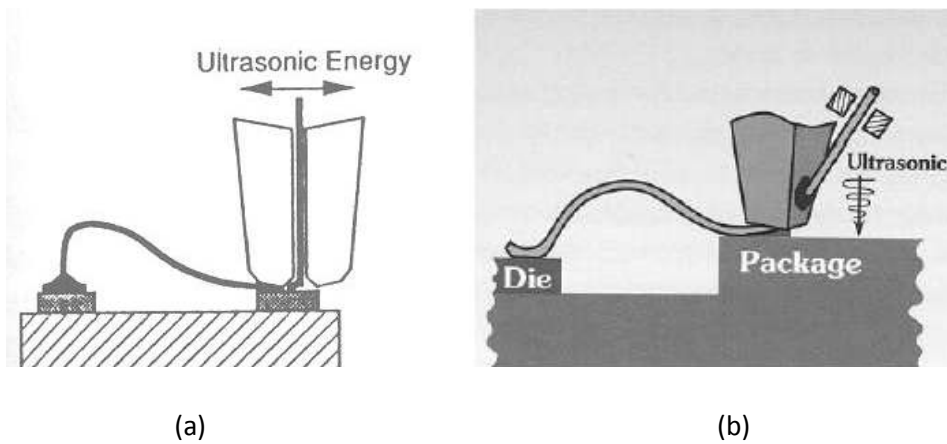


Figure 2.2. Sensors electrically connected to the substrate via (a) ball bonding; (b) wedge bonding [30].

There are three types of wirebonding; thermocompression bonding (TC), thermosonic bonding (TS), and ultrasonic bonding (US). All these methods create a solid state metal to metal contact between the chip bond pad and the wirebond. Table 2.1 illustrates the comparison of these three methods.

Wire bonding	Pressure	Temperature	Ultrasonic energy	Wire	Pad	Bonding technique	Ball bond	Wedge bond
Thermocompression	High	300-500°C	No	Au	Al,Au	Ball bond	Yes	No
Ultrasonic	Low	25°C	Yes	Au,Al	Al,Au	Wedge Bond	No	Yes
Thermosonic	Low	100-150°C	Yes	Al	Al,Au	Ball and Wedge Bond	Yes	Yes

Table 2.1. Comparison of three wirebonding methods [30].

Au and Al metallization are used for wirebonding. The Au-Au system is an extremely reliable bond. It requires either TC or TS techniques during bonding. This system is also highly biocompatible and can potentially be used as the bonding technology for the swallowable capsule. The Au-Al system is the most commonly used wirebonding process, but is prone to various reliability problems due to the formation of such intermetallic compounds as - Au₅Al₂, Au₄Al, A₂Al, AuAl and AuAl₂. Furthermore when this Au-Al system comes in contact with a humid environment it could lead to corrosion of Al by the formation of an electrolyte solution whereby the driving force could provide the electrochemical potentials between these dissimilar metals in the presence of an external bias [31].

The Al-Al system is a very reliable bond. No corrosion or intermetallics are observed in this bond system. It requires US, although a TC bond can be created by high deformation. Al is prone to corrosion if it comes into contact with HCl which is present in the stomach [32] or salt water which is present in the small intestine [33]. Consequently, it cannot be considered applicable to the swallowable capsule use.

2.2.1.1. Sensor interconnection methods used in diagnostic sensing pills

Smartpill

Smartpill [34] has an open recess in the dome of the biocompatible material through which the GI fluids come in contact with the sensor as shown in Figure 2.3. It contains a Microelectromechanical system (MEMS) based pressure sensor, a conventional ion-sensitive field effect transistors (ISFET) type pH sensor [22,35] and a temperature sensor. The ISFET sensor is derived from Metal Oxide Semiconductor Field Effect Transistor (MOSFET) technology where the current between the source and the drain is controlled by the gate voltage. The gate has a chemical layer which is sensitive to free hydrogen ions. Due to the commercial nature of the product no real information could be obtained about the interconnection of the pH and the pressure sensor. Liby et al [36] showed that for ISFET sensors used in catheters, both flip chip (FC) and wirebonding techniques could be used to achieve the interconnection. Ramesham et al [37] point out that a MEMS structure is at risk of structural failure during wirebonding because the small features tend to resonate at similar frequencies to those used during wire bonding. They also point out that there is a risk of damaging the thin diaphragm of the pressure sensor during FC bonding. However Shaw et al [38] outlined a design for a high volume MEMS pressure sensor which could be obtained by the addition of a dam to the wirebonded sensor and a film assisted mould process. Considering the fact that wirebonding technology is a mature technology often used in large scale high volume production, it can be said that wirebonding would be the preferred technology for the sensor attachment for smartpill.

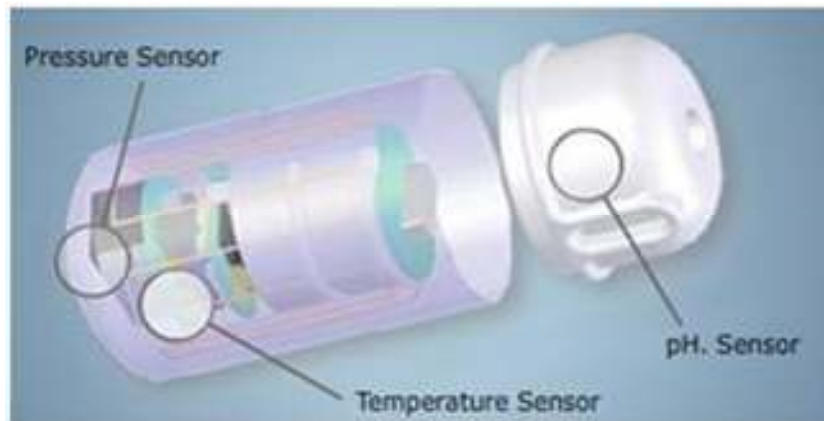


Figure 2.3. Smartpill [34].

Intelligent Pill (iPill)

The intelligent Pill (iPill) [21] contains a pH sensor, temperature sensor and a fluid pump. Once again due to the commercial nature of the product no information could be gathered about the pH or temperature sensors or the interconnection technology used. However, the mechanical design of the iPill shows that wirebond technology was being used as the interconnection method for the pH sensor; this is shown in Figure 2.4.

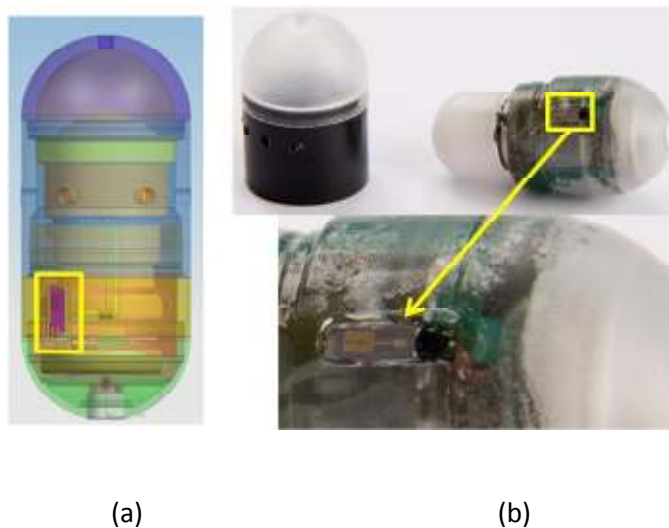


Figure 2.4. iPill by Philips (a) mechanical design showing the wire bonded pH sensor; (b) picture of the wire bonded sensor with the wire bond covered by epoxy [21].

The IDEAS (Integrated Diagnostics for Environmental and Analytical Systems)

Project

The IDEAS project device combines lab-on-a-chip (LOC) and a system-on-a-chip (SOC) technology as shown in Figure 2.5 [24,28,39]. It is a remote chemical imaging pill comprising of an ISFET pH sensor with an integrated Ag/AgCl reference electrode, a PN-junction silicon diode temperature sensor, a dual-electrode direct-contact conductivity sensor, electrochemical oxygen sensor, and NiCr resistance thermometer. The interconnection between the sensor chip and the chip carrier was achieved via wire bonding. The interconnection is protected from any fluid environment by placing it further away from the sensor. Access to these electrodes was achieved through a polyimide window opening on top of the electrodes. The batteries, electronics and the magnet (to enable tracking of the device in the GI tract) are either protected by a hard chemical resistant epoxy resin (Araldite 2020) or by integrating into a biocompatible capsule made from Polyether-terketone (PEEK). The package sensor access is achieved by either drilling a hole in the plastic cup attached to the sensor or via a rubber seal in the PEEK capsule.

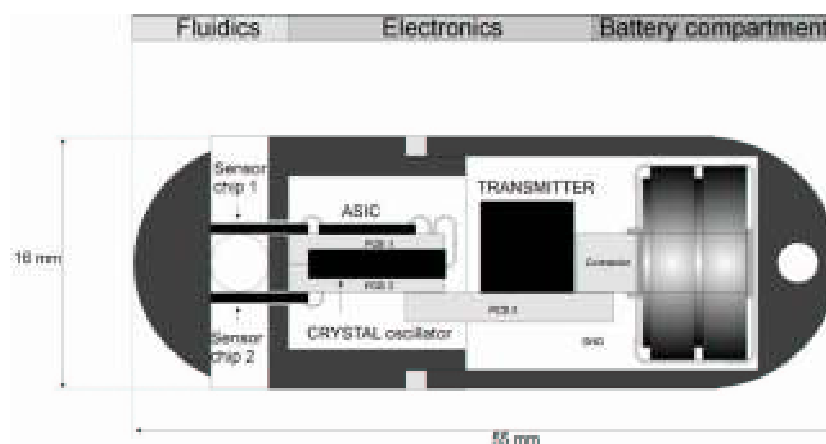


Figure 2.5. Schematic of first version of IDEAS [37].

Wire bonding seems to be the sensor interconnection method for the exposed sensor that is used in the diagnostic pills. Flip Chip (FC) is another interconnection method that could be used to interface

the sensor to the external environment [40-42]. The following section reviews the FC interconnection, the interconnection process and the choice of interconnection method for the DAS.

2.2.2. Introduction to Flip Chip (FC) and Flip Chip Over Hole (FCOH) technology

As seen in Figure 2.6, FC interconnection involves attaching the bond pads of a chip face down on to a substrate directly through interconnect material. This technology was first developed by IBM as a direct chip attachment method [43-45]. FC has the following advantages [46]:

- Small Size: Unlike wire bond technology, FC interconnection does not need peripheral space for electrical connection. Therefore the package footprint size is reduced.
- Highest performance: The short interconnection provides high speed electrical performance. Direct chip attach leads to a reduction of resistance, inductance and capacitance in comparison to wirebond technology.
- High Input/Output (I/O) Flexibility: FC technology utilizes the whole die surface area for interconnection and thus provides flexibility in the bond pad distribution.
- Rugged: Once the interconnection is complete, the use of underfill adhesive forms a solid block that provides mechanical strength to the joint.

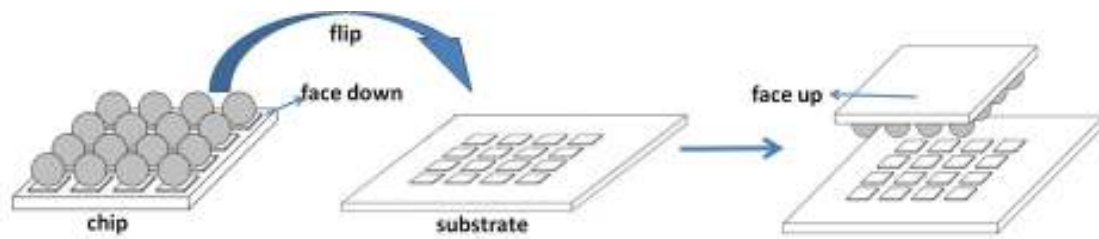


Figure 2.6. Schematic of FC process.

FC also has certain disadvantages some of which are described below:

- Unlike the wirebonding process where the chip is first placed on a substrate before interconnection, in the FC process the interconnection and the attachment occur at the same time. Therefore for some of the FC processes (adhesive FC), it is not possible to easily replace the chip.
- A flat surface is required to carry out the bonding. This flatness is hard to maintain as the board heats and cools during the interconnection process.
- The short connections are very rigid; as a result, the coefficient of thermal expansion (CTE) of the chip needs to be matched to the board so that no cracks or open circuits can occur in the connection.

The fact that there are more advantages in using FC than disadvantages has led to its use in high end applications such as the computer and electronics industries. In recent years it has been used in many electronic products such as LCD, mobile phones, calculators, watches, etc.

2.2.2.1. Flip Chip interconnection process

Figure 2.7 shows the different chip to substrate interconnection methods that are available to carry out the FC interconnection process. They are either metal joint interconnection, or contacting interconnection.

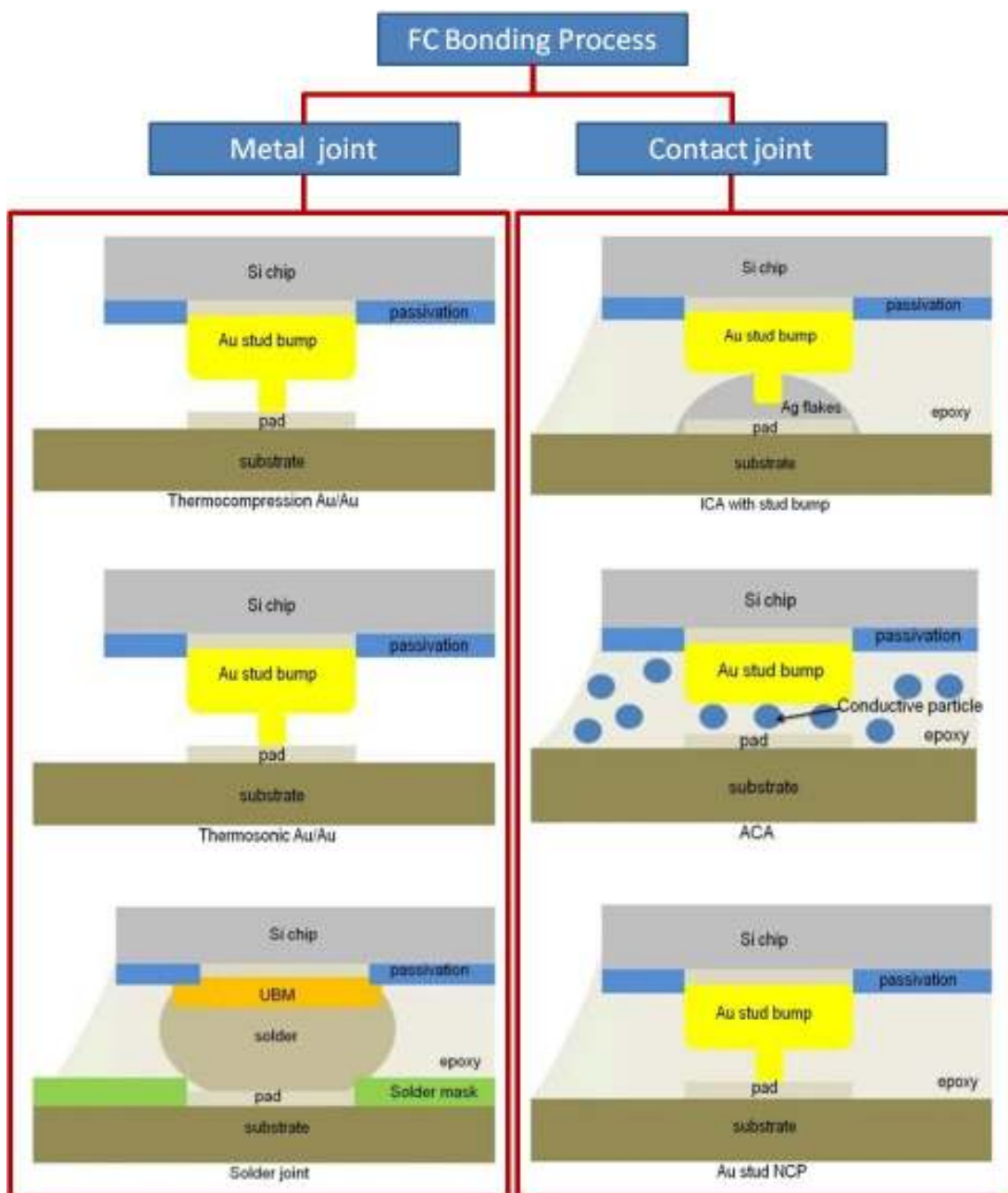


Figure 2.7. Different FC interconnection processes.

Flip Chip metal joint interconnection

In FC metal joint interconnections, the electrical connection is produced by intimate contact – metal diffusion – between the metals used in the chip pad and the substrate pad. This metal joint interconnection can be subdivided into three categories: thermocompression bonding, thermosonic bonding and soldering for the purposes of discussion.

Thermocompression (TC) bonding

Thermocompression bonding (TC) is a solid state metal to metal contact between the chip and the substrate achieved through applied pressure and temperature. In most cases, electroplated gold or gold stud bumps on the chip are bonded to either a gold or aluminium pad on the substrate. The bonding process is as follows: first the chip with gold stud bumps or electroplated gold on pads is aligned face down to the pads on the substrate. Then the chip is pressed down by the bonding tool while temperature is applied. The temperature and the pressure deform the gold and make intimate contact with the metal on the substrate bond pad, thus creating a metal-to-metal contact. This process requires a high temperature and pressure during the bonding process [46]. The applied bonding temperature is around 300°C while the applied pressure is around 156.25MPa and requires a rigid substrate to carry out the process [47,48]. As a consequence, this is not suitable for certain substrates such as FR4. In addition, high precision placement equipment which provides high accuracy parallel alignments between die and substrates with high planarity is required. Furthermore, the pressure imposed during the process could cause the die to crack. Underfill is not always necessary in the Au-Au interconnection processes but it does provide structural integrity to the assembly. It also helps minimize the stress that might occur due to thermal mismatch (CTE) between the die and the substrate.

Thermosonic (TS) bonding

Like TC bonding, thermosonic bonding (TS) also provides a solid state metal to metal contact. Once again, gold is the preferred interconnection material in this process. Either gold stud bumps or plated gold are used for chip bond pads. The considered metallization for the pad on the substrate side is either electroplated gold or gold thin film. The bonding process is similar to TC bonding except that the TS process uses ultrasonic vibrations to replace part of the thermal bonding energy. This enables the temperature used in TS bonding to be lowered from $>300^{\circ}\text{C}$ to around 150°C while high bonding pressures of around 75MPa are required [49,50]. This ultrasonic vibration softens the Au material during bonding process and thus helps Au-Au diffusion. It also greatly lowers the bonding process time [50]. It is used in LED technology, and in magnetic recording head technology [51]. In his work on FC of LED on silicon substrate, Kun et al [50] showed that an increase in temperature, pressure or bonding power has an adverse affect on the strength of the metal to metal bond. This work showed that although the initial temperature rise gives rise to a high contact area, any further increase in temperature causes the strength of the joint to decrease. This is attributed to substrate warpage due to high temperature. They also suggest a force of over 18N might cause damage to the device. They showed that a substantial increase in US power over 1.7W deteriorated the bump. TS require a high substrate planarity of $<3\mu\text{m}$ as well as stud bump height consistency [52], high precision placement equipment and high accuracy in parallel chip-substrate alignments [49]. High US power is required on organic substrates to get the same results as on ceramic substrates [52]. This is due to the “energy absorption effect” of the US power by oscillation of soft materials. Cheah et al [49] pointed out that any misalignment might cause misalignment of the joints while the lack of co planarity and parallelism will cause a cold joint on one of the sides due to a lack of pressure. High US power can also cause die cracking and pad damage [52]. US FC is relatively well suited for small IC connections but large ICs require high levels of planarity and homogeneity, so it becomes less suitable. Furthermore it requires an additional underfill process.

Solder bonding process

Solder bonding is the most traditional form of bonding used to provide an electrical connection. Tin based solders are often considered for the bonding purpose. However, due to environmental concerns relating to lead based solder in microelectronics and the alpha particle emission from lead isotopes issues for FC application have led to the increase use of lead free solder in the microelectronic industry [53]. A typical solder FC process starts with deposition of Under Bump Metallurgy (UBM) on the bond pads of the chip. The UBM is normally created by Physical Vapour Deposition (PVD), plating or a combination of these processes. The main purposes of the UBM are to:

- Provide good adhesion to bond pad metallization;
- To act as a diffusion barrier during solder bonding;
- To provide a solder wettable metal finish;
- To prevent oxidation of the surface [46].

Different UBM is used for different bumping processes as shown in Table 2.2. Solder deposition can be carried out via evaporation, electroplating, stencil printing, electroless plating, dispensing and solder jet printing techniques. The pad metallization could be copper/nickel/gold. The electrical connection is achieved by reflowing solder after chip/substrate to pad alignment. This provides better electrical performance by providing a low and stable contact resistance [54]. It is a well known process and it is easy to carry out rework of the solder interconnection. Most of the technical flaws associated with solder joints are known and tolerable during the manufacturing process. The short solder interconnection leads to low inductance at the connection [45,46]. Furthermore, solder has good thermal performance because heat as well as electrical current can be transferred through the joints [55]. Surface tension of molten solder 'self aligns' the chip to the substrate during the reflow process [56,57]. This minimizes any requirement for high precision placement equipment. However, in some cases, for example. solder bonding in fine pitch assembly, bridging of adjacent bond pads may occur. The CTE mismatch between the silicon chip and the organic substrate exerts large shear

stress on the joints [58]. This shear stress is proportional to the distance from the “neutral point” at the centre of the chip. This situation can lead to failure of the solder joint during thermal cycling. Underfill is always used with the soldering process [59]. It is introduced between the die and the substrate where it forms a solid block once cured. This solid block provides mechanical stability to the solder joint and can enhance the solder joint fatigue life. The use of underfill reduces the thermal stress on the solder joint by redistributing it among the chip, underfill, substrate, and all the solder joints. Thus the stress concentrations on the peripheral joints are reduced. Numerous process steps are involved in solder bonding. These include pre cleaning of the chip/substrate, and post cleaning of the flux residues before underfilling the reflowed assembly. It also requires a solder mask to stop the solder from bridging to an adjacent pad, and most important of all, a solderable surface finish is required to carry out the soldering process.

UBM	Evaporated (typical of C4)	Plating I	Plating II	Solder Paste printing	Electroless Nickel
Adhesion layer	Cr	TiW	CrCu	Al	Ni
Solder diffusion layer	Phased Cr-Cu	Cu stud/mini bump	CrCu	Ni	Ni
Solder wettable layer	Cu	Cu	Cu	Cu	Au
Oxide prevention	Au	Au	Au	Cu	Au

Table 2.2. Different UBM used in different bumping process [46].

FC contact bonding

In FC contact bonding, the electrical connection between two metals is obtained by bringing the chip pad and the substrate pad into contact via another metal. There is no diffusion between the metals and there are three ways of producing these contacting joints. They are isotropic conductive adhesive (ICA), which conducts in all directions, anisotropic conductive adhesive (ACA) which only

conducts perpendicular to the substrate/chip surface and non-conductive adhesive (NCA) which is essentially glue and provides isolation in all directions.

Isotropic conductive adhesive bonding

ICAs are adhesive materials which are loaded with conductive particles in a thermosetting polymer matrix which provide electrical conduction and thermal conduction in all directions [60]. Silver (Ag) is the most common conductive particle used for ICA formulation. It is normally screen printed on to the substrate bond pads or dip transferred on to the bump on the chip bond pad. When using the dip method Au stud bumps are pre-formed on the chip pads which are flattened to a certain height (coined). These studs are then dipped on to ICA whereby conductive material is transferred on to the bump. This is followed by the chip and substrate alignment and the bonding takes place by applying temperature at around 150°C. ICA has around 25-35 volume percent filler content [61] which is above the percolation threshold (this is the point at which the electrical resistivity drops suddenly due to a high concentration of particles forming a conductive network). The electrical contact is obtained through a network of contact points between individual particles [62,63]. It requires an additional underfill step to compensate for the thermal mismatch [46,64] and to increase bond strength. ICA has been mostly used in flip chip and surface mount technology (SMT). Its application ranges from die attach for small passive chips in automotive electronics, RFID tags [65] and LCD displays [62]. Some of the main draw backs of ICA include moisture absorption, silver migration and galvanic corrosion between dissimilar metals [61,65]. For further development in the ICA field an excellent review of this topic has been provided by Morris et al [65]. In the ICA process no self alignment is possible, and therefore there is a requirement for high precision chip to substrate alignment equipment.

Anisotropic conductive adhesive bonding

ACA can be applied in different forms: paste (ACAP) and film (ACF) and is generally composed of conductive particles dispersed in an epoxy based polymer matrix. The most widely used epoxy resins are diglycidyl ether of bisphenol A (DGEBA) and diglycidyl ether of bisphenol F (DGEBF) [66]. In the work of Lin et al [66] it was suggested that the outstanding performance of the resin was attributed to the bisphenol chemistry (toughness, rigidity, and elevated temperature performance). In this material the ether linkages are responsible for the chemical resistance, while the hydroxyl and epoxy group are responsible for reactivity with various chemical curing agents. Bisphenol F epoxy has the same characteristics as bisphenol A but has lower viscosity. The conductive particles are either metallic or metal coated polymer spheres. The chip bond pads are Au stud bumped. As with ICA, these Au stud bumps are then coined to be of a specific height. ACAP is dispensed or screen printed on to the substrate bond pad which has bondable metallization such as Au-plating [46,67]. This is followed by chip and substrate alignment using fiducial marks and then the bonding takes place by applying a bonding pressure of 50MPa, and applying temperature of around 180° - 200°C for 5 – 10sec [67]. The electrical connection is made by trapping the conductive particles between the raised pads of the chip and substrate. The volume fraction of particles used in ACA is around 5-10 volume percent, which is well below the percolation threshold [63,68]. Due to this low volume fraction of particles, there is no conductive path in the x-y direction and conduction only occurs in the z direction and therefore no risk of shorts between the closest pads arises [61,63].

ACA has been used in several applications such as Application Specific Integrated Circuit (ASIC) in radio transmitters, Personal Digital Assistants (PDAs), sensor chip in digital cameras, memory chips in laptop [69], LCD panels [70,71], etc. Numerous studies have been carried out on the bonding conditions and the contact resistance. For example, Yim et al [70] developed an electrical conduction model with a physical contact mechanism to understand the electrical conduction of ACF. They suggested that the electrical contact resistance depended on pressure, the number of particles, their

size, the material properties of the particle and their mechanical and electrical properties. As the pressure increased the resistance decreased until a certain critical pressure was reached where the contact resistance remained constant but further pressure increase led to increased contact resistance. This was explained by the viscoelastic behaviour of the epoxy after the pressure release (Viscoelasticity is the property of a material to exhibit both viscous and elastic behaviour when deformed). Instead of the customary volume percent used to present the fraction of the particles present in ACA, Yim et al [70] presented the fraction of particles present in the ACA in weight percent. They concluded that the increase in the number of particles decreases contact resistance and becomes constant for over 4 weight percent of the particles. This was explained by the two opposing factors that come into play as the number of particles is increased. The increase in particle numbers exerts less pressure per particle thus reducing the contact area but the number of particles present causes the resistance to decrease. They also suggested the mismatch in CTE between the Ni particles and metal coated conductive particles in an assembly will have a high impact on reliability. A theoretical characterization of electrical contact in ACA was studied by Fu et al [72]. They suggested that the spatial position of the conductive particles also affects the contact resistance. Frisk et al [71] studied the effect of different chip and substrate thicknesses on the reliability of the ACA FC joints. They concluded that a thin substrate and a thin chip had a higher performance during temperature cycling test than the thicker samples. This is due to the fact that both the thin chip and substrate are both more pliable and consequently the assembly may warp thus leading to lower shear strain. The effects of different temperatures on the reliability performance was studied by Chan et al [73], who concluded that the degree of cure of the ACA was determined by the bonding temperature. With too low a temperature, the epoxy and the conductive particles move at a slow rate. Moreover, there is under curing of the epoxy. Too high a temperature cure will prevent the particles from spreading evenly and might cause the chemical bonds in the cross link to degrade. The effect of temperature ramp rate on FC ACA joint quality and reliability has also been studied by Gustafsson et al [74]. Their study suggested that a slow temperature ramp rate provided a better

joint quality than a high temperature ramp rate, as a high temperature ramp rate will risk the adhesive being cured before a full compression of the particle was reached. Bivragh et al [43] suggested that a planar bump would provide a better reliability than an undeformed gold bump. The low process temperature favours the use of different substrate materials. Unlike the soldering process where a solderable surface is required to make the interconnection, the ACA process is compatible with a wide range of surfaces including non-solderable ones. There is no requirement for a solder mask in order to keep the adjacent bond pads from being shorted and it also has considerably less process steps. As seen with ICA, the ACA process does not allow self alignment between the chip and the substrate which is necessary in order to obtain good reliability [67,75]. This approach also requires high accuracy placement equipment. On thermosetting polymer adhesive, no rework can be carried out.

Non-conductive adhesive

Non-conductive adhesives (NCA) are epoxy based polymers (b-stage epoxy) or thermoplastic materials without conducting particles [75]. Different bump types such as electroplated Au bumps, electroless Ni immersion Au bumps or Au stud bumps could be used for the chip bond pad. The most common method is the stud bump method. Again the bonding is carried out by picking, aligning, placement and attachment of the chip to a substrate with any bondable metallization such as Cu, Au, Al etc [76]. The contact between the stud bump and the metallization on the substrate bond pad is obtained by applying pressure and temperature. Typical bonding pressure is around 100MPa with an applied temperature of around 175°C for a period of 10sec [75]. It is a physical/mechanical contact and no metallurgical joints are obtained [77]. However, Pendse et al [78] argue that the connection between the stud bump and the metallization on the substrate pad is metallurgical. However, they never performed fracture analyses on the surface of the bond pad to prove that the stud bump used with NCA produced an intimate metal contact. Recently

thermosonic FC with NCA on to flex has been demonstrated by Cheng-Li et al [79]. Once again a precise alignment and coplanarity is required to get a good interconnection.

Conductive adhesives are made up of polymeric materials, which makes the material susceptible to moisture absorption. ICA moisture absorption could lead to galvanic corrosion between dissimilar metals [61,65]. Moisture absorption of the ACA has been reported in literature [66,80,81]. Moisture penetration is also of concern for the NCA assembly because this could lead to pad corrosion if Al was used as the chip metallisation [78].

Figure 2.6 showed an example of the structure of the die where all the above mentioned processes could be applied. It can be seen that the face up side of the chip is just bare silicon (Si) which makes it easy for the bond head to be placed to apply pressure during bonding. In the case of a sensor that needs to be exposed, the sensor will be placed in the die face up, otherwise the FC tool could not be used; and this means that the FC interconnection method has to be considered as a second level interconnection (Ball Grid Array – BGA), as shown in Figure 2.8. This method will considerably increase the cost of the product and would take up a lot of space in a swallowable capsule. This would force a fall back to the wirebonding version as mentioned when considering the interconnection method used in the Smartpill. For a capsule package it is crucial to keep the size of the first level packaging to a minimum and this is only attainable by using bare die flip chip and this type of FC package for sensor is explained in the next section.

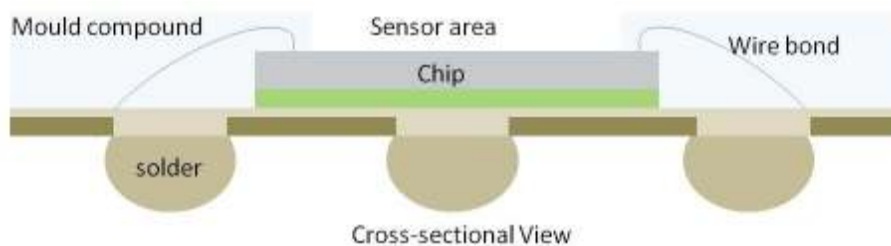


Figure 2.8. Schematic of sensor placed face up on the same side as the bond pad for FC interconnection.

2.2.2.2. Flip Chip Over Hole (FCOH) or Direct Access Sensor (DAS)

FCOH is a variation of FC interconnection whereby the sensor is placed on the side of the interconnecting bond pads, as shown in Figure 2.9. The sensor attachment is carried out by flipping the die and attaching it face down on to a Printed Circuit Board (PCB) which has an opening to allow interaction between a sensor die and the environment it is supposed to be measuring. This is illustrated in Figure 2.10.

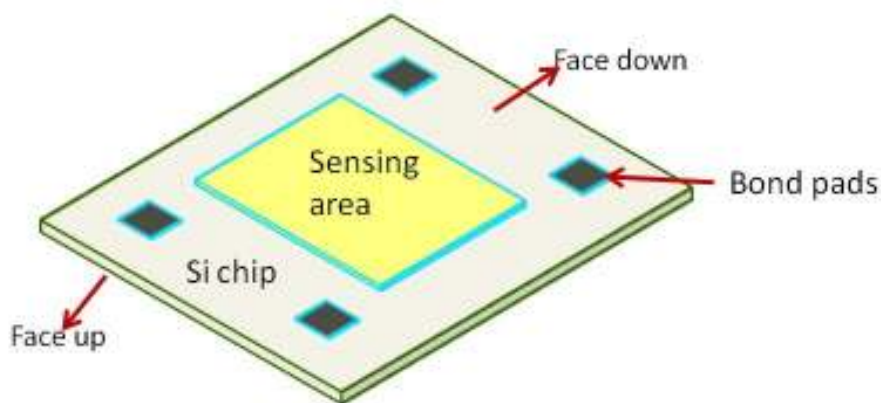


Figure 2.9. Schematic of sensor face down.

FCOH is of particular interest for systems with low I/O count technology such as sensor attachment [40-42]. However, there are certain constraints with FCOH for Direct Access Sensor (DAS) attachment and it is necessary to:

- Avoid covering the electrode with any material used in the interconnection process.
- Provide mechanical strength to the joint during sensor integration into the capsule.
- Provide electrical insulation to the joint and the underlying electronics while the sensor is exposed to stomach acid and powerful digestive enzymes for 72hr.

All the above mentioned interconnection processes are viable options for the FCOH DAS. However, one of these interconnection processes has to be selected for the microelectronic sensor developed for this research. The next section will detail the microelectronics pad metallization scheme and explain the choice of the interconnection process chosen for the FCOH DAS capsule application.

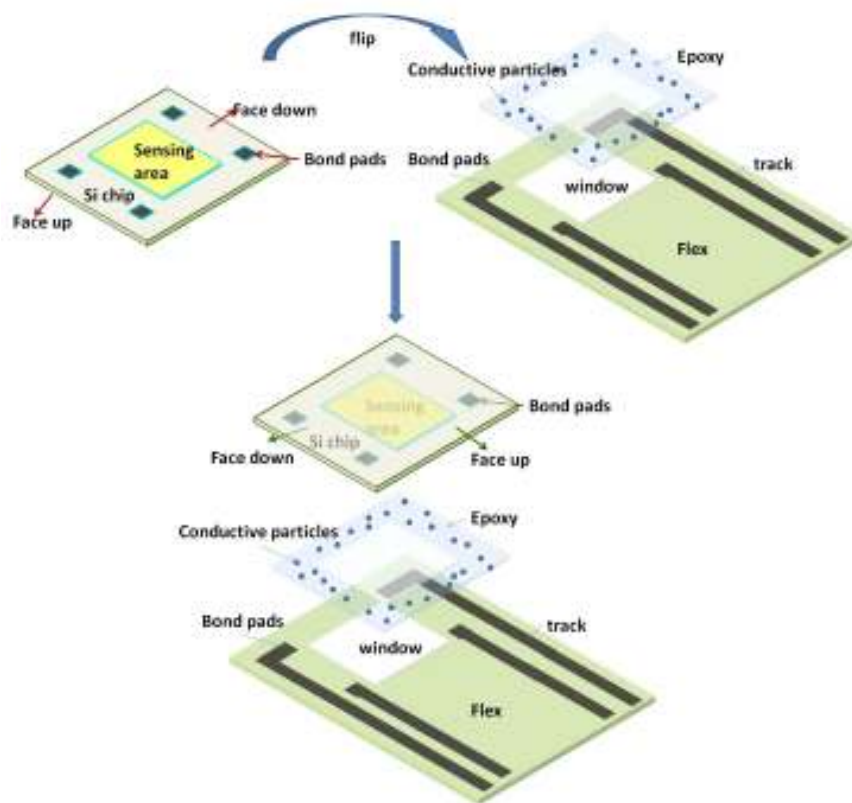


Figure 2.10. Expanded schematic of FCOH process.

2.3. Choice of interconnect scheme for the swallowable capsule project

2.3.1. Microelectronic sensor chip – pad metallization scheme

Figure 2.11 shows the pad metallization scheme used in the microelectronic sensor. It can be seen that a gold finish has been used in the chip finish as a protective layer. In a solder bonding approach, a chemical reaction between the solder, surface finishes and the underlying metal can lead to inter-metallic formation. It is well known that the inter-metallic layers between the solder material and base metal are a sign of good metallurgical bonding. It is also known that during soldering the gold layer dissolves and an inter-metallic layer is formed with the underlying metal [82].



Figure 2.11. Schematic of deposited stack layer of the microelectronics sensor.

Gold dissolution in molten solder

The rate of dissolution depends on the base metal, solder composition, temperature, cleanliness and solder velocity [82]. Figure 2.12, acquired from efunda solder guide lines [83] shows the dissolution rate of different metals used in the surface finish of most of the bond pads.

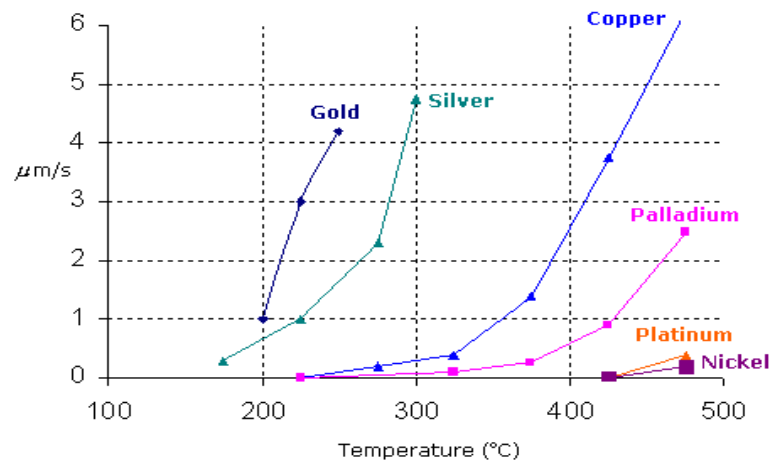


Figure 2.12. Dissolution rate of gold.

It can be seen from this that at around 250°C 4μm of gold metal would be dissolved per second. However, from Figure 2.11 it can be noted that there was only 200nm of gold deposited on the microelectronic sensor chip pad. This means that all the gold will dissolve into the solder and the solder has to form intermetallics with the underlying chromium. But chromium is not solderable [84,85]. This meant that solder was not an option for this application.

Since Au is a biocompatible material that can be used in the body environment, thermocompression Au-Au bond is a viable option to be considered for the DAS interconnection for the capsule. The fact that only the rigid substrates are suitable for TC bonding means that a high cost will be added to the final product. Even though underfill is not required for other applications, in a capsule environment it is a requirement because it will protect the underlying electronics. This makes it a two step process. Furthermore, the high temperature that is normally used in the curing of the underfill could harm the electronic components that would have been included in the final prototype substrate. Keeping in mind that the final product is for single use, the cost of the DAS attachment should be kept to a minimum. Taking into account the cost issue; the other additional step require for FC

process and other issues that could occur during bonding, the TC bonding was deemed to not be an option for this application.

TS bonding is also a feasible option due to the reasons mentioned for the TC bonding but it is not suitable for large dies as it might cause the die to crack during bonding. It also required an additional underfill process when considered for the capsule application. Due to these reasons the TS bonding was not considered for this application.

ICA has been applied for other applications as mentioned in the above sections and is still a viable option to be considered for the DAS. Similar to TC and TS interconnection, ICA requires an additional underfill process to achieve a reliable DAS. The issue involved with underfill curing in relation to the final prototype was the reason in not considering ICA interconnection for the DAS.

ACA and NCA are once again perfect candidates for the DAS interconnection. Similar to ACA, The NCA process could involve bonding and curing at the same time. Even though the Au stud bumping is biocompatible, there is no information on the epoxy's biocompatibility that is used in ICA, ACA and NCA. Although fully cured epoxy is generally considered non toxic [86], an incomplete curing of the epoxy might lead to release of potentially allergic compounds into the body. Bivragh et al [43] showed that for a similar type of ACA that is used in this research, there was 95% cure in the epoxy matrix at 200°C. Even though they obtained a 98% cure in the epoxy matrix at 220°C, they concluded that it was preferable to carry out the processing at 200°C in order to reduce the processing time and thermally induced processing stress. In this research, as suggested by Bivragh et al [43] and Gustafsson et al [74], a planar bump, a slow temperature ramp rate and the cure temperature of 200°C was considered for the FC process. Bivragh et al [43] also suggested that a 100% cure in the

epoxy matrix was very difficult to achieve. Furthermore as there is no biocompatible ACA available in the market, this thesis aims to develop a reliable DAS process based on ACA and then assess the biocompatibility issues after a reliable process has been defined.

In comparison to NCA assembly, the ACA assembly would add an extra height to the assembly due to the presence of the conductive particles that have to be trapped in-between the bond pads to provide conduction. This extra height in the ACA assembly might create additional mechanical stress on the assembly [87], but Bivragh's work [43] showed that the coining of the bump provided better reliability. The risk with NCA assembly is the application of high pressure as this might endanger the chip and cause chip cracking. Due to this reason NCA process was not considered and ACA process will be used in the DAS interconnection.

2.4. Conclusions

In this chapter, a review of different interconnection technologies that could be used for sensor interconnection for a direct access sensor-capsule environment has been presented. First, wire bonding technology was presented with its different processes; their advantages and their disadvantages. A review of all the diagnostic sensing pill sensor interconnection showed that wirebonding was the preferred interconnection method.

The second part showed that FC interconnection is also possible for direct access sensor interconnection. In FC interconnection the processes are classified into metal bonding or contact bonding depending on the nature of the bond. Metal bonding consists of TC, TS and solder bonding where an intimate contact between is obtained during bonding. The advantages and disadvantages of each process were presented along with their application in other fields. Contact bonding

comprises ICA, ACA and NCA bonding where a contact is provided by either the conductive particles or the metal used in the process. These are polymeric materials and possess their own advantages and disadvantages with respect to their application. It was shown that these processes apply to a technology where the chip's upper side was bare silicon, thus making it easy to place the bonding head.

In a DAS using a variation of FC technology the sensors are placed on the same side as the bond pads and the bonding substrate contains a hole so that the sensor can interact with the external environment. The challenge in using such a technology is that care must be taken not to cover the electrode with any material used in the interconnection process, because covering the electrode might hinder the sensor functionality. It is also crucial that the interconnect survives the system integration and continue to function reliably in the gut for 72hr.

With the exception of solders, all the FC interconnection processes were feasible options for the DAS attachment. This is because the bond pad structure used in the chip does not accommodate the soldering process. After considering the pros and cons of each FC process with respect to the development of the DAS and its integration in the final capsule prototype, ACA was deemed to be the suitable one. Furthermore as there is no biocompatible ACA available in the market, this work aims to develop a reliable DAS process with ACA before its biocompatibility can be assessed.

This review chapter showed that although FCOH was used in other areas such as neonatal catheters, it has never been considered for sensor attachment in a diagnostic sensing capsule and more specifically the use of ACA in the DAS. This thesis aims to develop a DAS using ACA interconnection method. The challenges include the development of the ACA interconnection without covering the sensor electrodes and to qualify the joint for sensor integration and its final application. Chapter 3

provides a detailed insight into the choice of DAS placement with the development of the DAS using ACA and its qualification via shear testing.

Chapter 3 Development of the DAS

3.1 Introduction

As shown in Figure 2.10, a direct access sensor (DAS) needs to be mounted as Flip Chip Over Hole (FCOH) on a flexible substrate. Anisotropic conductive adhesive (ACA) is the material of choice to achieve electrical interconnection while simultaneously sealing the interconnect area from the sensor area.

ACA is available in two forms: film (ACF) and paste (ACP). The overall aim of this work was to produce a low cost, disposable capsule. It was therefore essential to limit the cost of development of the DAS/FCOH sensor. Both ACF and ACP are good candidates to develop the DAS. With ACF there is good control of volume, density of particles in a sample, and the distribution of the particles within the sample. Due to these advantages, it is mostly considered for fine pitch applications [69]. For the DAS, the use of an ACF would require an additional tool to be made to cut the film and remove the window area so that the sensor can be exposed. In addition, ACF adhesion to the chip was found to be very poor. This poor adhesion could be explained by the processing issues. In comparison to ACF, ACP cannot provide the same level of adhesive volume control or particle dispersion. ACPs are generally less expensive than ACF and were also found to have better adhesion to the chip. For these reasons, ACF was rejected and ACP was chosen to use as in-house dispensing equipment could be utilized. Hereinafter, during the whole thesis, ACP will be addressed as just ACA.

The downside of using ACA is that it needs to be selectively dispensed and doesn't allow FC alignment before dispensing. As a transparent ACA could not be found, a brown opaque ACA was chosen as the interconnect material. Due to the opaque ACA, the pad features on the substrate will

not be visible for chip bond pad alignment. In a sensor FCOH, the presence of the large sensing area, the peripheral placement of the bond pads on the chip and the presence of the window on the substrate inhibits the placement of fiducial marks and the only option is to dispense the ACA within the confines of the bond pads. Screen printing and stencil printing are the most commonly used methods for depositing materials like ACA before bonding. However, for this work with 300 μ m wide bond pads, a liquid dispense system was used to deposit the paste in the form of dots on to the substrate before the FC bond pad alignment. The ACA can be directly dispensed on top of the bond pads while a separate pattern can be used for insulating and sealing off the sensor. This chapter describes the experimentation carried out which resulted in the qualification of a suitable ACA dispense pattern through shear testing. Finally, it reviews the sensor placement options for a capsule environment.

3.2. Experimental details

The objectives of this work are to: (i) identify the parameters that control the dispensing of the ACA so that a small deposit footprint and volume can be achieved on the bond pads, thus achieving a repeatable deposition process so that identical interconnect joints could be formed; (ii) qualify the dispense pattern through shear test after hygrothermal aging, and to monitor the mechanical behaviour of the adhesive joint exposed to environmental effects; (iii) demonstrate that the process provides a DAS with proper sensor and interconnect functionality and finally (iv) review DAS sensor placement options. Details of the sensor die, the flexible substrate, ACA, and the bonding process are presented in the following sections.

3.2.1. Materials

3.2.1.1. Sensor chip

The test chip is a 6mm x 6mm die with a thickness of 0.525mm. It was fabricated on a wafer using a silicon multi-layer process and photolithography techniques. The sensing chip has five interconnect pads on the periphery with a pad size of 300 μ m square as shown in Figure 3.1. A 500nm silicon nitride passivation layer was applied over the chip with open areas around the electrodes and the bond pads. The sensor comprised of three gold (Au) working electrodes (WE) of 1mm diameter, a platinum (Pt) counter electrode (CE) of 2mm diameter and a platinum reference electrode (RE) of 1mm diameter. The distance between the centres of the counter electrode and the working electrode was set at 0.5mm. The sensor chip electrodes are used to evaluate the liquid medium with cyclic voltammetry.

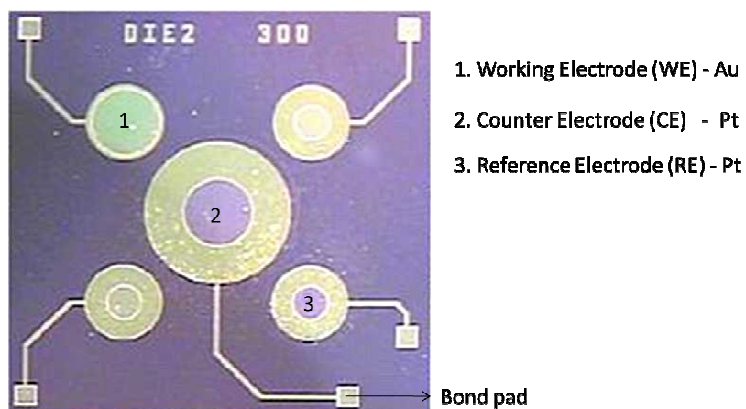


Figure 3.1. The direct access sensor chip.

3.2.1.2. Test substrate

Figure 3.2 shows the 0.025mm thick single layer thin polyimide substrate that was used to test the sensor. The copper tracks on the flexible substrate were 15 μ m thick while on the substrate bond pads an additional 5 μ m Ni and 0.05 μ m of electroplated flash gold were deposited. The flexible substrate was 77mm long, with a circular section of radius 6mm on one end, a 3mm wide middle section and 11.25mm wide fanned-out section on the other end. A square window of 4.4mm was cut from the centre of the circular section of the board with a laser cutting tool to expose the sensors to the external environment.



Figure 3.2. Flexible substrate with window opening for sensor access.

3.2.1.3. Anisotropic Conductive Adhesive paste (ACA)

The ACA Henkel & Loctite (FP5300) was chosen for this research. This material contains hard conductive particles of gold (Au) coated nickel (Ni) particles with an average particle size of 7 μ m. As it was not possible to measure the ACA properties due to lack of availability of test equipment, the manufacturer's data was used throughout the thesis. Table 3.1 gives the specification of the ACA used in this research. The ACA material was dispensed on the test board using a CAM/ALOT 1414 liquid dispense system.

Properties	ACA
Colour	Brown
Matrix Material	Epoxy
Conducting particles	Au-Coated Ni spheres
Average particle size (μm)	7
Glass transition temperature ($^{\circ}\text{C}$)	126
Coefficient of thermal expansion (45 to 90°C) – CTE ($\text{ppm}/^{\circ}\text{C}$)	47
Viscosity (cP)	87000
Particle density per cm^2 †	8.3×10^4
Dielectric Constant	3.56
Resistivity (Ω)	< 0.1
Insulation resistance ($\Omega \text{ cm}$)	2×10^{13}
Dielectric Strength (V/cm)	2×10^5

† Measured by experiment in section 3.2.3

Table 3.1. Material specification for the conductive adhesive.

3.2.2. Bonding process

A pre-cleaning procedure was carried out separately for both the chip and the substrate. This involved placing the chips and the substrates into a barrel type chamber of a March Plasmod system and exposing them to an oxygen plasma for 40sec at 150Watts. This was followed by IPA immersion in a bench top Ultraware ultrasonic precision cleaner for 5min followed by a deionised water rinse. The samples were then dried in a Heraeus vacuum oven at 150°C for one hour. Any grease, oil and solid residues present on the chip and the substrate are removed at this pre-cleaning stage [89].

Gold stud bumps were formed on the die pads using a Kulicke and Soffa ball wedge gold bonder. Figure 3.3(a) shows the stud bump which had a mean diameter of $103\mu\text{m}$ and a mean height of $108\mu\text{m}$. This was followed by coining the gold stud bump onto a glass substrate using a Finetech Fineplace 96 Lambda flip chip bonder. The main purpose of the coined stud bump is to maximize the contact area during the assembly of the device onto the substrate. The gold stud bump was coined

at 26MPa at a coining temperature of 180°C for 20sec. Figure 3.3(b) shows the diameter and the height of a coined stud bump which are around 123µm and 19µm respectively.

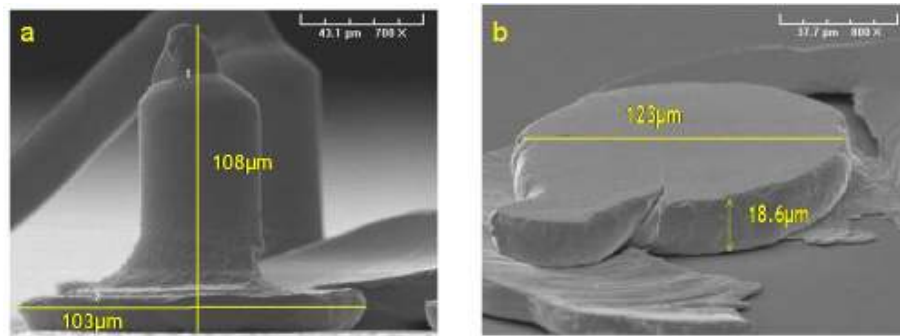


Figure 3.3. SEM image of: (a) a gold stud bump; (b) a coined stud bump.

The alignment and bonding of the chip/substrate was performed using the same Finetech Flip-Chip bonder. Bonding was carried out at a ramp rate of 2°C/sec with a hold at 200°C for 50sec and a cool down rate of 3°C/sec, as shown in Figure 3.4. During the bonding process of a 300µm square bond pad chip, a bonding pressure of 22MPa for 8sec was used to achieve a satisfactory bonding. The average bond line thickness of the adhesive taken from 10 samples was approximately 7µm with a standard deviation of 1µm.

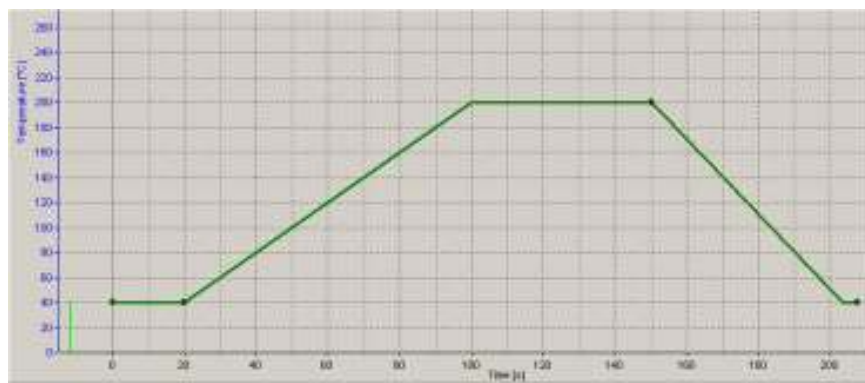


Figure 3.4. ACA Reflow Profile.

The next section will look into the development of the interconnect, more precisely the ACA dot footprint qualification by using design of experiments (DOE), environmental testing and the characterisation techniques.

3.2.3. Estimating the number of conducting particles

To estimate the number of particles per bond pad, ACA was dispensed on to the bond pads and then bonded to a thin piece of microscope slide glass. The thin glass microscope slide was then separated from the bond pads and the bond pad area was magnified 90 times under an Olympus SZX12 microscope. Image J [90] is a public domain, Java-based image processing program. The magnified images were then processed via image J software to count the number of conductive particles in the bond. Figure 3.5(a) shows the mosaic picture of a 300µm square pad with its processed image from image J shown in Figure 3.5(b). The processed image showed that there was an average of 8.3×10^4 particles per square centimetre. So for a 300µm square pad, there are on average 79 particles, 10 particles per 100µm square pad and 363 particles per 500µm square pad.

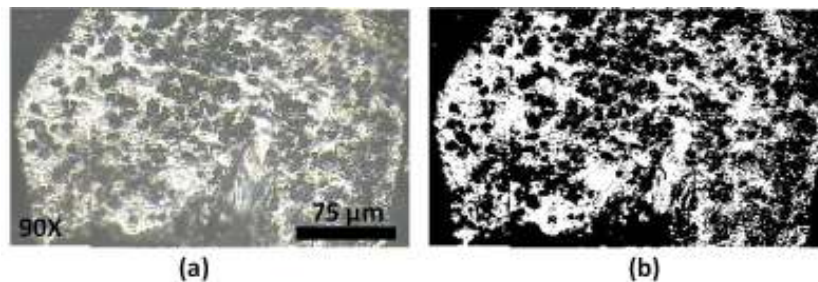


Figure 3.5. Images of ACA particles: (a) Composite image of 300µm square pad with ACA particles in gray scale; (b) processed image via Image J software showing just the conductive particles on the right side.

3.3. Design of Experiments (DOE)

3.3.1. Dot diameter qualification through DOE to achieve the smallest footprint

For this research, a CAM/A LOT contact dispensing system was used to dispense ACA. It can dispense either dots or lines. Preliminary trials with this in-house dispensing system showed that the width of the dispensed lines weren't repeatable while there was good repeatability on the size of the dispensed dots. Furthermore, the dispensed lines would cover the bond pad and thus impede the alignment of the chip to the substrate during the bonding process. Due to the control of the repeatability of the ACA dispensed dots, these were chosen as the preferred method of deposition. In a contact dispensing method the main factors that influence dot consistency and diameter are: temperature, pressure, needle inner diameter, dispensing height (needle height from the substrate), shot time (needle release speed from one dot to another as it controls the occurrence of the tails for each neighbouring dot), and the properties of the ACA such as viscosity, surface tension, as well as the paste condition.

West et al [91,92] pioneered the dot dispensing method of the adhesive for surface mount technology. Their study showed that the presence of a bubble during the flow could cause material variability during dispensing (the presence of a bubble in the flow could lead to either increased dot size or decreased dot size). The material variability could also lead to adhesive trails during dispensing. They attribute this material variability to the temperature, and pressure variation with the syringe adhesive. The effect of dispensing height on both dot size and dot consistency has been reported by Deng et al [93]. Temperature has an effect on the viscosity and consequently, the flow of the paste. Material viscosity has to remain constant so that consistent dots can be obtained. Therefore, in accordance with the manufacturer's suggestion, the paste was brought to room

temperature before use. The following practices were utilized to minimize variations in the material properties; in order to maintain the same viscosity, the paste was maintained at a constant temperature by using a controlled temperature in the working environment, the same rigorous cleaning procedure was used on all the substrates to maintain the same quality of surface tension, and only relatively new pastes were used to eliminate any effect from the paste condition.

The dots were dispensed on to the bond pad and around the perimeter of the substrate. The objective was to get a dot small enough to fit within the 300 μ m square bond pads. As stated in Table 3.1, the ACA has a high viscosity and a 23 gauge needle with inner diameter of 0.33mm was the smallest needle that would dispense the ACA. The variables remaining for the study were dispensing pressure, dispensing height, and shot time. A full factorial design was selected with three factors at 2 levels. There were in total 8 runs with 2 repeats. Response variables, factors and the levels were as follows:

- Response variable: dot Height, Diameter and Volume.
- Factors: Pressure, Shot time, and Dispensing Height.
- Levels: levels of each factor are shown in Table 3.2.

Factors	Low Level	High Level
Pressure (MPa)	0.28	0.41
Shot Time (ms)	100	500
Dispensing Height (mm)	0.1	0.3

Table 3.2. Levels of each factor.

3.3.2. Hypothesis testing

In many engineering problems, there is a requirement to decide whether a statement about some parameters is to be accepted or rejected [94]. The statement is called the hypothesis, and the process involved in the decision making is called hypothesis testing. It is a useful statistical inference. A statistical inference makes use of information from a sample to draw conclusions about the population under study.

The null hypothesis (H_0) is the hypothesis to be tested. It is basically a statement about a theory that is believed to be true but not yet proven. It must contain conditions of equality such as lower than or equal to (\leq), equal to ($=$), higher than or equal to (\geq). The alternate hypothesis (H_1) statement is one that somehow differs from the null hypothesis. The alternate hypothesis (H_1) statement can be: not true (\neq), or lower than ($<$), or higher than ($>$) the statement that was used for the null hypothesis. The main goal of hypothesis testing is to observe whether there is enough evidence to reject the null hypothesis.

Hypothesis testing involves the calculation of a test statistic, a value that is calculated from a random sample [95,96]. The test statistic is based on a certain distribution (usually z (Standard Normal Distribution), t (Student's t Distribution), F (F Distribution) or χ^2 (Chi-Squared Distribution)) [96] and is used to determine whether to accept or reject the null hypothesis. Some of the popular types are outlined below:

1. The z test could be used to test a claim about a population proportion,

$$z = \frac{\hat{p} - p}{\sqrt{\frac{pq}{n}}}, \quad (3-1)$$

where: \hat{p} is the number of elements (x) per sample size (n); p is the population proportion and $q = 1 - p$

2. The z test could also be used to test a claim about a population mean where σ is known,

$$z = \frac{\bar{x} - \mu}{\frac{\sigma}{\sqrt{n}}} \quad (3-2)$$

$$\bar{x} = \frac{\sum_{i=1}^n x_i}{n}, \quad (3-3)$$

$$\mu = \frac{\sum_{i=1}^N x_i}{N}, \quad (3-4)$$

$$\sigma = \sqrt{\frac{\sum_{i=1}^N (x_i - \mu)^2}{N}} \quad (3-5)$$

where: \bar{x} is the mean, μ is the population mean and σ is the standard deviation.

3. The t test would be used to test a claim about a population mean where σ is unknown,

$$t = \frac{\bar{x} - \mu}{\frac{s}{\sqrt{n}}} \quad (3-6)$$

where: \bar{x} is the mean, μ is the population mean, σ is the standard deviation and s is the sample standard deviation.

$$s = \sqrt{\frac{\sum_{i=1}^N (x_i - \bar{x})^2}{N-1}} \quad (3-7)$$

In the proposed DOE, the σ is unknown and therefore a t test will be considered in the statistical calculation. The following paragraphs show the steps involved in a manual calculation of the t test.

3.3.2.1. Statistical inference for a single sample on the mean of a population, σ unknown

Central Limit Theorem

The Central Limit Theorem states that when a random experiment is replicated, the random variable that equals the average (or total) result over the replicates tends to have a normal distribution as the number of replicates becomes large, as shown in Figure 3.6[94].

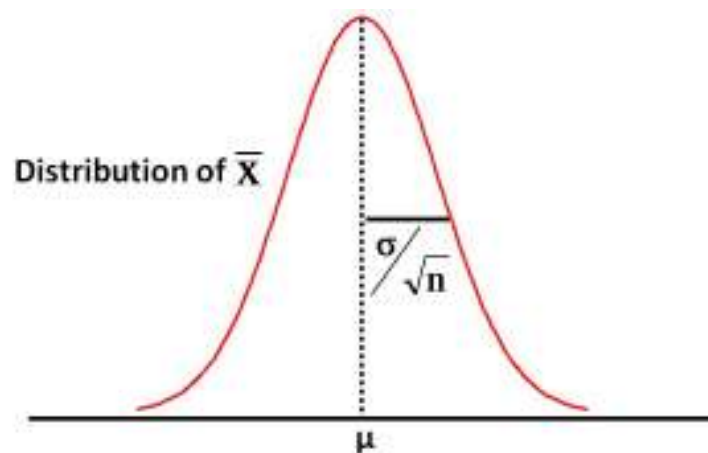


Figure 3.6. Sampling distribution of the sample mean.

Inference on mean of a population when σ is unknown

Suppose that a hypothesis is to be tested. The following shows the steps that would be involved in the hypothesis testing.

Step 1: the hypothesis to be tested and the alternative hypothesis are stated

$$H_0: \mu = \mu_0$$

$$H_1: \mu \neq \mu_0$$

Step 2: involves the test statistics calculation using equation (3-6)

There are two different ways of carrying out the hypothesis testing:

Step 3: Carry out hypothesis testing using either method 1 - test statistic approach or method 2 – p -value approach

1. Test statistic approach - method 1

This method uses the critical value approach. This is the more traditional method of hypothesis testing. This is carried out via a tail test. The alternative hypothesis dictates what type of tail test to use. In this case, a two tail test has to be considered as shown in Figure 3.7. The critical (rejection) region is defined by the significance level (α). The significance level (α) is the probability that the test statistic calculated in step 2 will fall in the critical (rejection) region when testing the null hypothesis. For a two tail test, α is the total area in the two tails of the rejection area. The significance level (α) is chosen by the analyst. The most common choice for α is either 0.01 or 0.05. If the calculated test statistics falls in either of the rejection regions ($t < -t_{\alpha/2}$ or $t > t_{\alpha/2}$), the null hypothesis will be rejected.

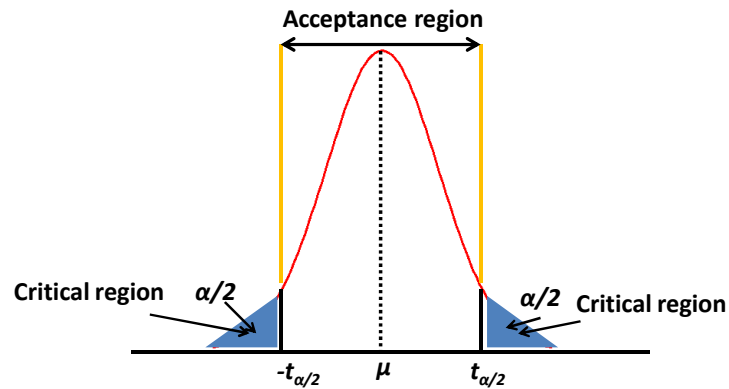


Figure 3.7. The distribution of t , where $H_0: \mu = \mu_0$ is true, with critical region for $H_1: \mu \neq \mu_0$.

2. P-value approach – method 2

This method uses the p -value approach. p -value is the smallest value of α at which the statistic is significant and H_0 could be rejected. The calculated p -value is compared to the chosen alpha value by the analyst. If p -value $<$ α , then the null hypothesis is rejected, as shown in Figure 3.8. If it is lower than α , then it shows strong evidence that the null hypothesis was wrong.

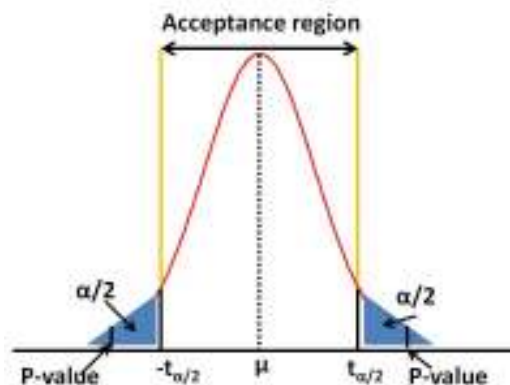


Figure 3.8. The distribution of t , p -value null hypothesis test.

Instead of manual calculation, a specialized statistical software Minitab-15 [97], was used to plot the effects of each factor and their interaction on the dot diameter. It investigates the significant factors that affect the response variable, the dot diameter via null hypothesis testing. In this case, the null hypothesis H_0 considers that there is no effect of a given factor τ_i in response variable Y ; i.e. τ_i equal

to zero while the alternative hypothesis H_1 assumes there is a value of τ_i which is different from zero. The hypothesis test in the factorial experiment examines the factorial model to see if the response at any level of the investigated factor is significantly different from that at the other levels. If this is not the case and the response at all levels is not significantly different, then it can be concluded that the investigated factor does not affect the response. The test on the factorial model is carried out by checking to see if any of the treatment effects τ_i is non zero. Therefore, based on the above factors the statements for the hypothesis are the following:

1. $H_0: \tau_{P1} = 0$ (No main effect of factor $P1$, pressure)

$H_1: \tau_{P1} \neq 0$ for at least one level

2. $H_0: \tau_{S1} = 0$ (No main effect of factor $S1$, shot time)

$H_1: \tau_{S1} \neq 0$ for at least one level

3. $H_0: \tau_{H1} = 0$ (No main effect of factor $H1$, needle height)

$H_1: \tau_{H1} \neq 0$ for at least one level

4. $H_0: \tau_{P1H1} = 0$ (No interaction $P1H1$)

$H_1: \tau_{P1H1} \neq 0$ for at least one level

5. $H_0: \tau_{S1P1} = 0$ (No interaction $S1P1$)

$H_1: \tau_{S1P1} \neq 0$ for at least one level

6. $H_0: \tau_{S1H1} = 0$ (No interaction $S1H1$)

$H_1: \tau_{S1H1} \neq 0$ for at least one level

7. $H_0: \tau_{S1P1H1} = 0$ (No interaction $S1P1H1$)

$$H_1: \tau_{S1P1H1} \neq 0 \text{ for at least one level}$$

Assuming the standard normal distribution, the critical value or the significant level (α) that could lead to the rejection of the null hypothesis is chosen as $\alpha=0.05$. p -value is the smallest α at which the null hypothesis could be rejected. Table 3.3 contains in the last column the p -values for each term under study which statistically determines the significance of the term in explaining the response variable diameter. Those p -values which are less than $\alpha=0.05$ are significant, i.e. the shot time, and pressure. However, there are some interactions that exist between shot time and dispense height, shot time and pressure, dispense height and pressure and these are shown in Figure 3.9.

Estimated Effects and Coefficients for diameter (coded units)					
Term	Effect	Coef	SE Coef	T	P
Constant		475.170	41.55	11.44	0.000
shot time	202.230	101.115	41.55	2.43	0.041
dispense height	-6.437	-3.219	41.55	-0.08	0.940
pressure	196.800	98.400	41.55	2.37	0.045
shot time*dispense height	19.662	9.831	41.55	0.24	0.819
shot time*pressure	19.070	9.535	41.55	0.23	0.824
dispense height*pressure	-15.058	-7.529	41.55	-0.18	0.861
shot time*dispense height*pressure	95.832	47.916	41.55	1.15	0.282

Table 3.3. p -values for significant terms.

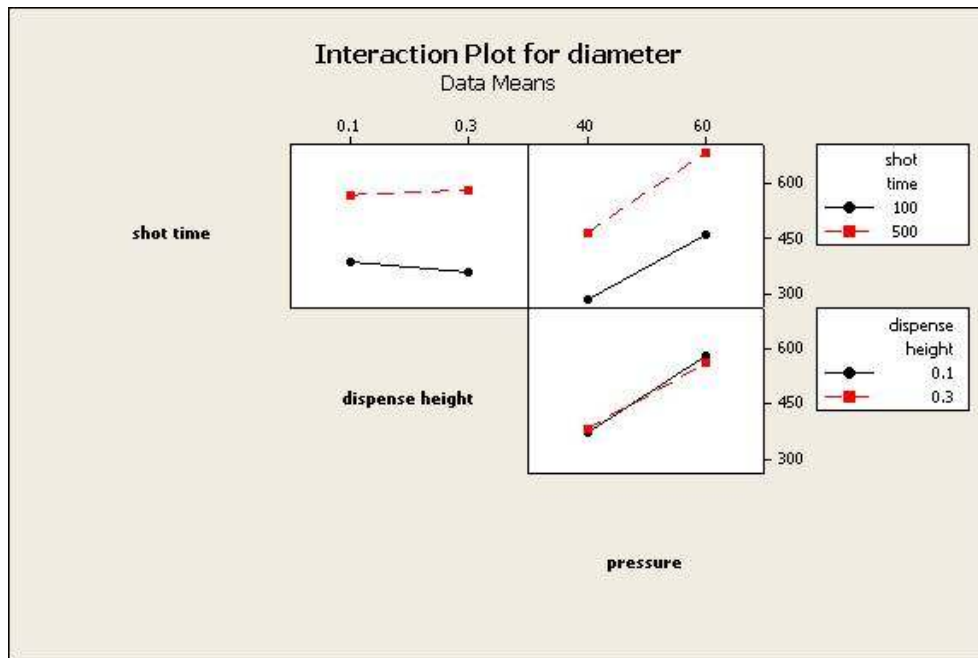


Figure 3.9. Interaction plot for dot diameter.

As explained above, the smallest diameter of a dot is required to enable the user to see the pad during the alignment process. The software showed that for a 300 μ m bond pad, a dispense time of 100ms, a needle dispense height above the bond pad of 0.23mm and a pressure of 40psi was required to get the target dot diameter within 300 μ m. As the paste was brought to room temperature, the material in the needle might have a lower viscosity than the material in the tube. The first 10 dots dispensed were not consistent, this was the reason the first 10 dots were discarded. After the first 10 dots a more repeatable dot size was achieved. The dots were then dispensed on to a glass substrate and the height and diameter of the dispensed deposits were measured. The shape of the dot after deposition is close to a spherical dome with a small peak on top, as illustrated in Figures 3.10(a), (b) and (c). Approximating the dot to a smooth spherical dome, the volume V_{cap} of the dispensed dots was calculated with the following formula:

$$V_{cap} = \left(\frac{1}{6}\right)\pi h(3a^2 + h^2), \quad (3-8)$$

where a is the base radius and h is the spherical dome height. For a $300\mu\text{m}$ pad, the dot obtained was $280\mu\text{m}$ wide and $60\mu\text{m}$ high. Hence the volume of the dot was calculated to be $1.96 \times 10^{-3} \text{mm}^3$. This shows that the ACA dispense foot print will allow room for alignment before bonding. In order for the DAS to be complete, the area around the chip and the substrate has to be sealed and the following sections describe the dispense pattern qualification through moisture aging and shear testing.

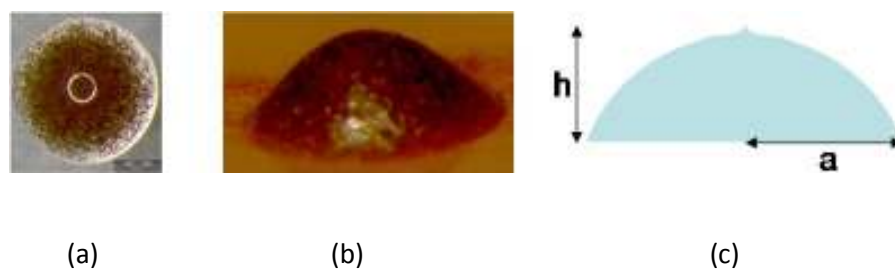


Figure 3.10. Micrograph showing the shape of the dot: (a) top view; (b) The profile view and (c) schematic of a side view of the dot.

3.4. Dispense pattern qualification

3.4.1. ACA spread

The values calculated by the Minitab software for pressure, height and shot time were used to dispense the ACA dots on to the substrate. The thermocompression bonding stage causes the ACA to spread under the chip and substrate area. The dots should spread evenly and seal off the area in between the chip and substrate and thus seal off the electronics from the external environment to which the sensor is exposed.

In order to assess the spread, a single dot of ACA was dispensed on to flex board and the final bonding pressure was applied. This gave a circular shape giving an indication of the dot spread, as shown in Figure 3.11. The average dot spread of 10 samples showed that the spread diameter was approximately $550\mu\text{m} \pm 39\mu\text{m}$ with thickness of around $8.25\mu\text{m}$.

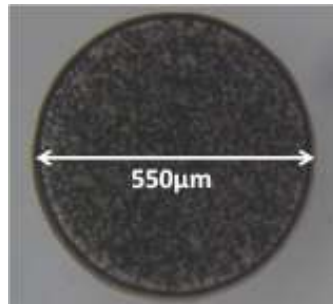


Figure 3.11. Picture showing a spread of dot.

The number of dots required and the dot spacing was calculated from the dot spread and the amount of space available between each bond pad. Therefore 9 dots of $300\mu\text{m}$ diameter with a spacing of $300\mu\text{m}$ to cover the window length were required for the bond pad-bond pad spacing of $5187\mu\text{m}$, 7 dots were required for the bond pad-bond pad spacing of $4350\mu\text{m}$ and 2 to 4 dots were required for the bond pad-bond pad spacing of $555\mu\text{m}$. As it was difficult to reliably place dots in a regular pattern with centres closer than $600\mu\text{m}$, the dispense pattern considered had three sets of offset dots so that there would be a good overlap of the ACA paste.

The first rows of dots were positioned at $150\mu\text{m}$ from the window. The second rows of dots were positioned at $300\mu\text{m}$ from the first rows with an offset of $300\mu\text{m}$ so that they took up the space between the first rows of dots. The third rows of dots were positioned at $300\mu\text{m}$ from the second rows and in line with the first rows, as shown in Figure 3.12(a). The SAM image of the dispense

pattern in Figure 3.12(b) shows that there was enough epoxy to cover and fully seal the entire chip-substrate area. If there was enough paste, it would tend to manifest itself along the chip edge thus resulting in a fillet, and the presence of a fillet has been shown to considerably increase the adhesion strength [98]. Figure 3.12(c) shows that a fillet was observed for the considered dispense pattern. Thus good adhesion would be expected. The volume of ACA used in the dispense pattern was approximately $20 \cdot 10^7 \mu\text{m}^3$. The area covered by the ACA for the dispense pattern was $46 \cdot 10^6 \mu\text{m}^2$.

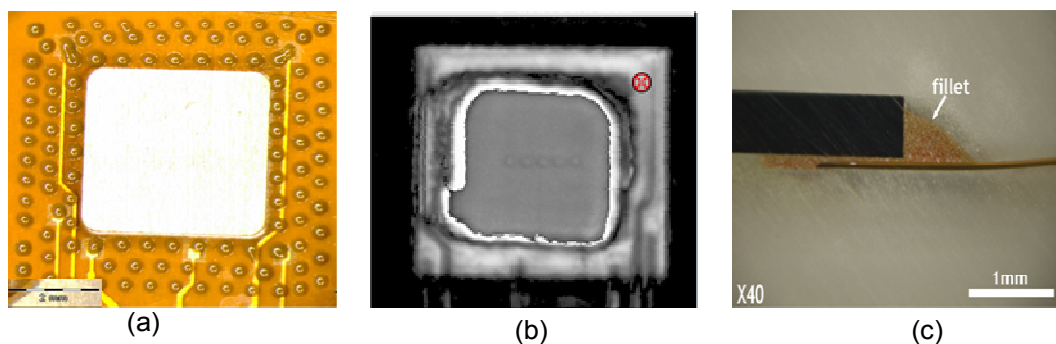


Figure 3.12. The dispense pattern; (a) micrograph of the dispense pattern; (b) SAM image of the dispense pattern and; (c) cross-section showing the fillet for the dispense pattern.

3.4.2. Shear test

3.4.2.1. Test method

Scanning acoustic microscopy (SAM) was used to assess the sealing efficacy of the direct access sensor. Currently there are no established test standards for conductive adhesives, and although there are ongoing studies in this area, one of the problems is that researchers do not always mention or control the shear rate when testing. In this work, die shear adhesion tests were carried out with a Royce instrument using the MIL-STD-883G method 2019.7 [99] to qualify the dispense pattern. The minimum shear stress that should be supported for good adhesion is approximately

0.7N/mm² [99]. As no standard test conditions could be found for biomedical humidity aging, the moisture humidity test was carried out at 50°C/95%RH (so that the humidity test could be close to the body temperature). A temperature of 50°C was used to accelerate any aging process, but this was not too high a temperature so as to accelerate other competing degradation mechanisms [100,101]. The samples were subjected to hygrothermal aging using a Heraeus Vötsch HC7033 humidity chamber at 50°C/95%RH and adhesion tests were carried out using the shear tester at aging times of 24hr, 168hr, and 336hr. As a comparison, control samples without exposure to hygrothermal aging were subjected to adhesion testing. All of these tests were performed at room temperature. The samples were glued to a glass slide and the shear test was carried out at a shear rate of 0.025mm/s, as shown in Figure 3.13.

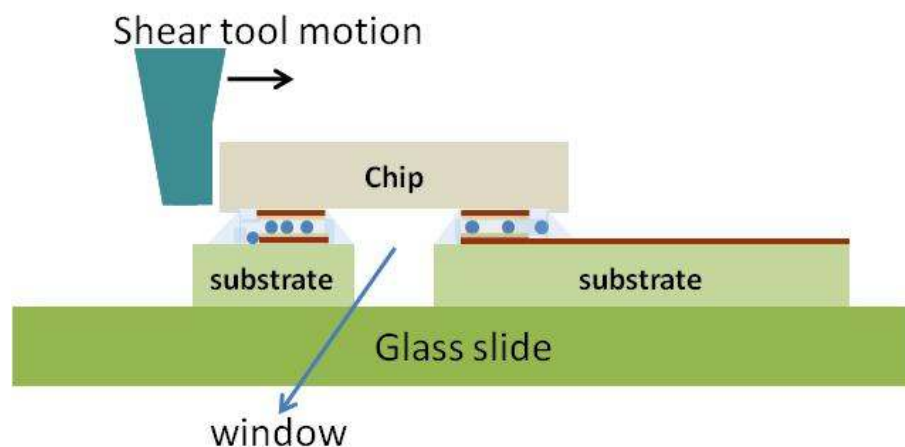


Figure 3.13. Schematic showing the shear testing of the sensor chip.

As seen in Figure 3.1, each electrode in the direct access sensor chip had its corresponding bond pad on the chip periphery. These bond pads are connected via the ACA joint to the matching bond pad on the substrate thus making individual joint connections for each electrode. The DAS structure developed in this research was destined to be tested via electrochemistry and therefore an online four point measurement of the contact resistance was not possible. As a result the contact resistance of the ACA interconnect was measured using a HP 3441A multimeter acting as a two

probe ohmmeter. The resolution of the resistance measurement was $1\text{m}\Omega$. The measurement was made by placing the probe tip on the electrode surface and at the conductor surface of the substrate. The resistance was separately measured for the chip, and the substrate. The same measurements were conducted on the device (chip) mounted on the substrate via ACA. The measurement carried out on the substrate and the chip was subtracted from the contact resistance measurement on the device, consequently measuring the contact resistance of the ACA joint. This was systematically carried out for each period of soak.

3.4.2.2. Shear test results

Four batches of FC assemblies were prepared. The control batch was not subjected to aging while the other three batches were subjected to hygrothermal aging. The initial resistance of the five adhesive connections of all the samples was under $500\text{m}\Omega$. These patterns were subjected to hygrothermal aging at $50^\circ\text{C}/95\% \text{RH}$ to accelerate the degradation process of the ACA joints. The control samples were subjected to shear testing and were compared to the hygrothermally aged samples. The hygrothermally aged samples were taken out of the chamber after 24hr, 168hr and 336hr respectively and subjected to shear test. Even though moisture and temperature have known to have a detrimental effect on the mechanical properties of the epoxy resin [102], during the whole hygrothermal aging test the dispense pattern did not fail at $120\text{N}/\text{mm}^2$, which was the limit of the machine. This was attributed to the adhesive volume that was present in the dispense pattern. The dispense pattern had enough adhesive to spread and cover the entire area between the window and the edge of the chip, thus providing a large area of contact on the chip and the substrate and hence required increased shear stress to de-bond the chip from the substrate. The electrical measurement showed that the resistance of the joints was stable for the duration of the hygrothermal aging process.

As the dispense pattern did not fail, an alternative dispense pattern was developed to evaluate the potential failure modes of the ACA adhesive when subjected to hygrothermal aging in a DAS environment. This alternative dispense pattern had only one row of dots around the window area and therefore would not provide a good seal of the window in the DAS. The lack of sufficient ACA adhesive in this dispense pattern signifies that it would produce failure below 120N/mm². Another four batches of FC assemblies with this alternative dispense pattern were prepared. Figure 3.14 shows the relationship between the shear stress and the hygrothermal soak time for the assemblies that failed. The trendline showed that there is a strong linear relationship ($R^2 = 0.9965$) between the measured shear stress and the hygrothermal aging time. If the trendline is extrapolated, the hygrothermal aging would cause the assemblies to fail, without any applied shear stress, at around 500hr. After 24hr of hygrothermal aging, the shear stress was approximately 7.9N/mm².

The percentage decrease of the shear stress relative to 24hr aging was 26.8% and 65.5% corresponding to hygrothermal aging times of 168hr and 336hr. Epoxy resin is prone to moisture uptake and it has been shown in previous studies [80,102,103] that moisture absorption and temperature have a deleterious effect on the physical properties of epoxy resin. Plasticization and hydrolysis which occur due to moisture uptake [104] affect the mechanical properties of the epoxy and in addition to the moisture absorption, temperature also contributes to this degradation process by facilitating increased moisture diffusion and chain mobility [105]. As a result the shear stress required to de-bond the chip from the substrate decreases.

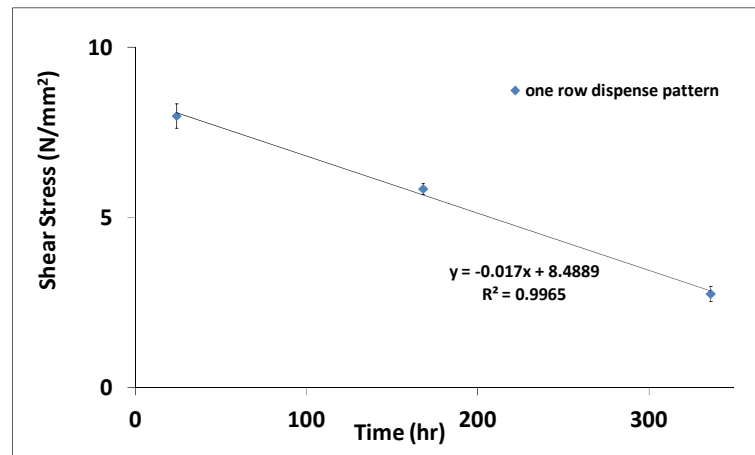


Figure 3.14. Plot of shear stress of dispense pattern that failed after hygrothermal aging.

3.4.2.3. Fractographical analysis

As shown in Figure 3.15 the failure mode of the adhesive-chip-substrate system can be classified as follows [80]: (i) interfacial failure – i.e. a fracture that occurs at the interface of chip/adhesive or adhesive/substrate; (ii) cohesive failure - a fracture within the adhesive and (iii) mixed mode failure – a fracture which combines (i) and (ii)

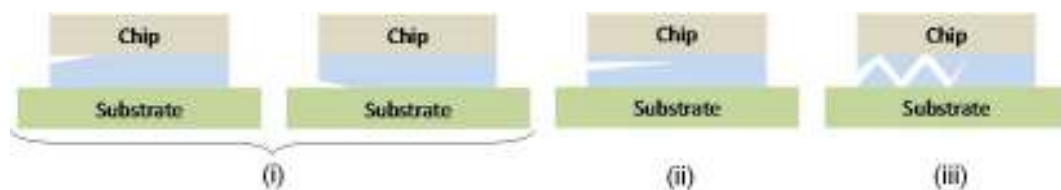


Figure 3.15. Schematics of types of failure in adhesive-adherent system: (i) interfacial failure; (ii) cohesive failure and (iii) mixed failure.

Fractographical analyses of the failed samples that underwent shear testing was carried out using Scanning Electron Microscopy (SEM). Figure 3.16(a) shows the SEM image of the chip and substrate

side after 24hr hygroscopic aging followed by shear test. It can be seen on the chip and the substrate that there are small plastic deformations where the material has elongated in the direction of shear before breaking (at the crack tip in the direction of the shear loading). This occurs when the adhesive joint yields to high stress at the crack propagation site. This material elongation indicates a moderate ductile fracture. Furthermore, it can be seen that the fracture is mostly on the chip side and the failure seems to be interfacial and cohesive in nature. Figures 3.16(b) and (c) show the SEM images of the shear tested samples after 168hr and 336hr hygrothermal test. All samples at both 168hr and 336hr showed mixed mode failure, i.e. the failure occurred at both chip and substrate interfaces as well as exhibiting cohesive adhesive failure. As a result of moisture absorption, the disruption of the hydrogen bonds may occur causing plasticization in the short term [106,107], and hydrolysis [102] causing chain scission which results in chain mobility, thus leading to the loss of ductility in the adhesive joint. Figures 3.16(b) and (c) show that with increasing aging time, the small plastic deformation at the crack tip disappears and the edge of the crack tip is much smoother. These flat surfaces depict a brittle fracture. Brittle fractures takes place when there is a relatively small or negligible amount of plastic strain and is accompanied with rapid crack propagation resulting in cleavage of the surface. Thus, it can be concluded that the transition from ductile to brittle failure could be correlated to the moisture absorption, this was reflected by the low shear stress required to de-bond the chip from the substrate.

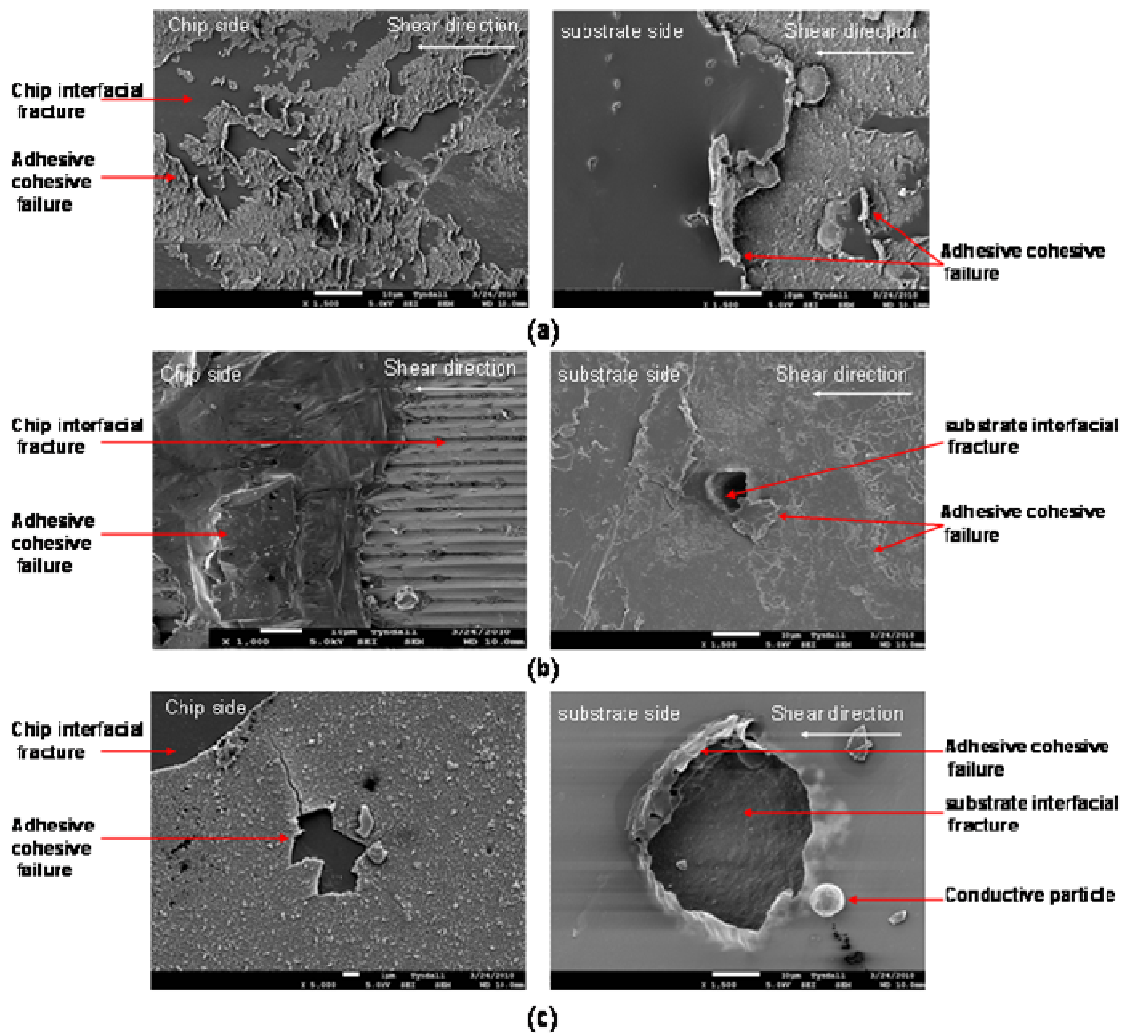


Figure 3.16. SEM images of the failed samples: (a) after 24hr; (b) 168hr and; (c) 336hr.

Summary

This DAS development process showed that for a 300 μ m bond pad, a dispense time of 100ms, a needle dispense height above the bond pad of 0.23mm and a pressure of 40psi would provide a small print dot on to the pad so that the chip/sub bond pads could be aligned and connected. It also showed that the dispense pattern provided satisfactory sealing between the chip and the substrate area. With this prior knowledge, DAS were fabricated and tested in an electrochemical environment to observe the functionality of the sensor and the interconnect.

3.5. Electrochemistry - Direct Access Sensor testing

Cyclic voltammetry of the three electrode cell was used to interrogate the sensor. In a first system, the three electrode cell consisting of Au Working Electrode (WE), Pt Counter Electrode (CE) and an external Ag/AgCl Reference Electrode (RE) was used to perform the electrochemistry. As the DAS was required to conform to capsule environment, there was no room for the brittle glass Ag/AgCl RE normally used in these measurements. An alternative option was to use one of the Pt electrodes already present in the chip as a pseudo RE. The electrochemical reactions occurring at the interface between the WE and the solution were monitored using a CH instruments 620B computer controlled potentiostat. As shown in Figure 3.17, the fabricated test assemblies were dipped into a solution of 0.5M of H_2SO_4 and cyclic voltammetry test at a scan rate of 0.2V/sec was applied to the electrode system. The chemical reactions that occurred at the Au WE in this solution are well documented [16] and any change in the performance of ACA would be identified at this stage.

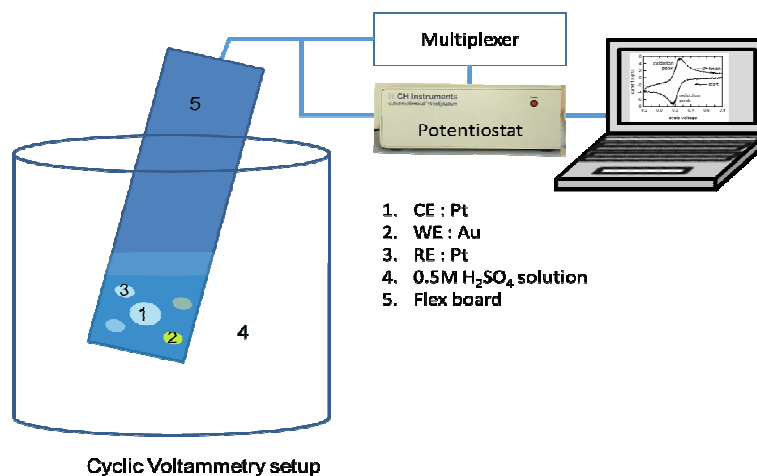
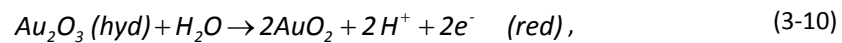
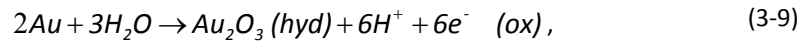


Figure 3.17. Schematic of cyclic voltammetry setup.

Figures 3.18(a) and (b) show the plots of current versus potential for a forward and reverse sweep as a result of the cyclic voltammetry. It can be seen in Figure 3.18(a) that, for the system using an external RE, each voltammogram showed a similar response. A peak was obtained at 1.4V during the

positive voltage sweep (oxidation (ox)) - from 0 to 1.5V, and a corresponding peak was obtained at 0.9V during the negative voltage sweep, (reduction (red)). The corresponding gold reactions taking place are [16]:



The difference in the voltammogram shape could be attributed to the different sensor batches as the properties of Au may vary slightly from one batch to another. Figure 3.18(b) shows the result obtained for the system using Pt as the RE and it can be seen that the oxidation peak has been shifted to around 1.2V during the positive voltage sweep from 0 to 1.5V while the reduction peak has moved to around 0.6V during the negative voltage sweep. This 0.2V difference for each peak could be attributed to the change in reference electrode. However, these gold peaks were due to gold oxide formation and reduction, and they illustrated the correct function of the sensor and interconnect. Also since the measurement was supposed to be done in the body without a glass RE it was felt that the pseudo Pt RE on chip would be more representative.

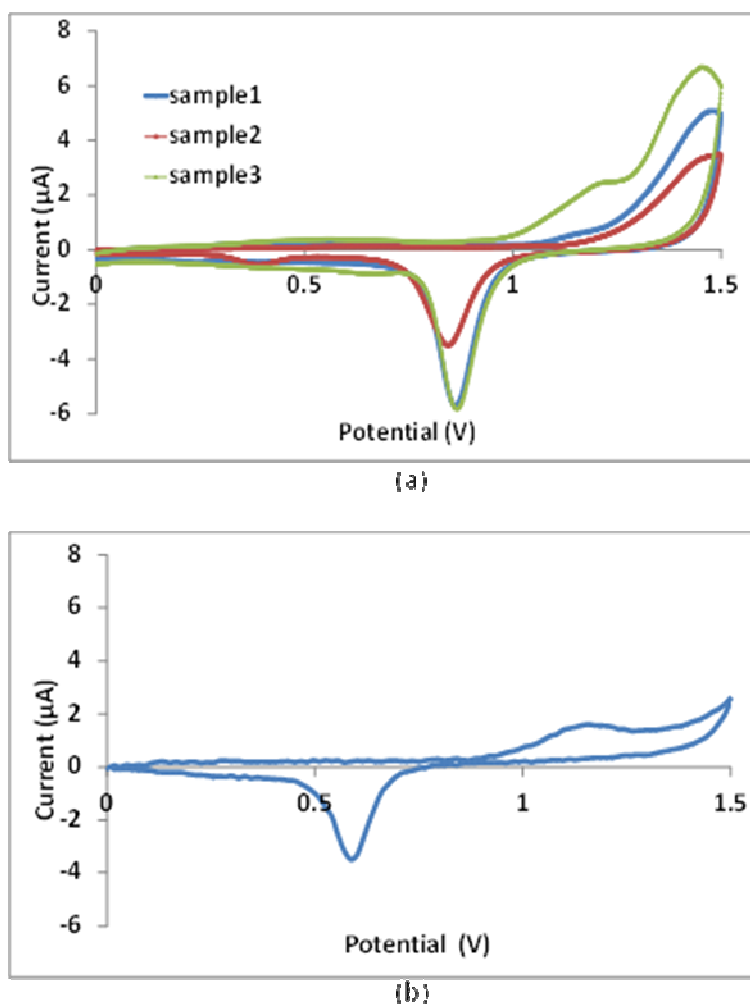


Figure 3.18. Cyclic current-voltage curve of the Au WE with: (a) an external RE. electrode and (b) with pseudo Pt RE.

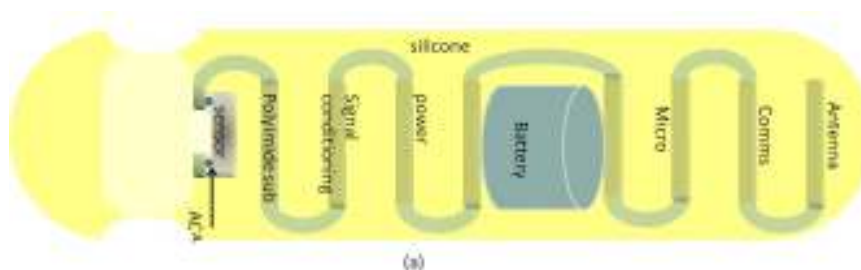
Summary

A DAS was fabricated and tested electrically in a solution and the electrochemistry showed that the sensor and interconnect functioned perfectly albeit with a 0.2V shift between classical RE and on chip pseudo RE. The next stage is to place this DAS in a capsule. Here different placement options were considered and the following section reviews the different sensor placement options.

3.6. DAS capsule placement

3.6.1. Sensor placement option

Prior to the final prototype selection, an initial capsule packaging solution was considered. This initial capsule packaging solution with its design selection is described in Appendix A1. Figure 3.19 shows the schematic of the final prototype with different mounting positions for the DAS. Even though Figure 3.19(a) is a viable option, it can be seen that this placement method leaves a lot of empty space at the front of the capsule leaving little room for the electronics to be fitted in. In addition the opening on the side of the capsule could be of concern as the intestinal collapsing walls may push the solids through and may clog the sensor as it passes through the GI tract. The design considered in Figure 3.19(b) also provides a lot of empty space at the front of the capsule and therefore could have the same integration issue as Figure 3.19(a). Once again the collapsing digestive wall might clog the sensor by pushing the solids on top of the sensor and thus inhibiting the proper function of the sensor. The final design, as shown in Figure 3.19(c) places the sensor at the front of the capsule. This design maximises the space in the capsule while at the same time the sensor and the interconnect material are exposed to the GI fluids. The final design was chosen as the sensor position in the DAS capsule for this reason.



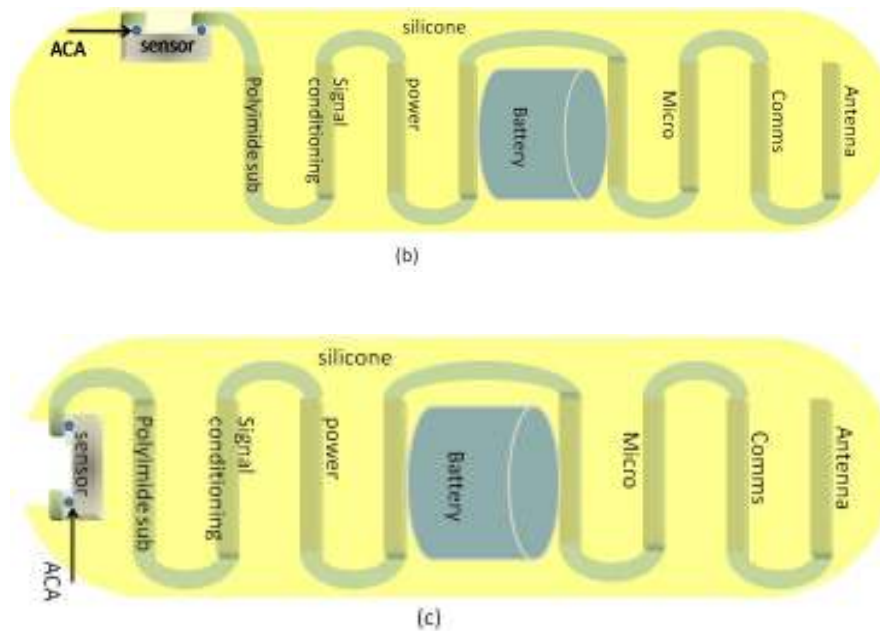


Figure 3.19. Schematic of different viable sensor placement options.

3.6.2. Preliminary DAS packaging

A preliminary sensor packaging experiment was carried out which consisted of the following steps: the first step involved dispensing silicone on the perimeter of the window using CAM/A LOT and curing it in the oven at 80°C for 3hr. The cured silicone acted as a dam around the window. Then protection of the sensor was carried out using AZ photoresist, Diazonaphthoquinones (AZ Electronic Materials GmbH) [108]. The photoresist was applied using the pendant drop method (i.e. 6 drops of AZ on the sensor area, and then cured at 80°C for 1hr). The resulting photoresist film had a height of around 596.7 μm and acted as a plug covering the exposed area of 19.36 mm^2 . Once the dam and the plug were ready, the assembly was inserted into a 15mm gelatine glycerine capsule and mechanically secured in place. The fixed assembly was then filled with silicone and cured at room temperature for 24-48hr. This was followed by immersing the capsule in warm water (50°C) for 10-15min to dissolve the glycerine capsule. The sensor was exposed by dissolving the AZ photoresist in acetone for 5-10min, as shown in Figure 3.20.

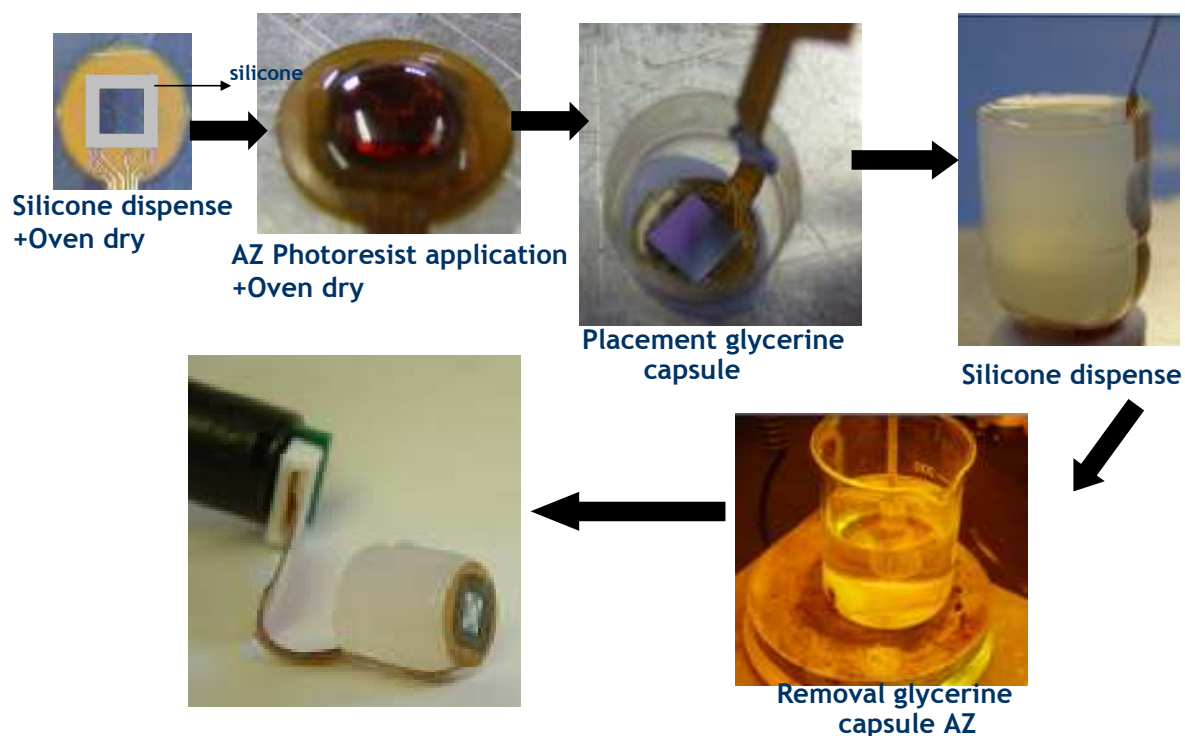


Figure 3.20. Process flow of the sensor encapsulation method.

To prove the quality of the encapsulation process the cyclic voltammetry test was carried out on both an un-encapsulated sensor and an encapsulated sensor with the use of an external Ag/AgCl RE. The derived voltammograms are shown in Figure 3.21. A similar response was obtained for both of the tested sensors. Oxidation and reduction peaks were obtained at 1.4V and 0.9V for both sensors; minor changes in the shape of the voltammograms can be related to standard voltammogram dispersion as a result of differences between surface of the WE on the sensing chips and decreasing of the leakage current in the case of the encapsulated sensor. Thus these test results allow the conclusion that the assembly process for the sensor encapsulation did not affect the sensor operation.

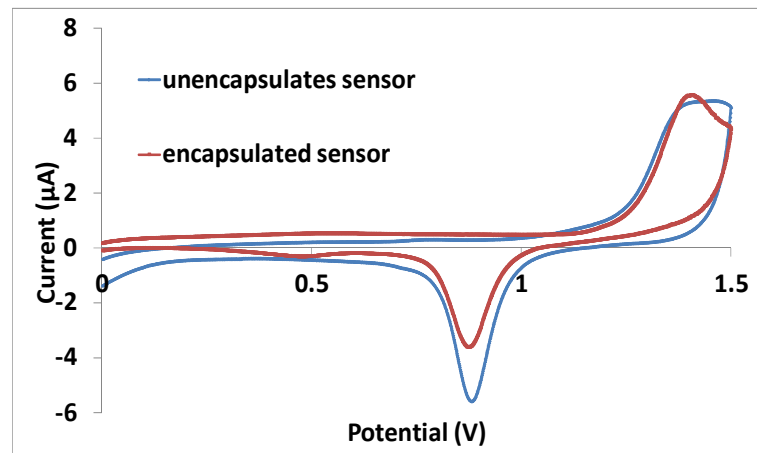


Figure 3.21. Voltammetric responses of an unencapsulated sensor and an encapsulated sensor.

3.7. Conclusion

The first part of the study was based on the development of a direct access sensor based on ACA FC assembly. The ACA was used to obtain good interconnection and at the same time seal off the area between chip and substrate. This work involved development of a small deposit of ACA on to the bonding pads for the interconnect part of the technology so that the pads would be visible during the alignment before bonding. A DOE showed that the dispense parameter pressure and the dispense time had the most influence on the diameter of the dot of ACA dispensed and thus on the volume. The optimal dispense parameters were a dispense time of 100ms, a needle dispense height of 0.1mm and pressure of 0.28MPa; and these were used to achieve the smallest dot of 280µm in diameter that would fit onto a 300µm square pad.

The dispense pattern had enough adhesive material between chip substrate area to provide a sufficient seal. This was reflected by the fillet observed in the cross section. The mechanical shear loading after hygrothermal aging showed that the dispense pattern did not fail at 120N/mm², which was the limit of the machine. This showed that the large contact area and the amount of adhesive

have an impact on the longevity of the sensor attachment. An alternative dispense pattern was developed to evaluate the potential failure modes of the ACA adhesive when subjected to hygrothermal aging. Sheared samples that had undergone hygrothermal aging showed a ductile to brittle transition with less plastic strain and rapid crack propagation resulting in cleavage of the surface. This showed that the moisture absorption had a deleterious effect on the physical properties of epoxy resin and thus lowered the shear strength of the adhesive joint.

The second part of the work was to fabricate the DAS with the optimised parameters and to test it in the liquid environment using cyclic voltammetry. The cyclic voltammetry results showed that the functionality of the sensor and interconnect was not compromised. The results showed that the Au oxidation peaks were obtained at 1.4V or at around 1.2V during the positive voltage sweep, depending on the RE used. For a negative sweep, depending on the RE used the peak were obtained at either 0.9V or at around 0.6V. This showed that the on-chip Pt electrode could be used as a pseudo RE for the capsule integration.

A choice of the design of the DAS placement was reviewed and the placement of the sensor at the front of the capsule maximised the space in the capsule and was the chosen design for the final capsule integration. A preliminary capsule packaging was carried out using the test substrate and the die which showed that the packaging of the die in the capsule does not affect either the sensor or interconnect functionality. This chapter could be concluded with the note that ACA FCOH is a viable option for DAS and could be integrated into a capsule to achieve a DAS capsule.

As mentioned in the DAS packaging into a capsule section, the sensor has to be mechanically fixed in the capsule. Although the preliminary results show that the interconnect was not affected, it is

crucial to understand how the mechanical stresses affect the joint. The following chapter will focus on the mechanical characterization of the ACA joint during capsule insertion and sensor fixing.

Chapter 4 Mechanical characterization of the ACA joint for a DAS

4.1. Introduction

As mentioned in Chapter 3, during DAS integration into the swallowable capsule, a mechanical force is applied to push the sensor assembly through the length of the capsule before securing the chip and the substrate in the capsule for the encapsulation process. A preliminary test was performed to assess the force that was experienced by the ACA joints during the capsule insertion and securing process. This preliminary test will be presented in detail in the experiment section of this chapter. In Chapter 3, it was shown that the DAS packaging was reliable and that the mechanical securing did not degrade the ACA joints. But it did not provide any information about the joint behaviour during the capsule insertion process.

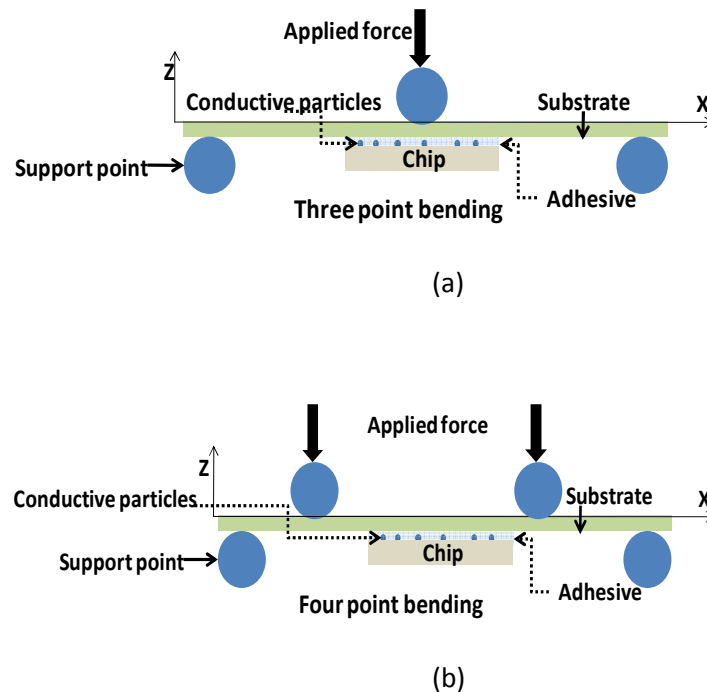


Figure 4.1. Schematic of: (a) three point; and (b) four point bending.

Figures 4.1(a) and (b) show the three point bending and four point bending [109-113] that are often used to assess the mechanical reliability of ACA joints. Depending on the position of the die on the substrate and the Z axis, the bending could be classified into two categories [114,115]: (i) the outward bend characterized by the die positioned on the negative part of the Z axis as shown in Figures 4.1(a) and (b) and (ii) the inward bend distinguished by the die positioned on the positive side of the Z axis as shown in Figure 4.2.

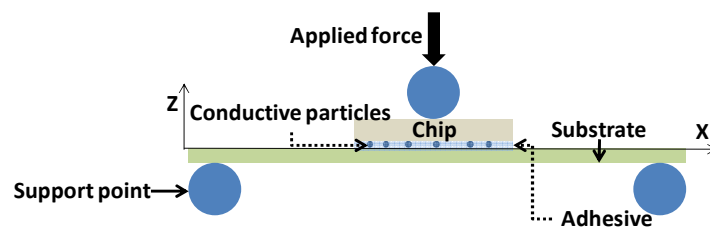


Figure 4.2. Schematic of three point inward bending.

Most of the literature deals with the outward bending using three or four point bending. A study conducted by Rizvi et al [109] on the outward three point bending on the ACA joint behaviour showed that the stresses were high on the corners where the chip and ACF were connected together. The high stress at the corners led to increased ACF thickness at the corners and eventually caused a greater gap between the chip and the substrate at the corner positions and the failure of the corner joints. Yip et al [110] conducted a study on the effect of aging of the Chip-on-Flex (COF) ACF assembly using outward four point bending. Their study revealed that aging of the COF assembly decreased the flexibility of the assembly and changed the mode of failure of the ACF from cohesive to interfacial fracture between the ACF and the substrate. Although, Lai et al [116] conducted reliability testing on FR4 rigid and polyimide flexible substrate and came to the conclusion that the different stiffness of the substrate and increasing bump height has an effect on the reliability of the joint, they did not perform a mechanical study on the failure mode of the joint. Lin et al [80] showed

in their study that this change in ACA failure modes was due to the increased reduction in the interfacial fracture energy due to hygrothermal aging. Another outward four point study was carried out to analyse the bending fatigue reliability of the Au bumped FC with ACF [111]. This study showed that the differential bending between the substrate and the chip was shown to be the main cause for the occurrence of failure in the package during the bend test. It also showed that for an ACF package, the bending stress was concentrated at the conductive particles between the Au bump and the Electroless Nickel Immersion Gold (ENIG) pad during the bending fatigue test. Lu et al [112,113] conducted a reliability study of the Ultra-thin-Chip-on-Flex (UTCOF) with ACA joints. Once again an outward four point bending technique was used to study the flexibility of the UTCOF assembly. This study showed that an UTCOF assembly made with ACA was able to provide a stable resistance with a small (10%) variation throughout 1000hr of bending test.

Cai et al [114,115] reported on the reliability evaluation of a flexible RFID tag using ACA. The flexibility reliability test showed that the outward bend was more destructive on the contact conductivity than the inward bend. It was concluded that the outward bend caused a tearing effect and that the bend cycle caused the particles between the bump and the pad to undergo an open-close-action. Furthermore the inward bending created constant compressive stress on the ACA joints providing a stable contact resistance during the test.

This chapter describes the work carried out to mechanically characterize the ACA joints during the capsule insertion process and to determine the smallest capsule diameter that could be used without imparting excessive stress on the interconnect in the DAS integration process for a specific substrate and chip design. The following section describes the mechanical testing; initially the preliminary capsule insertion is considered, followed by silicon compression testing and ACA

assembly insertion test into different diameter holes to determine the smallest diameter of the capsule which could be safely used for a specific assembly.

4.2. Mechanical testing

4.2.1. Preliminary capsule insertion

As mentioned in Chapter 3, the DAS is inserted into a gelatine glycerine capsule and secured in place for the encapsulation process. In order to assess the force that the ACA joints experience during the capsule integration process, the following test was carried out.

Using a temporary adhesive, an iron rod of 11mm was glued to the back of the chip. The 13mm diameter glycerine capsule was temporarily glued to a base plate as shown in Figure 4.3. Care was taken to position the rod with the sensor in the centre of the capsule before starting the test. The compressive mechanical test was carried out via an Instron 5565 with a load cell of 500N with a cross head speed of 2mm/min and the results were recorded using Series 9X software.

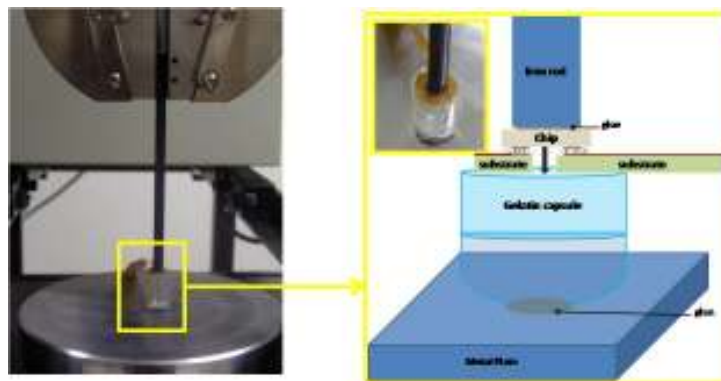


Figure 4.3. Mechanical setup for preliminary capsule insertion.

Figure 4.4, shows the force measured during insertion and securing of the DAS in a gelatine capsule. The variation of the force was minor until approximately 23mm into the capsule. This was characterized by the rod and the flexible substrate with the sensor moving into the capsule smoothly without real contact with the capsule sidewalls. The different stages of the insertion process are shown in Figure 4.4. At approximately 23mm into the capsule the edges of the flex substrate came in direct contact with the capsule wall due to the semicircular edge of the capsule. The contact between the assembly and the semicircular edge of the capsule wall led to the increase in the compressive force that was observed in the graph. From 23mm to approximately 27mm, the compressive force increased to 6N. This increase in force could be explained by the circular end of the flex substrate, which is 12mm in diameter (according to Figure 3.2), bending as the DAS is pushed into the final end of the 13mm diameter capsule, as seen in the last two photos in Figure 4.4. As mentioned in the introduction, this preliminary test does not provide any information about the joint behaviour during the capsule insertion process. The next section deals with the mechanical characterization of the ACA joints during the capsule insertion process and determination of the smallest capsule diameter that could be used in the DAS integration process for a specific substrate and chip design.

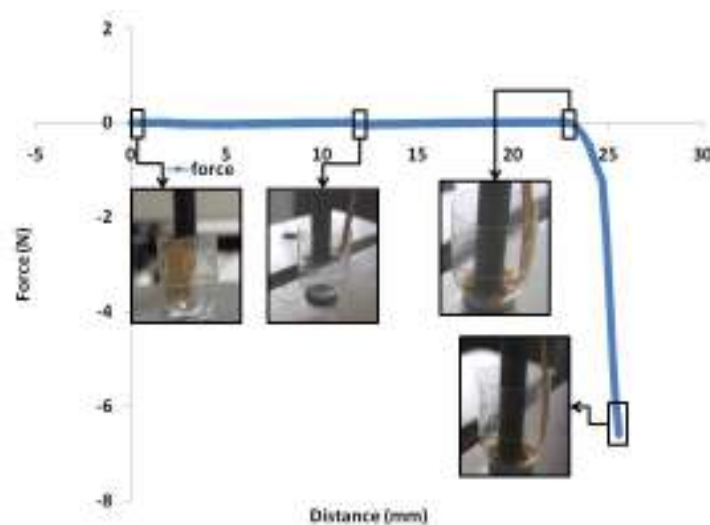


Figure 4.4. Plot of force required to push through gelatine capsule and to fix the DAS.

4.2.2. Mechanical testing of the ACA joints during capsule insertion

4.2.2.1. Material and methods

Chip

The test chip was a 5mm x 5mm die with a thickness of 0.5mm. This test chip is smaller than the final microelectronic sensor chip described in Chapter 3. As described in Chapter 3, the microelectronic sensor was designed for electrochemical analysis and it was impossible to get a quantitative analysis of the ACA joint behaviour during the mechanical integration. For this reason a new test chip was used in the following mechanical test. This new test chip was designed specifically for FC reliability investigation and had an array of 144 (100 μ m X 100 μ m) pads, with a pad pitch of 400 μ m, as shown in Figure 4.5. Interleaved sequences of connective pads were laid out on the chip so that it could be used as a daisy chain in the final assembly and thus monitor the continuity of the FC joints during the mechanical insertion of the assembly. The unbumped die had aluminium pad metallization. The die was then gold (Au) stud bumped and coined. The height of the coined stud bump was around 40 μ m. The main purpose of the coined stud bump was to maximize the contact area during bonding.

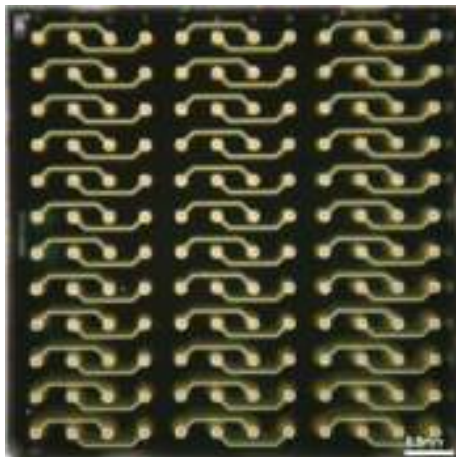


Figure 4.5. Micrograph of test chip with coined gold stud bumps.

Substrate

Figure 4.6(a) shows the Protel layout of the flex substrate. It was 8cm x 8cm single sided flex in the form of a cross. Information about the window selection will be described in Appendix A2. In the centre of the cross, at around 4cm from the edge of the cross, a 2.4mm window was laser cut to expose the centre of the chip to the surrounding environment as shown in Figure 4.6(a). At around 3.3cm from the four edges of the cross, slits with circular edges of radius 0.95mm were cut to facilitate the folding of the flexible substrate during the encapsulation process. The conducting tracks on the board were terminated with a connector pad which had 2mm holes to enable soldering of wires to carry out electrical testing. The thickness of the flex substrate was 0.1mm. The copper tracks on the flexible substrate were 15 μ m thick, while on the substrate bond pads, an additional 5 μ m Ni and 0.05 μ m of electroplated flash gold were deposited. The adhesive manufacturer's design rule required that the interconnection area be left uncovered by solder mask or by coverlay because it might lower the effective bond pad height and as a consequence would not provide a good mechanical contact between the conductive particles, the bump and the substrate pad as shown in Figure 4.7. The flexible substrate manufacturer's tolerance for positioning the coverlay is around 0.1mm. An additional 0.5mm was added to all the sides of the chip placement area so that there was enough room for the chip during the bonding process. Hence an area of 30.25mm² under the chip was left uncovered by the coverlay. Figure 4.6(b) shows the manufactured flexible substrate while Figure 4.6(c) shows the alternating conductive line pattern that was used in the bonding process to achieve the daisy chain required for testing.

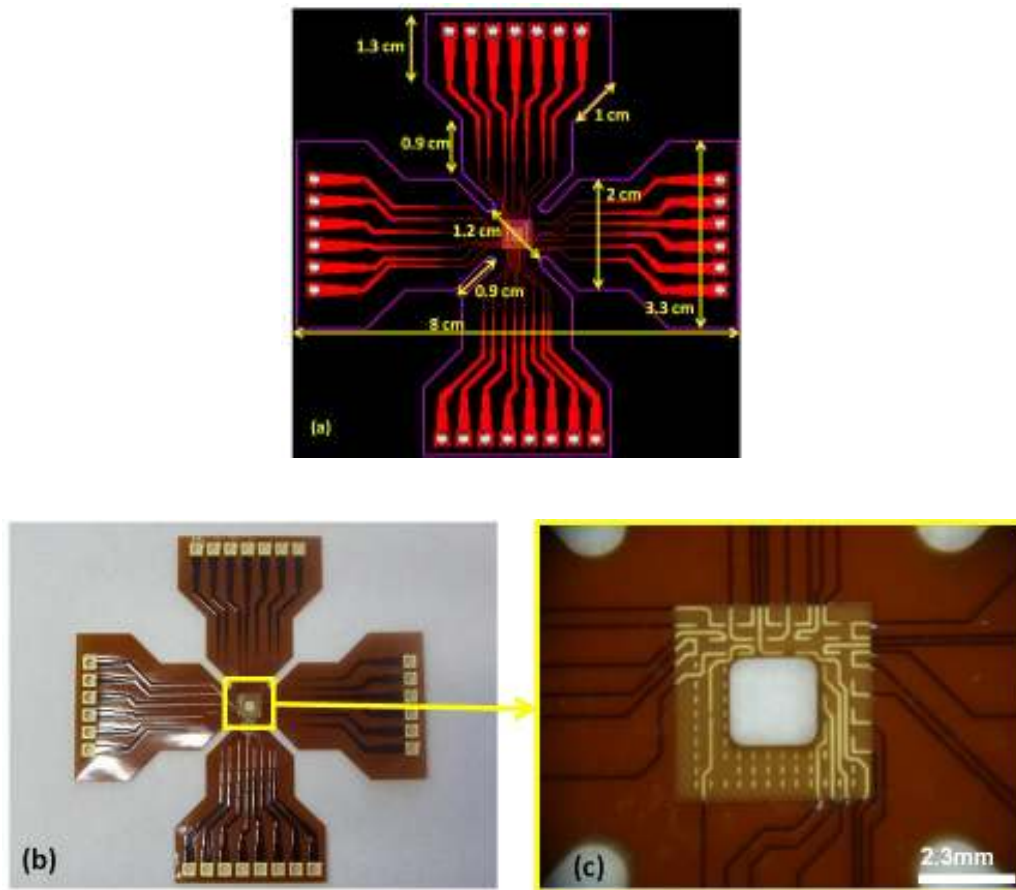


Figure 4.6. Flexible substrate: (a) Protel layout, (b) micrograph of the entire substrate and (c) micrograph showing conductive lines for daisy chain measurement.

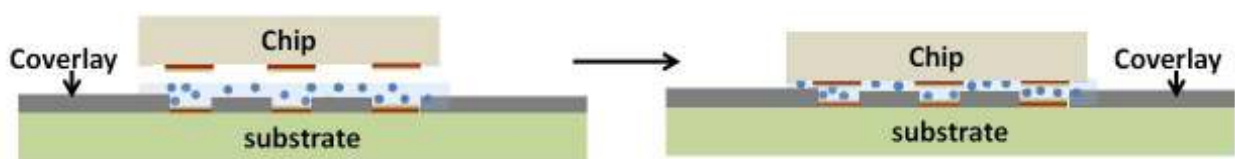


Figure 4.7. Schematic of coverlay issue.

Bonding process

ACA from Henkel & Loctite (FP5300) was once again used for bonding the chip to the substrate. ACA was dispensed on the board using a CAM/ALOT 1414 liquid dispense system. Once again dots were dispensed close to the bond pads and alignment and bonding of the chip/substrate was performed

using the same Finetech Flip-Chip bonder. Bonding was carried out at a ramp rate of 2°C/sec with a hold at 200°C for 50sec and a cool down rate of 3°C/sec. The average bond line thickness of the adhesive taken from 10 samples was approximately 21µm with a tolerance of 1µm.

Test preparation

Silicon compression test

The following test setup was devised to test the maximum compressive strength of the silicon test die that was used in the mechanical insertion test. As shown in Figures 4.8(a) and (b), the silicon die was glued with Araldite fast cure to a 0.2mm thick metal frame which had a 2.4mm square window at its centre. This was done to replicate the assembly. Once more the test method chosen was exactly the one that was used in the preliminary capsule insertion, although the cross head speed was reduced to 0.25mm/min and the results were recorded via computer.

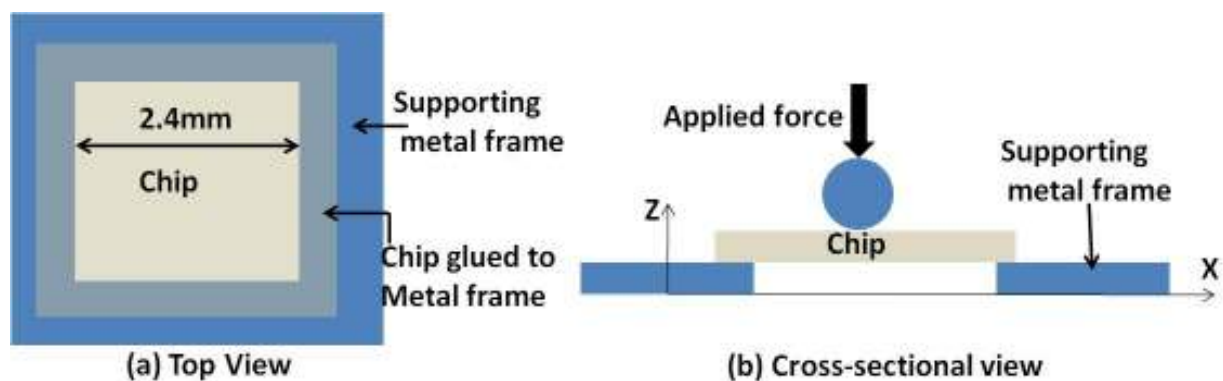


Figure 4.8. Schematic showing: (a) the top view, and (b) the cross-sectional view of the silicon compression test.

Assembly insertion test

Figure 4.9 shows a polycarbonate block of 75mm x 100mm x 27mm in which 23mm, 21mm, 19mm, 17mm, 15mm and 13mm diameter through holes were drilled to carry out the mechanical testing. These holes represent different diameter capsules. Due to the fact that the circular section on the flex board had a 12mm diameter, the minimum diameter hole was set at 13mm.

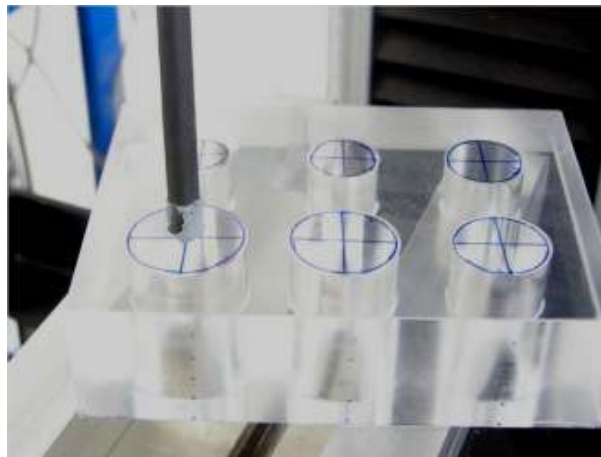


Figure 4.9. Polycarbonate block with different diameter holes.

In order to carry out the mechanical testing, the ACA assembly had to be placed on top of each hole and then pushed through. An 11mm iron rod with its tip covered in 1mm of silicone was used as a pushing tool. Before each test, the pushing tool and the ACA assembly were placed in the centre of each diameter hole with the hole setting becoming progressively smaller. This was carried out to ensure that the assembly went down the middle of each diameter through hole.

After centring the rod and the ACA assembly, the mechanical test was carried out by placing the iron rod directly on the middle of the back of the chip and pushing the assembly through the hole. Unlike three or four point bending where the end of the substrate is clamped, the substrate was free to go

through the hole. Figure 4.10 shows the mechanical test setup and the electrical setup that was used for testing the ACA joints during capsule insertion. Since the die was positioned on the positive side of the Z axis, this setup could be classified as an inward bending process. The test method that was used in the preliminary capsule insertion was used to carry out and record the data of the mechanical test.

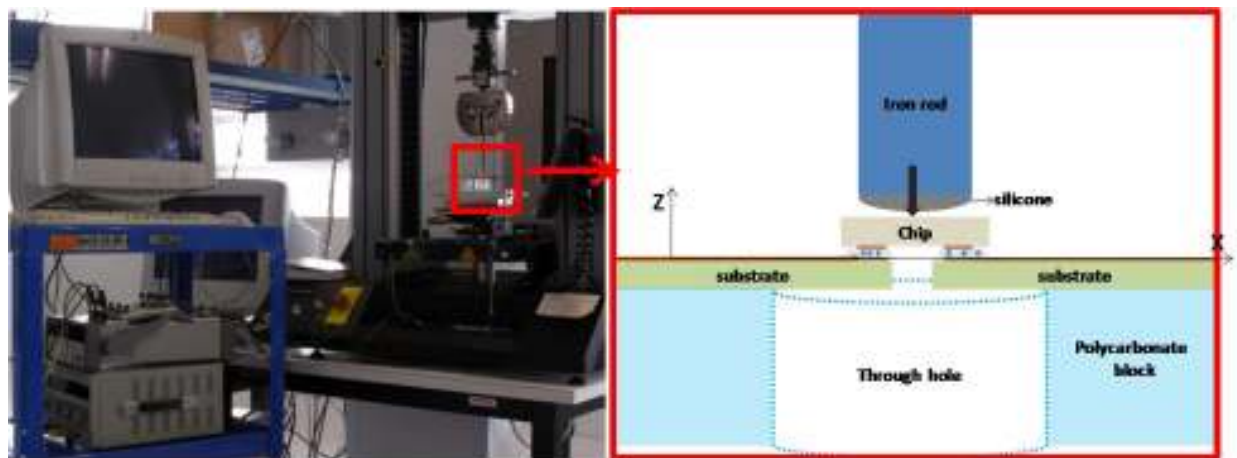


Figure 4.10. Intron mechanical test setup and electrical test setup for testing ACA joints.

Electrical testing

Figure 4.11 shows the schematic of the test assembly and the electrical test setup that was used to record the electrical behaviour of the assembly during the mechanical test. Due to the symmetry of the assembly only half of the assembly was considered for electrical characterization. As shown in Figure 4.11, the test assembly contained four partial daisy chains defined as x1, x2, x3 and y and a total daisy chain as z – all four daisy chains connected together. Three partial daisy chains were positioned in the x direction while one was positioned in the y direction. The partial daisy chain x1 was located 1mm from the window, x2 was located 0.6mm from the window, x3 was located 0.2mm from the window and y was located at 0.2mm from the window. In order to electrically assess the joints a four point measurement was devised by applying a constant current of $100\mu\text{A}$ to the total daisy chain while the voltage was measured at the total daisy chain (z) and the partial daisy chains

x1, x2 and x3 as shown in Figure 4.11. As the electrochemical measurements showed that the current that passed through the joint was in the range of microamps, $100\mu\text{A}$ was used in the four point electrical measurement test.

An electrical circuit was made to make sure that it supplied $100\mu\text{A}$ to the test assembly. The Digimess HY3003 power supply, set to deliver $\pm 5\text{V}$, was connected to a $50\text{k}\Omega$ resistor which was connected in series with the negative input of an operational amplifier OP177. The positive input of the operational amplifier was connected to the ground of the Digimess HY3003. This setup allowed for $100\mu\text{A}$ to be obtained at the operational amplifier output which would be supplied to the test assemblies. All the voltage measurements from the individual daisy chains and the total daisy chain were transmitted to the computer via GPIB. LabView was used to automate the measurements and the data was collected with an Agilent 349901A 20 channel multiplexer and recorded into Microsoft Excel.

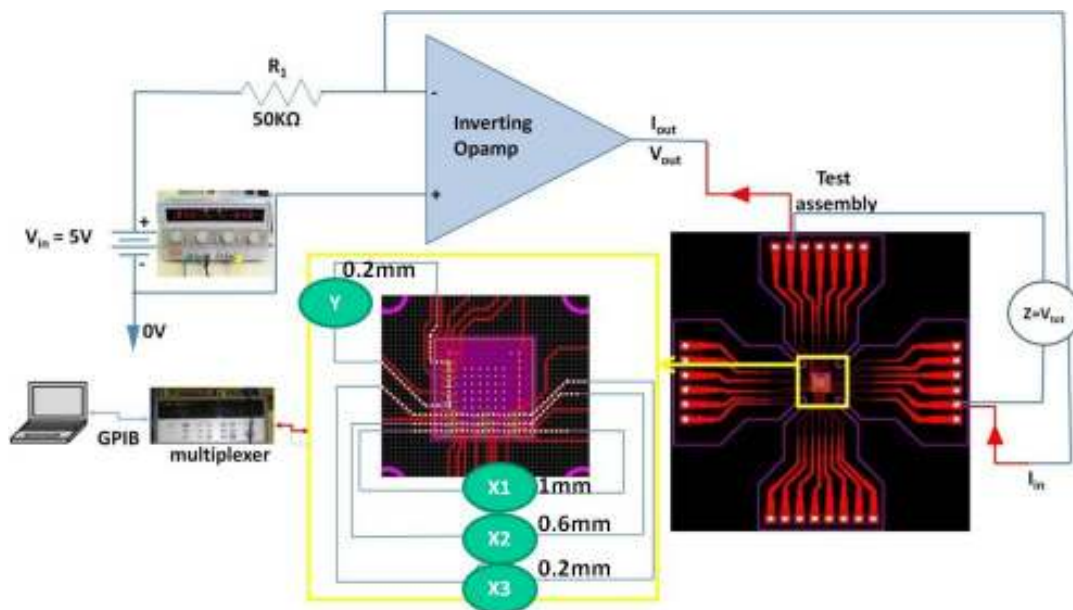


Figure 4.11. Schematic of the four point measurement test setup during mechanical test.

4.2.2.2. Results and discussion

Silicon compression test

Figure 4.12 shows the variation of force versus distance in the Z direction travelled by the chip. In the graph travel from 0mm to 0.2mm was characterized by the deformation of the silicone on top of the chip. After 0.2mm the pressure was directly applied to the back of the chip. From 0.2mm the force increased in a non-linear manner up to 70N where it plateaued. The plateaued region corresponds to the silicon break as shown in Figure 4.12. Therefore the maximum strength that the silicon test die could withstand in compression was around 70N. This was in accordance with the finding that a die of thickness of around 0.4mm would require a break load of about 70N [117]. It can be noted that the die had a slight depression towards the middle of the chip where significant cracks were present. From the centre of the chip where the cracks were present, finer cracks followed and traversed the length and the width of the chip. This could signify that the stress was higher close to the centre of the chip.

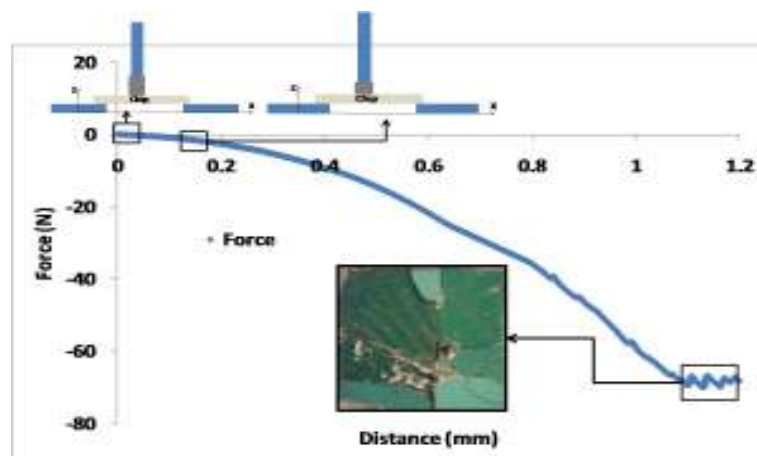


Figure 4.12. Plot showing the force variation during silicon compression test.

Mechanical testing of the ACA joints during capsule insertion

Two assemblies were subjected to mechanical testing. Each assembly was passed from the largest diameter hole to the smallest diameter hole successively until failure occurred. Each assembly was passed through each diameter hole twice and data was gathered before moving on to the next one.

In Figure 4.13, the primary axis represents the variation of the force with respect to the distance travelled by the ACA assembly in each diameter hole. The secondary axis shows the variation of the voltage measured in the total daisy chain of an ACA assembly as the sample was pushed through different diameter holes. An analysis of the insertion curve in the 23mm diameter will be used to explain the general form of the force curve obtained in the other diameter holes. The general form of the force curve consisted of an initial linear part which corresponds to preliminary insertion of the assembly into the hole. This was characterized by the slow folding of the flex assemblies' arms into a conical form when pushed through the diameter hole. In this linear region the flex assembly acts as a spring and opposes the assembly being pushed through the diameter hole. Therefore this region could be approximated by Hooke's Law in the form:

$$F1 = -Kd , \quad (4-1)$$

where K (N/mm) is the spring constant; $F1$ (N) is the force and d (mm) is the distance.

Figure 4.15, shows the linear part of the force curve in a 23mm diameter hole until position A. The slope of the linear part provided the spring constant and for the 23mm hole it is -0.2729N/mm. At around position A, the side corners of the extended arms of the flex cross of the fanned out region,

close to the slit came in contact with each other, as shown in Figure 4.14. This corresponds to the end of the linear region where the assembly had folded into a conical form the hole. From this point forward, there was no spring reaction from the assembly and the only force encountered by the assembly was the friction from the side walls of the hole. As the surface of the side wall is polished little friction was experienced by the assembly when pushed through the hole. This could be approximated by a horizontal straight line until the end of the test. This constant force to push the assembly was disrupted by the corners of the extended arms catching up at around position E as shown in Figure 4.14. As soon as the arms slip out from each other, the force applied returned to its original constant value until the end of the insertion test.

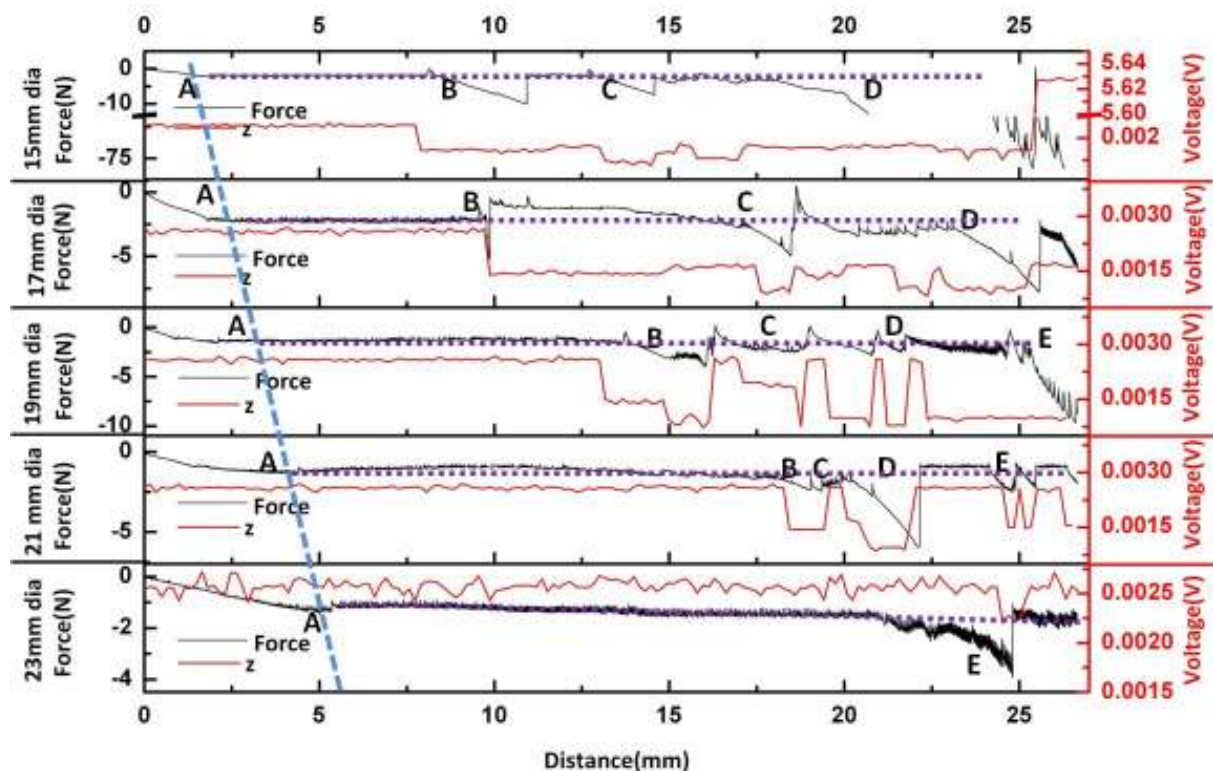


Figure 4.13. Plot showing the variation of the force and the measured voltage as a function of distance.

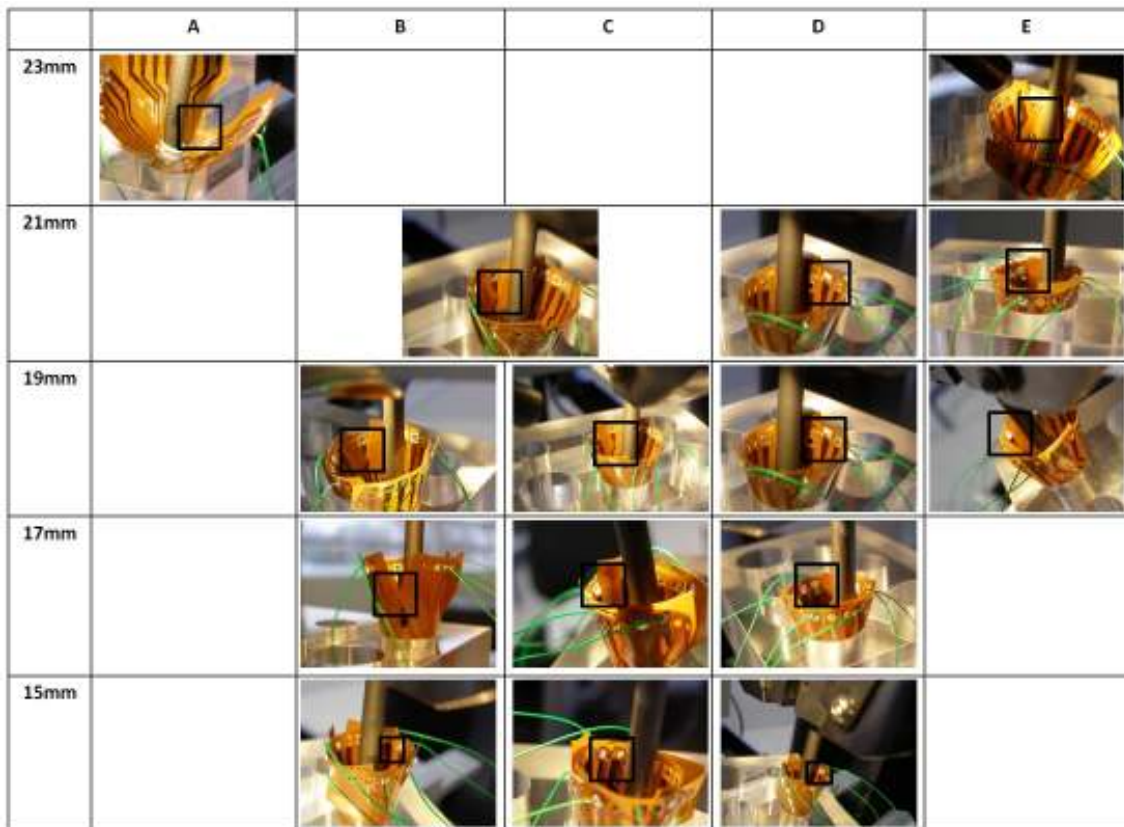


Figure 4.14. Images of the corresponding positions depicted in the force plot in different regions.

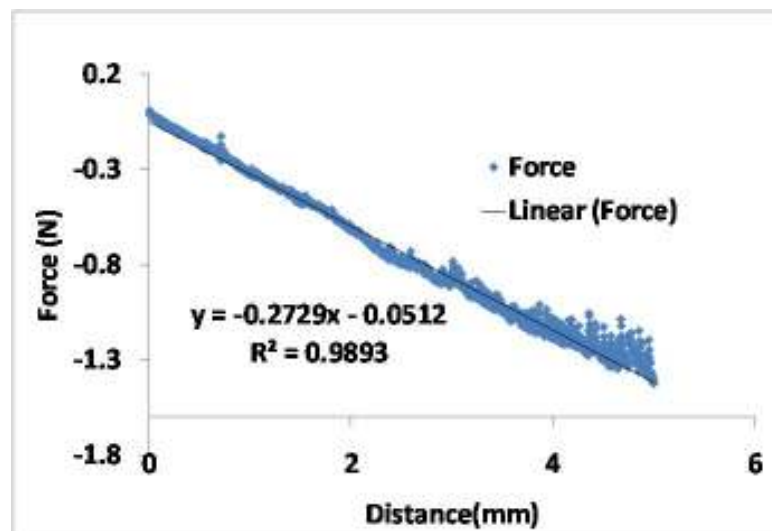


Figure 4.15. Plot showing the linear part of the force curve in a 23mm diameter hole until position A.

Figure 4.16 shows the spring constant calculated from the slope of the linear part of the graph in Figure 4.13 as a function of the diameter. It can be seen that spring constant decreases linearly as the diameter is increased. This signifies that for the same distance, less force will be required in a larger diameter hole than in the small diameter holes.

The conical shape occurs at an earlier stage as the diameter of the hole reduced. This also led to the catching of the extended flex side arms to occur at an earlier stage. This was indicated by position B and C as shown in Figure 4.13 and Figure 4.14. Further curling of the assembly on itself led to one of the tips of the fanned out arms being caught up with its neighbouring soldered bond pad as shown in Figure 4.14, position D and E. In the 15mm diameter hole, this was characterized by the chip break which occurred at around 70N.

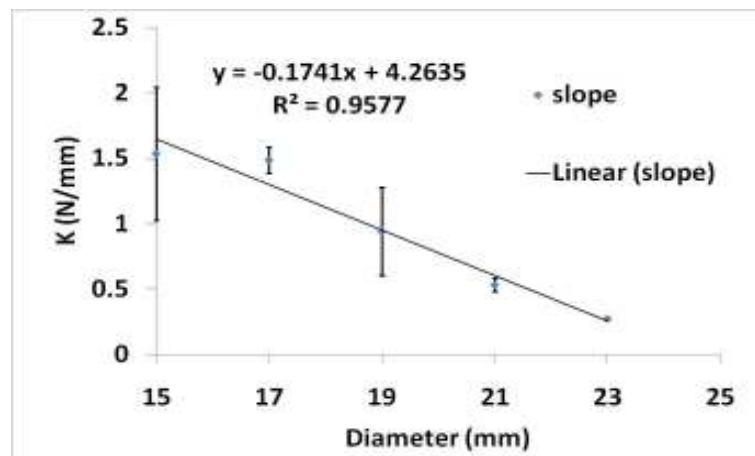


Figure 4.16. Linear part spring constant as a function of the diameter.

The electrical response of the total daisy chain during insertion into a 23mm diameter hole was characterized by a constant voltage with the exception of position E where there was a 15% drop in the measured voltage. This drop in the measured voltage was only momentary (i.e. the voltage after position E returned to its original value) and corresponded to the increase in the force at position E. The next section dealing with the resistance path of an ACA assembly will provide a detailed

explanation into the decrease observed in the measured voltage corresponding to the increase in the force experienced by the assembly. At positions B and C, the average decrease in the measured voltage was around 44%, 53%, 46%, and 44% corresponding to 21mm, 19mm, 17mm, and 15mm diameter hole respectively. A step decrease in the measured voltage was also observed for assemblies pushed through 19mm, 17mm and 15mm diameter holes. This step reduction in the measured voltage in the total daisy chain will be explained in detail when dealing with the partial daisy chains.

Total resistance calculation

The entanglement of the edge of the neighbouring fanned out arm or soldered bond pad caused the force on the back side of the chip to increase. As shown in Figure 4.17 the total resistance of an ACA assembly (for one conductive particle) could be composed of the following parts:

$$R_{AB} = \sum_{i=1}^n R_i , \quad (4-2)$$

where $n = 17$ and:

R_1 : Bulk resistance of the copper foil

R_2 : Bulk Resistance of substrate Ni pad

R_3 : Bulk resistance of substrate Au pad

R_4 : Contact resistance between the bond pad and the conductive particle

R_5 : Bulk resistance of the conductive particle

R_6 : Contact resistance between the bump and the conductive particle

R_7 : Bulk resistance of chip Au bump

R_8 : Bulk resistance of chip Al pad

R_9 : Bulk resistance of chip Al track

R_{10} : Bulk resistance of chip Al pad

R_{11} : Bulk resistance of chip Au bump

R_{12} : Contact resistance between the bump and the conductive particle

R_{13} : Bulk resistance of the conductive particle

R_{14} : Contact resistance between the bond pad and the conductive particle

R_{15} : Bulk resistance of substrate Au pad

R_{16} : Bulk Resistance of substrate Ni pad

R_{17} : Bulk resistance of the copper foil

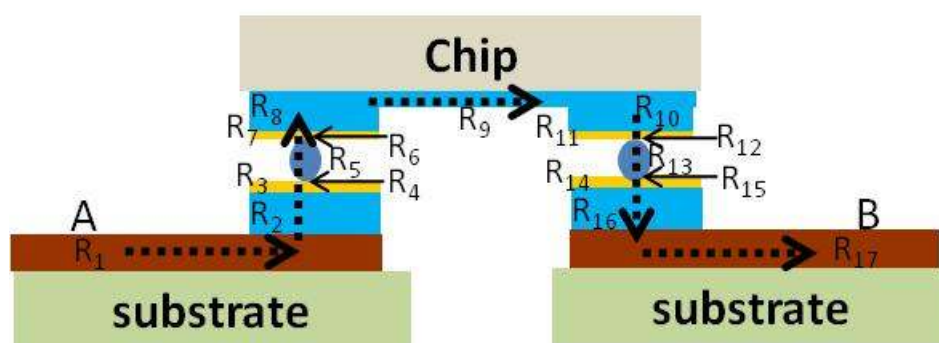


Figure 4.17. Schematic showing resistance path between A and B.

Generally the bulk resistance of the copper metal is stable and could be omitted from the test. If the assembly was well bonded then the contact resistance could also be omitted [115]. The copper foils

have high ductility and the fact that they are present close to the neutral surface in bending, means that the bending strain generated on the surface is very small [118,119]. This means that the resistance variation on the copper track on the substrate close to the chip area during the bend can be neglected.

Estimation of the chip, substrate, Cu track and Al track resistance

In order to estimate the chip and substrate pad resistance, the bond pad metals were assumed to have slab geometry as shown in Figure 4.18.

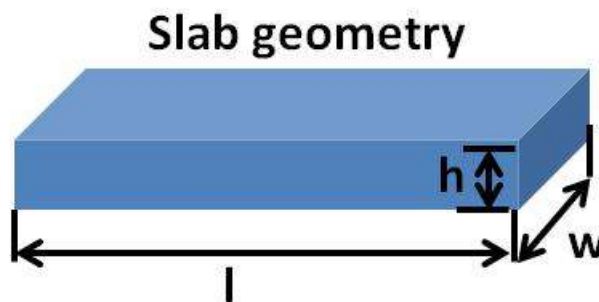


Figure 4.18. Slab geometry to estimate chip and substrate bond pad resistance.

The resistance of each layer was calculated using:

$$R = \frac{\rho l}{A} \text{ or } \rho = \frac{1}{S} \text{ so } R = \frac{l}{SA}, \quad (4-3)$$

where R is the resistance (Ω), ρ is the resistivity (Ωm), l is the length (m), A the area of the slab (m^2) and S is the conductivity of the materials ($1/\Omega\text{m}$).

Table 4.1 shows the resistance calculated for chip and substrate pad using the above approximation.

	material	Length, l (μm)	width, w (μm)	Height, h (μm)	conductivity, s ($1/\Omega \cdot \mu\text{m}$)	Resistance (Ω)
substrate	Au	100	100	0.05	45.2	$1.10619 \cdot 10^{-07}$
	Ni	100	100	5	14.3	$3.4965 \cdot 10^{-05}$
	Cu	100	100	15	59.6	$2.51678 \cdot 10^{-05}$
chip	Au bump	100	100	40	45.2	$8.84956 \cdot 10^{-05}$
	Al	100	100	1	37.7	$2.65252 \cdot 10^{-06}$

Table 4.1. Chip and substrate pad resistance.

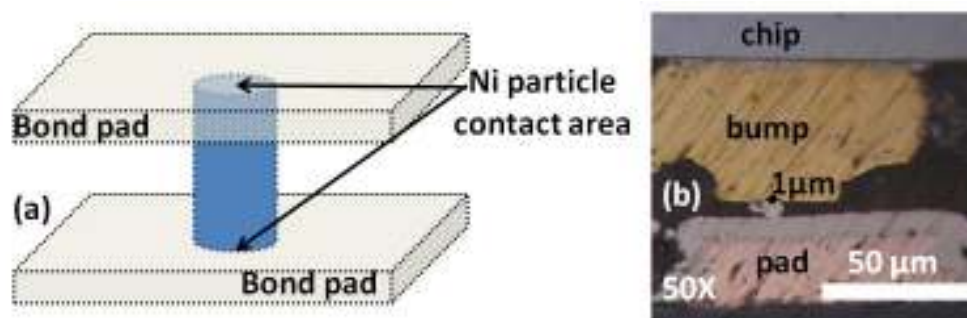


Figure 4.19. Ni particle contact: (a) contact cylindrical approximation and (b) cross-section showing the $1\mu\text{m}$ contact.

Figure 4.19 (a) shows the cylindrical approximation used to calculate the resistance of one nickel (Ni) particle in contact with substrate and chip bond pad. Figure 4.19 (b) shows the cross-sectional image of an ACA assembly with the $1\mu\text{m}$ contact made by the Ni particle on the chip and on the substrate bond pad. Therefore the area obtained was $1.57 \cdot 10^{-12}\text{m}^2$. Using the Ni resistivity of $7 \cdot 10^{-8}\Omega\text{m}$ [120], the length between the bondpads of $7\mu\text{m}$ and equation (4-2), the resistance was calculated to be 0.312Ω .

There are 10 particles per $100\mu\text{m}$ square pad. Due to the variation in the Ni particles (the particles vary from $5\mu\text{m}$ to $12\mu\text{m}$ with an average particle size of $7\mu\text{m}$), it could be assumed that just one particle made contact between the bond pads. Therefore $R_{AB}=0.624\Omega$. In a FCTC chip connection,

there are 25 connections (including two joints at a time). So $R_{tot}=15.608\Omega$. For a constant current of $100\mu A$, the corresponding voltage to be measured would be $1.56mV$. This is in the range of what was observed for the measured total voltage that was presented in the above section.

Table 4.2 shows the materials involved in the mechanical test. As mentioned above, an iron rod was placed on the back of the chip and pushed the assembly through the cylindrical hole. This would generate stress on the chip, flexible substrate and the adhesive that holds the chip and the substrate together. As the assembly is pushed through, the stresses generated on the chip and the substrate are compressive and tensile in nature, respectively. The elastic modulus of the chip is greater than that of the flexible substrate, it will not bend as much as the substrate. Due to the relatively low elastic modulus of the ACA, it will tend to compress or deform in-between the chip and the substrate [109]. As a consequence the increased pressure on the backside of the chip will be reflected by further compression of the joints.

Properties	ACA	PI flex	Chip
Young's modulus, E (MPa)	5900	4826	131,700
Poisson's ratio, ν	0.3	0.3	0.3

Table 4.2. Material parameters of the materials used in the mechanical test, collected from [121, 122].

The momentary decrease in the measured voltage was followed by it returning to its original value as soon the applied force decreased or recovered to its primary values. As the entanglement passes through, the brief compression exerted on the joint was relaxed. This could explain the decrease in the measured voltage recovered at position E during insertion into the 23mm hole.

Figure 4.20 shows the variation of the measured voltage in each partial daisy chain with respect to the distance travelled by the assembly as the mechanical test was carried out in a 23mm diameter hole. For the partial daisy chains situated in the x axis, x1 and x2, which are located further away from the window, showed no variation in the measured voltage while x3 – close to the window – showed a temporary 50% decrease at a depth of 25mm in the measured voltage before returning to its original value. As stated in the previous section, the average decrease in the total daisy chain was approximately 15%. This decrease corresponds to the increase in the force applied to the assembly, corresponding to position E as shown in Figure 4.13 and Figure 4.14. Furthermore, the decrease in the measured voltage in the total daisy chain and the partial daisy chain happened at the same time. This was in perfect agreement with the result observed for the total daisy chain as it was just an addition of all the partial daisy chains. No decrease was observed on the partial daisy chain y situated close to the window in the y axis. At the end of the test (insertion) all the measured voltage values remained at or regained their original value, thus suggesting that in a capsule insertion the joint would not be under stress during further processing.

Since the rod was placed in the centre of the back side of the chip during insertion, the maximum stress could be expected at the middle of the chip close to the window area [109]. Moreover, Figure 4.12 showed that for the same configuration die test, that the stress was high close to the centre of the chip. Figure 4.21 shows that for an assembly pushed through a cylindrical hole, the flexible substrate bend was limited by the slits made for facilitating the folding of the substrate during the insertion. As the full bend was not achieved, the adhesive holding the chip and the substrate at the chip perimeter might not be under high maximum shear stress, as indicated in Figure 4.21. The high stress region for this assembly could be at the flip chip end of the window opening where the chip is interconnected with the substrate. At position E (edge of the flex arm being caught up with solder connector bond pad), shown in Figure 4.14, the ACA might not compress uniformly from the window

opening until the edge of the chip. Instead, the compression is greater at the window opening close to the centre of the chip than at the edge of the chip because of this. This could be the reason that the momentary increase in force which was observed at a depth of around 25mm (position E) into the hole was reflected by a brief decrease in the measured voltage at the partial daisy chain x3 – close to the window.

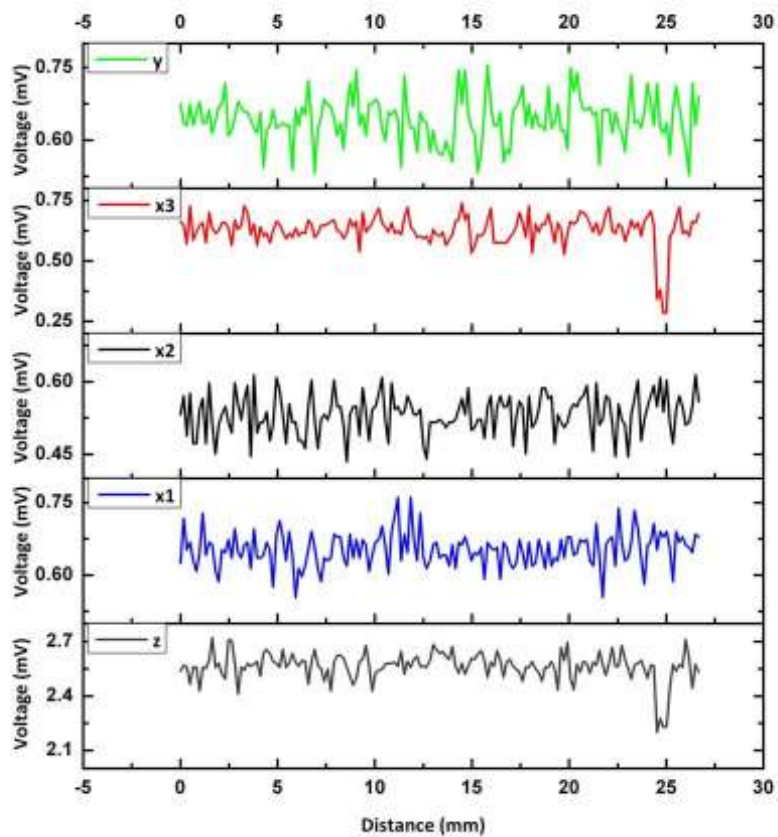


Figure 4.20. Figure showing the variation of the measured voltage as a function of the distance travelled in a 23mm diameter hole.

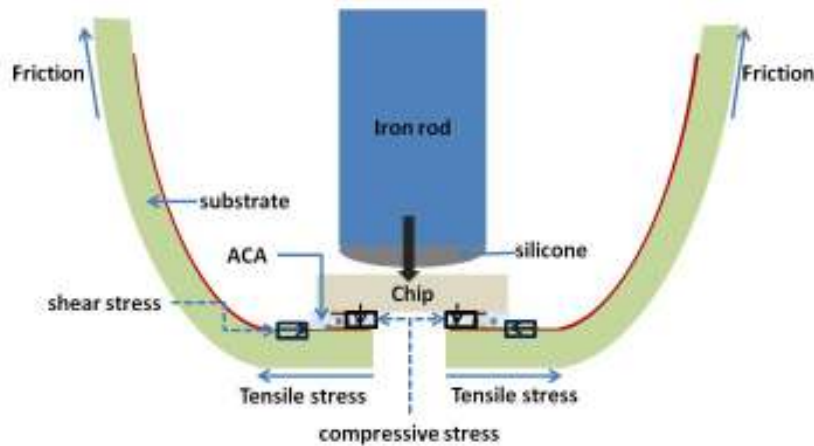


Figure 4.21. Schematic showing the regions of stress in the assembly during insertion.

Figure 4.22 shows the variation of the measured voltage in the individual partial daisy chains with respect to the distance travelled by the assembly as the mechanical test was carried out in 21mm, 19mm, 17mm and 15mm diameter holes. In order to illustrate the contribution clearly from individual daisy chains, the plots have been offset. As it can be seen in Figure 4.13, the step like behaviour observed in the total daisy chain voltage in the 19mm diameter hole could be explained by the addition of the decrease observed in each partial daisy chain i.e. x3 and y (closest to the window) showed an earlier sign of decrease in the measured voltage at around 14mm into the hole. These had a percentage decrease of around 86% and 78% respectively. This, as mentioned earlier, was due to the applied force on the back of the chip that resulted in the compression of the joint. This decrease in x3 and y was responsible for the initial lowering of the total daisy chain voltage. The partial daisy chains x1 and x2 had a voltage decrease of about 88% and 90% at a depth of around 15mm. As seen in Figure 4.22, the decrease in the daisy chains x1 and x2 further away from the window occurred on top of the reduction that was already observed in x3 and y. This induced an additional reduction in the measured voltage, thus resulting in a step like behaviour observed in the total daisy chain.

The major information to be gathered from these graphs is the fact that, as the diameter of the insertion decreased (due to the increased applied force to counterbalance the wall friction and mechanical contact) the measured voltage from the joints decreased. Another crucial piece of information to be gathered was that this voltage reduction was first observed in the partial daisy chains x3 and y that were closer to the window edge. For example, going through the graphs in descending order, i.e. from 21mm diameter hole to 15mm diameter hole, it can be noticed that the first reduction in the measured voltage always occurred at the partial daisy chains x3 and y that are close to the window. It was also clear that as the diameter was reduced, the depth at which the

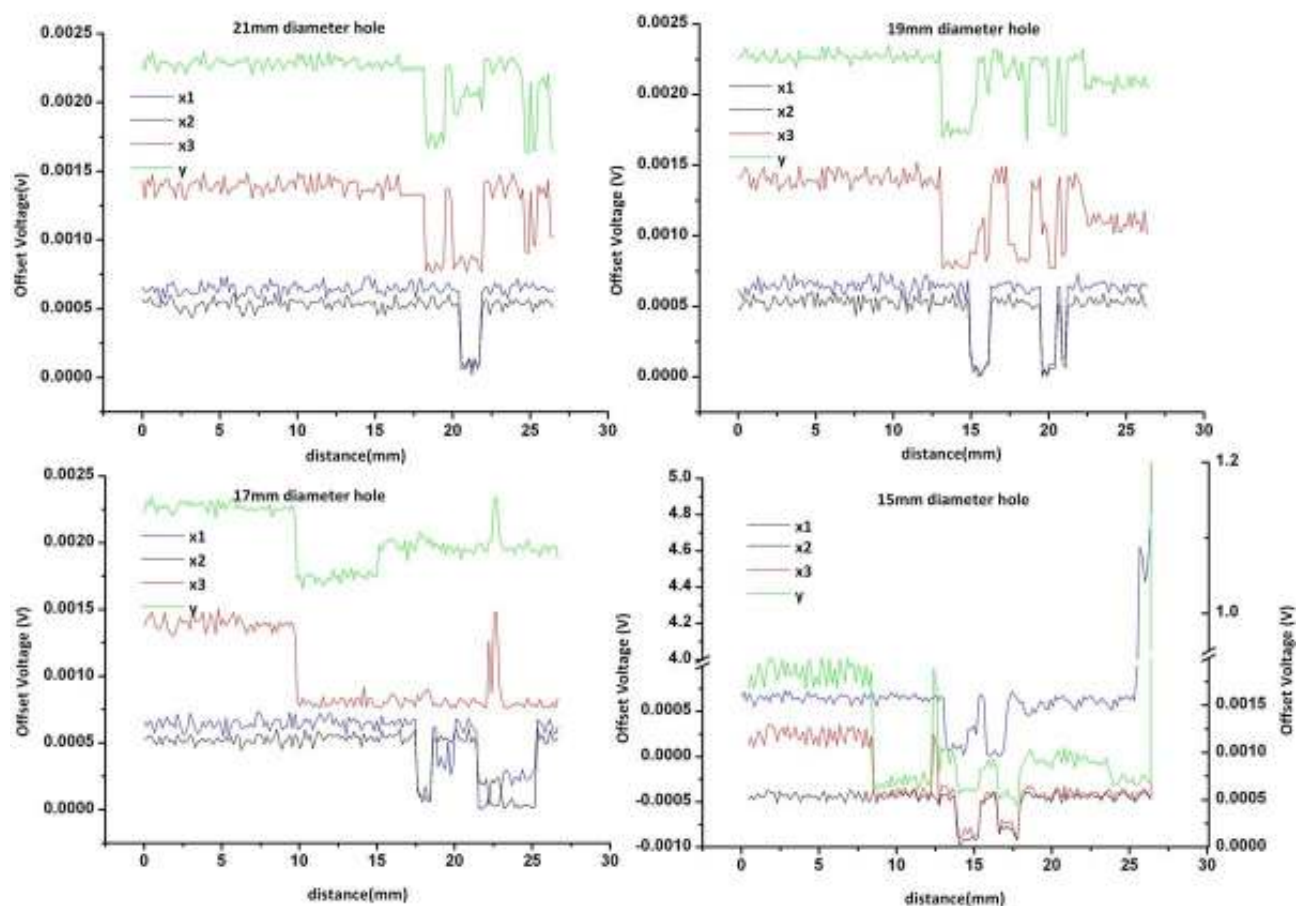


Figure 4.22. Plot showing variation of voltage in individual daisy chain as a function of distance travelled in

21mm, 19mm, 17mm, and 15mm diameter holes.

voltage reduction occurred also reduced. It should be noted that as the diameter decreased, the reduction of the measured voltages in these daisy chains did not return to their normal value until an open circuit was obtained at the 15mm diameter insertion due to the die cracking. As the diameter decreased, the drop in the measured value in the daisy chains x1 and x2 (further away from the window) experienced more compression on the joints due to the higher force required overcoming friction and the mechanical contact. Once again these measurements help to confirm the hypothesis that there was a high compressive stress on the chip close to the window joints and this should be taken into consideration for future interconnection design for capsule integration.

Figure 4.23 shows the micrograph of the assembly after the open circuit occurred. It shows the micrographs of two cracked dies after the mechanical test. In Figure 4.23(a), the crack seems to have traversed the length of the chip with some cracks running laterally across the chip. The cracks seem to widen near the centre of the chip and also close to the void that was present in the ACA, thus implying that they started simultaneously at the centre and at the corner of the chip and that the stress was high in these regions. Figure 4.23(b) shows an image of another cracked die. It can be seen that the silicon die at the centre of the chip seemed to lift and there is a slight depression close to the edge of the window. It can also be noticed that the cracks seem to widen at the point where the silicon die appeared to lift off. The depression and the wide crack close to the window imply that the stress was high in this region. An analysis of the failed ACA contacts after the mechanical test was carried out by cross-sectional analysis. Figure 4.24 shows the cross-sectional micrograph of one of the flip chip ACA contacts. Figure 4.25 shows the position where the cross-sectional micrograph was taken.

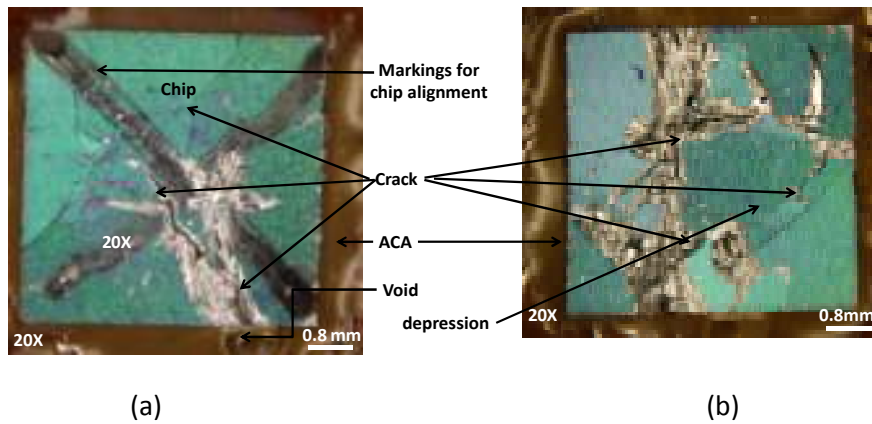


Figure 4.23. Micrograph showing the cracked dies after mechanical test.

It can be noticed in Figure 4.24(a), that the crack was widest close to the bump and gradually decreased towards the top of the silicon chip. From Figure 4.25 and Figure 4.24(b), it could be perceived that the bond pad was close to the applied force and that the crack was oriented towards the applied force. It also suggests that the stress was elevated closer to the edge of the window and that the stress was built up in the epoxy before being released by the die cracking and the pad lifting off. It could also be observed that the ACA adhesion to the substrate was still strong with acceptable contact to the ACA conductive particle. This may be the reason why the x1 and x2 resistance showed a sudden open contact. This showed that the weakness was on the chip pad side and not on the ACA contact.

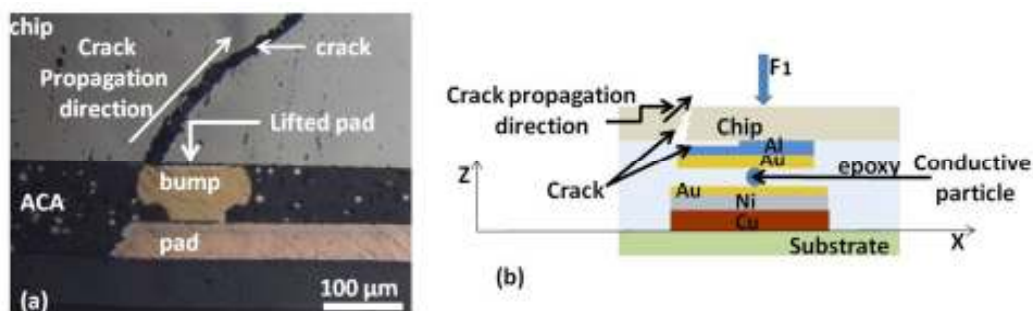


Figure 4.24. Crack propagation in the ACA assembly: (a) cross sectional micrograph of the assembly and (b) schematic of the cross section showing force and direction of propagation.

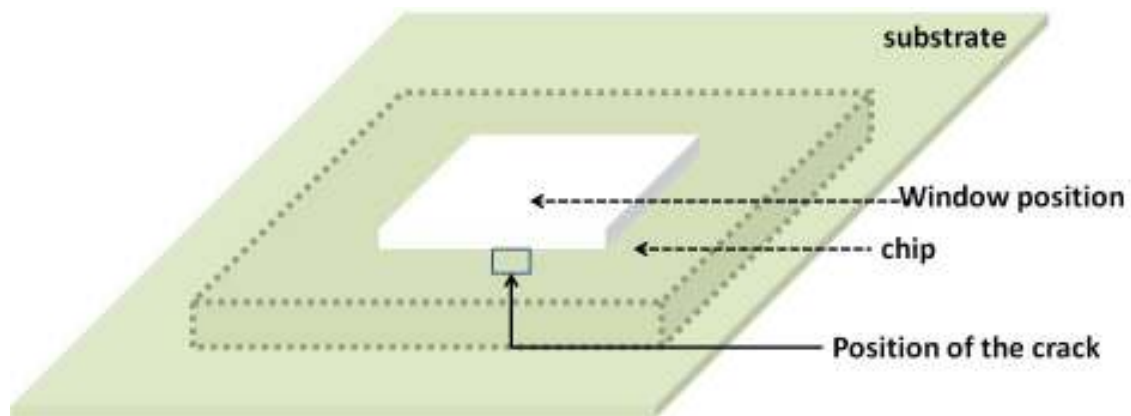


Figure 4.25. Schematic showing the position of the cross-section micrograph.

4.3. Conclusion

This study has described the testing performed on the mechanical reliability of the ACA joint during the insertion of the assembly into different sized diameter holes representing different capsule diameters. The insertion test detailed in this chapter could be assumed to be that of an inward bend defined by the die positioned on the positive side of the z axis. During insertion into the holes, the force curve was characterized by a linear part and a constant part identified by the constant low friction of the assembly. The linear region of the flex assembly acts as a spring and opposes the assembly being pushed through the diameter hole and was approximated using Hooke's law. The spring constant during the 23mm diameter hole insertion was calculated to be -0.2729N/mm . The spring constant decreased linearly as the diameter was increased signifying that for the same distance, less force would be required in a larger diameter hole than in the small diameter holes. After the initial linear part, further pushing through the hole was characterized by a conical form of the assembly. The conical shape occurred at an earlier stage as the diameter of the hole shrank. This also led to catching of the extended flex side arms occurring at an earlier stage. The electrical measurement in the total daisy chain made during insertion closely matched the insertion force, i.e.

every increase in the insertion force was matched by a corresponding decrease in the measured voltage.

During insertion, the stress in the assembly was greater towards the centre of the chip and the window than at the edge of the chip and the ACA fillet. This was characterized by it exhibiting lower voltage values measured in the partial daisy chains that were nearest to the window rather than the ones that were situated further away from the window. In these daisy chains, as the diameter was reduced, the depth at which the voltage reduction occurred also decreased, and they did not return to their original value until an open circuit was obtained in the 15mm diameter insertion. It also showed that high compressive stress was applied to the middle of the chip and close to the window compared to the edge of the chip and the ACA fillet.

This mechanical test showed that the assembly inserted into a 23mm diameter hole experienced the least amount of insertion force. In addition the electrical measurements showed more stable values throughout the insertion test suggesting that the 23mm diameter hole would be the smallest suitable hole for insertion of this assembly. This implies that a minimum capsule diameter of 23mm was the smallest capsule diameter that could be used in the DAS integration process for a specific substrate and chip design.

Failure analysis showed that cracks were noticed close to the centre of the chip while smaller cracks were visible near the edges of the chip suggesting high stress around the centre of the chip. The cross-sectional analysis showed that the failure occurred within silicon/silicon chip pad and that the ACA contacts form a strong joint and was able to withstand the -6N required to secure the ACA sensor in place before encapsulation.

In this chapter the mechanical stability of the ACA joint in a DAS while being inserted was studied. This study showed that the joints were stable during insertion and that the force required to secure did not affect the joints. Since the ACA sensor has to be immersed in a fluid environment for it to work, the next chapter will look into the short term electrical response of the ACA joints in the presence of a fluid.

Chapter 5 Electrical characterization of ACA in a DAS

5.1. Introduction

As discussed in Chapter 3, the development of the DAS involved FCOH technology in which ACA was used as the adhesive interconnection. This adhesive interconnect was a contact joint where the electrical function of the FCOH assembly relied on the contact pressure on the conductive particle during the total duration of the operation of the assembly. In the case of the DAS, the adhesive provided electrical contact via the joint and also assured the sealing of the area between the chip and the substrate. As shown during electrochemistry test, the sensor as well as the ACA comes into direct contact with the fluid environment in which the sensor assembly is placed. The adhesive is more prone to moisture uptake than the chip or metals used in track and pads. A preliminary test was performed to assess the time required to saturate the thin ACA used in a DAS. As mentioned in Chapter 3, the electrochemical results presented for the Au WE showed that the observed current at the WE during the cyclic voltammetry has to be balanced by the current passed through the CE. The currents in the WE and the CE are passed via ACA interconnect to the bond pads on the flex substrate. Once more it is crucial to point out that during these measurements the ACA comes into direct contact with the liquid environment. However, the cyclic voltammetry does not provide any information about the effect of moisture on leakage current between adjacent bond pads.

The electrical characterization of ACF in terms of leakage current in the x-y plane was studied by Basavanhally [123]. This study revealed that in a dry environment, 50V was enough to break down ACF's electrical isolation in the x-y plane by inspection of leakage current across the film. It was shown that 50V was required to exceed the leakage current of 1nA. In another study Kumbhat et al [124] looked into the reliability of 30 μ m pitch copper interconnects using nano-ACF/NCF. They also studied the leakage current between adjacent bond pads. In their work, one of the interconnection

processes used was a nano-ACF with 20nm Ag particles. The leakage current measured between the adjacent bond pads in a dry environment in this material, for a voltage sweep of 0.1V to 2V, was in the range of pA. These leakage current measurements were carried out in a dry environment but in this chapter, the objective was to study the leakage current of the ACA in a liquid environment. A study by Lai et al [116] was restricted to temperature cycling reliability of the ACA flip chip joint with FR4 rigid and polyimide flexible substrates. Studies by Frisk et al [125] and Kokko et al [126] were limited to a study of the effect of moisture reliability on the ACA FC joints in a constant humid environment, whereas Chang et al [127] studied the leakage current in the ACA between adjacent bond pads in a humid and bias test. Their study showed that the insulation resistance degradation was more than three to sixteen orders of magnitude in the ACA. They also proposed that the enhanced electric field around the particles and cavities in the polymer matrix was the driving force for corrosion, migration and dissolution of metallic elements from metal conductive particles.

This chapter describes the work carried out to measure the leakage current in the x-y plane of the ACA between the CE and the WE to observe the effect of the moisture and more particularly to discover the effect of artificial GI fluids on the electrical isolation in the x-y plane. The following section describes the leakage testing; initially the preliminary gravimetric analysis of the thin ACA is considered and subsequently the ACA leakage study with its result and discussion are presented.

5.2. Leakage testing

5.2.1. Preliminary gross gravimetric analysis

The materials such as the test chip and flex substrate, used for this test were described in Chapter 3. A gross gravimetric analysis was carried out to estimate the saturation time of the thin layer (21 μ m) of ACA used in the DAS. Five samples of the test substrate, test chip and the fabricated device were

baked in a Heraeus vacuum oven at 100°C for three days. Each day the samples were taken one by one out of the oven and their weight was measured with a Toledo XS105 dual range analytical balance with an accuracy of 0.1mg. After day one none of the samples showed any variation in weight. Samples were kept an additional two days in the oven was to ensure all the moisture was removed from them. Since no weight change was observed on day two or three, the samples were moved from the oven to a Heraeus Vötsch HC7033 humidity chamber at 50°C / 95%RH. The samples were taken out individually every 24 hours and weighed. The weight of the substrate and the chip were subtracted from the weight of the device so that the weight gain of the ACA could be obtained. The percentage weight gain of the ACA in all the samples was calculated from equation (5-1):

$$M_t = \left(\frac{W_t - W_0}{W_0} \right) * 100 \quad (5-1)$$

where W_t is the weight of the wet specimen at time t , and W_0 is the weight of the dry specimen.

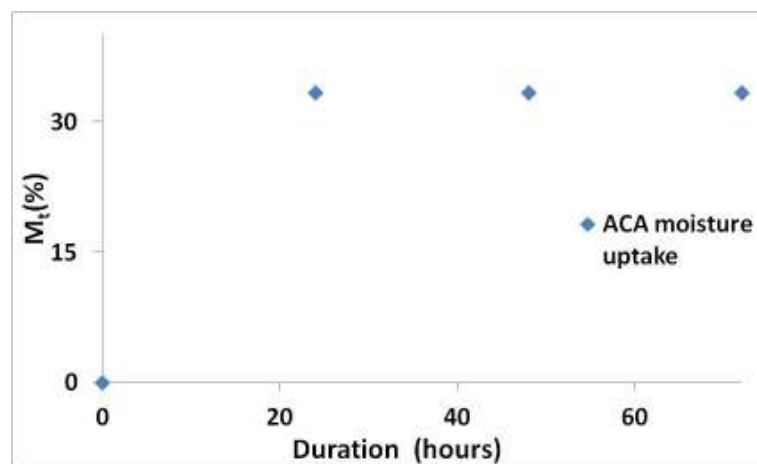


Figure 5.1. Variation of ACA weight gain versus the duration of the soak.

Figure 5.1 shows the variation of the weight gain of the ACA over a 72hr period. The gross gravimetric test showed that the epoxy of 21µm thick was saturated with water at 30% mass within

the first 24hr and remained saturated until the end of the test. The saturation of the epoxy could be explained by the moisture penetration from both sides that occurred at the window and at the edge of the chip / ACA fillet as shown in Figure 5.2.

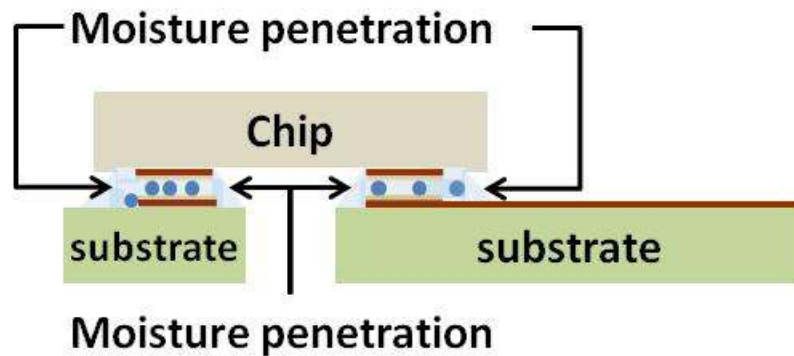


Figure 5.2. Schematic showing moisture penetration in the chosen setup.

Even though the gross ACA saturation measurement does not provide any information on the diffusion behaviour, a Fickian diffusion behaviour in the chosen epoxy could still be assumed [128].

5.2.1.1. Fick's law

The moisture diffusion in an epoxy system could be described using Fick's second law. Different materials absorb moisture and expand at different rates [129] causing hygroscopic stress to occur between the materials. If the stress increases enough, it may cause failure in the system (for example a crack, delamination or an open circuit). When the epoxy comes into contact with a humid or liquid environment, the diffusion of the moisture/solvent is in the direction of the concentration gradient. In the case of a thin flat ACA structure it can be described by the one dimensional equation (5-2) [130-134]:

$$\frac{\partial C}{\partial t} = D \frac{\partial^2 C}{\partial x^2}, \quad (5-2)$$

where C is the moisture concentration, t is time, and D is the diffusivity defined as the amount of water passing per second through a unit area under the influence of the concentration gradient and can be expressed as:

$$D = D_0 \exp\left(-\frac{E_D}{R1T}\right), \quad (5-3)$$

where D_0 is a pre-exponential factor, E_D is activation energy, T is temperature in Kelvin, and $R1$ the universal gas constant.

For samples soaked in a humidity chamber, the saturated moisture concentration of water C_s for one-dimensional diffusion is given by:

$$C_s = RH * H * P_{sv}, \quad (5-4)$$

where RH is relative humidity, P_{sv} is saturated vapour pressure, and H is Henry's law coefficient which can be written as:

$$H = H_0 \exp\left(-\frac{E_H}{R1T}\right), \quad (5-5)$$

where H_0 is the pre-exponential factor and E_H is the activation energy.

For samples soaked in water, the moisture concentration C_s can be calculated from:

$$C_s = \frac{\rho_e M_w}{\rho_w M_e}, \quad (5-6)$$

where M_w and M_e are the masses of water and the dry epoxy, respectively; ρ_w and ρ_e are the densities of water and dry epoxy, respectively.

Assuming that the epoxy initially contained no moisture/water/solvent, the diffusion into the epoxy continues until the concentration reaches C_s over the entire epoxy system. Using the initial and final boundary conditions:

$$C(x,0) = 0; C(x,t) = C_0; C(x,\infty) = C_s, \quad (5-7)$$

the solution to the partial differential equation (5-2) for one-dimensional moisture/water/solvent diffusion problem can be obtained as:

$$C(t) = C_s \left(1 - \frac{4}{\pi} \sum_n \left(\frac{-1^n}{2n+1} \right) \exp \left[-\frac{(2n+1)^2 \pi^2}{h_2^2} Dt \right] \cos \frac{(2n+1) \pi l}{h_2} \right), \quad (5-8)$$

where h_2 is the thickness of the sample and the l is the length of the sample.

Another analytical solution to the one-dimensional equation (5-2) is given by:

$$C(t) = C_0 \left(1 - \operatorname{erf}(x/\sqrt{4Dt}) \right), \quad (5-9)$$

where x is the distance and t is the time.

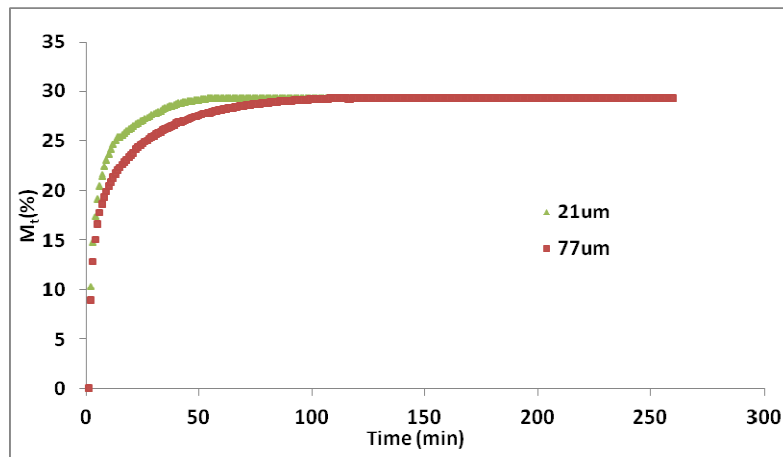
In equation (5.8), ignoring all terms in the series except for the first one, the solution to the diffusion equation for a flat plastic package can be approximated by the following simple expression:

$$C(t) = C_0 \left(1 + \frac{4}{3\pi} \exp \left[-\frac{9\pi^2 Dt}{h_2^2} \right] \cos \left(\frac{3\pi l}{h_2} \right) \right), \quad (5-10)$$

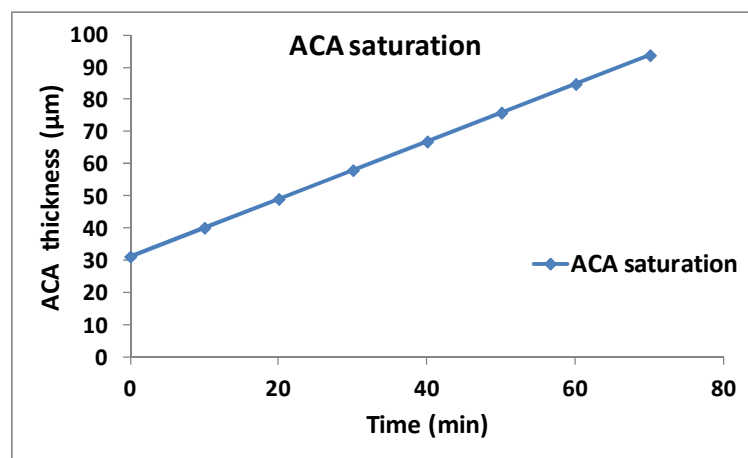
and ϑ the saturation time is given by:

$$\vartheta = \frac{4l^2}{\pi^2 D}, \quad (5-11)$$

where l is the length of the flat system.



(a)



(b)

Figure 5.3. Plot (a) analytically calculated moisture concentration for thin ACA and (b) relationship between thickness and time.

In the above section, the gross gravimetric analysis of the ACA used in the DAS showed that the thin ACA saturated within the first 24hr of soak. For a thin 21 μm and 77 μm ACA, an analytical solution was calculated using equation (5-8). Table 5.1 shows the parameters that were used in the analytical calculation. For a given temperature, the activation energy governs the diffusion into a sample. Therefore a sample immersed in water and in 100%RH at 37 $^{\circ}\text{C}$ will have a similar diffusion curve and moisture concentration. Figure 5.3(a) shows the variation of the analytically calculated percentage weight gain over the period of soak. It can be seen that both 21 μm and 77 μm thick ACA fully

saturated with moisture within 50min and 100min of soak respectively. The 21 μ m thick ACA saturates twice as fast as a 77 μ m thick ACA. Figure 5.3(b) shows the relationship between the thickness and the soak time. It can be that there is a linear relationship between the thickness and the soak time.

D (mm ² /s)	D_0 (mm ² /s)	E_D (eV)	$R1$ (J/mol K)	H_0 (mg/mm ³ Pa)	E_H (J/mol)	T (K)
9.7 *10 ⁻⁶	5.9 *10 ⁻⁷	0.451	8.3145	2.07 *10 ⁻¹¹	-3.02 *10 ⁴	323
RH (%)	P_{SV} (Pa)	ρ_e (mg/mm ³)	M_w (mg)	ρ_w (mg/mm ³)	M_e (mg)	
100	12340	1.9	1000	0.98	125	

Table 5.1. Table of parameters, collected from [88,130,135-137].

The preliminary test in section 5.2.1 showed that the thin ACA saturated within 24hr of soak. The analytically calculated percentage weight gain over the period of soak showed that the ACA fully saturated with moisture within 100min of soak. Both the analytical solution and the weight gain test do not provide any information about what contributes to the leakage current between adjacent bond pads in a soaked environment. The next section deals with the electrical characterization of the ACA between adjacent bond pads in a liquid environment.

5.2.2. ACA leakage current in a DAS

5.2.2.1. Materials and methods

As shown in Figure 5.4, the test substrate contained bond pad connections for four working electrodes (WE) called s1, s2, s3, s4 and a counter electrode (CE). All bond pad measurements were taken with respect to the centre of the CE. It can be noted that the centre of s1 is positioned at

5.48mm in the y direction and at 0.3mm in the x direction; centre of s2 at 0.2mm in the y direction and 0.3mm in the x direction; centre of s3 at 4.65mm in the x direction; and centre of s4 at 5.48mm in the y direction and at 4.65mm in the x direction from CE respectively.

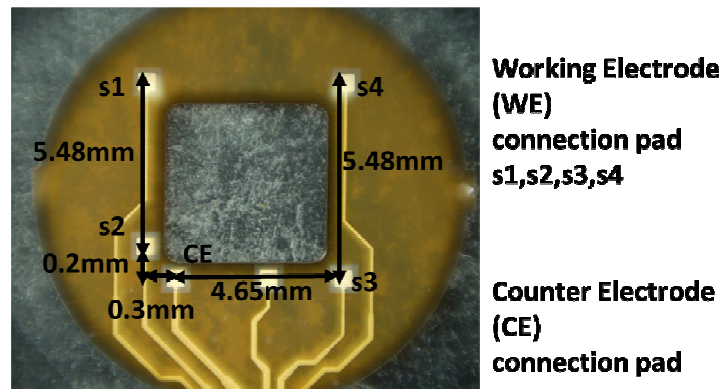


Figure 5.4. Micrograph of test substrate.

As shown in Figure 5.5 and in Chapter 3, the area inbetween the chip and the substrate is covered by ACA. In order to determine the device that will be used for leakage testing, the resistance was measured separately on the chip CE and on the substrate between the CE and the WEs. As s2 was the closest bond pad to the CE, it was chosen to study the leakage current. The resistance between the CE and the s2 WE on the chip electrode was around $2M\Omega$ while the resistance on the substrate between CE and the s2 WE was several $G\Omega$. The insulation resistance of the ACA was given by the manufacturer to be $2*10^{13} \Omega\text{cm}$ [88]. The leakage current is known to take the least resistant path and from these values, all or most of the current will tend to flow between the WE and the CE on the chip. As the objective of this chapter is to study the leakage current of the ACA in a liquid environment, any contribution from the chip has to be eliminated. Therefore the chip was not used in any of the leakage current tests that are described below. Stencil printing was used to dispense ACA onto the board to cover the area in-between the bond pads. As shown in Figure 5.6, the stencil was made up of a $70\mu\text{m}$ thick polypropylene sheet in which two square bracket-shaped tracks

1.5mm wide were produced. These square brackets were held by a small section which covered the window of the substrate while the ACA was dispensed. The stencil was set directly in contact with the substrate, aligning the substrate window to the thin rectangular section of the polypropylene sheet and exposing the bond pads on the substrate. ACA was dispensed on top of the stencil and a squeegee was used to apply the ACA on to the board. After application the stencil was removed and the two square bracket sections were connected manually by brush coating. The assembly was then cured in a Finetech Flip-Chip bonder with a ramp rate of 2°C/sec with a hold at 200°C for 50sec and a cool down rate of 3°C/sec. Figure 5.7 shows the ACA bondline over the bond pads and the average bond line thickness of the adhesive taken from six samples was found to be approximately 77µm with a standard deviation of 15µm.

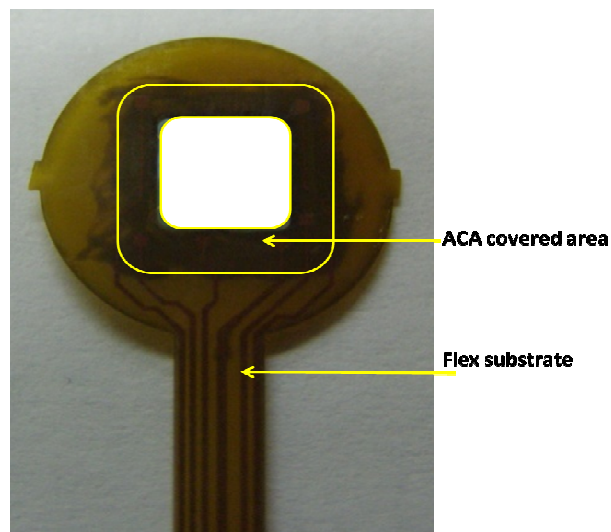


Figure 5.5. ACA bonded DAS on flex substrate.

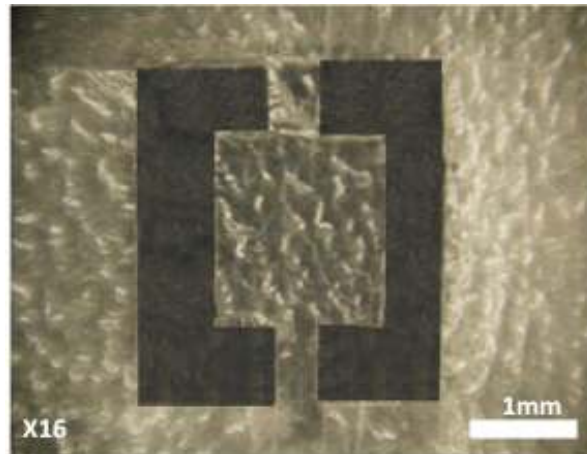


Figure 5.6. Micrograph of stencil.

As shown in Figure 3.2, the copper track was covered by a passivation layer with passivation opening for the bond pads. Before soak testing, the devices (substrate and the ACA) leakage current was measured between the CE and the WE. In parallel, the leakage current was measured on a separate substrate without ACA. The former leakage current measurement was subtracted from the latter to get the leakage current of ACA in a dry environment.

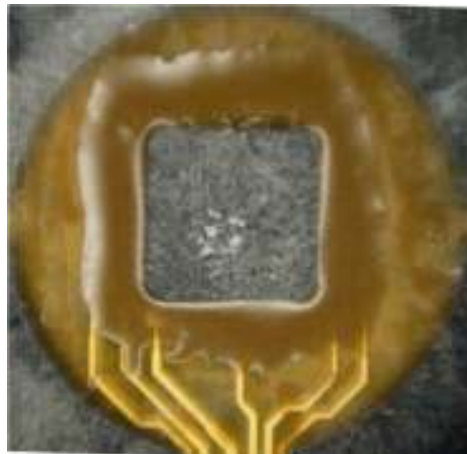


Figure 5.7. Micrograph showing ACA bondline around the substrate bond pad.

Figure 5.8 shows the experimental setup used for measuring the leakage current of the ACA in the x - y plane inbetween the chip and the substrate during the soak testing. In order to measure the leakage current flowing in the test devices, just the circular part of the device (substrate and ACA)

and the bare substrate were placed in a small test tube containing different pH solutions; the circular edge of the test tube was sealed with silicone plugs and placed in a temperature controlled recirculating water bath at 37°C. A Keithley 2400 was used as a voltage source, which was connected to the connector pad of the CE and supplied a voltage from -5V to +5V with a step of 0.25V. A digital multimeter (Agilent 3458A) was used to read the leakage current from the connector pad of different WEs while connected to the ground of the Keithley, thus providing the path for the current to flow through the ACA of the WE. As shown in Figure 5.8, the four connections connecting the four WEs were tested from right to left in the following numbering order: s1, s2, s3 and s4. The leakage current was measured on the device and on the substrate every hour. The bond pads on the bare substrate were directly exposed to the solution and thus had a different response to the devices. Therefore for the soak test, only the leakage current of the device were considered. s2 was the closest bond pad to the CE; therefore it was chosen to study the leakage current. All the measurements were automated via LabView and the results recorded into Microsoft Excel.

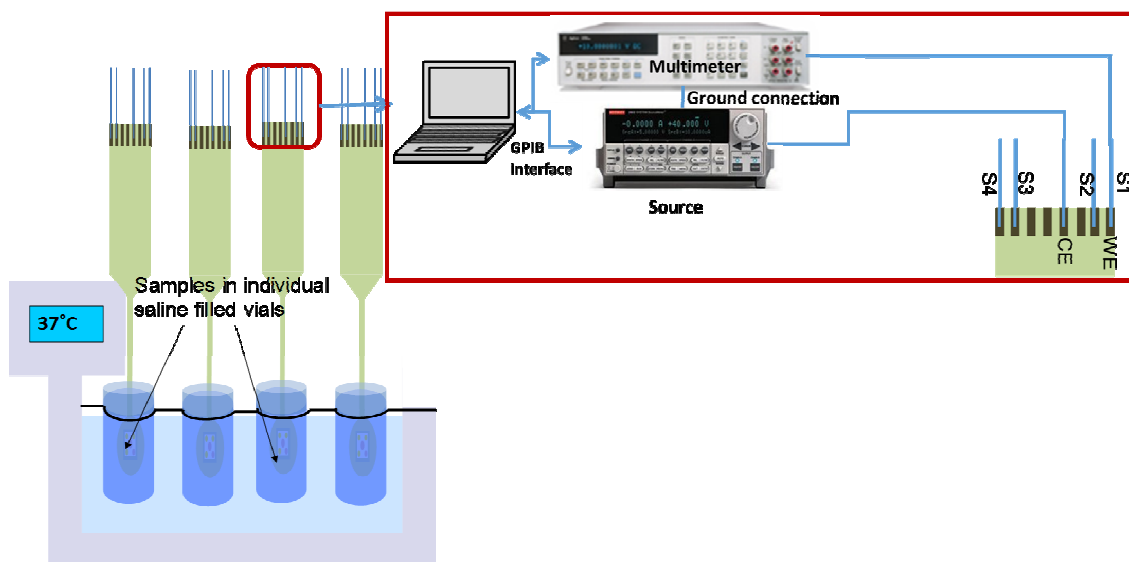


Figure 5.8. The experimental set up for leakage current measurement.

5.2.2.2. Testing solutions

Artificial gastrointestinal solution

Artificial gut fluids were made to test the leakage current in the x-y plane of the ACA in a GI environment. Accordingly, a fluid representing gastric juice of pH1.2 was made from 2g sodium chloride (NaCl), 3.2g pepsin ($800 - 2500 \text{iu mg}^{-1}$) and 7ml 37wt% hydrochloric acid (HCl) was made up to 1000ml in DI water. Likewise, a fluid representing intestinal juice of pH6.8 was made up from 6.8g potassium phosphate – monobasic (KH_2PO_4) dissolved in 250ml DI water, 77ml of 0.2M sodium hydroxide (NaOH) and 10g pancreatin made up to 1000ml with RO water, and adjusted to pH6.8 with 0.2M HCl [28].

Buffer solution

A buffer solution of pH7.4 was made up from 10 ml of phosphate buffer saline – PBS (1M sodium phosphate, 17wt% NaCl of pH6.8) by diluting it 10 fold by adding DI water to 100ml of PBS mixed with 900ml of DI water. This made 1000ml of PBS solution of pH7.4. The ACA x-y plane leakage current measured with PBS solution was used as a control test to compare the results obtained with the artificial gut solution.

5.2.2.3. Results and discussion

5.2.2.3.1 Measured leakage current.

The epoxy used in this research was a Bisphenol-A epichlorhydrin resin with a molecular weight of around 700 and had an amine based hardener – Triglycidyl-p-aminophenol. During the curing process of the epoxy based ACA, cross linking of the molecular segments takes place where the end

group of the epoxy and the hardener react. In this reaction a covalent bond between the nitrogen of the hardener and the carbon of the epoxy is formed while hydrogen and oxygen form a polar hydroxyl group [138]. This cross linking process forms a 3-D structure in which each molecule moves towards its equilibrium position with a volume around it that is excluded for other molecules which is termed an occupied volume [139]. The free volume, defined as the difference between the measured volume of the polymer and the occupied volume is caused by packing irregularities. As the polymer is cooled through the glass transition temperature T_g , the free volume continues to decrease until a critical free volume fraction of about 1/40 (2.5 +/- 0.3%) of the total volume occupied by the polymer is obtained [139]. These free volumes create nano pores whose diameter range from 5-10Å and form a network all the way throughout the polymer. The water molecules that diffuse and occupy the free volume or the nano pores are deemed to be in an unbound state, as shown in Figure 5.9(a). On the contrary, the bound state refers to the water molecules that interact with the amine or the hydroxyl group, disrupting the hydrogen bonding and causing swelling of the epoxy. This is shown in Figure 5.9(b) [138-141].

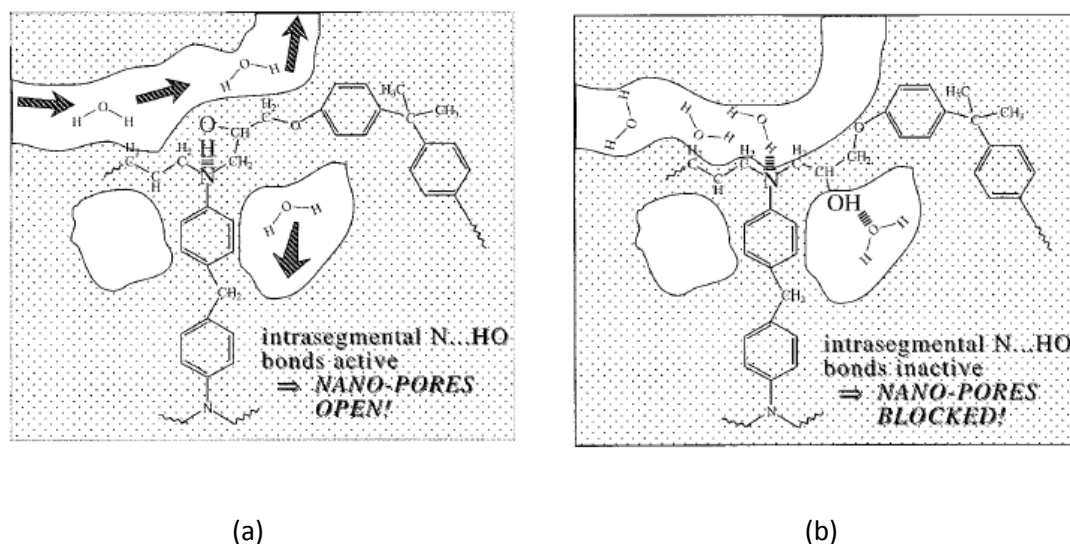


Figure 5.9. Polymer matrix with nano pore network showing: (a) water in unbound state and (b) in bound state diffusion [140].

For all the samples that were subjected to the leakage test, the leakage current was measured before the soak and every hour during the soak in buffer, pH6.8 and pH1.2. s2 was the closest bond pad to the CE, therefore it was chosen to study the leakage current.

Figure 5.10 shows the initial I-V characteristics of the leakage current measured on dry samples. Due to the variability in the measured data, the measurements for the substrate and the devices were averaged and the response of the ACA was obtained by subtracting the averaged device response from the averaged substrate response. It shows the voltage applied and the average current measured in the ACA inbetween the CE and s2 WE contact pad. It can be observed that the leakage current measured is in the range of around -1.3×10^{-10} A to around 1.2×10^{-10} A. In dielectric films, at low voltage the I-V curve is linear (ohmic region) [142]. As the voltage applied was low, a linear fit was considered and it showed that the average conductance given by the slope was around $2.4604 \times 10^{-11} \Omega^{-1}$. The trendline showed that there is a strong linear relationship ($R^2 = 0.9961$) between the measured leakage current and the applied voltage. The fact that a different substrate was used to measure the substrate effect and the use of coax cables in the experiment could have caused noise to be part of the data and thus reduced the measured leakage current which is reflected in the insulation resistance.

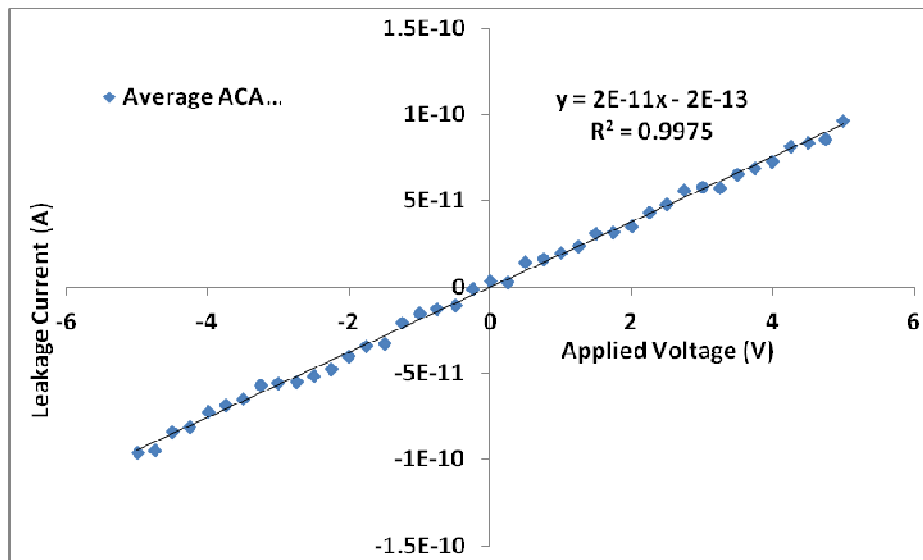


Figure 5.10. Initial I-V characteristics of the leakage current measured on a dry sample.

The same WE ACA bond pad connection s2 was considered to show the effects of different fluid environments on the leakage current. Figure 5.11 presents the measured average device leakage current versus the applied voltage after 1hr soak in different fluid environments such as buffer, pH6.8 and pH1.2. During the soak test, the device measurements were not subtracted from the bare substrate due to the fact that the bond pads in the bare substrate came in direct contact with the fluid environment as opposed to the device. Once more due to the variability of the data, the average device results are presented.

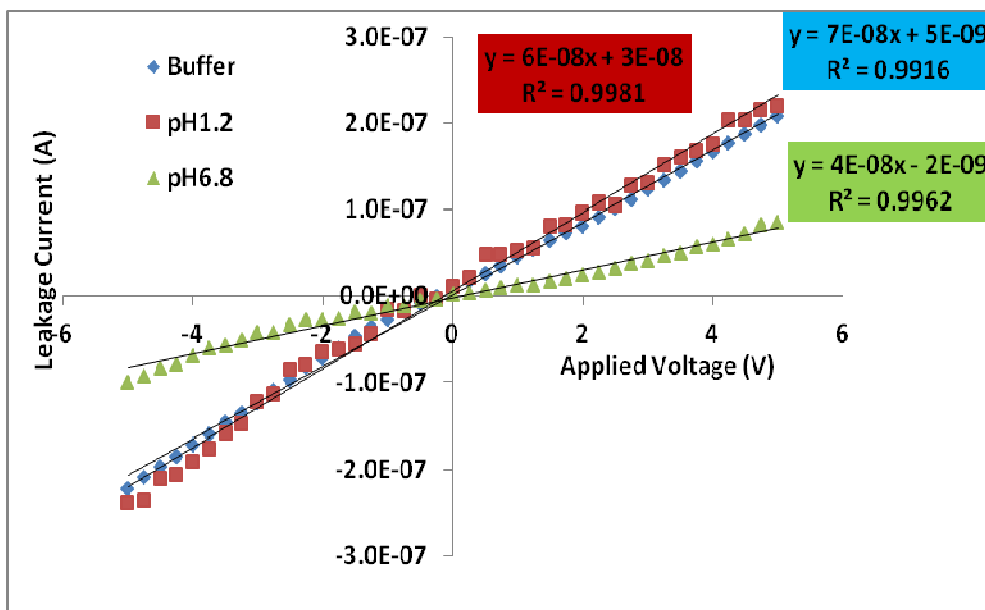
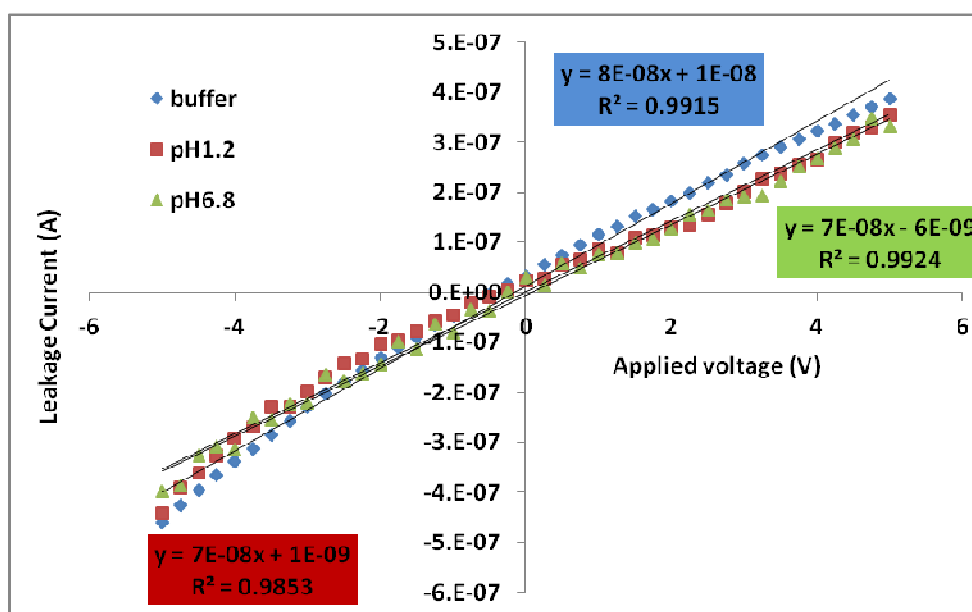
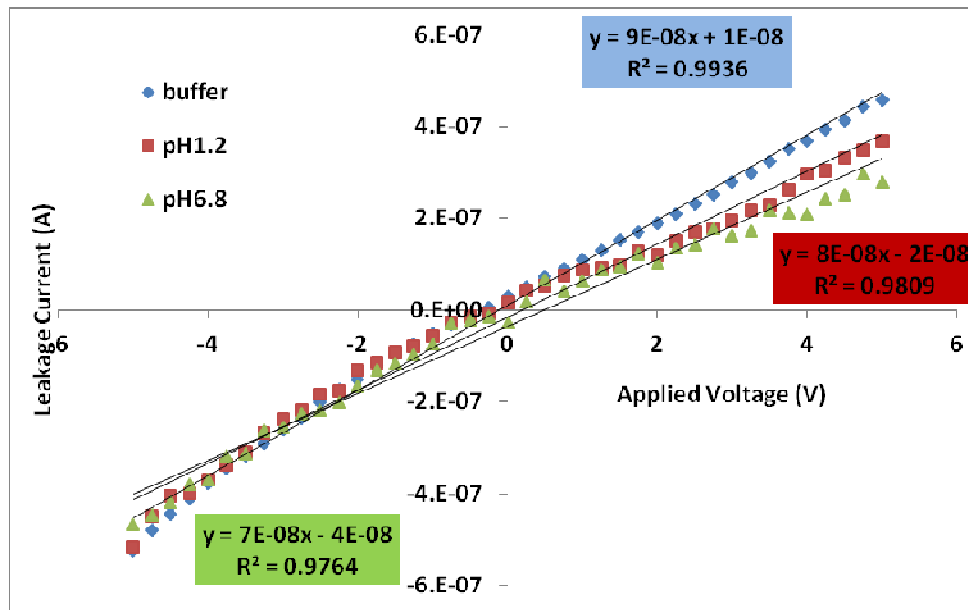


Figure 5.11. I-V characteristics of the leakage current measured after 1hr soak.

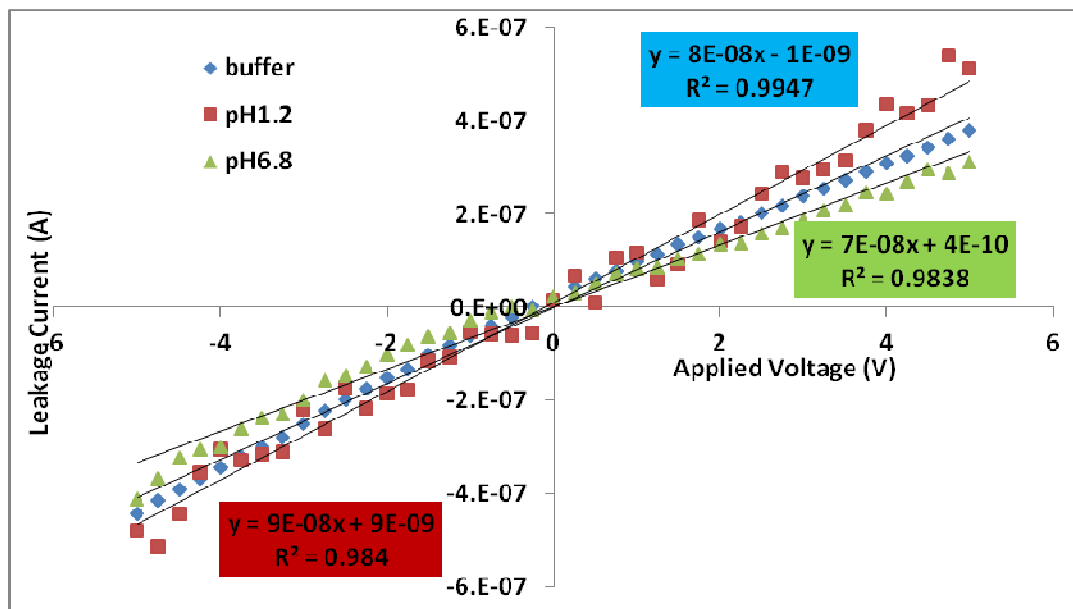
It can be seen, the average device response shows a linear trend with high R^2 values in all the fluid environments. Figure 5.11 also shows that after 1hr soak in different fluids, the leakage current increases on average from 100pA to 100nA. The high leakage current measured in the buffer solution could be attributed to the absence of the pepsin and the pancreatin present in other pH solutions.



(a)



(b)



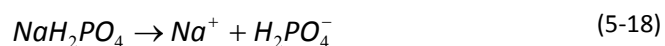
(c)

Figure 5.12. I-V characteristics of the leakage current measured after (a) 2hr, (b) 3hr and (c) 4hr soak.

Figures 5.12(a), (b) and (c) show the variation of the measured leakage current with applied voltage in buffer, pH6.8 and pH1.2 after 2hr, 3hr and 4hr soak test respectively. As can be seen the measured leakage current was in the range of 100nA in each of the tested solutions during the 2hr, 3hr and 4hr soak period. It can be noted that during the 4hr soak, the average device response showed a linear trend with high R^2 values in all the fluid environments. This indicates a good correlation between the measured leakage current and the applied voltage in all the fluid environments but does not provide any information about the ionic contribution to the leakage current. The following paragraph will provide a more detailed explanation of the ions and the leakage current.

5.2.2.3.2. Discussion of the measured leakage current result

As discussed in the artificial gastrointestinal solution, each solution is formed by dissolving certain amount of solutes into water. Equations 5-12 – 5-18, shows the dissociation of the solutes in water used in different solutions.



As can be seen most of the salts and the acids totally dissociate into ionic compounds when dissolved into the water and thus form a strong electrolyte. Potassium phosphate salt dissociates into potassium and dihydrogen phosphate ions which undergoes partial dissociation into hydrogen and hydrogen phosphate. The hydrogen phosphate further partially dissociates into phosphate ions and hydrogen ions. Therefore, dihydrogen phosphate and hydrogen phosphate will form a weak electrolyte in the pH6.8 solution. In buffer solution, sodium phosphate dissociates in a similar manner to potassium phosphate in pH6.8 solution. Thus, dihydrogen phosphate and hydrogen phosphate will also form a weak electrolyte in the buffer solution.

A study conducted by Lyons et al [143,144], showed that phosphate and the other ions are transported through epoxy at the same rate as the water. As shown in Figure 5.9, the polymer matrix forms a porous network. The polymer network is left to permeate with the gut solution and voltage is applied for the leakage testing. In the soaked epoxy, the applied voltage will cause the diffusivity of the charged species i and will be related to its partial conductivity κ_i [145,146]. This relationship is known as the Nernst-Einstein equation:

$$\kappa_i(t) = \frac{F^2 z_i^2 D_i C_i(t)}{RT} , \quad (5-19)$$

where F is Faraday's constant, T is the temperature in Kelvin, R the universal gas constant, z_i is the charge number on the species, D_i is the diffusion coefficient, C_i is the concentration of each species and κ_i is the ionic conductivity.

By substituting equation (5-9) into equation (5-19), the relationship between conductance and the soak time is given by:

$$\kappa_i(t) = \frac{F^2 z_i^2 D_i C_0 (1 - \operatorname{erf}(x/\sqrt{4Dt}))}{\pi R l T} \quad (5-20)$$

In Chapter 3, the bond pads were shown to be formed from 15 μm of Cu, 5 μm of Ni and 0.05 μm of Au and therefore had a thickness of 20.05 μm . The solder mask clearance around the bond pad is around 50 μm , thus leaving the sizes of the bond pad exposed. The current will pass through the flat parallel surface of the bond pad and therefore will contribute to the leakage current. Approximating the bond pads to parallel plate electrodes with an area A and separated by the length l , the relationship between conductivity and the resistance is given by:

$$\kappa_i = \frac{l}{R_i A} \quad (5-21)$$

where substituting Ohm's law, the correlation between conductivity and the current is given by:

$$\kappa_i = \frac{i_i l}{VA} \quad (5-22)$$

thus from equation (5-19) and equation (5-22), the leakage current of the ions can be expressed as equation (5-23):

$$i_i(t) = \frac{F^2 z_i^2 D_i c_i(t) VA}{R l T} \quad (5-23)$$

which can be rewritten as follows:

$$i_i(t) = \frac{F^2 z_i^2 D_i C_0 (1 - \operatorname{erf}(x/\sqrt{4Dt})) AV}{\pi R l T} \quad (5-24)$$

where the conductance is:

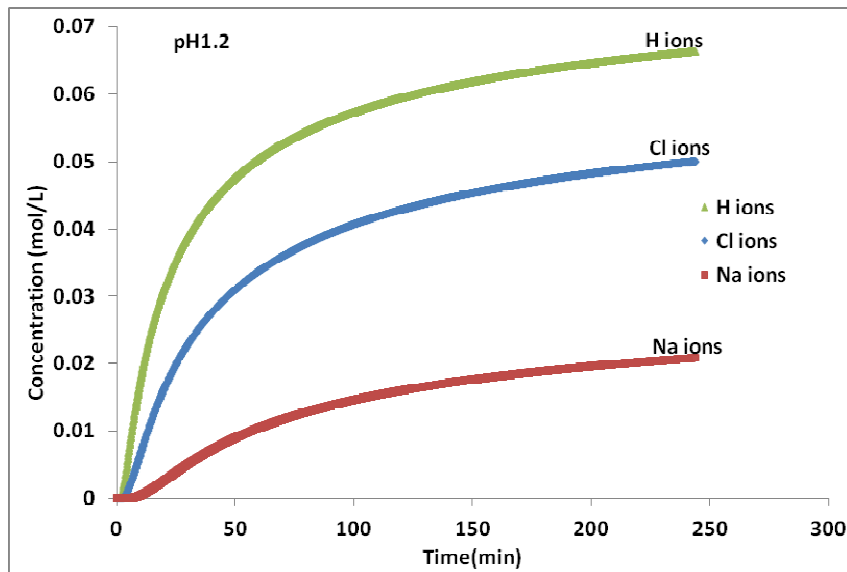
$$G = \frac{F^2 z_i^2 D_i C_0 (1 - \operatorname{erf}(x/\sqrt{4Dt})) A}{\pi R l T} \quad (5-25)$$

Each of the ions will carry a certain amount of current when a dc voltage is applied. The analytical solution for ion concentration was calculated for each ion in the different solutions using equation (5-9). Table 5.2 shows the diffusion coefficient of the cations and anions used in the analytical ion concentration calculation.

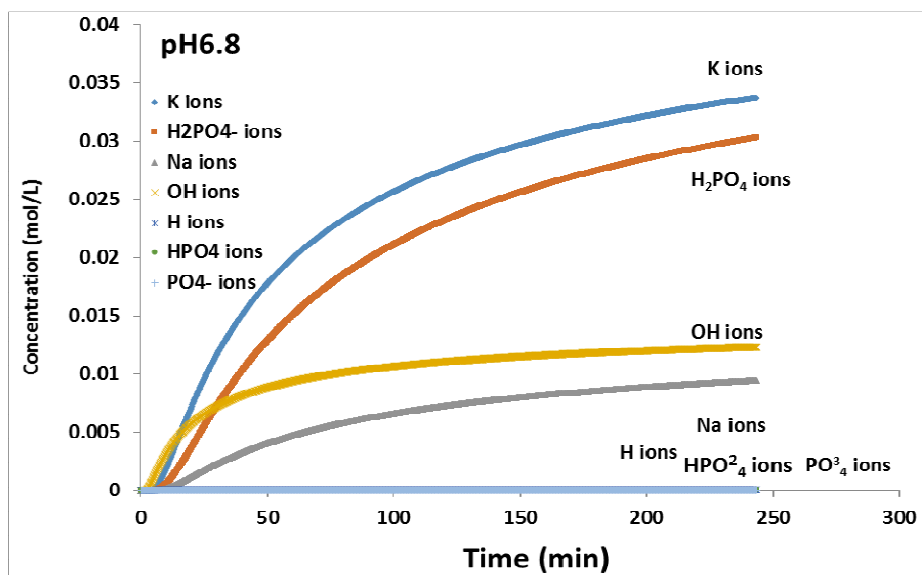
Ion	$D_i (10^{-6} \text{mm}^2/\text{s})$
Inorganic cation	
Hydrogen (H^+)	9.311
Potassium (K^+)	1.957
Sodium (Na^+)	1.334
Inorganic anion	
Hydroxide (OH^-)	5.273
Chloride (Cl^-)	2.032
H_2PO_4^-	1.3
HPO_4^{2-}	0.759
PO_4^{3-}	0.843

Table 5.2. Table of diffusion coefficients of ions, collected from [147,148].

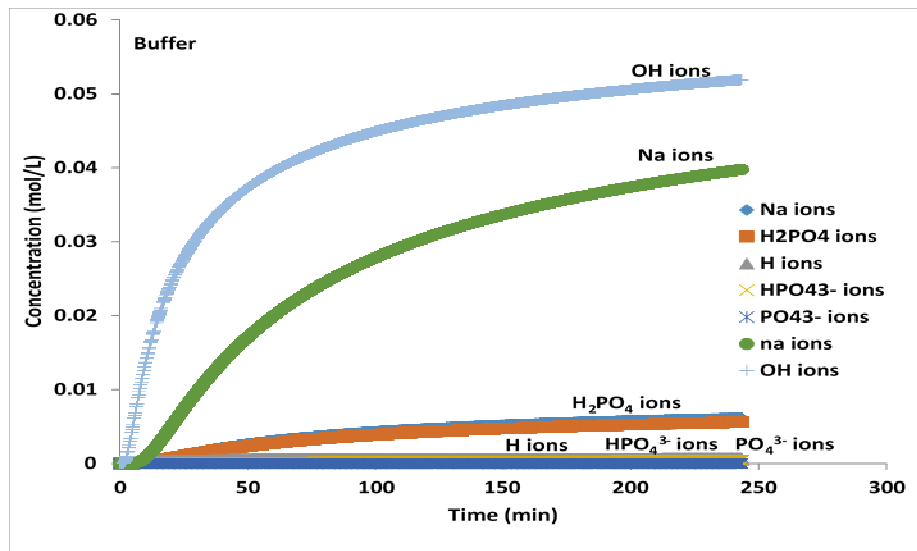
Figures 5.13(a), (b) and (c) show the variation of the of the analytically calculated ion concentration in pH1.2, pH6.8 and buffer soaking solution respectively over the period of soak. In all three graphs, it can be noticed that the penetration rate vary during the course of the experiment with high penetration rate observed at the start of the soak.



(a)



(b)



(c)

Figure 5.13. Plot of analytically calculated ion concentration in thin ACA in (a) pH1.2, (b) pH6.8 and (c) buffer solution.

Only 7.9% and $1.52 \times 10^{-7}\%$ of partial dissociation occurs at dihydrogen phosphate and hydrogen phosphate respectively. Extrapolating these theoretical calculations show that the ions in the acid environment will totally saturate the epoxy at around 55hr of soak; in pH6.8 and in buffer solution, the hydroxide ions, the sodium ions, potassium ions and dihydrogen phosphate ions will take between 60 – 70hr to saturate; the other ions due to their low concentration will take longer to totally saturate the epoxy.

Ions	Concentrations of ions (mol/l)
	4hr
pH1.2	
Cl ⁻	5*10 ⁻²
Na ⁺	2*10 ⁻²
H ⁺	7*10 ⁻²
pH6.8	
K ⁺	3.4*10 ⁻²
H ₂ PO ₄ ⁻	3*10 ⁻²
Na ⁺	9*10 ⁻³
OH ⁻	1.2*10 ⁻²
H ⁺	4.75*10 ⁻⁵
HPO ₄ ²⁻	2.8*10 ⁻⁵
PO ₄ ³⁻	16.3*10 ⁻¹³
Buffer	
H ₂ PO ₄ ⁻	5.6*10 ⁻³
H ⁺	7*10 ⁻⁴
HPO ₄ ²⁻	4*10 ⁻⁴
PO ₄ ³⁻	5.2*10 ⁻¹³
Na ⁺	4.5*10 ⁻²
OH ⁻	5*10 ⁻²

Table 5.3. Summary of ions and their corresponding calculated concentrations that is present in each solution after 4hr soak.

Figures 5.14(a) and (b) shows a representation of the assumed conduction path through ACA between adjacent bond pads. Figure 5.14(a) shows the plane and side view of the bond pads with the conduction path through the ACA. As it can be seen the conduction path through ACA between two adjacent bond pads was 360.6µm long. For each of the ions present in pH1.2, pH6.8 and buffer solution, the leakage current was calculated between these adjacent bond pads using Equation (5-23) and the parameters shown in Tables 5.4 and 5.5.

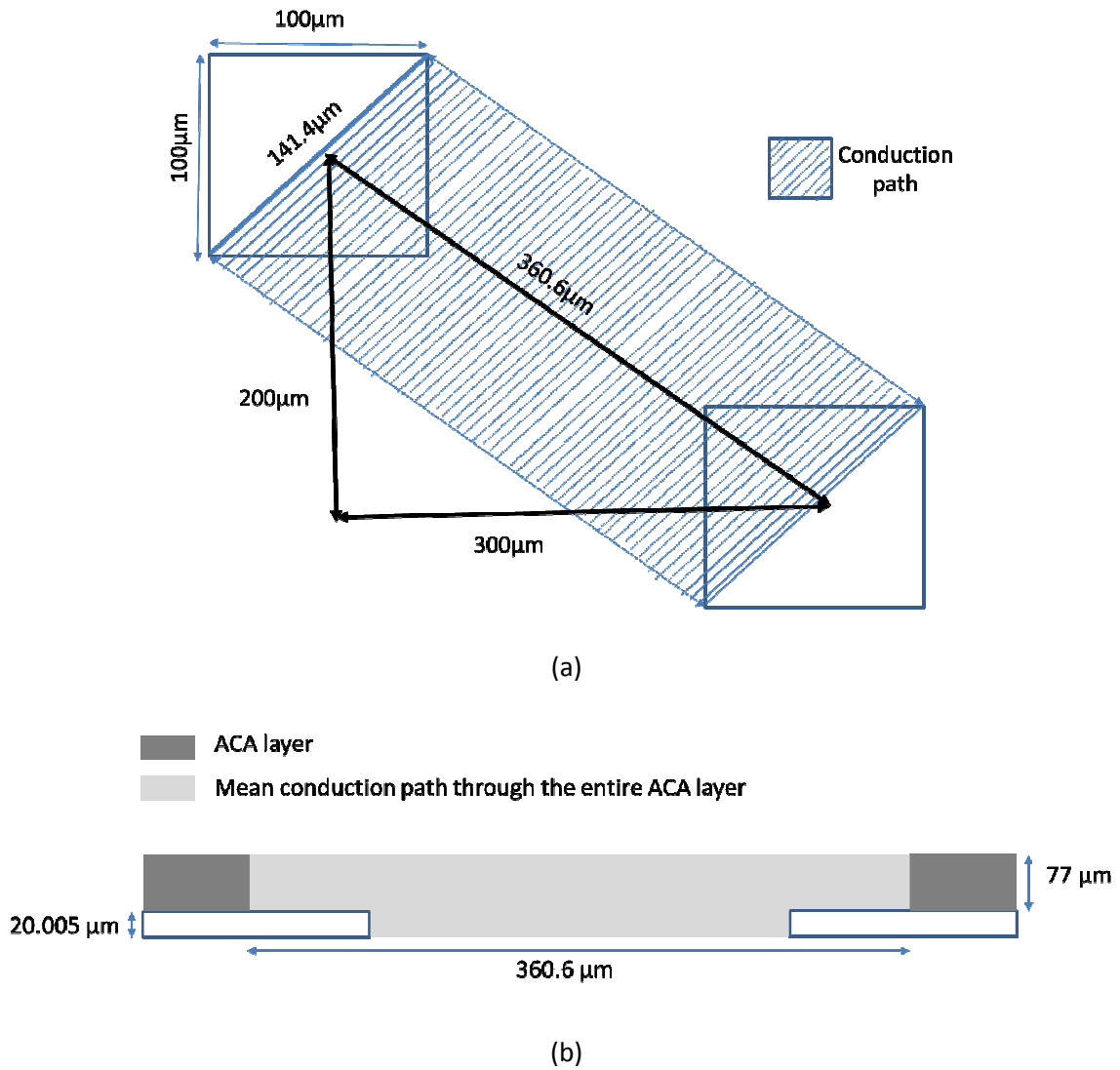


Figure 5.14. Bond pads with conduction path through ACA (a) plan view of bond pads, (b) side view of bond pads.

F (coulomb/ mol)		$R1$ (J/mol K)	Z_{Na}	Z_{Cl}	Z_K	$Z_{H_2PO_4}$	$Z_{H_2PO_4^{2-}}$
96485.3399		8.3145	1	1	1	1	1
Z_H	$Z_{PO_4^{3-}}$	Z_{OH}	T (K)	Volt (v)	Diagonal distance between pads (m)	Area (m ²)	length(m)
1	1	1	323	4	$1 \cdot 10^{-4}$	$1.09 \cdot 10^{-8}$	$3.606 \cdot 10^{-4}$

Table 5.4. Table of parameters, collected from [149,150].

Ion	Concentrations of ions (mol/l)			
	1hr	2hr	3hr	4hr
pH1.2				
Cl ⁻	3.4*10 ⁻²	4.6*10 ⁻²	5.2*10 ⁻²	5.6*10 ⁻²
Na ⁺	1*10 ⁻²	1.6*10 ⁻²	1.9*10 ⁻²	2.1*10 ⁻²
H ⁺	5.8*10 ⁻²	6.5*10 ⁻²	6.8*10 ⁻²	7*10 ⁻²
pH6.8				
K ⁺	1.9*10 ⁻²	2.7*10 ⁻²	3.1*10 ⁻²	3.4*10 ⁻²
H ₂ PO ₄ ⁻	1.5*10 ⁻²	2.3*10 ⁻²	2.7*10 ⁻²	3*10 ⁻²
Na ⁺	4.7*10 ⁻³	7.2*10 ⁻³	8.5*10 ⁻³	9.4*10 ⁻³
OH ⁻	9.3*10 ⁻³	1.1*10 ⁻²	1.2*10 ⁻²	1.2*10 ⁻²
H ⁺	3.9*10 ⁻⁵	4.4*10 ⁻⁵	4.6*10 ⁻⁵	4.7*10 ⁻⁵
HPO ₄ ²⁻	9.8*10 ⁻⁶	1.9*10 ⁻⁵	2.4*10 ⁻⁵	3*10 ⁻⁵
PO ₄ ³⁻	2.4*10 ⁻¹³	4.4*10 ⁻¹³	5.5*10 ⁻¹³	6.3*10 ⁻¹³
Buffer				
H ₂ PO ₄ ⁻	2.8*10 ⁻³	4.3*10 ⁻³	5.1*10 ⁻³	5.6*10 ⁻³
H ⁺	5.5*10 ⁻⁴	6.2*10 ⁻⁴	6.5*10 ⁻⁴	6.7*10 ⁻⁴
HPO ₄ ²⁻	1.4*10 ⁻⁴	2.7*10 ⁻⁴	3.4*10 ⁻⁴	4*10 ⁻⁴
PO ₄ ³⁻	1.9*10 ⁻¹³	3.6*10 ⁻¹³	4.6*10 ⁻¹³	5.2*10 ⁻¹³
Na ⁺	2.3*10 ⁻²	3.1*10 ⁻²	4*10 ⁻²	4.1*10 ⁻²
OH ⁻	4*10 ⁻²	4.6*10 ⁻²	5*10 ⁻²	5.2*10 ⁻²

Table 5.5. Calculated hourly ion concentrations.

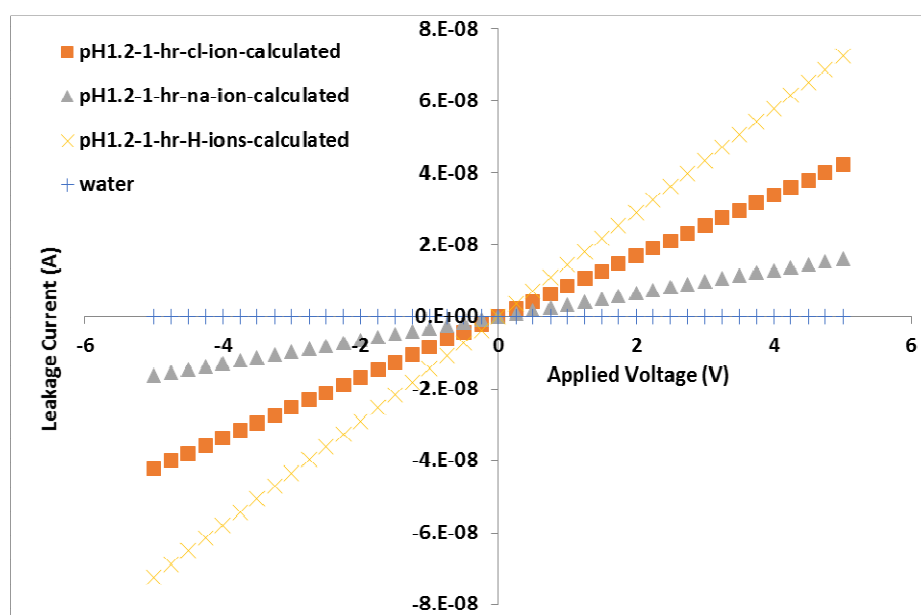


Figure 5.15. Plots of analytically calculated leakage current for 1hr soak in pH1.2.

Figure 5.15 show the variation of theoretically calculated leakage current with the applied voltage of water and other ions in an acid environment after 1hr soak. Figure 5.3 (a) shows that the water saturates the epoxy rapidly but its contribution to the leakage current is relatively low and is in the range of 0.02nA. As all the solutes completely dissociate in water, they all contribute equally to the

leakage current. It can be seen that the ionic contribution to the leakage current is as follows: i_H ions > i_{Cl} ions > i_{Na} ions. Table 5.6 summarises the calculated leakage current of each ions corresponding to the above mentioned concentration increase.

Ion	Calculated leakage current (nA)
pH1.2	
Cl⁻	42
Na⁺	20
H⁺	63.5

Table 5.6. Summary of the calculated leakage current of each ions in pH1.2.

The high leakage current contribution from the hydrogen ions could be explained by its high concentration and its high diffusion coefficient. An acid environment could explain the high concentration of hydrogen ions present in the solution. The high diffusivity and high concentration of the chloride could explain its leakage current contribution. The main contribution to the leakage current from the ions was from the hydrogen ions due to the acidity of the solution. It is also evident from Figure 5.13(a) and Figure 5.15 that the chloride ions and sodium ions actively participate in the leakage current during the soak.

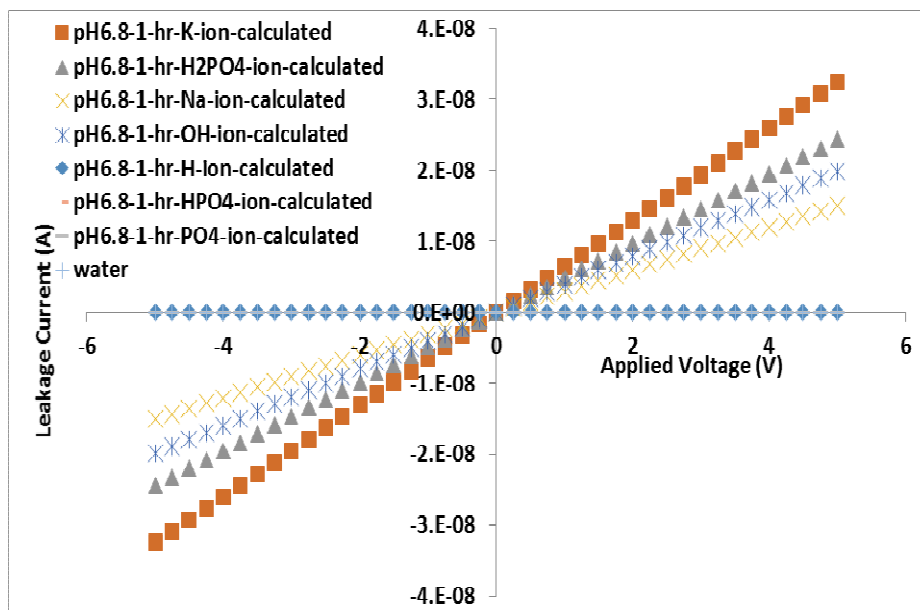


Figure 5.16. Plots of analytically calculated leakage current for 1hr soak in pH6.8.

Figure 5.16 show the variation of theoretically calculated leakage current with the applied voltage of water and different ions in a pH6.8 environment after 1hr soak. Once again the water contribution to the leakage current is relatively low and is in the range of 0.02nA. As most of the solutes completely dissociate in water, they should all contribute equally to the leakage current. The partially dissociated ions will have a lower impact on the leakage current. It can be seen that the ionic contribution to the leakage current is as follows: i_{K^+} ions > $i_{H_2PO_4^-}$ ions > i_{OH^-} ions > i_{Na^+} ions > i_{H^+} ions > $i_{HPO_4^{2-}}$ ions > $i_{PO_4^{3-}}$ ions. Table 5.7 summarises the calculated leakage current of each ions corresponding to the above mentioned concentration increase in pH6.8.

Ion	Calculated leakage current (nA)
pH6.8	
K^+	41
$H_2PO_4^-$	30
Na^+	7
OH^-	13
H^+	7.9×10^{-9}
HPO_4^{2-}	1.8×10^{-10}
PO_4^{3-}	3.3×10^{-19}

Table 5.7. Summary of the calculated leakage current of each ions in pH6.8.

The relative difference in the ionic contribution to the leakage current between OH, Na and K, H₂PO₄ ions could be attributed to the initial concentration of the potassium phosphate dissolved in the solution. This point is clear when comparing the potassium ions and sodium ions. Although potassium ions and sodium ions have similar diffusion rate, the ion concentration has a major influence on the leakage current. Similarly, the partially dissociated ions have a very low concentration and accordingly have very low contribution to the leakage current. This is particularly true when the partially dissociated hydrogen ions, hydrogen phosphate or the phosphate ions are compared to other ions present in the solution. In a base solution the main contributors to the leakage current are potassium ions, dihydrogen phosphate ions, hydroxide ions and sodium ions respectively.

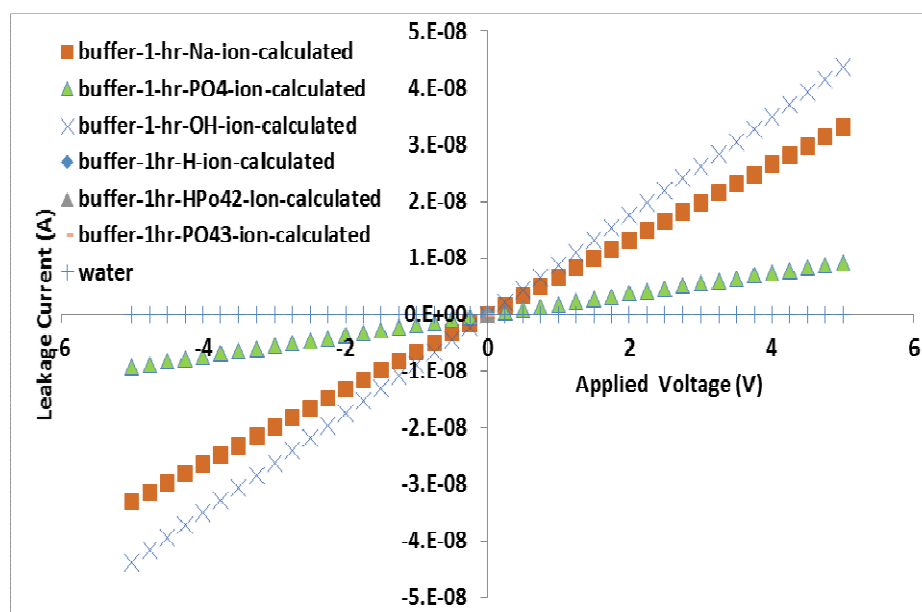


Figure 5.17. Plots of analytically calculated leakage current after 1hr soak in buffer.

Figure 5.17 show the variation of theoretically calculated leakage current with the applied voltage of water and different ions in buffer environment after 1hr soak. The water contribution to the leakage current is relatively low and is in the range of 0.02nA. As all the solutes completely dissociate in water, they all contribute equally to the leakage current. It can be seen that the ionic contribution to

the leakage current is as follows: i_{OH} ions > i_{Na} ions > $i_{H_2PO_4}$ ions > i_H ions > i_{HPO_4} ions > i_{PO_4} ions. Table 5.8 summarises the calculated leakage current of each of the ions corresponding to the above mentioned concentration increase in buffer solution. Once again it is clear that the concentration alone has a great influence on the leakage current.

Ion	Calculated leakage current (nA)
Buffer	
$H_2PO_4^-$	12
H^+	0.7
HPO_4^{2-}	8×10^{-8}
PO_4^{3-}	1.5×10^{-19}
Na^+	37
OH^-	55

Table 5.8. Summary of the calculated leakage current of each ions in buffer.

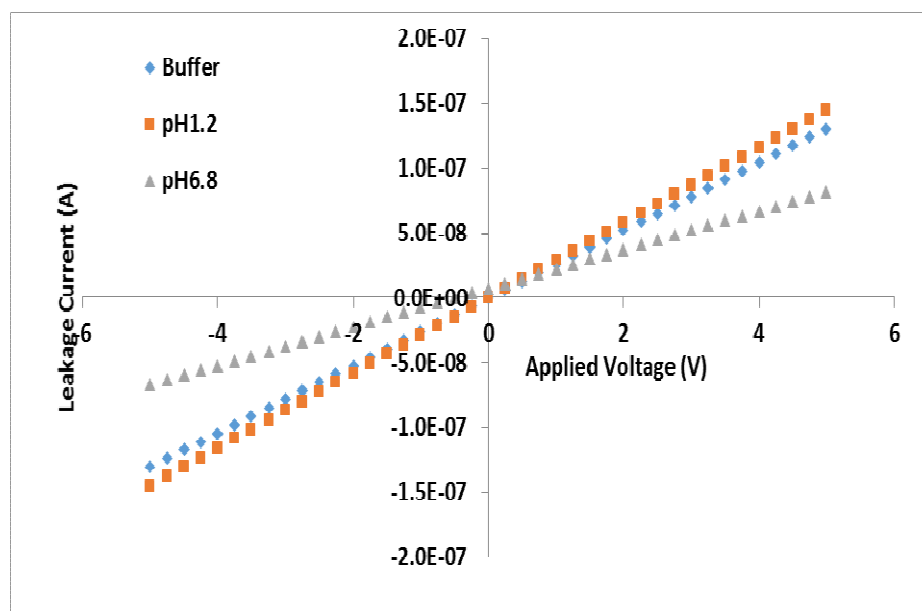


Figure 5.18. Plots of analytically calculated total leakage current (contribution of all ions) in all solution during 1hr soak.

Figure 5.18 shows the variation of the theoretically calculated leakage current corresponding to the total contribution of the ions and the water with applied voltage in buffer, pH6.8 and pH1.2 after 1hr of soak test. As can be seen, the calculated leakage current was in the range of 100nA in all the solutions during the 1hr soak and is in accordance to the range reported in Figure 5.12. Similar to Figure 5.11 and Figure 5.12, the calculated leakage current shows a linear trend in all the fluid environments indicating a good correlation between the calculated leakage current and the applied voltage.

5.2.2.3.3. Rate of change of conductance over time

Figure 5.19 shows the summary plot of the rate of change of conductance measured over the 4hr soak of the devices in each of the test solutions. It can be seen that the average rate of change of conductance in the buffer solution is around 1.19 and 1.3 times that of the ones measured in pH1.2 and pH6.8 respectively. Table 5.9 summarises the measured rate of change of conductance shown in Figure 5.19. In Figure 5.3(a), it was observed that water molecules with a diameter of 2.6\AA [140] were able to saturate the epoxy nano pores within 100min which meant that the rate of change of conductance would have been constant after 1hr soak. Figure 5.19 shows that the rate of change of conductance measured was not constant during soak and therefore the ions take part in the leakage current and as shown in the previous paragraph their concentration in the epoxy increased over time.

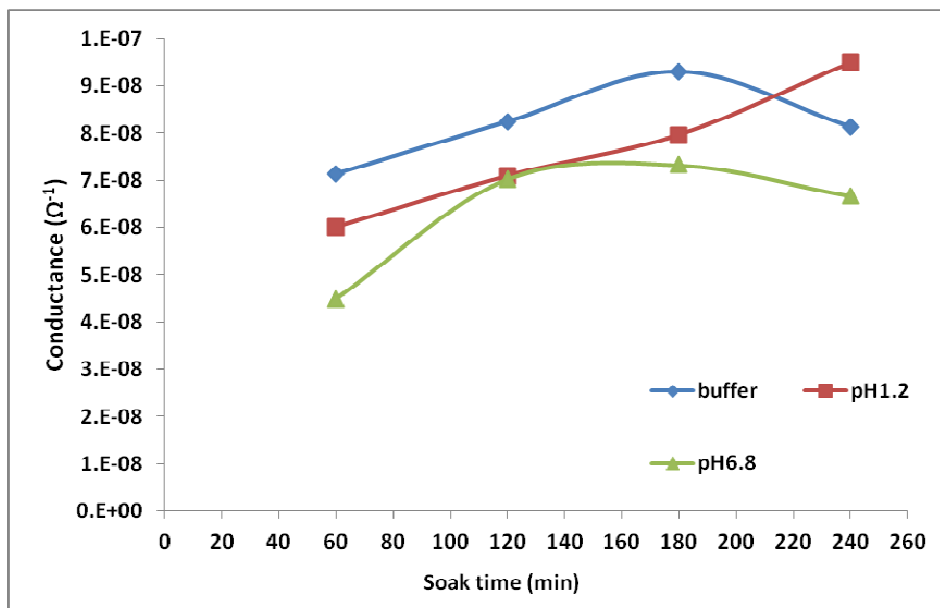


Figure 5.19. Measured rate of change of conductance of the device over time.

		1hr	2hr	3hr	4hr
Buffer	Conductance (Ω ⁻¹)	7.14*10 ⁻⁸	8.24*10 ⁻⁸	9.29*10 ⁻⁸	8.13*10 ⁻⁸
pH1.2	Conductance (Ω ⁻¹)	6.01*10 ⁻⁸	7.09*10 ⁻⁸	7.96*10 ⁻⁸	9.49*10 ⁻⁸
pH6.8	Conductance (Ω ⁻¹)	4.49*10 ⁻⁸	7.03*10 ⁻⁸	7.33*10 ⁻⁸	6.66*10 ⁻⁸

Table 5.9. Table showing the measured rate of change of conductance.

Figure 5.20 shows the theoretically calculated rate of change of conductance over the 4hr soak in each of the test solutions. The parameters shown in Tables 5.4 and 5.10 are plugged into Equation (5-25) to calculate the theoretical rate of change of conductance corresponding to the overall ions present in pH1.2, pH6.8 and buffer solution respectively. Table 5.10 shows the overall diffusion coefficients that were taken into account during the theoretical calculation of the rate of change of conductance in each solution. The rate of change of conductance in PH1.2 and buffer solution showed a similar rate of increase over the duration of the soak. The rate of change of conductance in pH6.8 is 1.2 times lower than the other solutions. This could be explained by the low concentration

levels of the ions in the pH6.8 solution. It should be also noted that the rate of change of conductance of the buffer solution is 1.1 times that of the ones calculated for pH1.2 after 1hr soak. This is in accordance with the experimental data reported in Figure 5.19 where a higher rate of change of conductance is observed for buffer solution than in pH1.2 and pH6.8.

	$D_{i,tot}$ (m ² /sec)
pH1.2	1.26*10⁻¹¹
pH6.8	2.08*10⁻¹¹
Buffer	2.01*10⁻¹¹

Table 5.10. Table of overall diffusion coefficients and concentrations of ions in each solution.

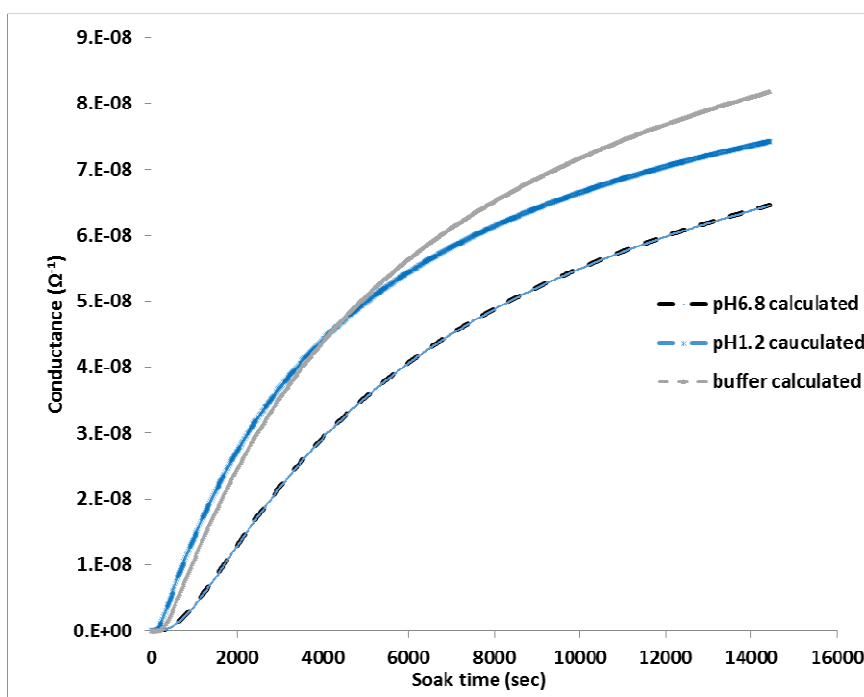
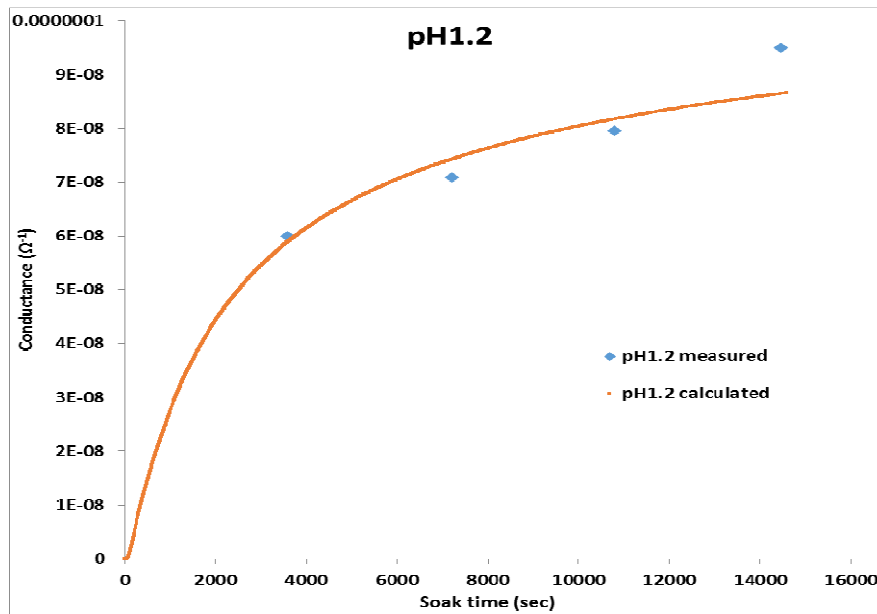


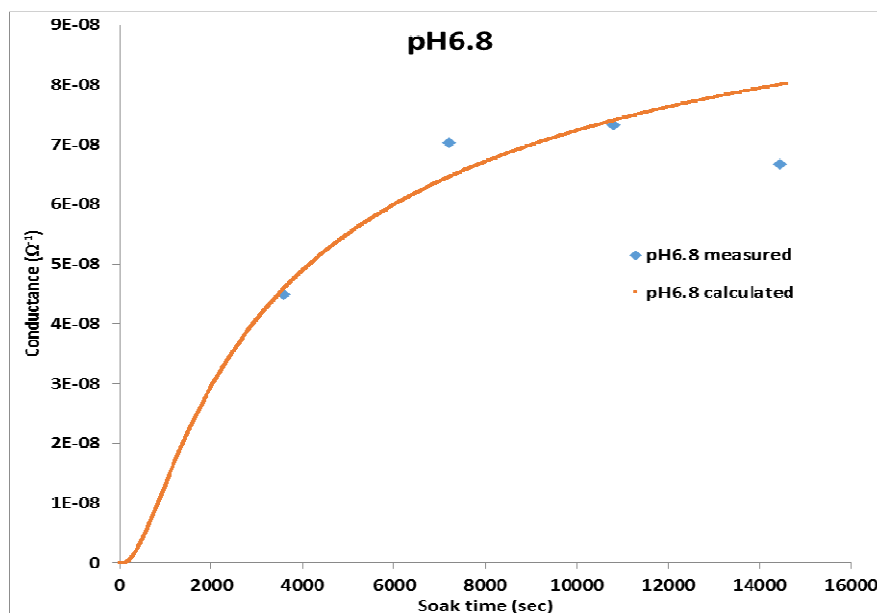
Figure 5.20. Calculated rate of change of conductance of the device over time.

Figures 5.21 (a), (b) and (c) compares the theoretical calculated data vs the measured data of the rate of change of conductance in pH1.2, pH 6.8 and buffer respectively. Although few experimental

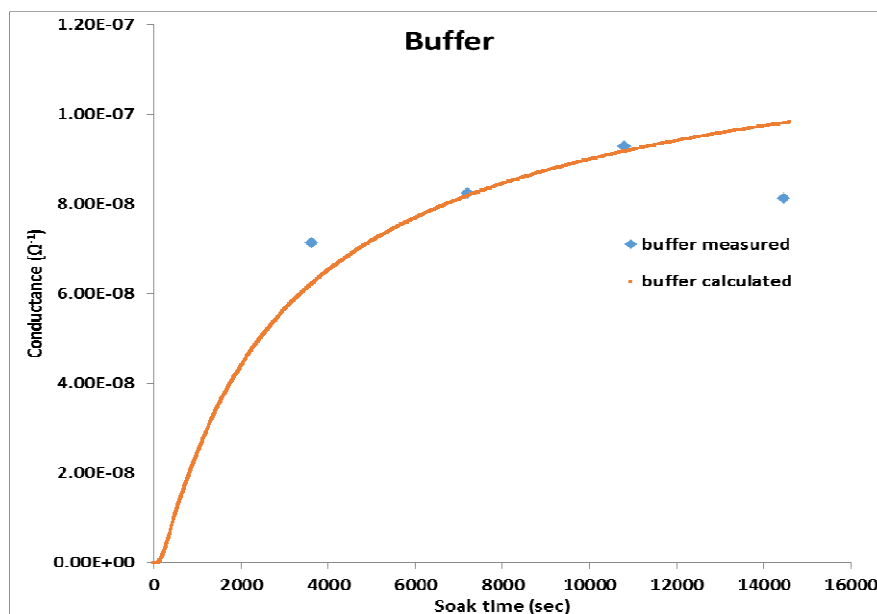
data was available, the theoretical calculated values matched the shape of the experimental values in all the tested solutions. This showed that all the ions present in the solution contribute to the leakage current.



(a)



(b)



(c)

Figure 5.21. Comparing calculated vs measured rate of change of conductance of the device over time in different solution.

In summary, it can be concluded that the ions in the solution penetrate epoxy and contribute to the measured leakage current. It should also be noted that the leakage current measured in the device in solution was higher than the leakage current measured from a dry sample. The leakage current after soak was around 100nA – including the noise, and was much lower than the current measured during the electrochemistry. Thus it was concluded that leakage through the ACA would not have any effect on the electrochemical measurements.

5.3. Conclusion

The ACA in the DAS will come in direct contact with the gut fluids when used in a gut environment. With respect to the final application, a preliminary study was carried out on the electrical characteristics of the ACA in a liquid environment. This part of the study dealt with the leakage

current with respect to different artificial gut liquid environments. The study showed that the average response of the ACA leakage current measured in a dried sample were in the range of 100pA with an average conductance of around $2.4604 \times 10^{-11} \Omega^{-1}$.

In comparison the average leakage current measured in the device (substrate and the ACA) after 1hr soak was in the range of 100nA in all the solutions. The artificial gastrointestinal solution in which the ACA was immersed contained different ions. Theoretical analysis of the ion concentration showed that the ions in the solution penetrate epoxy and contribute to the measured leakage current. It also showed that the ion concentration in the epoxy vary over time.

The rate of change of conductance during the 4hr soak was not constant and therefore confirmed the ionic contribution to the measured leakage current in different solutions. There is a good fit between the theoretical calculated values to the experimental values in all the tested solutions suggesting that the ions do take part in the leakage current. The rate of change of conductance in PH1.2 and buffer solution showed a similar rate of increase over the duration of the soak and was 1.2 times the rate of change of conductance in pH6.8. This difference could be explained by the low concentration levels of the ions in the pH6.8 solution.

This study showed that the measured leakage current after soak was around 100nA – including the noise, and was much lower than the current measured during the electrochemistry. Thus it was concluded that leakage through the ACA would not have any effect on the electrochemical measurements

This chapter described the electrical characterization of the ACA joint of a DAS in a fluid environment and found that the leakage current between connections was low and that it would not interfere with the electrochemical measurements. However, the soak test was only carried out for a short period of time. The next chapter looks into the long term reliability of the ACA interconnect in moisture and in the artificial gut environment.

Chapter 6 Long term reliability of the ACA interconnect in a DAS

6.1. Introduction

It is important to highlight that the ACA interconnect used in the DAS was destined to be used in the gut environment. This chapter covers the reliability of the ACA in terms of contact resistance with accelerated life time (ALT) testing. ALT was used to accelerate the degradation mechanism of the ACA joint and to identify the dominant failure mechanism. Two distinct phases of testing were undertaken: firstly a constant humidity aging of the ACA joint was carried out and this was followed by *in-vitro* testing.

6.2. Constant humidity testing

It was shown in the previous chapter that the epoxy matrix of the ACA was prone to moisture uptake. As the adhesive comes in contact with fluid, one of the most severe tests that could be considered was the moisture sensitive test. As previously mentioned in Chapter 3, there are no standardized test procedures that could be found for biomedical humidity aging, therefore the constant humidity aging was carried out at 50°C/95%RH to study the reliability of the ACA for a direct access sensor. This part of the work focused on the endurance of the ACA attachment for a direct access sensor.

6.2.1. Materials and methods

The materials such as test chip, flex substrate, the bonding process and the encapsulation process were described in Chapter 3.

6.2.1.1. Further encapsulation process

Wires were soldered on to each flex board connector bond pad. A two part polypropylene mould 95mm long, 13.25mm wide and 0.3mm thick was fabricated, where the first part had a base while the second part side was hollow. As shown in the cross-sectional Figure 6.1(a), the sensor encapsulated sample was sandwiched between the base and the hollow mould and the edges sealed with glue. Silicone was poured and cured for 24hr. The cured sample was taken out by pulling the moulds apart and the encapsulated sample is shown in Figure 6.1(b).

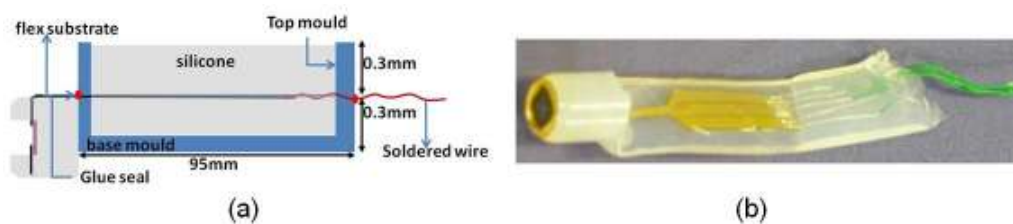


Figure 6.1. Second encapsulation process: (a) cross-sectional schematic of the mould and (b) picture of encapsulated sample for reliability testing.

6.2.1.2. Electrical measurement

As seen in Figure 3.1 each electrode had its corresponding bond pad on the chip periphery. These bond pads made connection via the ACA joint to the matching bond pad on the substrate thus

making an individual joint connection for each electrode. As explained in Chapter 3, the DAS structure developed in this research was destined to be tested via electrochemistry and therefore a typical online four point measurement of the contact resistance was not possible. As a result the contact resistance of the ACA interconnect was measured using a HP 3441A multimeter acting as a two probe ohmmeter. The resolution of the resistance measurement was 1mΩ. The measurement was made by placing the probe tip on the electrode surface and at the tip of the wire. The resistance was separately measured for the chip, and the substrate. The same measurements were conducted on the device (chip) mounted on the substrate via ACA and encapsulated in silicone. The measurements carried out on the substrates and the chips were subtracted from the contact resistance measurement on the device, consequently measuring the contact resistance of the ACA joint.

6.2.2. Results

A batch of nine samples was made. Each sample had five sensor connections. Figure 6.2 shows the variation of the adhesive joint contact resistance on the five different connections on the same sample versus the duration of hygrothermal aging at 50°C/95%RH. It can be seen that the initial contact resistance of the five adhesive connections range from 100mΩ to 600mΩ. This discrepancy in the contact resistance could be explained by the number of conductive particles trapped in parallel configuration.

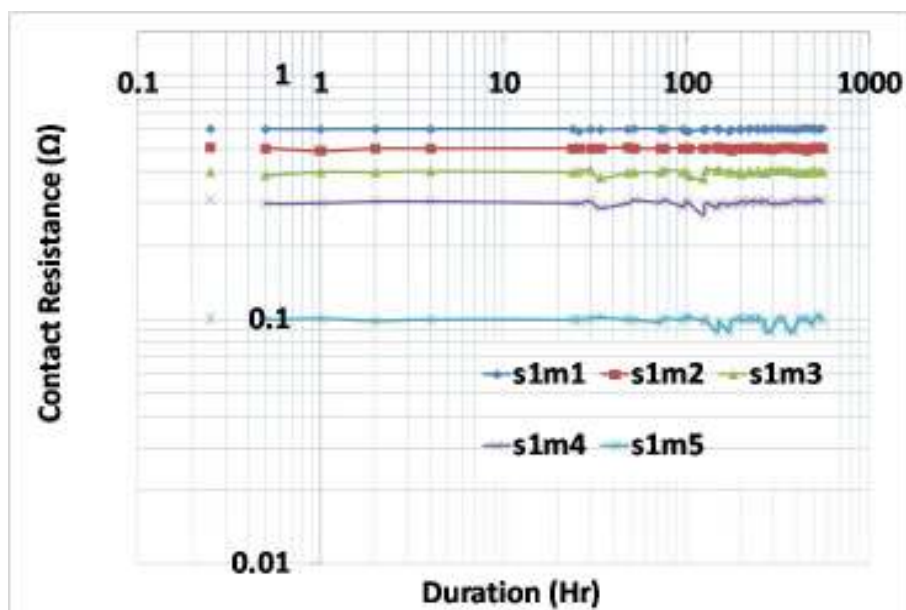


Figure 6.2. Plot of ACA contact resistance vs. the time in humidity aging of all the electrodes in one sample.

Figure 6.3 shows the variation of ACA contact resistance corresponding to the same electrode connection in all nine samples. Only two out of nine ACA connections showed a slow increase in contact resistance until an open joint was formed. It also showed that most of the samples showed no resistance drift during the whole reliability test. It can be seen in Figure 6.2 and Figure 6.3 that as the test went on, the contact resistance measurements showed some ripples that occurred at around 100hr of constant humidity aging.

As shown in Figure 3.1 in Chapter 3 and as numbered, only three electrodes noted 1, 2 and 3 were used in the electrochemistry. Only two out of nine samples showed failure after hygrothermal aging for the contact joints representing the three electrodes. A different percentage increase in resistance change could be used to set the failure criteria for any system. In order to preserve the integrity of the data during the cyclic voltammetry, a low limit of 100% increase was chosen for this system. With this failure criterion, it was observed that the samples s3 and s4 failed at around 50hr.

The daisy chains x2 and x1 failed at around 100 and 250hr respectively. In future an even tighter control could be exerted on the reliability of the system by choosing a lower limit such as 20% or 50% increase as the failure criterion.

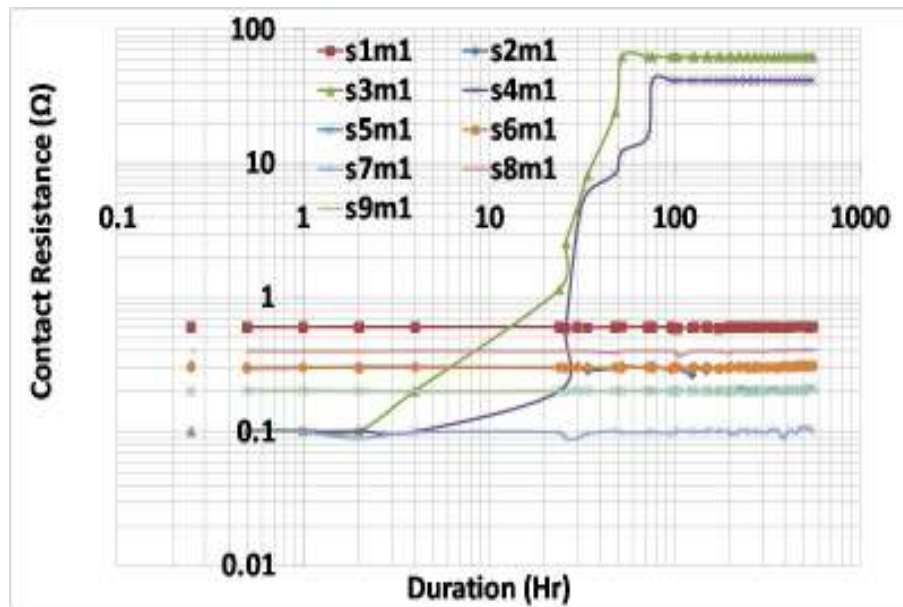


Figure 6.3. Plot of ACA contact resistance vs. the time in humidity aging corresponding to the same electrode in all nine samples.

6.2.3. Discussion

Epoxy expands due to moisture ingress while the silicon die and the other metal pads experience no expansion as they absorb no moisture [151]. These loading conditions create a coefficient of thermal expansion (CTE) and coefficient of moisture expansion (CME) mismatch between the chip, substrate and the adhesive. Typical material parameters are shown in Table 6.1.

	Silicon chip	Polyimide substrate	Gold bump	ACA
Coefficient of thermal expansion (CTE) (ppm/°C)	2.7	20	12.9	47
Coefficient of moisture expansion (CME) (mm ³ /g) (*10 ²)	0	1	0	4
Diffusion Coefficient (mm ² /s) (*10 ⁻⁶)	1e ⁻²⁴	5.0	1e ⁻²⁴	9.7
Specific Heat, <i>c</i> (J/KgK)	700	1090	800	1000

Table 6.1. Material parameters, collected from [121,129,135,152].

Both CTE and CME mismatch between materials lead to thermal stress and hygroscopic stress at the interface between epoxy/chip and epoxy/flex substrate system. The diffusion coefficient is greater for the adhesive. This will force the adhesive to absorb more water than other materials in the humidity chamber. Moreover, the CME of the adhesive is higher than the other materials. In the package configuration studied, the epoxy swelling due to moisture absorption produced a perpendicular as well as a parallel expansion of the epoxy with respect to the die and the substrate and induced tensile and shear stress at the ACF interface. However, former studies have shown that when the epoxy is saturated with moisture, this swelling is uniform and that the induced shear stress is insignificant when compared to the normal stress [129,151].

As shown in Chapter 5, it takes about 60min to saturate the thin adhesive with water. For moisture ingress analysis under 50°C/100%RH condition, H_0 and E_H in equation (5-5) were taken from Tsai et al [130] and were $20.68 \times 10^{-6} \text{mg/mm}^3 \text{MPa}$ and $-3.019 \times 10^4 \text{J/mol}$ respectively for an ACF material. Using equation (5-5), H was calculated to be $1.57 \text{mg/mm}^3 \text{MPa}$. For 50°C, the vapour pressure was taken from Fan et al [153] and was 0.01MPa. With H as $1.57 \text{mg/mm}^3 \text{MPa}$, 100%RH, and a vapour pressure of 0.01MPa, the saturation concentration was calculated to be $1.5 \times 10^{-5} \text{g/mm}^3$. In this structure,

there was 0.8mm ACA from the edge of the window to the edge of the chip. From the 1 dimensional analysis, the diffusion was assumed to be from the window towards the edge of the chip. Using equation (5-9), the thickness of 0.8mm and the diffusion coefficient taken from Yin et al [135] as $9.7 \times 10^{-6} \text{mm}^2/\text{s}$, the moisture saturation time was calculated as 26740sec (7hr).

T(°C)	RH(%)	[H2O] (g/m3)
-10	80	2
10	95	9
20	50	9
65	95	139
85	20	57
85	60	170
85	85	240

Table 6.2. Temperature, Relative Humidity, and water concentration in the air [155].

For contact resistance measurement the samples were out of the chamber for around 5 - 10min and the electrical measurements were carried out manually at 20°C/50%RH using a HP 3441A multimeter. Assuming that H_0 and E_H have not changed, the vapour pressure as 0.02MPa [153], the “desorption” saturation concentration was calculated as $4.98 \times 10^{-3} \text{g/mm}^3$. The desorption diffusivity was taken from the work of Teverovsky [131] and was $3 \times 10^{-7} \text{mm}^2/\text{sec}$, and using equation (5-9), desorption time was calculated as 864607sec (240hr). This diffusion was also reported by Vries et al [154,155]. Their study also suggested that the momentary transfer of the sample in and out of the humidity chamber caused a temporary concentration gradient which led to either absorption or desorption of water from the adhesive. Taking the sample in and out of the chamber for measurements would cause an epoxy to undergo thermal strain. The coefficient of linear expansion of epoxy was taken as $117 \times 10^{-6} (1/^\circ\text{C})$ [156] and the variation in length due to the temperature was

computed as $0.02457\mu\text{m}$. The thermal strain of the sample taken in and out of the chamber for the measurement was calculated as 0.004. Table 6.2 shows the temperature, RH and the water concentration in the air as reported by Vries et al [155].

In order to get an appreciation of the moisture induced strain, it can be noted that the water concentration between $65^{\circ}\text{C}/95\%\text{RH}$ (close to $65^{\circ}\text{C}/100\%\text{RH}$) and $20^{\circ}\text{C}/50\%\text{RH}$ had a gradient of $130\text{g}/\text{m}^3$. As calculated in the previous section the typical saturation concentration for epoxy is $15\text{-}25\text{mg}/\text{cm}^3$ [155]. Using these values, estimation of the moisture induced strain was calculated to be 0.0052. Once again the calculated thermal strain and the hygroscopic strain were similar to ones reported by Vries et al [155]. The thermal strain and the hygroscopic strain would cause the materials to expand and shrink. This constant movement of the sample in and out of the chamber for testing, with both hygroscopic strain and thermal strain could cause microscopic sliding. This slow fatigue like process coupled with slow relaxation of the contact pressure could lead to a slow but steady increase in contact resistance until an open joint was observed [157]. This could explain the slow and steady degradation of the contact resistance until an open joint was observed for samples s3 and s4. The ripples that are observed could be attributed to the error in pressure contact when placing the probes on the sample during the measurement.

6.2.4. Failure analysis

Polymer expansion due to moisture ingress and the mismatch of moisture expansion coefficients of materials may cause the formation of defects like cracks or small voids and delaminations [66,158]. It is more likely that there are some initial microscopical delaminations present at the ACA interface caused by the defects present on the chip, at the substrate surface or introduced by the process [151]. During moisture uptake, the moisture diffusion in the ACA along its interface was an order of

magnitude greater than the diffusion in the bulk material. This is due to the residual stresses and the presence of the nano- or micro-pores and voids at the interface [159]. Moisture has an adverse effect on the interfacial adhesion of ACA and this may accelerate the delamination process by weakening the polymer interface. This weakening of the interface occurs by a hydrolytic attack on the ester linkage ($R-(C=O)-OR'$) which breaks the polymer chain creating two new end groups, a hydroxyl and a carbonyl group, thus degrading the adhesion strength of the polymer [102,106,107,160,161].

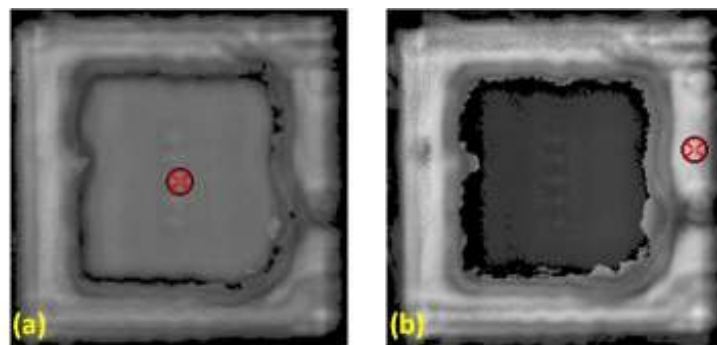


Figure 6.4. SAM images: (a) before and (b) after hydrothermal testing of one the samples that survived.

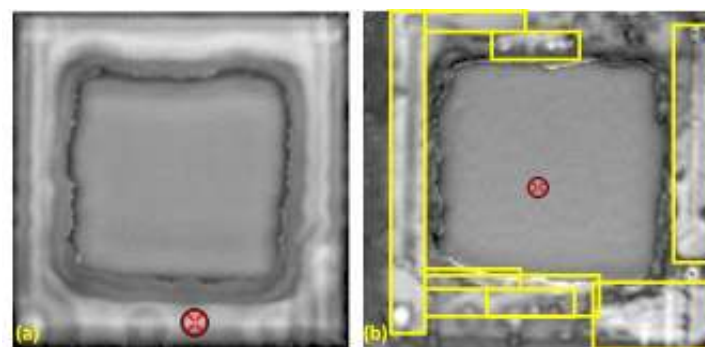


Figure 6.5. SAM images: (a) before and (b) after hydrothermal testing of one the samples that failed.

Figures 6.4(a) and (b) and Figures 6.5(a) and (b) show Scanning Acoustic Micrographs (SAM) that were used to assess the sealing efficacy of the direct access sensor before and after humidity testing. Figures 6.4(a) and (b) show the SAM images of one the samples that survived the hygrothermal testing. No delamination was observed in the sample before or after humidity aging. On the contrary Figures 6.5(a) and (b) show the SAM images taken on one of the failed samples after hygrothermal aging. It can be seen that there are delaminations present, shown by yellow rectangles, after the humidity aging. In Chapter 3, it was shown that the moisture aging has a deleterious effect on the adhesion strength and the weakening of the adhesion and that this is reflected by white patches in the SAM image. The SAM analysis does not show where the failure occurred and in order to get a precise picture of the failure a cross-sectional analysis was performed.

Olympus BH2-UMA Optical microscope images of the aged samples cross-sectioned are presented in Figures 6.6(a) and (b). It can be seen in Figure 6.6(a) that failure occurred by an interfacial delamination at the epoxy/silicon and epoxy/bump interfaces. Previous studies have shown that the ACA adherence to another polymeric material is higher than that for silicon [162,163]. In addition, the bump/pad interface was found to be open, resulting in the loss of conductivity and a considerable increase in resistance. The delamination seems to proceed along the chip passivation layer with a higher gap on the left side of the bump/pad towards the edge of the chip than on the right side of the bump/pad. This could imply that the delamination was initiated at the edge of the die. As explained in Chapter 5, the disruption of the hydrogen bonds by water molecules causes plasticization in the short term by spreading the polymer molecules apart and causing expansion of the adhesive joint [106,107]. In addition, temperature gives rise to different materials expansion rates due to the CTE mismatch between the adhesive and the other metals and this contributes to the degradation of the ACA interface. Thus the interface was under tensile and shear stress with a dominant shear stress at the bump and die/epoxy interface, which was due to the CTE mismatch between the materials. Looking at Figure 6.6(a), there is a gap on the left hand side of the bump, and

not on the right, this implies that the bump and chip on the top have moved to the right, or the pad and substrate on the bottom have moved to the left, probably (as shown in Table 6.1) due to the fact that the CTE of the substrate is nearly 10 times that of the silicon, and the CTE of the ACA is nearly 20 times that of the silicon. In the same way the diffusivity of moisture in ACA is twice that of the substrate. Both CTE and the hygrostrain will force the epoxy to expand in all directions pushing the die upwards (z direction) to release the residual stress. The flex substrate used in this system will tend to relax the stress developed in the system much faster than a rigid substrate because it has high potential to compensate the expansion of the adhesive matrix. But due to the silicone encapsulation, the flexible substrate relaxation possibilities would be limited. Furthermore the expansion of the epoxy in the z direction is limited by the chip and by the weight of the silicone of the back side of the chip. Thus it could be suggested that the epoxy expands more in the x-y direction than in the z direction and the dominant stress during the swelling process was the shear stress.

Figure 6.6(b) shows the cross-section of a sample that had survived the hygrothermal aging. It can be seen that moisture aging has not deteriorated the contact joint between the bump and the pad. However, the DAS sensor was destined to be used in the body to measure the gut fluids. The next part of the work was carried out *in-vitro* to see the effect of the gut fluids on the ACA interconnection.

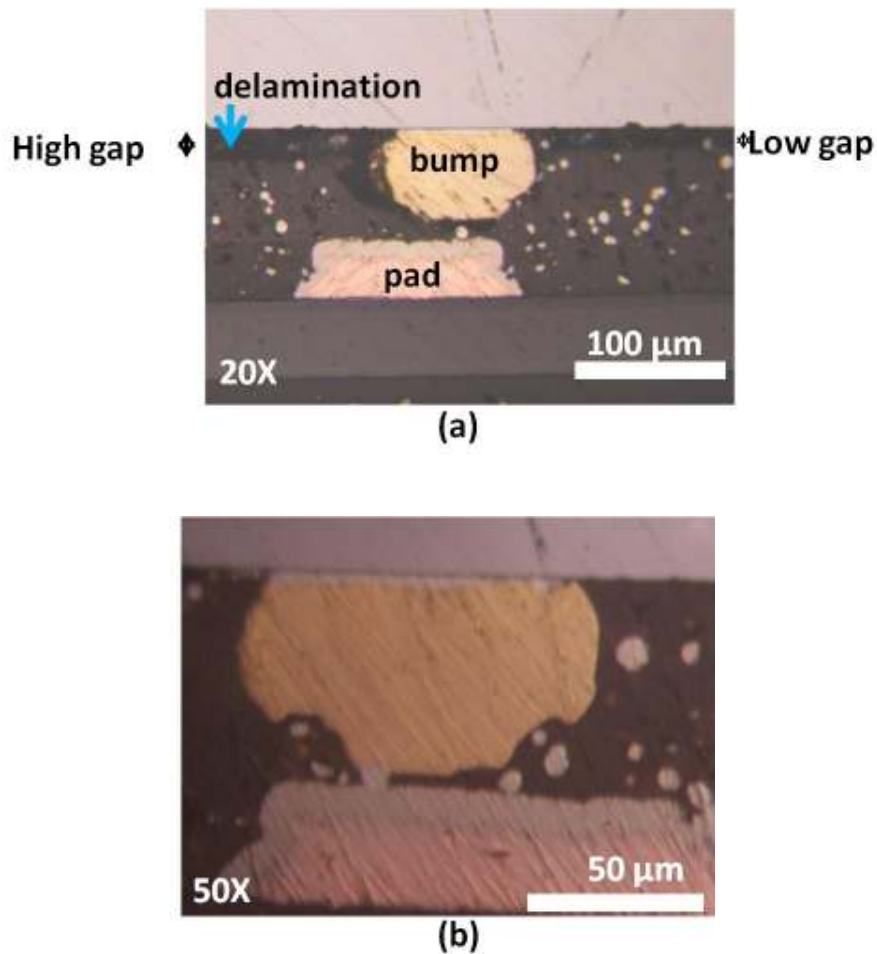


Figure 6.6. Cross-section of samples after humidity testing (a) failure by crack propagation and (b) non failed sample.

6.3. *In-vitro* testing

In medical applications, *in-vitro* testing is routinely conducted to assess the reliability and the biocompatibility of a device. The hygrothermal aging described previously would not provide complete information about the ACA performance in the gut environment and therefore it is vital to perform reliability testing for intended medical devices under the conditions which simulate the real body environment [164,165]. *In-vitro* tests are performed outside a living organism before being

accepted in clinical trials [165]. The *in-vitro* test for the DAS would be tested in the artificial gastrointestinal solution and the buffer solution that was used in Chapter 5.

In this work, reliability testing was carried out at 80°C and at 37°C using artificial gastrointestinal solution and buffer solution to test the reliability of the ACA in the DAS. The *in-vitro* reliability test at 80°C was carried out to accelerate the time scale of the degradation mechanism of the ACA used in a DAS. However, failure mechanisms occurring during the accelerated testing could mask the usual failure modes that would occur during the usual operating conditions [100,101]. This was the reason the *in-vitro* test was also carried out at 37°C thus simulating the gut environment.

6.3.1. Materials and methods

The materials such as test chip, flex substrate and the bonding process were described in Chapter 4.

6.3.1.1. Encapsulation process

After the bonding process, wires were soldered on to the substrate for electrical measurements and the encapsulation procedure was followed as explained in Chapter 3. The sole difference with the procedure explained in Chapter 3 was that the gelatine capsule which was used to insert the assembly was 23mm in diameter. This diameter was chosen because it was shown in Chapter 4 that the integration of the assembly into the 23mm capsule for packaging did not significantly affect the daisy chain resistance.

6.3.1.2. Electrical measurement

A plastic vial 40mm wide and 115mm in height was used to place the encapsulated sample in a hot circulating water bath to carry out the reliability test. A hole of 23mm diameter was made in the screw top cap of the plastic vials. The encapsulated samples were inserted into the screw top cap and the edges sealed with silicone; the plastic vials were filled, leaving a 15mm gap from the rim with the appropriate solutions; the screw cap was placed back on top of the vial and screwed in place. Circles of 40mm were cut out on a polytetrafluoroethylene (PTFE) sheet; the vials were inserted into the cut out circles and placed on top of a temperature controlled re-circulating water bath at 37°C and at 80°C respectively as shown in Figure 6.7. Four vials with solutions were placed in each water bath. Table 6.3 gives the contents of each vial and the time duration of the test.

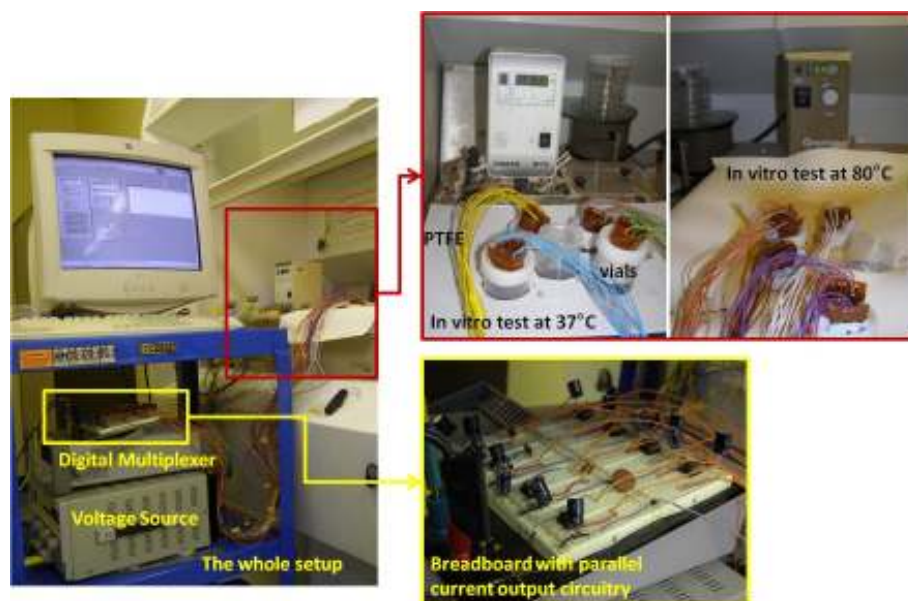


Figure 6.7. Experimental test setup.

Test solution	Test 1	Test 2	Test duration (Hrs)
pH 1.2	37 °C	80 °C	500
pH6.7	37 °C	80 °C	500
Buffer	37 °C	80 °C	500
Start pH 1.2 then transfer to pH6.7	37 °C	80 °C	First 50 hrs in pH1 then in pH 6.7

Table 6.3. Test Matrix.

As explained in Chapter 4, the four point electrical measurement was carried out during the *in-vitro* reliability testing. The power supply, set to deliver 5V, was connected to a solderless breadboard. The solderless bread board contained sixteen columns of connected clips. As shown in Figure 6.7, the connected clips were grouped into eight columns where each column was used to supply the same current to each of the eight samples that were tested simultaneously. For each set of columns, an inverting operational amplifier OP177 was used to achieve an output current of 100µA that was supplied to each test sample. These separate parallel circuits were chosen in order to ensure that any failed sample would not draw all the current and thus compromise the results of the other samples as shown in Figure 6.8. In each sample the daisy chain measurements were collected from the total daisy chain (z), the partial daisy chain in the x direction and the partial daisy chain in the y direction. All the measurements were automated via LabView and the data was collected with an Agilent 349901A 20 channel multiplexer and recorded into Microsoft Excel.

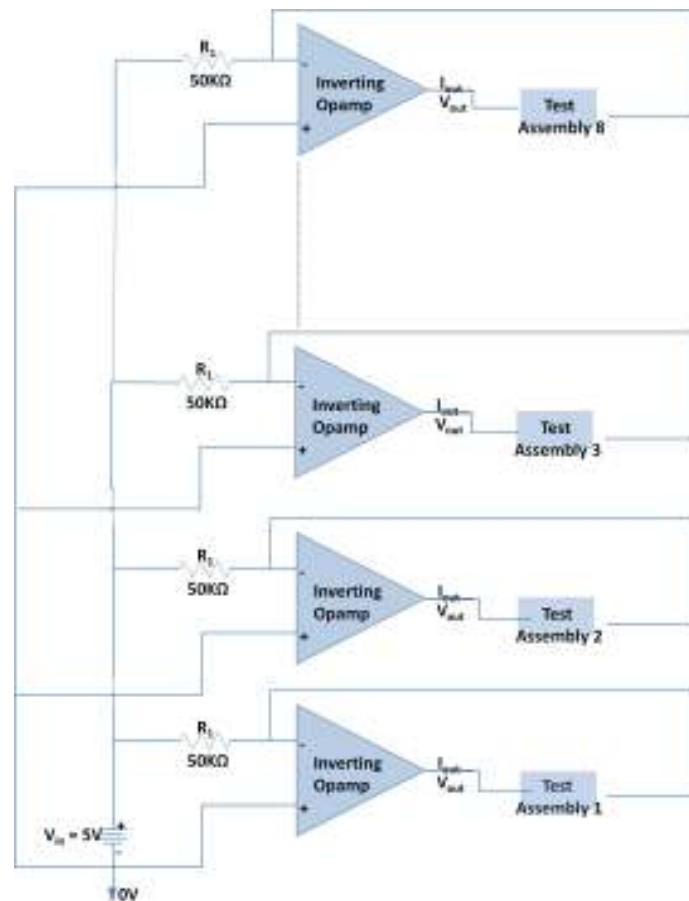


Figure 6.8. Circuit diagram for parallel circuits used testing.

6.3.2. Results and discussion

After assembly, before the *in-vitro* testing, SAM analysis was carried out on all the samples to assess the integrity of the sealing of the ACA between the chip and the substrate. Figure 6.9 shows one of the SAM images of the samples before *in-vitro* testing. As can be seen, there are no delaminations or voids that are present in the assembly before testing. This same observation was noticed on all the other samples that were prepared for *in-vitro* testing.

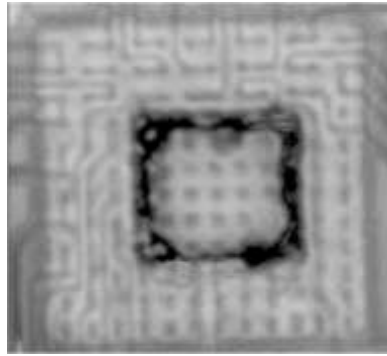


Figure 6.9. SAM image of the assembly before *in-vitro* testing.

The total resistance of all the samples was around 28Ω (corresponding to total voltage of 2.8mV) at the start of the *in-vitro* test. Figures 6.10(a) and (b) show the voltage measured in the total daisy chain of the samples subjected to different gut and control solutions for over 450hr testing at 80°C and at 37°C respectively. All the graphs are plotted side by side to show the effect of the testing fluids on the total daisy chain of the samples tested. A 100% increase in voltage was used as the failure criterion. Figure 6.10(a) shows that all the samples at 80°C failed during the first 150hr of testing. Three similar regions could be discerned from all the graphs. Region 1 characterized the stable resistance region where the resistance remained more or less constant during the *in-vitro* test. This region was very short for the sample immersed in HCl acid of pH1.2 while it extended to 50hr and 100hr in samples immersed in pH6.8 and buffer respectively. This was followed by region 2 which was defined by the slow increase in resistance. This increase in resistance could be attributed to the slow degradation of the contact joint. Once again region 2 was very short for the sample immersed in HCl acid at pH1.2 compared to samples soaked in pH6.8 and in control solution. The third region showed a sharp increase in resistance signifying a much more pronounced degradation of the interconnection. In samples immersed in pH1.2 and in the control buffer solution the pronounced degradation created a faulty contact which could explain the oscillation of the resistance before an open joint was observed. In the case of the sample immersed in pH6.8, the degraded joint had a faulty connection which remained functional until the end of the test. The

faulty contact could be explained by the fact that the hygroscopic swelling of the epoxy was limited by the bulk weight of the silicone on the back of the chip. In other words, the bulk weight of the silicone on the back of the chip did not allow the assembly to expand totally and maintained the chip at a certain distance where it could still provide contact. Most of the silicone on the back side of the chip was at room temperature; therefore any shift in temperature could have led to shrinking and expansion of the material which could have been reflected in the electrical measurement of the ACA joint.

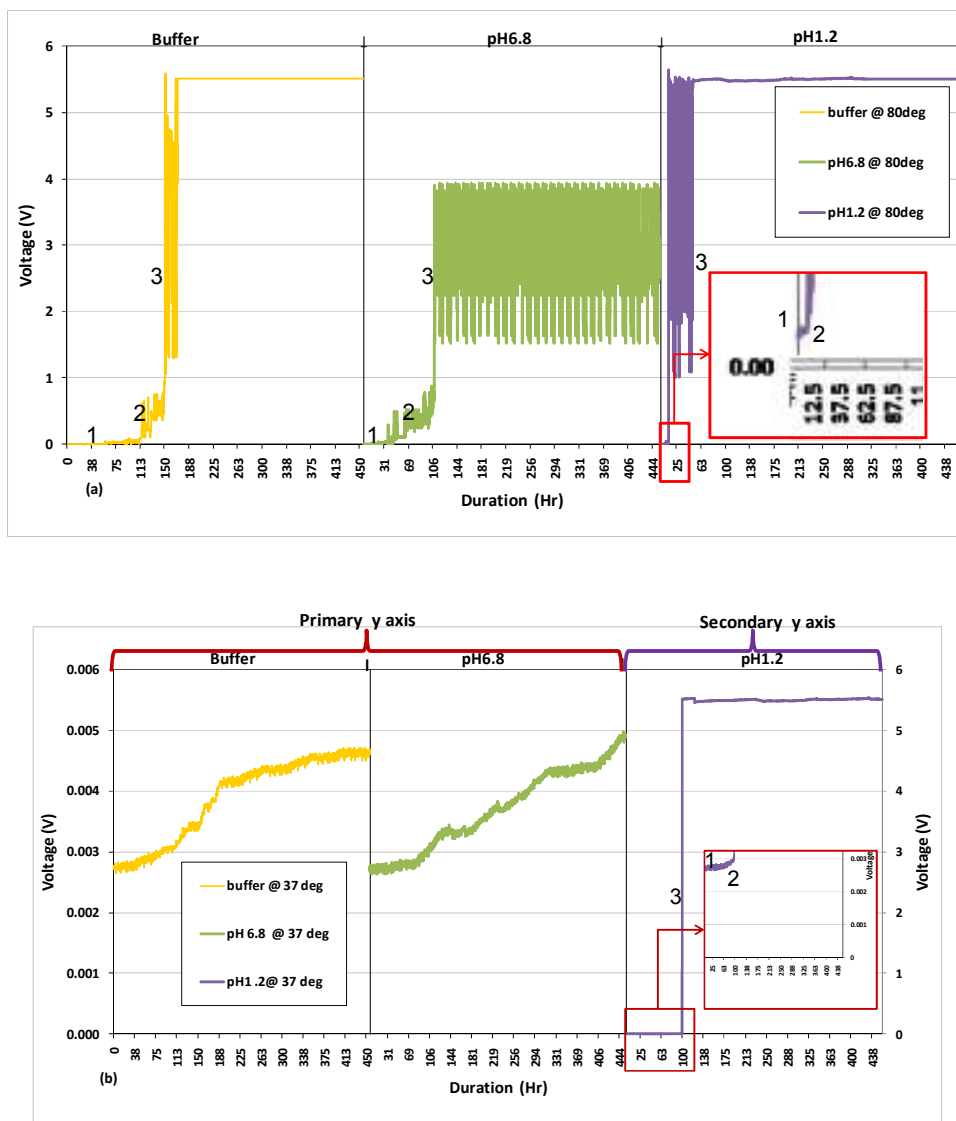


Figure 6.10. Plot showing the measured voltage variation vs. the duration of the test for total daisy chain of one of the samples immersed at: (a) 80°C and (b) 37°C.

The accelerated test was at 80°C/100% RH where the higher temperature may have accelerated the moisture absorption, as expressed in equation (5-3), leading to the swelling of the epoxy by the disruption of the hydrogen bonds; the exponential correlation of diffusivity with $1/T$ shows that diffusion is very strongly dependent on temperature and it could be assumed that for high temperature, high diffusivity of water and ions could be expected. In addition to the hygroscopic swelling of ACA due to humidity as well as their thermal expansion in the transverse direction, the acidity characterized by the concentration of hydrogen ions, other ionic concentrations, ion diffusion rate and the enzymes in the gut solution might have also helped in accelerating the chemical hydrolysis of the epoxy matrix. This chemical hydrolysis will be shown later in the SEM study of the surfaces during the duration of the test. A study conducted by Lyons et al [143,144], showed that phosphate and the other ions are transported through epoxy at the same rate as the water. Tables 5.2 and 5.3 provide a summary of the diffusion coefficient and the concentration of the ions present in each solution. It can be seen the combination of high ionic concentration with high diffusion can be categorised as: pH1.2 > pH6.8 > buffer. This could be the reason why the samples placed in pH1.2 and in pH6.8 failed at an earlier stage than the control buffer solution. It should also be noted that the stronger the acidity of the solution the more accelerated the chemical hydrolysis of the epoxy. This could be the reason for regions 1 and 2 to be shortened for the sample immersed in pH1.2. In Chapter 5, it was shown that at 37°C, the ions in the acid environment will totally saturate the epoxy at around 55hr of soak; in pH6.8 and in buffer solution, the hydroxide ions, the sodium ions, potassium ions and dihydrogen phosphate ions will take between 60 – 70hr to saturate; the other ions due to their low concentration will take longer time to totally saturate the epoxy. As discussed in this paragraph, the ionic saturation would have been shortened by the high temperature used in the test. Therefore the combination of high temperature, acidity and ionic concentration accelerated the aging and the disruption of the epoxy bonds.

From Figure 6.10(b), it can be noted that the sample immersed in pH1.2 failed while the samples immersed in pH6.8 and control buffer survived the *in-vitro* test. The failed sample had the same three distinctive regions. Unlike the sample immersed in pH1.2 at 80°C, the region 1 – region of stable resistance – in this failed sample lasted for around 80hr. The sample immersed in pH6.8 showed a more or less stable resistance till around 100hr after which it showed a slow but more linear increase in the measured voltage, indicating the slow degradation of the contact resistance. In Chapter 5, it was shown that the thin layer of epoxy rapidly saturated with moisture and other ions present in the solution but the degradation of the epoxy with slow relaxation of the contact pressure seemed to occur at around 100hr of soak. In buffer solution the stable resistance lasted till 60hr, further aging showed degradation of the epoxy and the contact joint. This could be due to the action of the water molecules disrupting the hydrogen bond making way for the other ions to penetrate deeper into the epoxy, thus causing the relaxation of the contact pressure at an earlier stage of the soak test.

In summary, the combination of the acidity, ionic concentration and the 116% larger thermal expansion in the systems soaked at 80°C could have accelerated the degradation of the contact joint.

Figures 6.11(a) and (b) show the variation of the voltage versus the duration of soak of different partial daisy chains immersed in pH6.8 at 80°C and at 37°C respectively. The measured voltage at each individual partial daisy chain was around 0.7mV. The partial daisy chain response shown in Figures 6.11(a) and (b) corresponds to the overall response recorded and represented in Figures 6.10(a) and (b). As discussed in Chapter 4, the partial daisy chains in the x direction are called: x1 which is furthest from the window, x2 the middle daisy chain and x3 closest to the window, while the partial daisy chain in the y direction was called y.

In Figure 6.11(a), the partial daisy chains x3 and y failed at an early stage during the *in-vitro* test. Once again three similar regions were observed for daisy chains x3 and y. Regions 1 and 2 corresponding to steady state and slow degradation respectively were extremely short for the daisy chains x3 and y. This was followed by region 3: pronounced joint degradation, but which still provided intermittent contact until the end of the test. A 100% increase in voltage was used as the failure criterion. With this failure criterion, it was observed that the daisy chains closest to the window x3 and y failed at around 70 and 50hr respectively. The daisy chains x2 and x1 failed at around 100 and 250hr respectively. Daisy chains x1 and x2 showed a more linear increase in voltage. This linear increase could be attributed to the combination of two factors, the slow oxidation of the exposed aluminium pad which is present under the gold stud bump [103,166] and the swelling of the epoxy. It was shown in Chapter 5 that a thin epoxy saturates with moisture in the first hour of soak and thus hydrates the exposed aluminium bond pads under the gold stud bump. Although other ions are present, the hydration will result in the formation of aluminium hydroxide. The aluminium hydroxide will turn into aluminium oxide by the contribution of the electrons from aluminium to oxygen atoms which will result in the increase in voltage and thus increase the electrical resistance [103]. It can also be noted that during the linear rise in the measured voltage, there were frequent and repeated dips in the voltage. This phenomena was not just limited to the daisy chains x1 and x2 but were also observed in x3 and y daisy chains. This occurrence started at around 65hr into the soak test. This could be attributed to the degradation of the epoxy which could be providing a channel for liquid medium containing ions and thus create a leakage current path between bond pads of adjacent daisy chains, as shown in Figure 6.12.

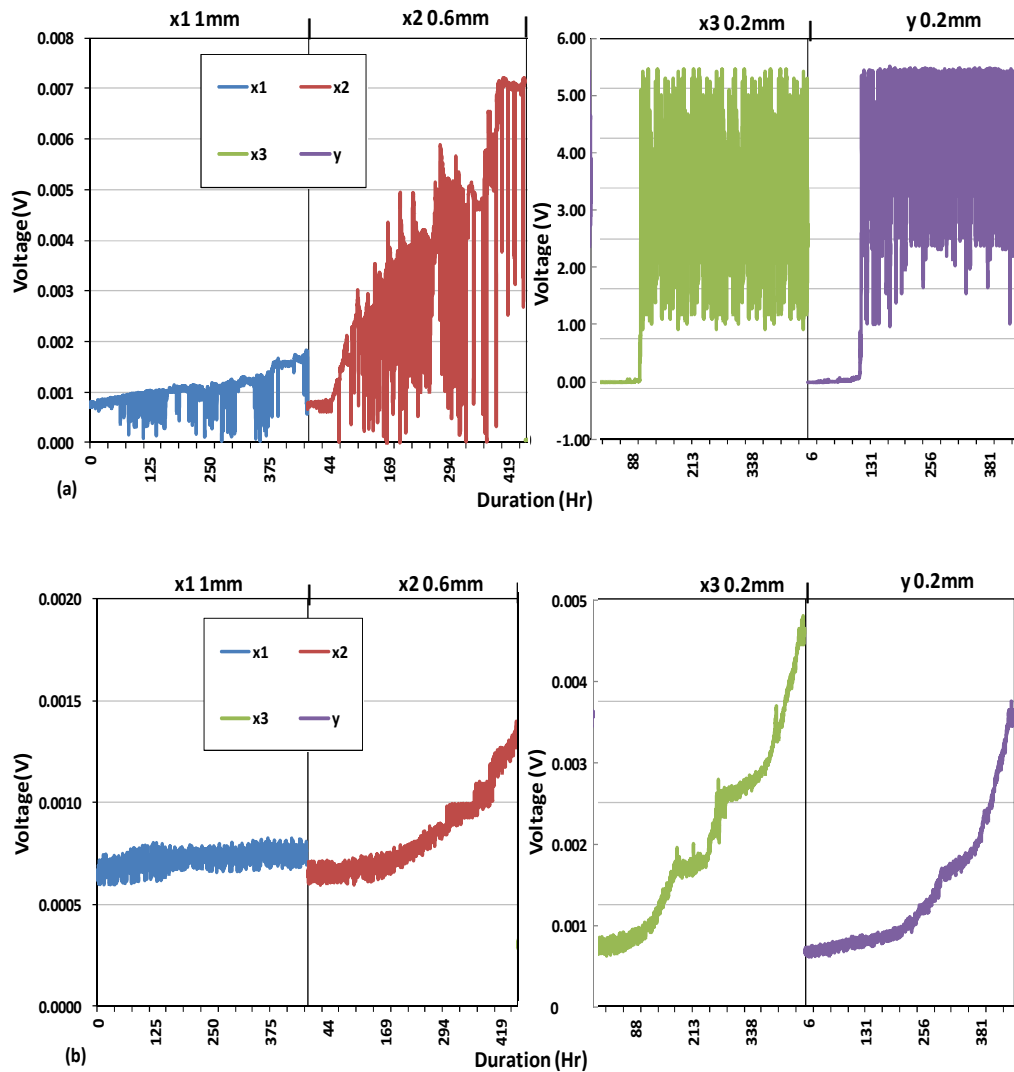


Figure 6.11. Plot showing the measured voltage variation vs. the duration of the test of the partial daisy chains of one of the sample immersed in: (a) 80°C and (b) 37°C.

Figure 6.11(b) showed that the measured voltage increase was more pronounced for the partial daisy chains x3 and y when compared to partial daisy chains x1 and x2. At the end of the test there was around a 400% increase in voltage of x3, around 500% increase in y, 100% in x2 and 17% in x1 daisy chain. With a 100% increase as the failure criterion, it was noted that x3 and y failed at around 160hr and at 290hr of soak respectively. The failure of x2 occurred at around 430hr of soak while the

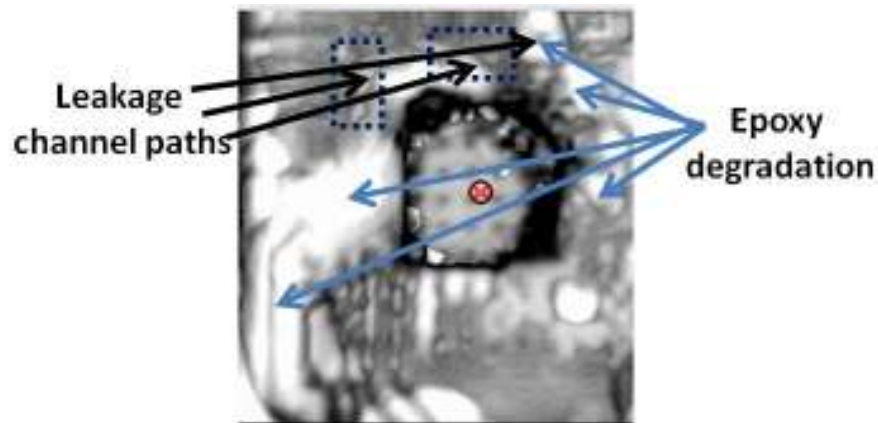


Figure 6.12. SAM image of sample aged at 80°C, after testing.

x1 did not fail during the whole duration of the test. This showed that the bond pads positioned at 1mm from the window survived the *in-vitro* test at 37°C which is over the 72hr period that is required for a diagnostic pill to pass through the GI tract. Positioning of the bond pad at around 1mm from the window in a DAS that will be used in the body means that the integrity of the joint will be preserved during the 72hr test. This result with the combination of the results that were obtained in Chapter 4 suggests that positioning the bond pad at 1mm or over from the window will ensure that the joint quality is preserved during integration and the subsequent *in-vitro* test. For the same pH and moisture level, the sample aged at 37°C does not show any leakage between bond pads of adjacent daisy chains, thus indicating that high temperature indeed accelerated the chemical reaction in the epoxy matrix [167].

Figure 6.13 shows the variation of the time of failure for individual partial daisy chains in different artificial gut and control solutions at 80°C and at 37°C respectively. As described in the previous section, a 100% increase in the measured voltage was used as the failure criterion. First, it could be noted that all the samples aged at 80°C failed earlier than the samples aged at 37°C. As stated in the previous section, this shows that high temperature has a detrimental effect on the polymer matrix.

Second, the failure time of the samples seems to be reduced as the acidity of the solutions were raised. Third, the daisy chains x3 and y closest to the window failed at an earlier stage in all the solutions at 80°C and at 37°C. Fourth, despite the different pH solutions, the daisy chains x1 and x2 which are furthest from the window failed when immersed at 80°C. At 37°C soak, for the samples soaked in pH6.8, the daisy chain x1 survived the whole *in-vitro* test. In the control buffer solution x1 and x2 did not fail during the whole test. At 37°C, the daisy chain x1 in all three samples soaked in pH6.8 and in all three samples soaked in buffer solution survived the *in-vitro* testing.

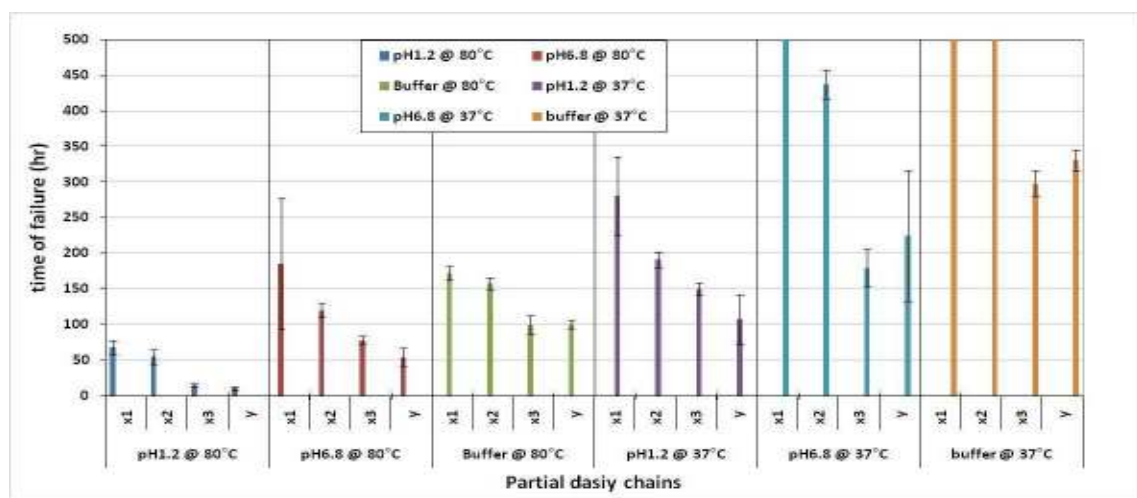


Figure 6.13. Plot showing the time of failure for individual partial daisy chains in different artificial gut and control solution at 80°C and at 37°C respectively.

Figure 6.14 shows the variation of time to failure of partial daisy chains y and x3 in different pH solutions. It shows the comparison between samples soaked in 37°C and in 80°C. For the same pH, the time of failure of the partial daisy chain y is approximately 83% higher at 80°C than at 37°C. An exponential trendline was used to fit the time of failure for daisy chain y at both 80°C and at 37°C. The high R² showed that there was a good correlation between the data and the trendline used to fit the data. This same observation was observed for daisy chain x3 which is also positioned at 0.2mm from the window. The exponential increase in the time of failure could be used to predict the failure

of daisy chain x3 and y in specific pH solution at different ageing temperature. For example, it can be predicted that the daisy chains x3 and y of a sample immersed in pH4.5 will fail at around 50hr of soak at 80°C while it will fail at around 180hr at 37°C. This once again shows that the acidity and the temperature have deleterious effects on the contact joints. It also shows that the daisy chain orientation does not affect the time of failure in different pH solutions. In addition the oxidation of the aluminium bond pads could also contribute to the degradation of the contact joint.

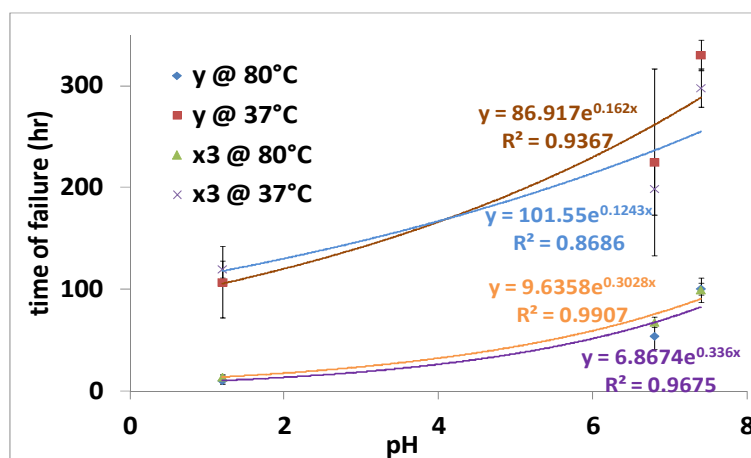


Figure 6.14. Comparison of time of failure of individual partial daisy chain y in different artificial gut at 80°C and at 37°C respectively.

For all the samples, the daisy chains x3 and y that are closest to the window failed first, followed by the middle daisy chain x2 and the furthestmost daisy chain x1. The daisy chains x3 and y were positioned 0.2mm from the window and the epoxy fillet at the window came in direct contact with the solutions when immersed. The fact that these two daisy chains failed first indicated that the degradation of the polymer seemed to have originated at the exposed epoxy surface at the edge of the window and slowly moved further away from the window as shown by the black arrows in Figure 6.15.

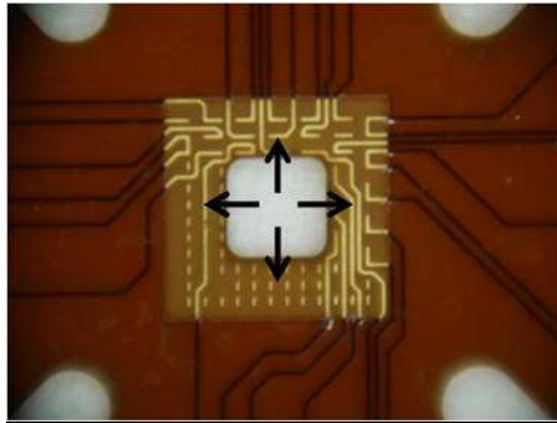


Figure 6.15. Picture showing the movement of the epoxy degradation in a DAS.

6.3.3. Failure analysis

Figure 6.16 and Figure 6.17 show the study of the epoxy fillet at the window using Scanning Electron Microscopy (SEM) before and after exposure to gut fluids during *in-vitro* test. SEM was carried out to confirm the failure mechanisms suggested by the results in the previous section.

Figure 6.16 shows the evolution of the surface in an acid and base condition aged at 80°C. At 0hr soak, it can be noted that the surface of the sample was smooth with few bumps representing the underlying conductive particles. After 24hr of aging, enzyme adhesion was found on the surface of the epoxy immersed in pH6.8. The epoxy resin aged in acid showed little enzyme adhesion with few micro cracks at its surface. The presence of the micro crack suggests that the degradation of the surface of the epoxy started within 24hr of soak in an acid environment.

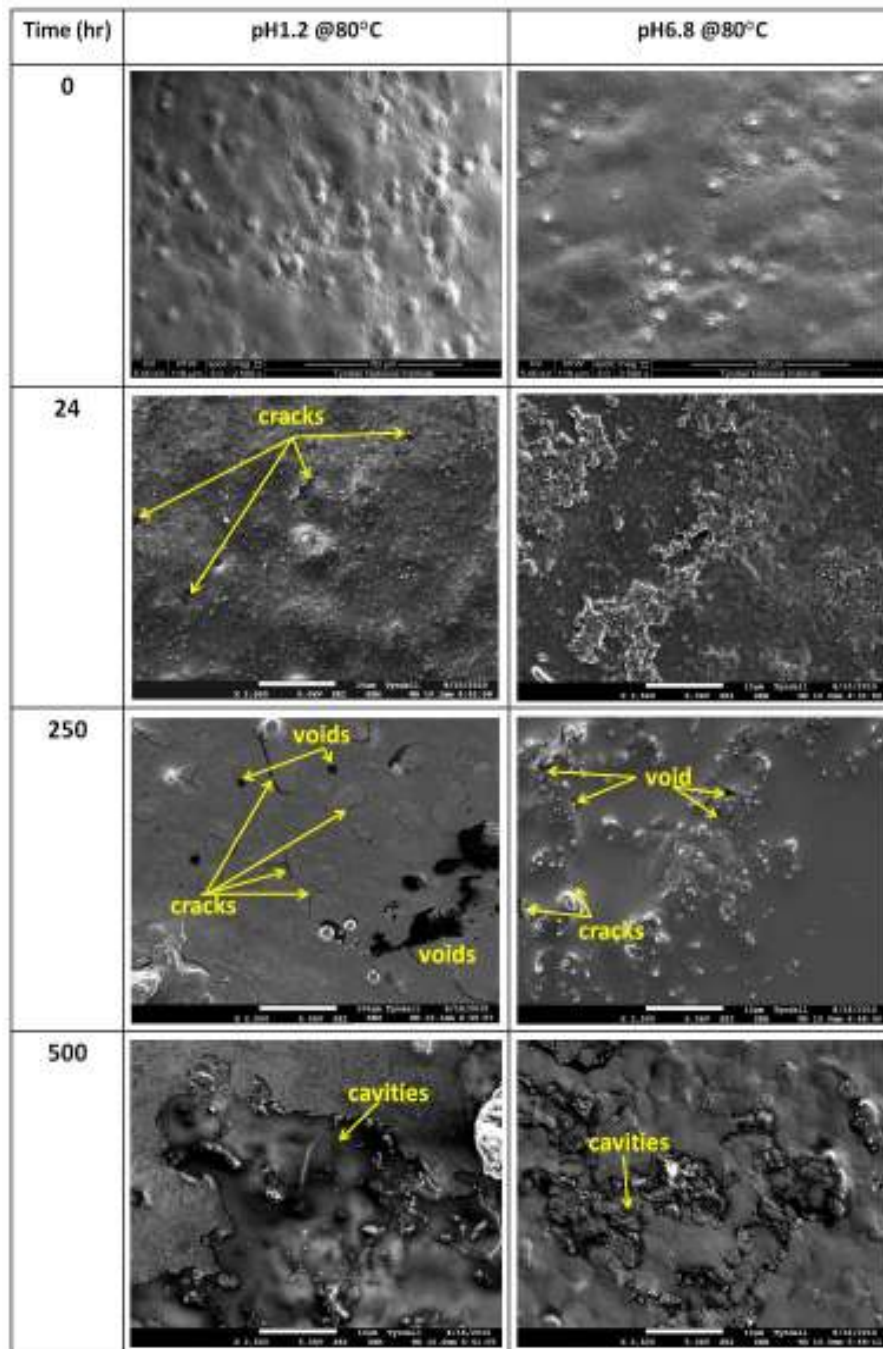


Figure 6.16. SEM surface study of samples before and after exposure to gut fluids during *in-vitro* test at 80°C.

After 250hr of immersion the surface of the sample immersed in pH1.2 was covered by numerous micro cracks and voids. In comparison, the sample immersed in pH6.8 showed less cracks and voids. It can be noted that these cracks and voids were at the edge of the islands formed on top of the epoxy surface. Large voids are due to the hydrolysis of the polymer which was a combination of

water absorption, temperature and the acidity content in which it was submerged. Further aging of the sample in pH6.8 induced surface erosion with massive cavities interlinking each other. These same phenomena were observed in the samples immersed in pH1.2 with the surface cavities being wider and deeper. This indicated that surface erosion exposed the underlying surface for further degradation to occur. Previous studies of moisture degradation on epoxy suggested the hydrolytic degradation of the ester linkage as such hydrolytic attack results in the polymer chain being broken into two new end groups, such as hydroxyl and a carbonyl [160,168].

Figure 6.17 shows the evolution of the surface aged in an acid and base solution at 37°C. Once again it can be noted that after 24hr *in-vitro*, the sample immersed in pH6.8 had a network of enzyme adhesion to its surface while the enzyme adhesion was sporadic and relatively limited for a sample immersed in pH1.2. Furthermore the sample aged in pH1.2 at 37°C exhibited no surface cracks. After 250hr of aging, the sample immersed in pH6.8 exhibited random micro voids on the surface of the sample, while larger voids and cracks were present in the sample immersed in pH1.2. Additional aging of the sample to around 500hr resulted in more degradation to the sample surface reflected by more cavities and crazing in the sample immersed in pH1.2 and pH6.8. These surface eroded cavities are not as significant as the ones that were observed in samples aged at 80°C. This suggested that the temperature had a significant impact on the degradation of the polymer. It should also be noted that the samples aged in an acid environment had a higher level of surface degradation when compared to the samples aged in pH6.8. This was true for the samples aged at 37°C and at 80°C. Therefore, it can also be concluded that the acidity of the environment also played a crucial part in degrading the epoxy surface.

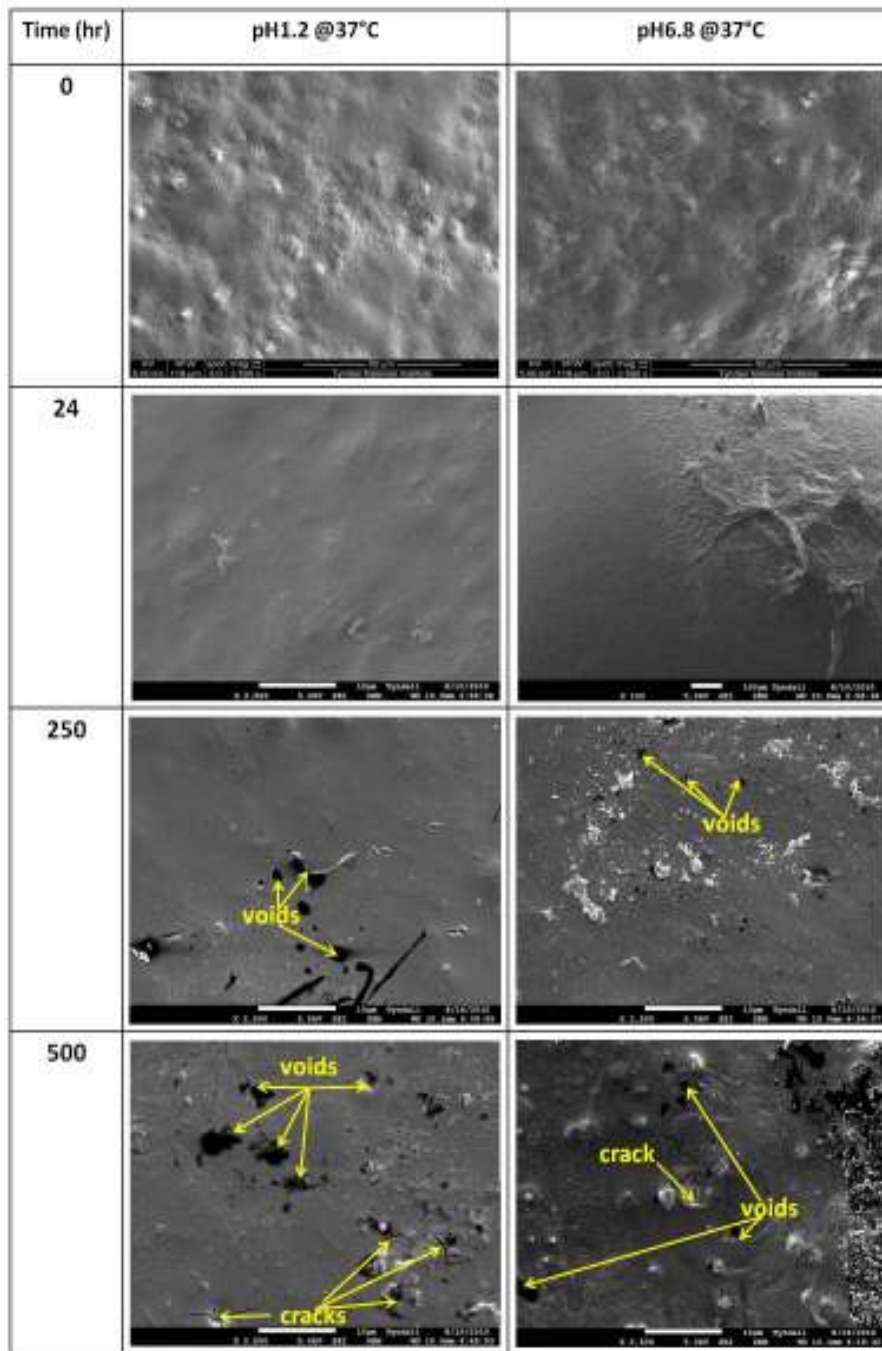


Figure 6.17. SEM surface study of samples before and after exposure to gut fluids during *in-vitro* test at 37°C.

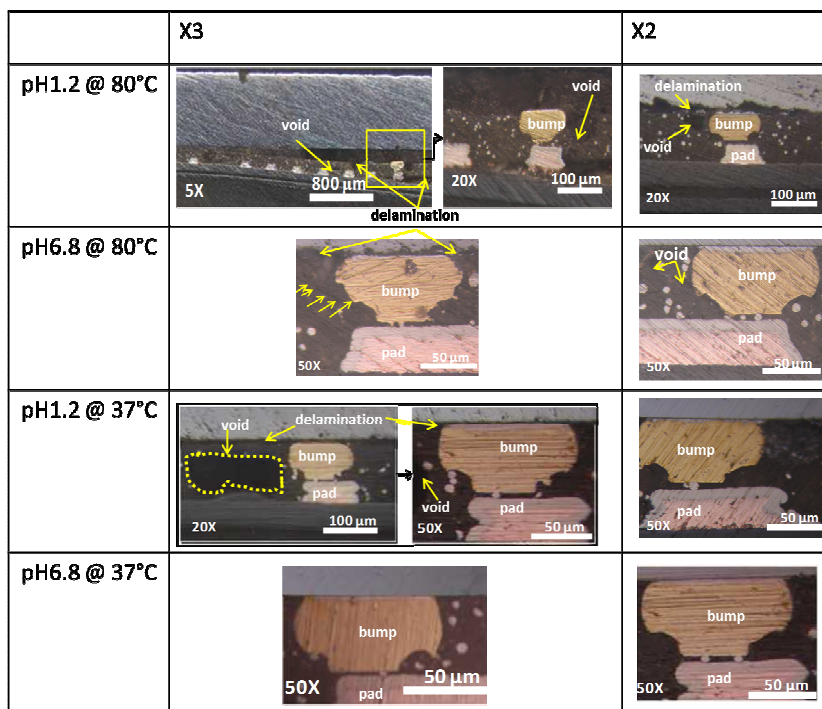


Figure 6.18. Cross-sectional analysis of the samples after *in-vitro* test.

Figure 6.18 shows the cross-sectional analysis carried out on samples after *in-vitro* test. The cross-sectional images of the y and x1 daisy chains are not shown in this figure because the failures that occurred are similar to the x3 and x2 daisy chains respectively. After 500hr of aging in pH1.2 at 80°C, it can be seen that the epoxy was delaminated from the chip and the substrate, and that the opening due to delamination was more pronounced towards the centre than towards the edge of the chip; the same observation was made on the substrate side as well. This implied that the opening was initiated close to the centre of the window and propagated toward the edge of the chip and the substrate. It can also be noted that there are numerous voids present close to the centre of the window. This was in agreement with the polymer surface degradation observed on the epoxy surfaces at the window. The delamination of the epoxy at the x2 daisy chain site was much smaller than at the x3 daisy chain site. As seen for x3, the epoxy delamination had pulled the bump clear from the chip, thus leading to the failure of the interconnection. This suggests that the swelling of the epoxy caused the bump to shear from the chip surface. Although bare aluminium exposed to the

acid solution might corrode from the Cl^- ions, the cross section showed no corroded bond pads. In a 500hr aging in pH6.8 at 80°C, once again the bump and the epoxy delamination was observed. The micrograph also revealed voids close to the bump delamination site which could be have been once more caused by the deep cavities observed on the surface of the SEM samples. On the x2 daisy chain only small voids were present, however the integrity of the interconnection was maintained.

For the sample aged in pH1.2 at 37°C for 500hr, the micrograph showed voids being present close to the interconnection area, while delamination was observed at the chip epoxy interface. This delamination continued into the bump area as the bump was lifted off from the chip. On the contrary, the integrity of the joint was maintained for x2. Samples aged in pH6.8 at 37°C showed no failure of the joints during the whole *in-vitro* test.

Summary

In general, cross-sectional analysis confirmed that the combination of high temperature and high acidity level had a deleterious effect on the samples. The main failure mode detected was interfacial delamination and open bump. Although bare aluminium exposed to the acid solution might corrode due to the presence of Cl^- ions, the cross section showed no corroded bond pads. However, the cross-section revealed that positioning the bond pad further away from the window will provide a good integrity of the joint during the capsule transition.

6.4. Conclusion

This chapter has dealt with the study of the reliability of the ACA in a DAS. The first part of the study was to investigate the constant humidity aging of an ACA joint. Since no proper standard test

procedures exist, the constant humidity aging was carried out at 50°C/95%RH to study the reliability of the ACA for a direct access sensor. At the end of the reliability test, out of the nine samples tested, for the same electrode in all nine samples, only two of the ACA connections showed a slow increase in resistance until an open joint was observed. The slow resistance increase of the failed joint was attributed to the fatigue like process, induced by the removal and replacement of the samples in the humidity chamber. Failure analysis of the failed joint after reliability testing showed that the constant movement of the sample in and out of the chamber for room temperature testing caused a thermal strain of 0.004 and a hygroscopic strain of 0.0052 resulting in swelling and shrinking of the adhesive and thus causing a crack to initiate and propagate along the die-epoxy interface.

The second part was involved in the study of the *in-vitro* reliability test of the ACA joint in gut fluids and in the control buffer solution. The resistance of all the samples at the start of the test was around 28Ω. The samples aged at 80°C showed three regions which consisted of region 1 – stable contact resistance, region 2 – slow degradation of the contact joint and finally region 3 which was the pronounced degradation of the contact joint. All the samples in the *in-vitro* test failed no matter the solution in which they were immersed, while only the samples aged in pH1.2 at 37°C showed a degradation of the contact joint. It also showed that the combination of the acidity and the temperature had accelerated the degradation of the contact joint. Furthermore for 37°C application, the DAS bond pad positioned at a minimum of 1mm from the window survived the whole *in-vitro* reliability test. This suggested that positioning the bond pad around or over 1mm from the window will ensure the joint integrity during integration and testing. The fact that the daisy chains x3 and y, closest to the window, failed first indicated that the degradation of the polymer originated at the exposed epoxy surface at the edge of the window and slowly moved further into the ACA.

Delamination of the epoxy from the chip interface and the bump delamination seemed to be the main failure modes of the contact joint in the *in-vitro* test.

This chapter described the humidity and the *in-vitro* aging of the ACA. The *in-vitro* test showed that placing the bond pad at 1mm from the window will survive the 72hr journey in the gut environment. Now that the ACA long term reliability in gut environment has been characterized, the next section will discuss the system integration of the DAS and the final prototype into a capsule format.

Chapter 7 Capsule integration

7.1. Introduction

In Chapter 3, different capsule integration methods were considered and the schematic of the final prototype (modular test board) and the sensor placement option was selected. The DAS attachment process was perfected using test substrates to get a repeatable and reliable contact and to provide a good coverage at the edge of the windows. This chapter will describe the last phase of the current work which involves transferring the repeatable ACA interconnect process to the modular test board and the integration of the modular test board with the DAS into a capsule format.

7.2. DAS in the modular flexible prototype

7.2.1. Modular flexible prototype board

The electronic system defined for the swallowable electronic capsule is complex [17], consisting of many elements. The sensor is interfaced to analogue circuitry for signal conditioning. A power supply is placed centrally for the integration of a single lithium ion cell. A processing unit, or microcontroller, controls the measurement and communication process. An ultralow power wireless communication system is added, which provides the transfer of the measured data to an external receiver module. This receiver has been developed to acquire the data and interface it to a PC host station.

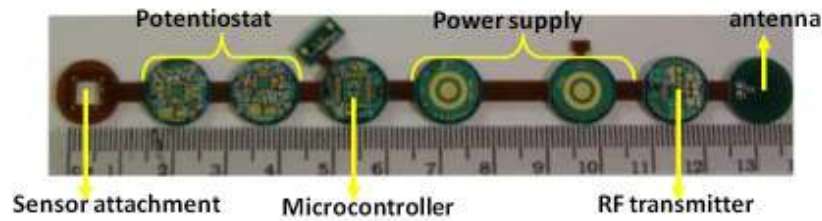


Figure 7.1. Modular flexible board.

Figure 7.1 shows the latest system prototype which implements the instrumentation in a modular fashion on circular PCB discs interconnected by flexible polyimide core. In this way the discs can be folded for encapsulation and the flexible core provides a reliable interconnect between them. Figure 7.2(a) shows the schematic of the folding that could be achieved during integration. It is crucial to note that the copper track was placed on the inside of the bend radius to achieve maximum reliability during integration. It was decided that a compressive force on copper might be better than a tensile force as this might tear the copper if repetitive bending was performed during integration. Figure 7.2(b) gives a representation of the thirteen layer structure used in the circular modular discs that were used in the development of the modular flex board [17] and where the copper track will be on alternate sides of the interconnecting strips. As can be seen, an extra layer of rigid FR4 is used to achieve structural integrity in the regions where the circuits are located.

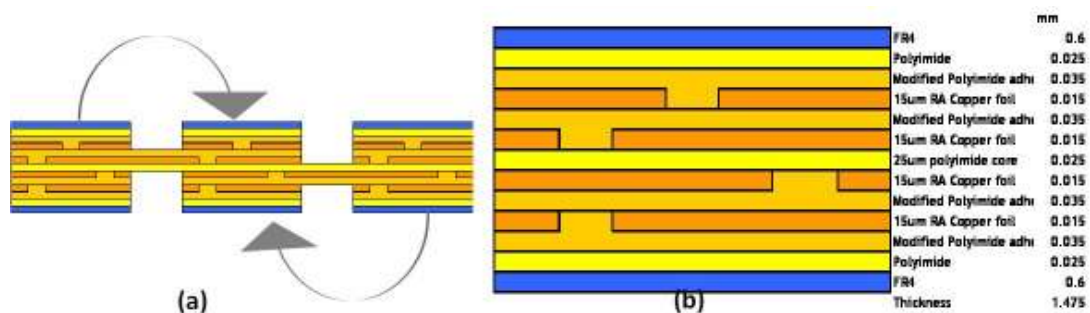


Figure 7.2. Schematic showing: (a) the folding in the modular flex board; and (b) the thirteen layer structure used in fabrication of the modular flexible board.

The power module did not comprise a battery holder; instead it was split into two modular circular PCB disks linked via a flex strip. These two modular circular PCB disks had an inner circular pad of 3mm surrounded by a concentric circular pad positioned at 1.06mm from the edge of the circular pad, as shown in Figure 7.3. The purpose of the outer concentric circular pads was to limit the spread of the conductive epoxy during integration. The left and the right modular disks with their circular bare pads correspond to the negative and positive battery inputs respectively. In order to stop the battery drain during its integration, a protruded section was designed on the edge of the positive modular disc. The right part of the protruded section was connected to an enable of a switched capacitor voltage converter, while the left part was connected to the V_{in} and the positive section of the circular pad.

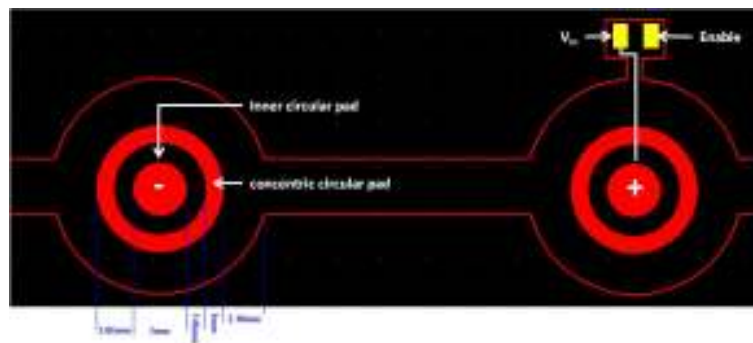


Figure 7.3. Protel design of the battery section showing the protruded section with enable and V_{in} .

7.2.2. Sensor attachment modular flexible board

Firstly, all the active devices and the passive devices required for the proper functioning of the flex board were assembled on it. This was followed by the sensor attachment. The sensor area for the board and the chip were cleaned and then the ACA was dispensed on to the board using the CAM/ALOT 1414 liquid dispense system. The dispense pattern described in Chapter 3 was used to

dispense ACA on to the board. Chip-board alignment was carried out using a Finetech Flip-Chip bonder and the bonding was carried out with the bonding parameters stated in Chapter 3.

7.2.3. Electrochemistry – modular flex board DAS testing

The protruding part on the microcontroller side was used to program the microcontroller and its functionality was checked. This was followed by sectioning the protruding part and the edges sealed with silicone and cured for 24hr. Wires were soldered on to the negative and the positive bond pads of the power supply circular discs and the sensor part was placed in a vial containing a solution of 0.5M of H_2SO_4 . The soldered wires were connected to an Agilent E3649A - dual output DC power supply as shown in Figure 7.4, and a constant 3V was supplied during the duration of the test. A bench top antenna receiver TH71102 [17] was used to collect the data transmitted by the modular flex substrate and the results were stored in Microsoft Excel. The whole test was automated using LabView.

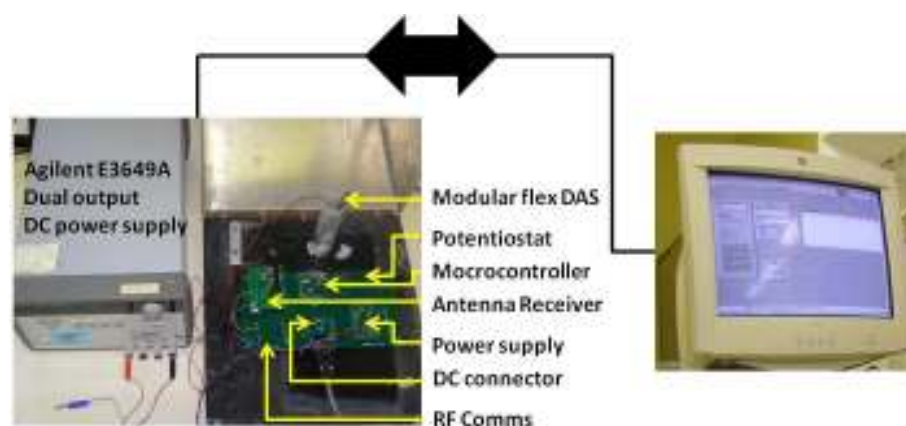


Figure 7.4. Benchtop electrochemistry setup for testing.

The electrical connection and the robustness of the packaging, as well as the functionality of the sensor, was tested using three electrode cell, cyclic voltammetry. The three electrode cell comprised of WE, CE and the pseudo Pt RE on the designed sensing chip. A scan rate of 0.2V/sec was applied to the electrode system and the chemical reaction that occurred at the Au WE in the solution was plotted in Figure 7.5. The plot shows the cyclic current-voltage curve of the Au WE taken 1-2 days after sensor attachment and also 6 months after sensor attachment before the capsule encapsulation was carried out. The measurement taken 1-2 days after sensor attachment showed that the oxidation peak occurred at around 0.9V during the positive voltage sweep from 0 to 1.5V, while the reduction peak was around 0.4V during the negative voltage sweep. This shift in voltage could be attributed to the pseudo reference electrode which is not as stable as the Ag/AgCl reference electrode. It was also observed that the current measured was twice that of the current measured for cyclic current-voltage curve of Au WE represented in Figure 3.18 in Chapter 3. The difference in current could be explained by the amount of Au WE exposed to the solution as a result of poor adhesion of the Au and the edge of the passivation layer. The measurement taken after 6 months for the same electrode from the same sample seems to show no oxidation peaks for the positive sweep while it shows a reduction in magnitude of the reduction peak occurring at around 0.4V for the negative sweep. Earlier studies showed that the decrease in the peak after a couple of cycles could be due to the reduction of the surface electrode [64]. Despite the electrochemical test showing that the sensor was damaged, it showed that the interconnect functioned perfectly. The sensor was left on a shelf for 6 months during which time sporadic resistance measurements were performed. During this period, the average temperature was approximately 10°C with an average RH of about 73%. The sporadic resistance measurements performed showed that the average resistance during the 6 months was 104.46mΩ +/- 2mΩ.

During 6 months, the samples were stored on a shelf at room temperature. According to the temperature data collected from [169], in the 6 month storage the maximum temperature and the minimum temperature recorded was 22°C and -3°C respectively. The relative humidity data gathered from [169] showed that it was around 83% with 3% deviation. The deteriorated samples after 6 months were visually inspected via Olympus BH2-UMA and Olympus SZX12 optical microscopes. A micrograph taken of one of the samples is shown in Figure 7.6. Peeling, blisters and passivation layer cracks were observed on the surface of the Au WE of the samples that were stored for 6 months. Likewise peeling was also observed on Pt CE and Pt WE.

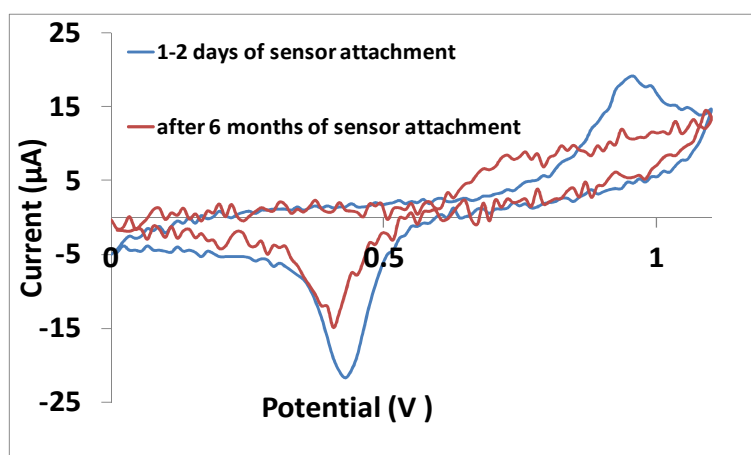


Figure 7.5. Electrochemical test results of a sample before and after storage.

Table 7.1 [170], shows the properties of the metal and the passivation layer used in the microelectronic sensor chip. At 22°C, the thermal expansion of Au, Cr, Pt and Si₃N₄ was computed to be 308ppm, 132ppm, 198ppm and 35.2ppm respectively. The thermal mismatch between Au/ Si₃N₄ and Pt/ Si₃N₄ at 22°C was 272.8ppm and 162.8ppm respectively. At -3°C, the thermal mismatch of Au, Cr, Pt and Si₃N₄ was computed to be -42ppm, -18ppm, -27ppm and -4.8ppm respectively. The thermal mismatch between Au/Si₃N₄ and Pt/Si₃N₄ at -3°C was -37.2ppm and -22.2ppm respectively. There was an 833% increase in materials expansion between Au/Si₃N₄ and Pt/Si₃N₄ due to CTE

mismatch. But there is not enough evidence to suggest that the CTE mismatch and the RH alone were responsible for the delamination between the passivation layer and the Au WE, as shown in Figure 7.7.

Properties of metal and passivation layer	CTE (ppm/°C)
Au	14
Cr	6
Pt	9
Si3N4	1.6

Table 7.1. CTE of the metal and the passivation layer used in the microelectronic sensor chip [170].

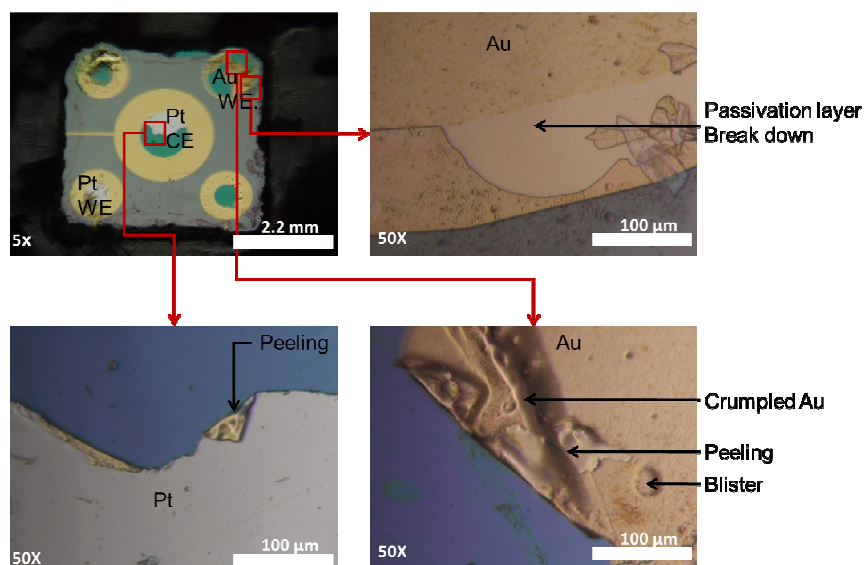


Figure 7.6. Micrographs showing the peeling, blisters and passivation layer crack on the surface of the Au WE and the Pt CE.

Further Scanning Electron Microscopy (SEM) and Energy Dispersion X-ray analysis (EDX) were performed on the failed samples to investigate the failures that had occurred on the surfaces of the electrodes. Figure 7.7 shows the SEM image of one of the Au WE. It is evident that there was

delamination between the passivation layer and the Au WE and that a crack had originated in its proximity.

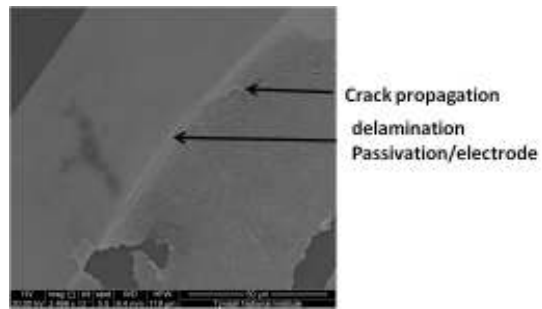


Figure 7.7. SEM image of the delamination between the passivation layer and the Au WE.

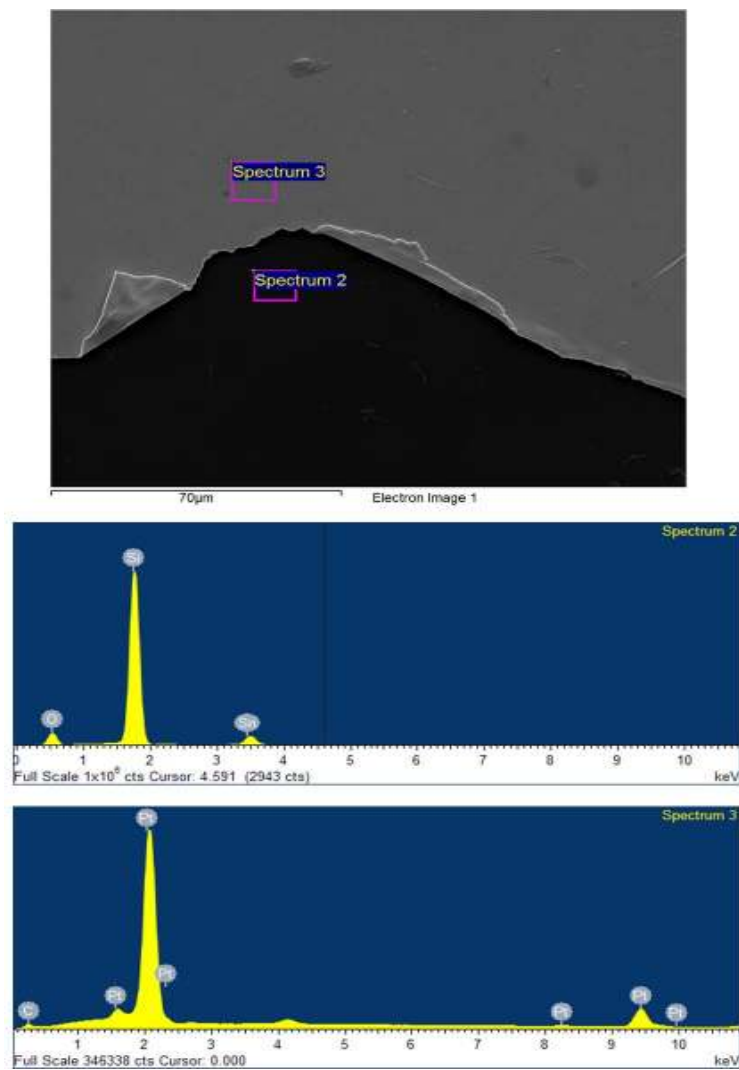


Figure 7.8. EDX picture of Pt CE.

Figure 7.8 shows EDX performed on one of the samples where the Pt CE was peeled off its surface. The EDX spectrum was taken from the peeled part – spectrum 2, and the unpeeled part – spectrum 3. Spectrum 2 showed that it only contained bare silicon in the area where the metal should be present. This indicated that the Cr and the Pt were completely stripped off the electrode surface.

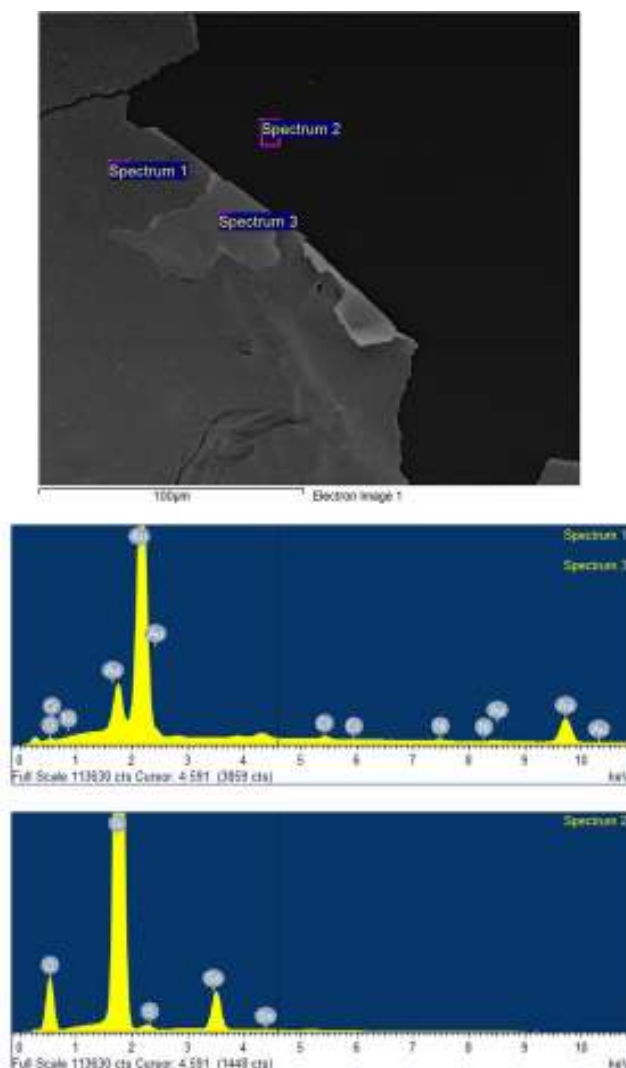


Figure 7.9. EDX analysis of the Au WE.

Figure 7.9 shows the EDX analysis performed on one of the samples where Au WE peeling was observed. EDX was performed on three regions noted 1, 2 and 3. The spectra from 1 and 3 were the

same and clearly indicated the presence of Au and Cr in the unpeeled region. Spectrum 2 showed just bare silicon indicating that the metal had been stripped from these parts. The crack present between the electrode and the passivation could have been the source for sulphuric acid diffusion during the voltammetry tests. Sulphuric acid getting under the electrode area could have resulted in the erosion of the underlying chromium and thus led to further flaking and peeling of the Au and Pt electrodes [171].

This part of the failure analysis showed that Cr was not a suitable metal to be used in developing the chip that was to be used for electrochemistry in an acid environment. Instead more reliable titanium could be used as an adhesion layer in developing such a chip [172].

7.3. Battery integration

An off the shelf Lithium/Manganese Dioxide (Li/MnO₂) battery – VARTA CR 1/3 N [173] – a cylinder shaped battery with a diameter of 11.60mm and a height of 10.80mm was used as a power supply for the capsule. It was a single unit battery with a maximum output voltage of 3V and a typical current capacity of 170mAh.

Before the battery integration, sensor protection was carried out by dispensing silicone on the perimeter of the window using CAM/ALOT and cured at room temperature for 24hr. The cured silicone acted as a dam around the window. Then the protection of the sensor was carried out via AZ photoresist – Diazonaphthoquinones (AZ Electronic Materials GmbH) with the method described in section 3.6.2 in Chapter 3, as shown in Figure 7.10.

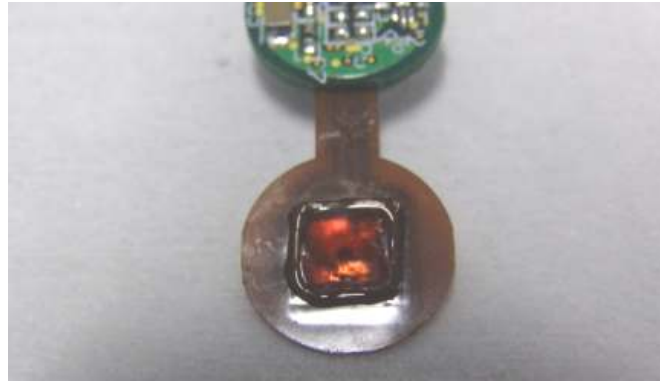


Figure 7.10. Sensor protection.

This was followed by the battery integration which consisted of the following steps as shown in Figure 7.11. First a wire was soldered onto the negative circular pad and then connected to the wire soldered on to the enabler. A third wire was soldered onto the V_{in} with connection to the positive end pad of the battery and was left open, see Figure 7.3. This was carried out to lower the battery consumption by going to a shutdown mode where only $0.01\mu\text{A}$ current would be drawn from the battery during the capsule integration process. The circular pads for the battery were then covered with temporary adhesive and the surrounding areas were spray coated with water and oil repellent thin film surface coating – RS 251-3700 [174]. This step was carried out to insulate the vias that were present around the circular pads. These vias provide a metal contact with active components that might drain the battery during the integration process. The insulating thin film was left to cure for approximately 2hr and the thickness of the cured film was around $1\mu\text{m}$. Silver loaded epoxy was dispensed onto the centre of the circular pads via a pendant method – the height and the diameter of one drop was approximately $159\mu\text{m}$ and $210\mu\text{m}$ respectively. The negative terminal of the battery was placed on the corresponding negative circular pad, the right circular pad folded on top of the positive side of the battery and clamped using a vice grip welding clamp. Silicone was dispensed with a hand held dispense system with a 23 gauge needle where the inner diameter of the needle was 0.33mm . A pressure of 20psi was used to dispense silicone at the edge of the battery so that it simultaneously covered about $4\text{mm} \pm 1\text{mm}$ on the battery side and around $1\text{mm} \pm 0.5\text{mm}$ on the

PCB side. After the silicone was dispensed, the system was left to cure for 24hr and the securely integrated battery is shown in Figure 7.11.

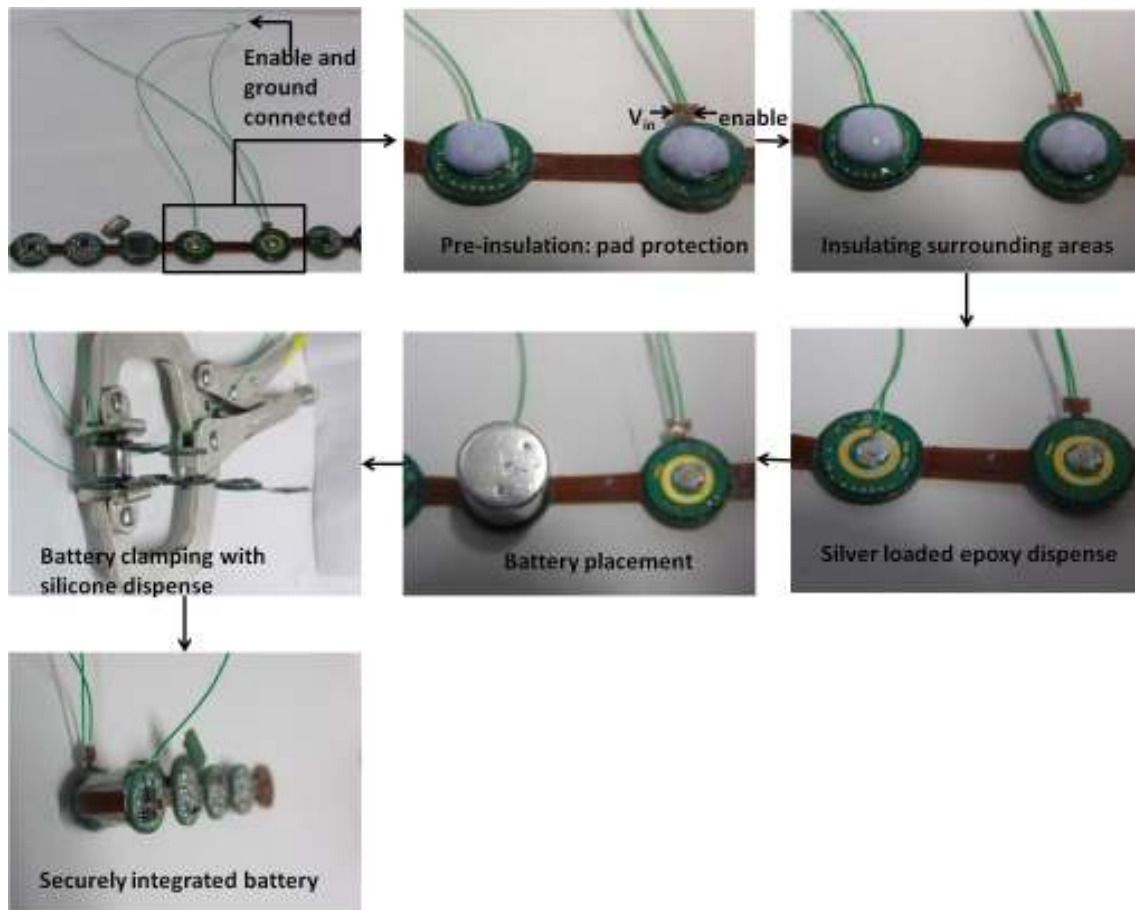


Figure 7.11. Battery integration process.

7.4. Capsule integration

Six circular discs (spacers) of 11.60mm diameter were cut from a 0.0254mm thick medical grade silicone sheet: MED94-5010-10 [175]. The following steps were followed to achieve the serpentine form:

1. A hand held dispense system with a pressure setting of 30psi and a 25 gauge needle - 0.25mm inner diameter – was used to dispense a small volume of 0.06mm³ silicone at the centre of the inner side of the circular disc representing the antenna.
2. A spacer was placed on top of the silicone dot followed by another silicone dot dispensed at its centre.
3. The RF circular disc was folded on top of the spacer and the silicone dot, thus forming the first fold of the serpentine form.

The above mentioned steps were repeated between the RF circular disc and the battery disc to obtain the 2nd fold of the serpentine form; between battery and microcontroller part to achieve the 3rd fold of the serpentine form; between microcontroller and potentiostat to obtain the 4th fold of the serpentine form; between the two potentiostat to achieve the 5th fold of the serpentine form and between the potentiostat and the back of the sensor die to obtain the 6th and final fold of the serpentine form.

A medical grade silicone was chosen to be used in the assembly. It was selected due to its ease of processing, its good thermal and electrical resistance and above all, it is not as expensive as insulating polyimide film.

Figure 7.12 shows the 3D picture of the Teflon mould which was used to set the serpentine form. The Teflon mould was made from a 50mm x 50mm block. A 41.84mm x 50mm cut was made on the block. The depth of the cut was 6.50mm. Two mirror imaged moving parts of 6.50mm thick were made so that they would slide into the cut section. The moving parts had grooves of 1mm x 1.29mm and were cut. Eight grooves were placed at 8.75mm, 11.57mm, 15.01mm, 18.45mm, 21.89mm,

33.67mm, 37.11mm and at 40.55mm respectively from the left edge of the block as shown in the CAD diagram, Figure 7.12. The groove at the farthest right, placed at 40.5mm was used to insert the antenna disc of the formed serpentine. RF was inserted into the groove at 37.11mm; battery at 33.67mm and 21.89mm; micro at 18.45mm; potentiostat at 15.01mm and at 11.57mm and the DAS at 8.75mm. The serpentine form inserted into the mould was cured for 24hr to obtain the free standing serpentine form.

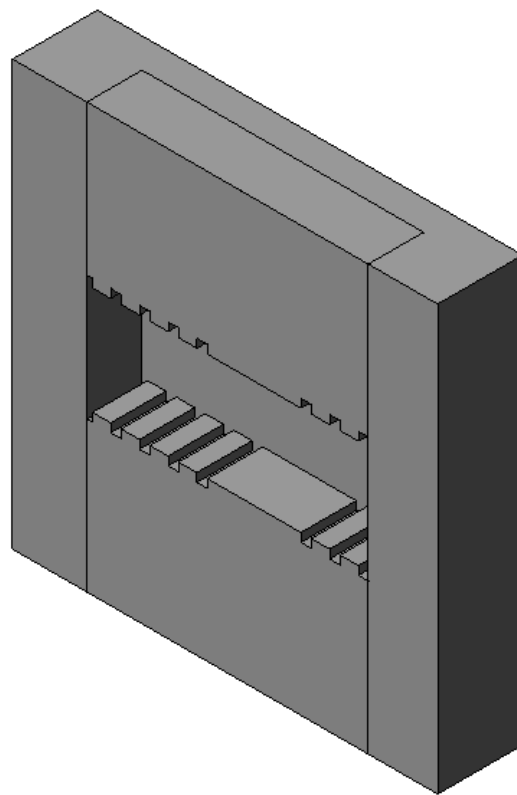


Figure 7.12. Solid Works technical drawing of the Teflon Mould.

The free standing serpentine form showed that the bend in the flex polyimide core increased the final diameter of the serpentine form to about 19mm. This means that the original glycerine capsule of 13mm diameter was not suitable for the final serpentine form. Therefore, a 22mm diameter and 45mm long two part glycerine capsule as shown in Figure 7.13(a) was used for capsule integration.

The first part measured 25mm long while the second part measured 40mm long as shown in Figure 7.13(b). Two holes were drilled out on part II of the glycerine capsule. A 1mm diameter drill was used to drill the first hole which was placed at around 28mm from its opening while the second hole was placed at the centre of the semi circular dome, as shown in Figures 7.13(b) and (c). The hole in part II will be used to bring out the wires used in the battery integration while the hole in the semi circular dome will be used to dispense silicone after capsule integration.

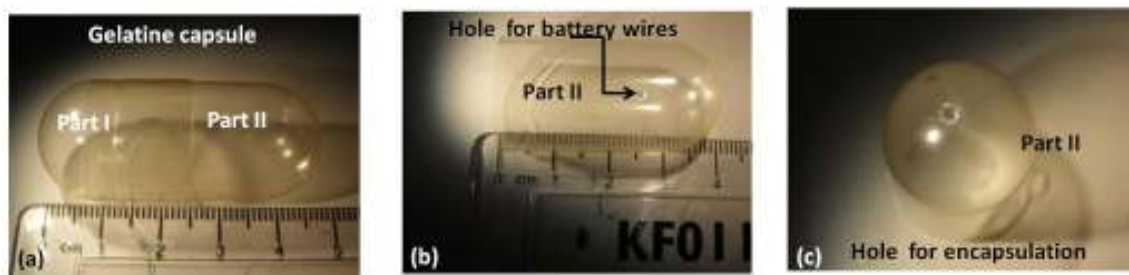


Figure 7.13. Photographs showing: (a) the entire glycerine capsule, (b) bottom part of the glycerine capsule with the hole at approximately 28mm for the battery wires and (c) 1mm diameter drill hole placed at the centre of the dome.

The DAS of the serpentine form was secured onto part I and fixed onto a glass substrate. Care was taken to position the serpentine form in the middle of the capsule. The wires from the battery were passed through the first hole on the second part of the capsule as shown in Figure 7.14. The hole used for the battery wires was sealed with silicone and cured for around 12hr. Once again a hand held dispense system with a pressure setting of 30psi and a 21 gauge needle - 0.51mm inner diameter - was used to dispense silicone into the capsule and left to cure for 48hr. The cured assembly was immersed in warm water (50°C) for 10-15min to dissolve the glycerine capsule. The sensor was exposed by dissolving the AZ photoresist in acetone for 10min but unfortunately, due to the damaged sensor, the entire capsule with the sensor and the battery could not be tested. The next section deals with the battery testing after encapsulation was carried out.

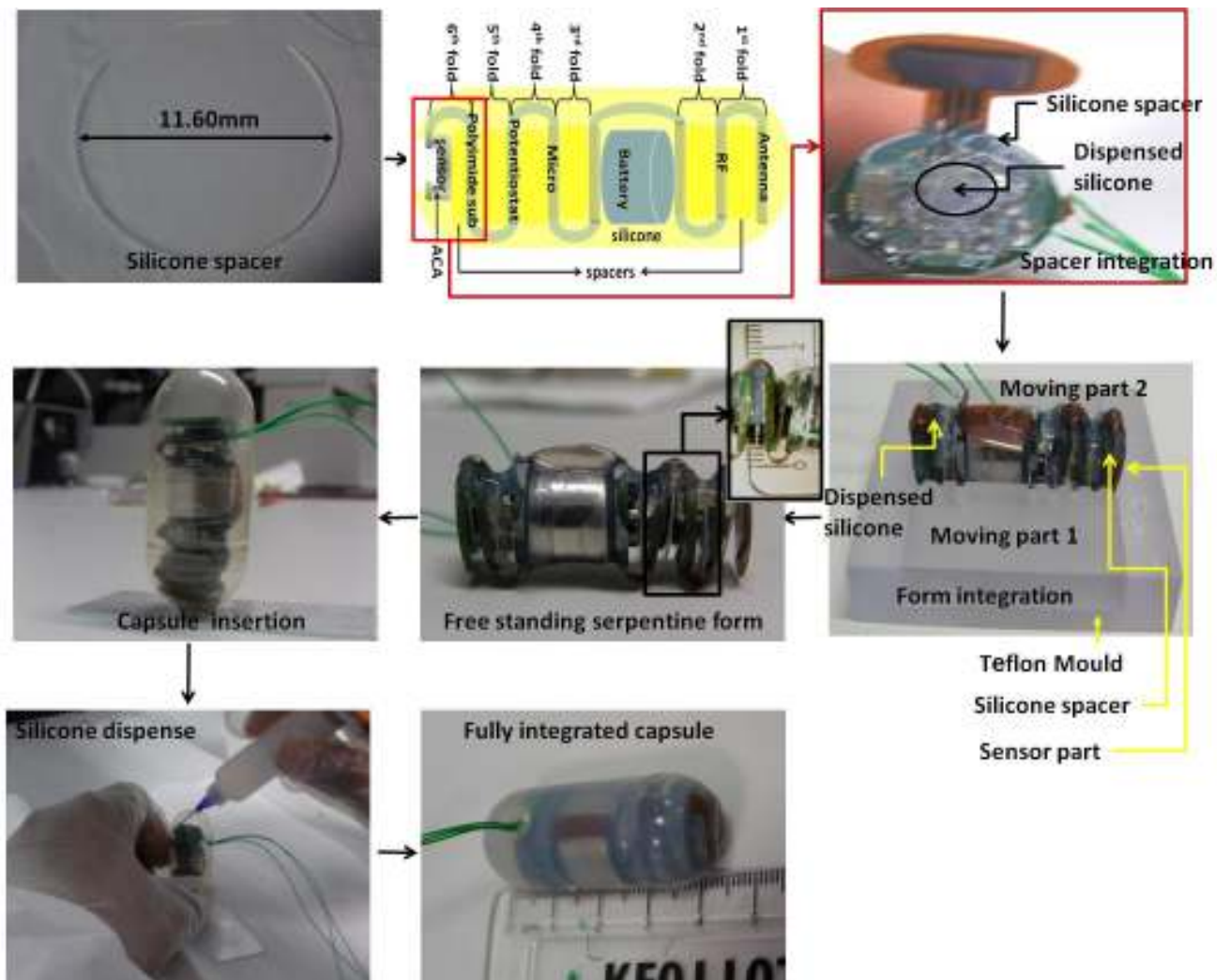


Figure 7.14. Capsule integration process.

7.4.1. Battery test - dry environment

As previously mentioned, the battery must survive the whole encapsulation procedure described in the above and still be able to provide the maximum current required by the capsule for the full 72hr. A simple circuit was developed to test the encapsulated capsule battery. The connection between the enable and the ground was severed and the enable was connected to the V_{in} to make the power supply operational. As shown in Figure 7.15, a 15k Ω resistor was connected between the ground

wire and the wire that connected enable and V_{in} , consequently forcing the current to pass through the resistor. A $15k\Omega$ resistor was chosen because it would consume only $200\mu A$ which is 10 times lower than the current consumption by the capsule in sleep mode and therefore will not impede with the battery consumption test. A Hewlett Packard 34401A multimeter was connected in parallel to the $15k\Omega$ resistor and the measured voltage was transmitted to the computer via GPIB, as shown in Figure 7.15.

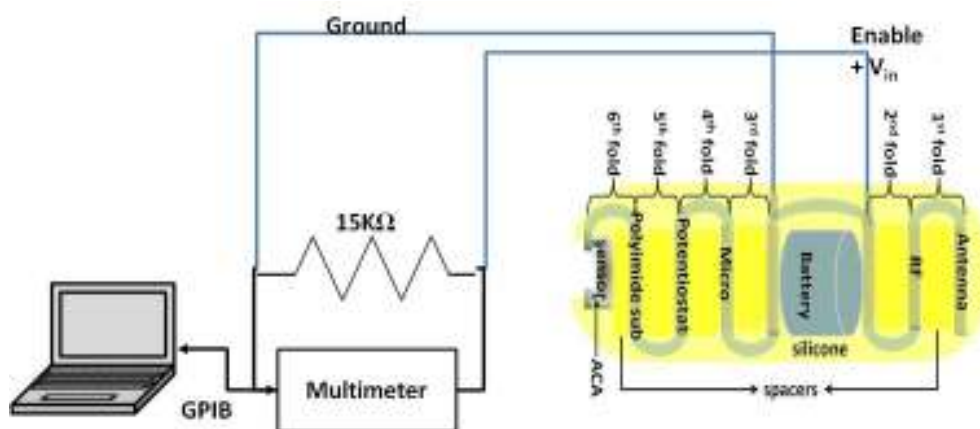


Figure 7.15. Schematic of the circuitry used in the battery test.

Even though electrochemistry was not possible due to the sensor damage discussed previously, once the battery was connected, three modes of operation of the capsule could be observed. Figure 7.16 shows the three modes with equivalent power consumption in each mode during a single capsule cycle.

The cycle started with a sleep mode and lasted around 40sec. It had a current consumption of approximately $25\mu A$. This was followed by the sensor mode which was characterized by the voltage drop – capsule function - of approximately 2.65V and by the large current usage of about 20mA. The sensor mode lasted about 20sec and was followed by the RF mode during which the voltage increased to about 2.8V for the duration of 20sec. This mode was distinguished by a current

consumption of about 6mA. The cycle came full circle by returning to the sleep mode where the voltage regained its primary value [17].

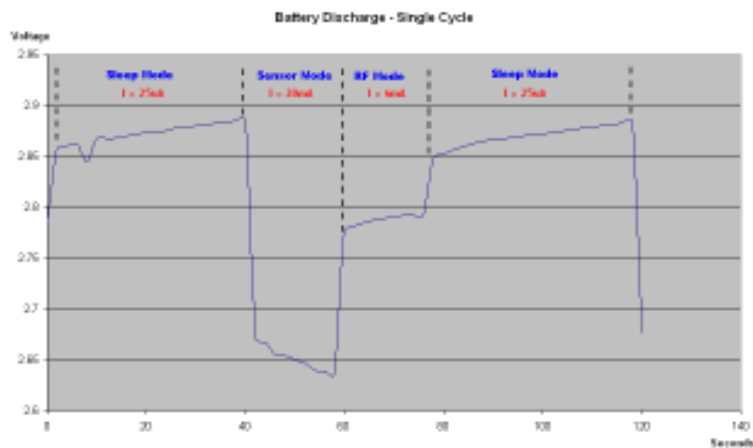


Figure 7.16. Battery voltage variation over one cycle.

The capacity of the battery was 170mAh. Therefore the energy of the battery was 510mWh. As mentioned in the previous section, during a cycle, the sensor mode is characterized by a voltage drop of 2.65V and current usage of about 20mA for 20sec; the RF mode is characterized by a voltage drop of 2.8V with current consumption of 6mA for another 20sec. With these values, the energy per cycle was calculated as 0.38mWh (one cycle takes 120sec to complete and consumes 0.38mWh energy). With the battery total storage energy of 510mWh, the time required for continuous running of the battery is 161052sec which is 45hr. In order for the battery to survive the 72hr gut journey, a 15min cycle was considered with a longer sleep mode of 14min in between the sensor mode. This 15min cycle (a 14min sleep mode in between the sensor mode), corresponding to 4 voltammetry tests per hour was chosen to assess the capability of the battery to deliver the power required for the proper functioning of the capsule during the GI transit, after the encapsulation process. The test failure limit was set at 2V, i.e. if the battery voltage dropped below 2V; the test was terminated and was noted as having failed.

Figure 7.17 shows the variation of the battery voltage versus the number of cycles the test was repeated. The inset shows a single cycle of the test where the voltage drop was about 0.15V during the sensor mode. This voltage drop quickly recuperated to its operation level at the completion of the cycle. Approximately 320 cycles were performed and it was observed that the voltage level remained constant during the entire test duration. This showed that the battery was able to survive the encapsulation procedure and still be able to provide sufficient energy for proper functioning of the capsule during the GI transit. Once more it is important to emphasise that the final application would take place in the gut environment, i.e. fluid environment. Accordingly the next section deals with the characterization of the encapsulated assembly with the battery in a fluid environment.

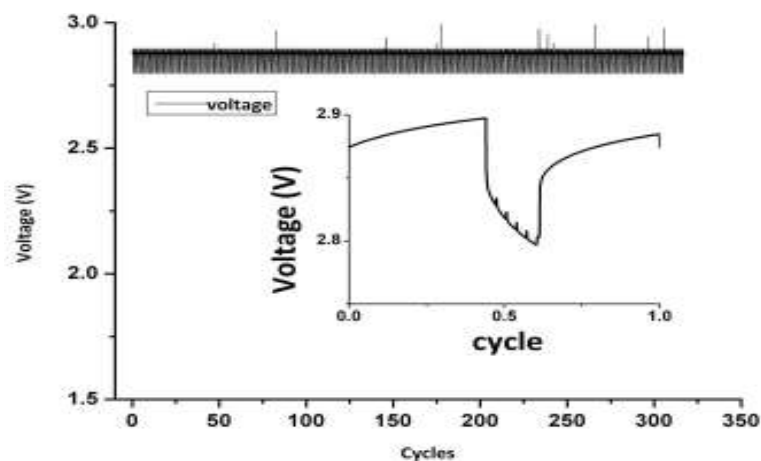


Figure 7.17. Battery performance over 72hr – 320 cycles.

7.4.2. Encapsulated assembly with battery - fluid environment test

After encapsulation of the assembly and the battery, it is crucial that the electronics and the battery function properly during the 72hr required for the GI transit. Even though biomedical silicone was used in the encapsulation, it is a known fact that it lets water vapour pass through it [176]. In

addition, the leads that were used to protect the battery discharge during encapsulation might prove to be a weak point for moisture and contaminant penetration. A test was devised to study the encapsulated assembly with the battery in a liquid environment. As there were not enough sensors, two substrates without sensors were used for this test. As mentioned in the previous section, as soon as the battery was connected, the electronics started to perform the capsule function. In order to decouple the capsule function, the first encapsulated assembly consisted of a bare substrate that had only the battery integrated to it. Once again the battery drainage was minimised by grounding the enable until the test was carried out. The second substrate had all the electronics, while a dummy silicone was used instead of the battery to fill the battery compartment. Wires were soldered to the negative and the positive circular pad so that the power could be supplied to the electronics during the soak test as shown in Figure 7.18. Both of these assemblies were encapsulated in silicone according to the encapsulation method described in the previous section.

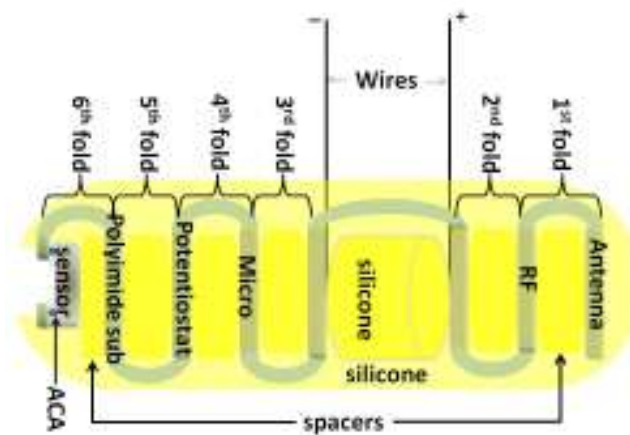


Figure 7.18. Schematic of the second substrate with silicone in the battery compartment.

Figure 7.19 shows the test setup that was used to assess the encapsulated assembly with the battery. The encapsulated samples were placed in plastic vials filled with buffer solution of pH7.4. The wires from the assembly were taken out via holes made on the screw top plastic cap. In order to avoid any evaporation of the liquid, the holes on the cap were sealed with temporary adhesives. As shown in Figure 7.19, capsule number 1 contained the battery while capsule number 2 relied on

the outside power supply. Both vials with their corresponding assemblies were placed in a temperature controlled recirculating water bath. The temperature of the bath was maintained at 37°C for the duration of the test. A Digimesh HY3003 power supply was used to supply a constant voltage of 3V to capsule number 2. The sole purpose of capsule 2 was to observe whether corrosion would occur on the electronics in the modular board.

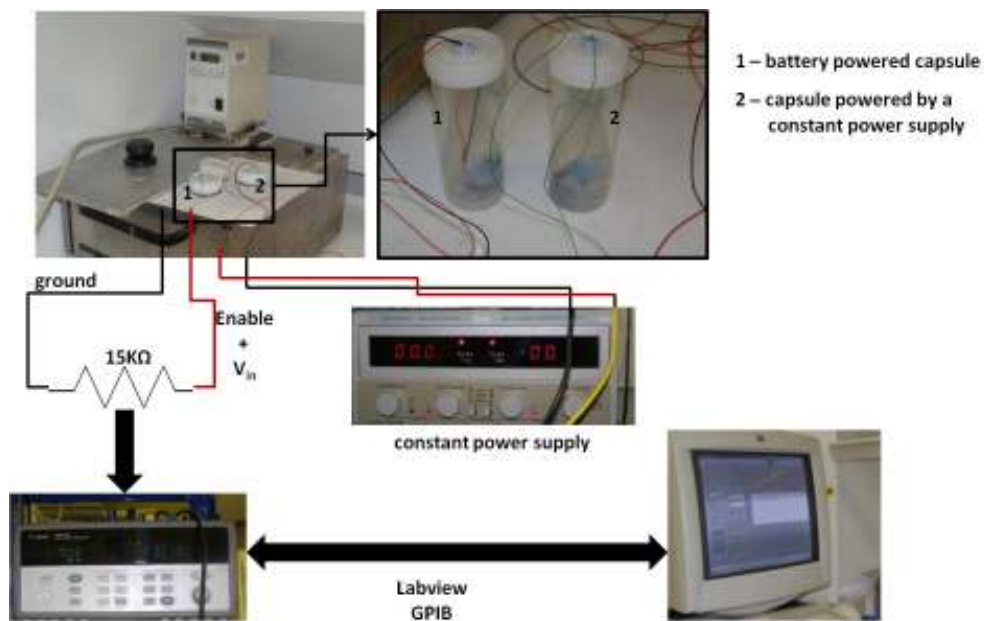


Figure 7.19. Test setup to test the battery in a liquid environment.

In capsule number 1, the enable was paired with V_{in} and connected to a 15kΩ resistor. As explained previously, the ground was also connected to the resistor so that the current could flow through it. Parallel wires were connected to a multiplexer and the voltage was recorded in a computer. For comparison, a battery, placed at room temperature, was also connected to a 15kΩ resistor and its voltage drain was also recorded in the computer via a multiplexer. A LabView program was used to automate the measurements to be taken every 5min for 72hr.

Figure 7.20 shows the variation of the battery voltage as a function of the duration of the test. The average measured voltage in both the control – non encapsulated battery at room temperature - and the encapsulated battery in buffer were approximately 2.90V. The voltage seemed to be constant for the duration of the test. At the start of the results, a delay of 15sec was observed between the two measured voltages. This 15sec lag was due to the delay in starting the voltage measurements.

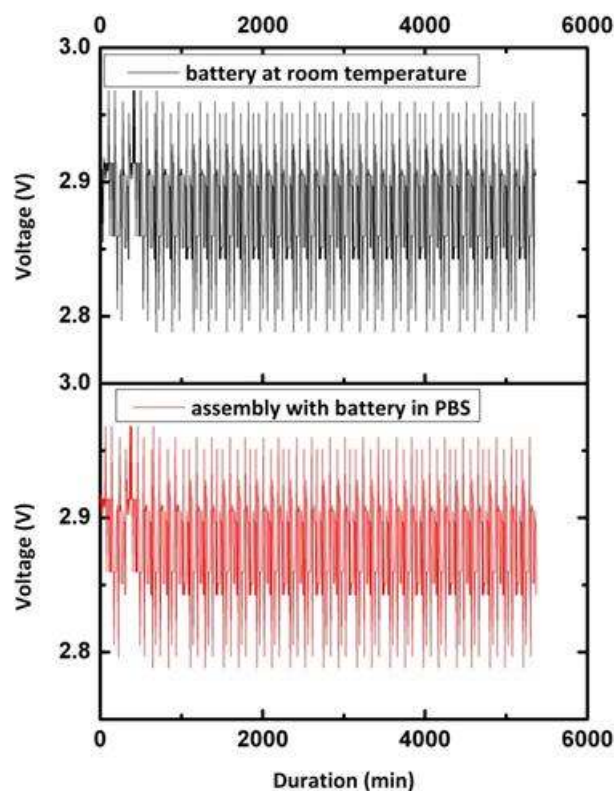


Figure 7.20. Plot showing the variation of the battery voltage as a function of time.

Capsules 1 and 2 were taken apart so that an inspection could be carried out to see if there was any sign of corrosion that had occurred in the assembly. Micrographs were taken with an Olympus SZX12 microscope. Figure 7.21(a) shows the micrograph of the electronics that were in capsule 2 after the soak test. Figure 7.21(b) shows an enlarged image of the solder joint of a resistor. The micrograph shows that the solder joint was still bright and no sign of corrosion could be observed. Figure 7.21(c) shows the micrograph of the battery from capsule 1 after the soak test. Once again no sign of

corrosion was observed on the battery. This test showed that the electronics and the battery were well protected by silicone encapsulation.

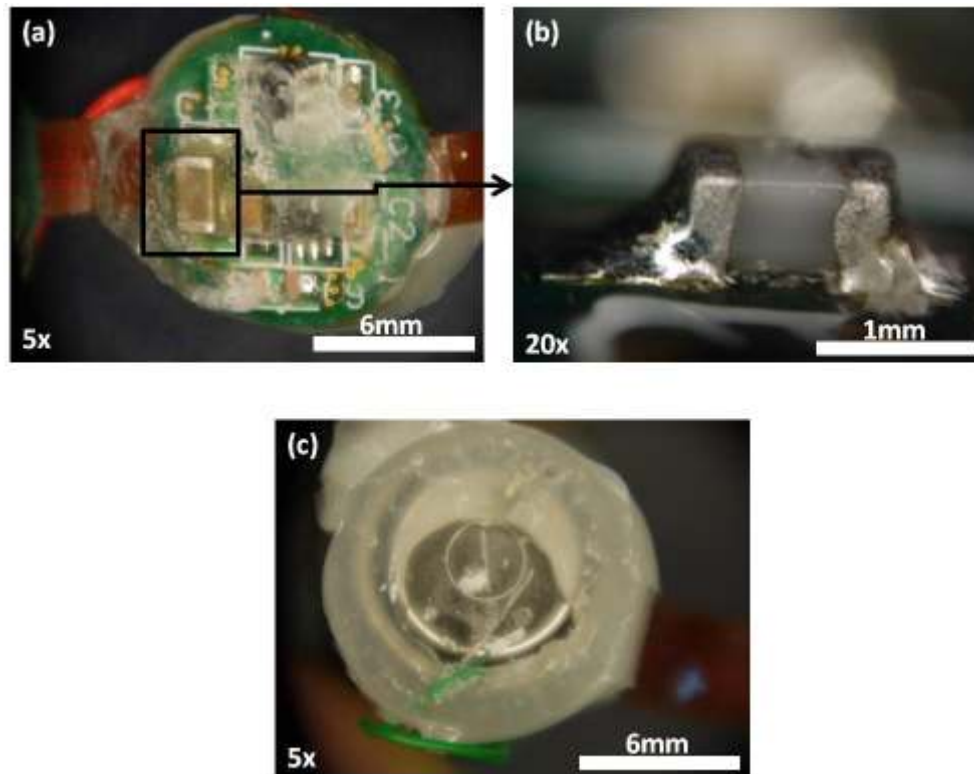


Figure 7.21. Micrographs of: (a) the soaked encapsulated electronic assembly from capsule 2, (b) one of the electronic components enlarged and (c) the battery from capsule 1 after the soak test.

7.5. Conclusion

In this chapter, the final capsule integration was presented. The final capsule integration was made possible by the modular flexible prototype which contained the sensor part and the analogue circuitry for signal conditioning. The repeatable ACA interconnect process shown in Chapter 3 was successfully transferred to the modular test board in order to obtain a reliable sensor attachment. This was shown by the electrical signal provided by the sensor even after a six month storage period.

However, electrochemistry measurements performed after six months storage showed that the sensor was damaged, as blisters, metal peeling and passivation cracks were observed. Investigations carried out using SEM and EDX showed that the delamination between the passivation layer and the Au WE was the point of entry for the sulphuric acid solution which slowly eroded the underlying chromium, leading to further flaking and peeling of the gold electrode. This same phenomenon was observed on Pt WE and Pt CE.

Battery integration was successfully achieved using silver epoxy as the conductive medium between the battery and its corresponding connection pads. Battery drainage was prevented by connecting the enable to the ground of the battery while the V_{in} was left open.

The capsule integration was accomplished by placing silicone spacers and 0.06mm^3 of silicone in between the modular discs, folded into a serpentine form and cured in a Teflon mould. The cured block was transferred into a glycerine capsule and secured in place. As the flex polyimide core increased the final width of the serpentine form, a 22mm diameter glycerine capsule was used to achieve the capsule integration. A 1mm diameter drill was used to place a hole at around 28mm from its opening to draw the battery wire outside of the capsule. Silicone was used as an encapsulant to encapsulate the whole assembly. The fully integrated capsule measured 22mm x 45mm. The encapsulated assembly battery test showed that it could survive the encapsulation procedure and could still provide sufficient power for the proper functioning of the capsule during the GI transit. The encapsulated assembly subjected to soak tests showed that the electronics and the battery were well protected by silicone encapsulation as none of them showed any sign of corrosion during the 72hr test.

Chapter 8 Conclusion and Future Work

8.1. Conclusion

The human gut is a complex ecosystem which is sometimes prone to disorder. In medicine, Inflammatory Bowel Disease (IBD) is a group of inflammatory conditions that affect the Gastro-Intestinal (GI) tract. Although IBD can be divided into several categories, the two major forms of IBD are Crohn's disease (CD) and ulcerative colitis (UC). There has been a rapid growth of IBD in Europe and North America during the second half of the twentieth century and it is becoming more prevalent in the rest of the world as they adopt the western life style. CD and UC are chronic diseases which can lead to long-term and sometime irreversible impairment of the GI tract.

One of the conventional methods to investigate any suspected pathology is to use an endoscope which is inserted through patient's mouth, nose or rectum. These procedures provide some information: gastroscopy provides information about the oesophagus and the stomach while the colonoscopy helps investigate the large intestine. These procedures are not only unpleasant for the patients but are also unable to provide information from the small intestine.

The swallowable electronic capsule technology is a relevant example of the development in microelectronics technology and the wireless technology being applied to the biomedical area to overcome the limitations of existing technology. The swallowable electronic capsule is an autonomous system which contains a sensor, the associated electronics for signal conditioning and amplifying and a radio transmitter all encapsulated in a biocompatible material. The swallowable capsule involves a non-invasive technique which can provide information about the whole GI tract.

Swallowable capsules can be classified into families of imaging (PillCam, Olympus Optical), drug delivery systems and sensing capsules. Unlike the imaging and the drug delivery capsules where none of the parts are exposed, the chemical sensing capsules have one or more sensors that measure biochemical variables related to the gut ecosystem through exposed sensors. However, in none of the diagnostic sensing capsules, is the sensor attachment, the first level packaging of the sensor in a swallowable capsule, achieved by Flip Chip Over Hole (FCOH) method using anisotropic conductive adhesive. This PhD work was undertaken to develop this novel sensor attachment method on foldable circuitry to be used in a capsule environment.

In this work, specific challenges relating to the development of the sensor assembly - DAS, sensor integration, battery integration and capsule integration using modular test boards - have been discussed. In order to expose the sensor to the external environment, the existing FCOH technique was combined with ACA technology in a capsule environment to achieve the DAS. In a DAS, ACA not only provides the electrical interconnection but simultaneously seals the interconnect area and the underlying electronics from the sensor area in a capsule application. This work characterized the ACA joint used in the DAS in terms of development qualification, mechanical reliability during integration, electrical characterization, hygrothermal reliability and artificial gut fluids reliability. It also characterized the final capsule integration and its reliability. The main conclusions from the current work can be summarised in the following five categories:

1. The development of the direct access sensor based on ACA FC assembly yielded distinctive results in terms of the process required to get reliable ACA interconnect while sealing off the area between chip and substrate. From investigation carried out in Chapter 3, it was concluded that a small footprint of ACA could be dispensed for good alignment of chip to

substrate before bonding to achieve reliable interconnection of the DAS. It showed that the dispense pattern provided a good seal between chip and substrate area. The work showed that the large contact area and the amount of adhesive have an impact on the longevity of the sensor attachment. A preliminary capsule packaging carried out showed that the packaging of the die in the capsule did not affect either the sensor or interconnect functionality.

2. Chapter 4 looked into the mechanical reliability of the ACA joint in a DAS during insertion into the capsule. For a particular chip and substrate design, the study showed that the 23mm diameter capsule would be the smallest suitable capsule for insertion without any deleterious consequences on the joint. The cross-sectional analysis suggested that the stress was high close to the edge of the window and that the stress was built up in the epoxy from where it was released by die cracking and pad lift off. It also showed that there was sufficient adhesion between the ACA and the substrate and that the ACA contacts formed a strong joint that was able to withstand the -6N required to secure the final sensor assembly in place before encapsulation.

3. Chapter 5 studied the electrical characterization of the ACA joint of a DAS in a fluid environment and found the leakage current in both dry and soaked environment. The study showed that the average response of the ACA leakage current measured in a dried sample was in the range of 100pA with an average conductance of around $2.4604 \times 10^{-11} \Omega^{-1}$. In comparison the average leakage current measured in the device (substrate and the ACA) after 1hr soak was in the range of 100nA in all the solution. The rate of change of conductance during the 4hr soak was not constant and therefore confirmed the ionic contribution to the measured leakage current in different solutions. This study showed that

the measured leakage current after soak was around 100nA – including the noise and was much lower than the current measured during the electrochemistry. Thus it was concluded that leakage through the ACA would not have any effect on the electrochemical measurements.

4. Reliability of the ACA joint in a DAS was studied under constant humidity aging and in-vitro aging in gut fluids in Chapter 6. A constant humidity study showed that the slow increase in resistance in the failed joint was attributed to the fatigue like process induced by the removal and replacement of the sample in the humidity chamber. Failure analysis showed that the constant movement of the sample in and out of the chamber for room temperature testing caused a thermal strain of 0.004 and a hygroscopic strain of 0.0052 resulting in swelling and shrinking of the adhesive and thus causing a crack to initiate and propagate along the die-epoxy interface. The *in-vitro* study showed that the combination of the acidity and the temperature had accelerated the degradation of the contact joint. The daisy chain *in-vitro* study at 37°C study showed that a contact joint positioned at around 1mm would survive the GI fluids and would be able to provide a reliable contact during the entire 72hr of the GI transit time. Failure analysis showed that delamination of the epoxy from the chip interface and the bump delamination were the main failure modes of the contact joint in the *in-vitro* test.

5. The final capsule integration described in Chapter 7 was made possible by the modular flexible prototype which contained the sensor part and the analogue circuitry for signal conditioning and communications. The ACA interconnect process was successfully transferred to the modular test board and a reliable sensor interconnection was obtained. Battery integration was successfully achieved using silver epoxy as the conductive medium between the battery and the corresponding connection pads. The battery drainage was

prevented by connecting the enable to the ground of the battery while the V_{in} was left open. The capsule integration was accomplished by placing a cured serpentine form into a glycerine capsule and encapsulating with silicone. Unfortunately, a larger 22mm diameter capsule had to be used due to a width increase produced by the flex polyimide core during the serpentine fold. The final fully integrated capsule measured 22mm x 45mm. The encapsulated assembly battery test showed that it could survive the encapsulation procedure and could still provide sufficient power for the proper functioning of the capsule during the GI transit. The encapsulated assembly subjected to soak test showed that the electronics and the battery were well protected by silicone encapsulation as none of them showed any sign of corrosion during the 72hr test.

One of the major issues with an industrial driven project is that there are too many areas to focus on and lack of sufficient manpower can cause problems in yield and the final success.

8.2. Future work

Based on the current work, further work can be carried out in the following areas:

1. First further miniaturization of the capsule could be considered. This could be achieved by:
 - a. Omitting the coverlay on the flexible polyimide core might make the flexible polyimide core even more flexible so that it will be able to bend more and thus not add to the overall diameter of the capsule.
 - b. In addition to omitting the coverlay, moving the flexible polyimide to the inner perimeter of the circular PCB discs as shown in Figure 8.1 will further reduce the width of the capsule.

- c. Replace the existing battery with a smaller size battery so that overall length could be reduced.

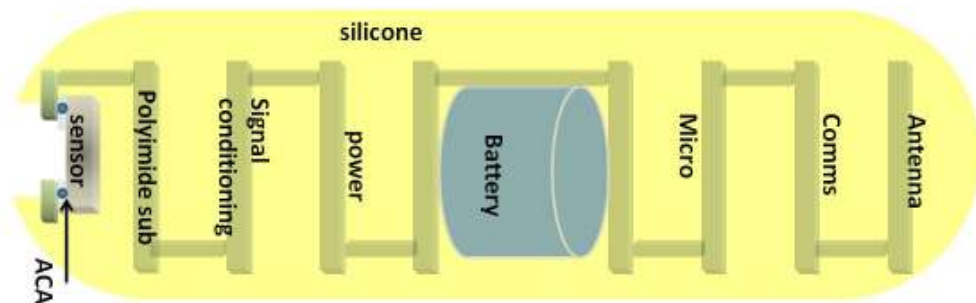


Figure 8.1. Schematic of improved modular test board.

2. After miniaturization of the first step, the second step would be to mould the electronics and the sensor in a biocompatible material such as Polyether Ether Ketone (PEEK). PEEK is a hard shell material and is highly chemical resistant. This would be the route to go if the capsule was to be commercialized. Figure 8.2, shows a schematic of the two part assembly that could be used if a pre-moulded PEEK capsule was used. The first part of the assembly could contain the sensor part which could be integrated into the one of the PEEK moulds where there could be a window provided for sensor access. The second part of the assembly could contain the battery and the RF part and could be integrated into the other PEEK mould. It could be noticed that a battery holder could be integrated into the design so that the battery could be slotted in at the last minute before setting the test. These two parts of the assemblies could be connected via board mount flat flexible cables. Once again this connection could be established once the battery was placed into the assembly. The two parts could be simply screwed together with a silicone O-ring to provide hermiticity to the capsule.

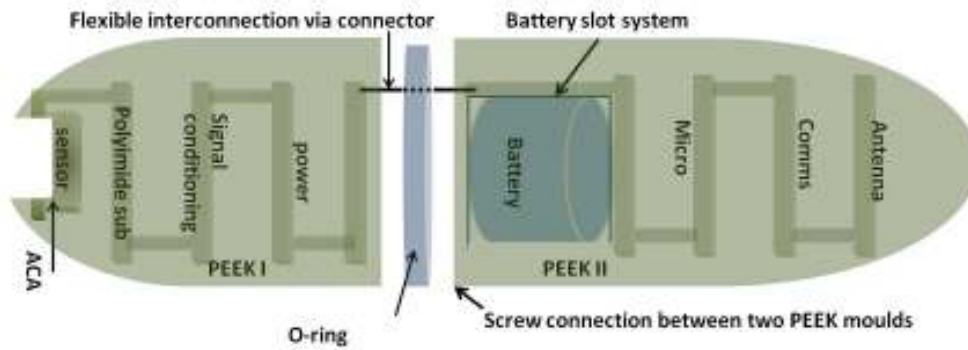


Figure 8.2. Schematic of capsule for commercialization route.

3. Further biocompatibility study of the ACA has to be carried out to qualify the material for a biomedical environment.

If the ACA used in this thesis was deemed not biocompatible, then Parylene could be considered as a coating option on top of the ACA material to render the final product biocompatible.

Appendix A1: Initial capsule packaging solution - design selection

This appendix describes the initial proposed packaging solutions for a DAS capsule integration. Three different board layout and capsule integration methods were considered.

Figure A1.1 depicts one of the packaging solutions that was considered. In this design, wirebond was considered as the first level interconnection of the sensor to the PCB. The sensor PCB interface would be connected to the battery, positioned at the far end of the capsule assembly, via stacked PCBs. The communication between the stacked PCBs could be achieved via the edge connectors placed at the sensor interface and at the battery interface.

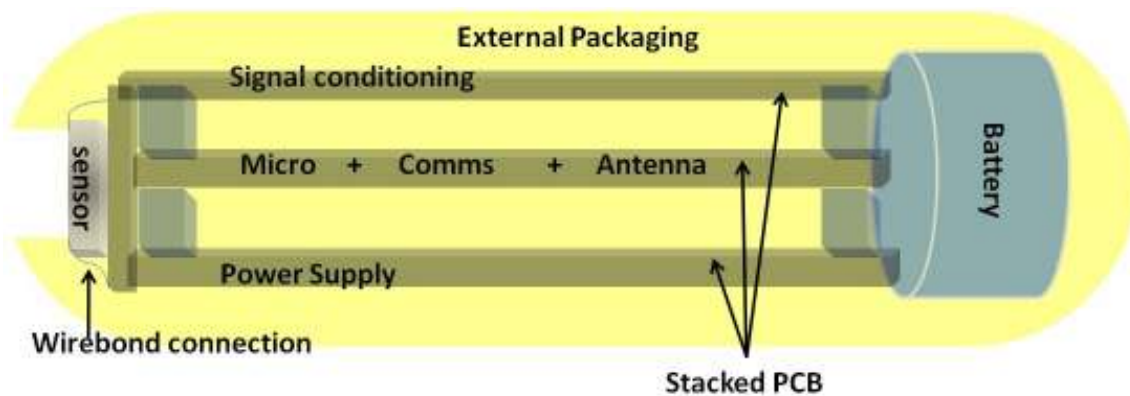


Figure A1.1. Schematic of solution 1 – Stacked PCB model.

Figures A1.2(a) and (b) show the schematic of another design that was considered. In this design the circular PCB modules would be interconnected via single pin connectors. Wire bond - Figure A1.2(a) or Flip chip - Figure A1.2(b) methods were considered for the first level packaging of the

sensor to the circular PCB. The battery positioning was envisioned to be at the far end of the capsule assembly.

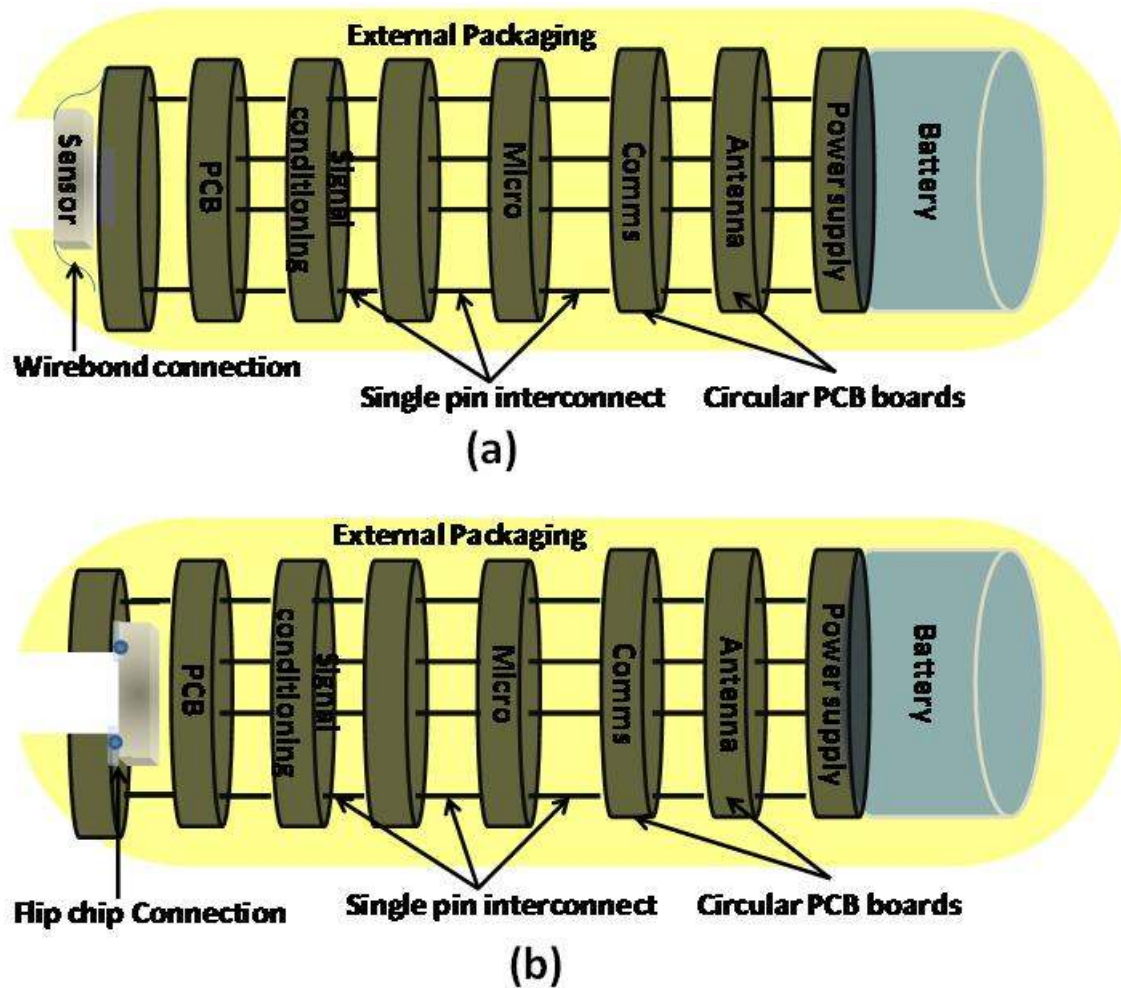


Figure A1.2. Schematic of packaging solution II: (a) wire bonded and (b) Flip chip version.

Figures A1.3(a) and (b) show the schematics of the last design that was considered. In this design the circular flex modules would be interconnected via flexible polyimide core. Wire bond and Flip chip methods were again considered as options for the first level packaging of the sensor to the circular flex. Again the battery positioning was envisioned to be at the far end of the capsule assembly.

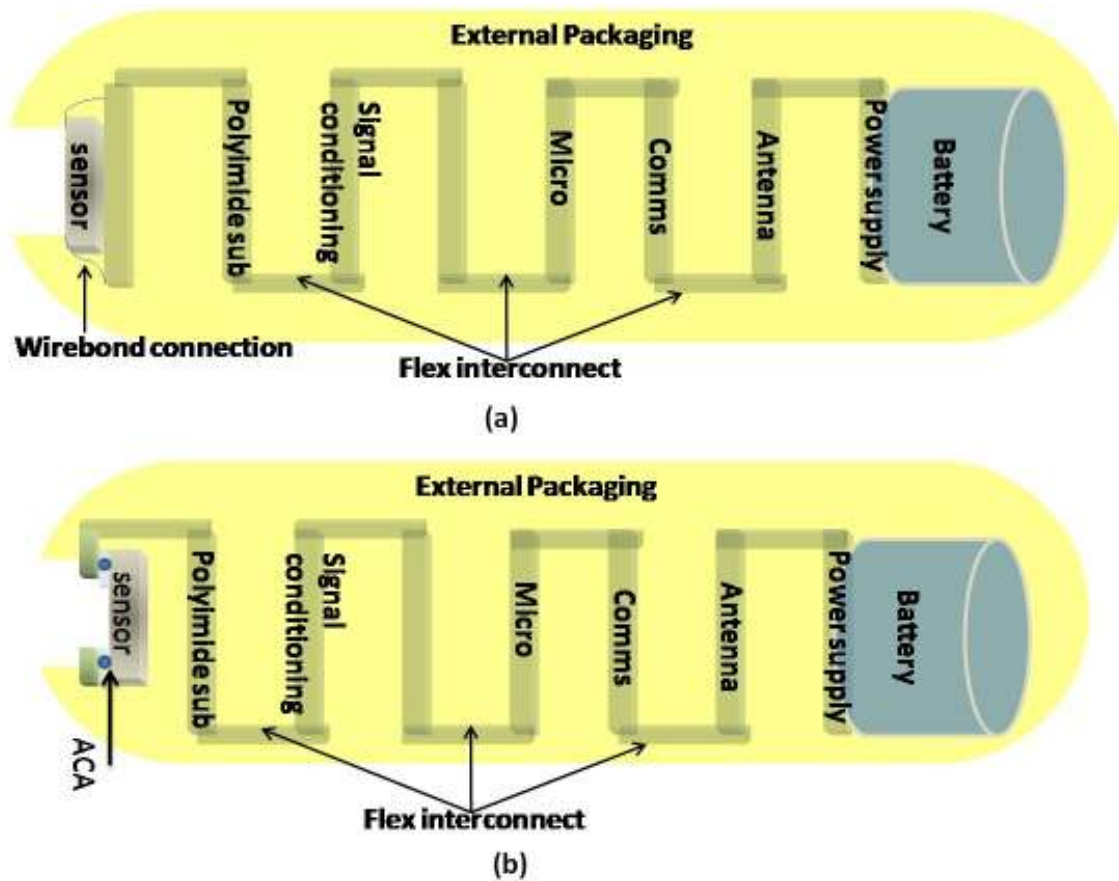


Figure A1.3. Schematic of packaging solution III (a) wire bonded and (b) Flip chip version.

As described in Chapter 2, FC technology was chosen to carry out the DAS interconnection. Therefore, all the wire bonded versions were discarded during the final selection of the design process. In addition 0.1mm clearance [177] required for each pin could ultimately result in an increased PCB size. Accordingly the final system will be developed on a flex system and FC technology will be used to achieve the DAS.

Appendix A2: Window selection

The FCTC test chip is a 5mm x 5mm die with a thickness of 525mm which is smaller than the 6mm x 6mm chip described in Chapter 3. Therefore the selection of the window should be carried out accordingly. A 6mm x 6mm chip has a window of 4.4mm x 4.4mm; accordingly a chip of 5mm x 5mm should have a window of 3.66mm x 3.66mm as shown in Figure A2.1.

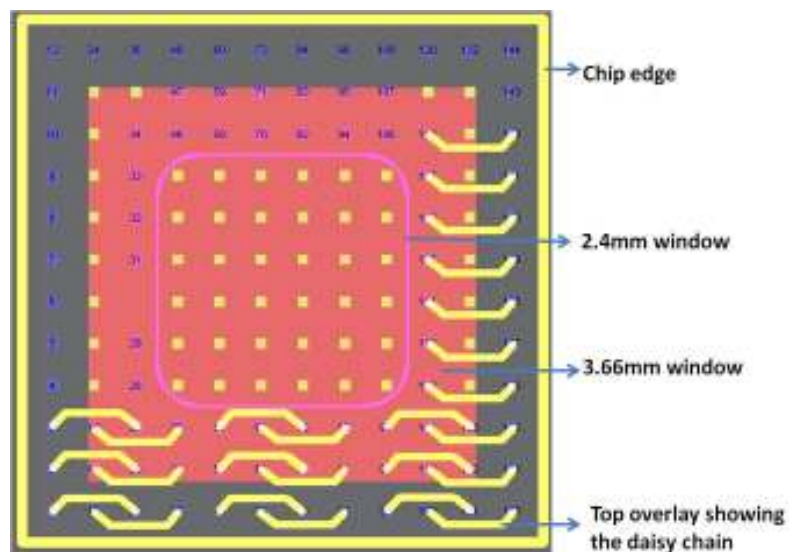


Figure A2.1. Protel design window for 5mm x 5mm chip.

As shown in Figure A2.1, a 3.6mm x 3.6mm window, shown in red, would nearly fill the whole area of the chip and might not be able to provide any information about the different horizontal and vertical daisy chains. As a consequence, the 3.66mm window was not chosen for the FCTC substrate. If a smaller window was to be chosen and which is half the size of 3.66mm x 3.66mm, then the window for a 5mm x 5mm will be 1.83mm x 1.83mm as shown in Figure A2.2.

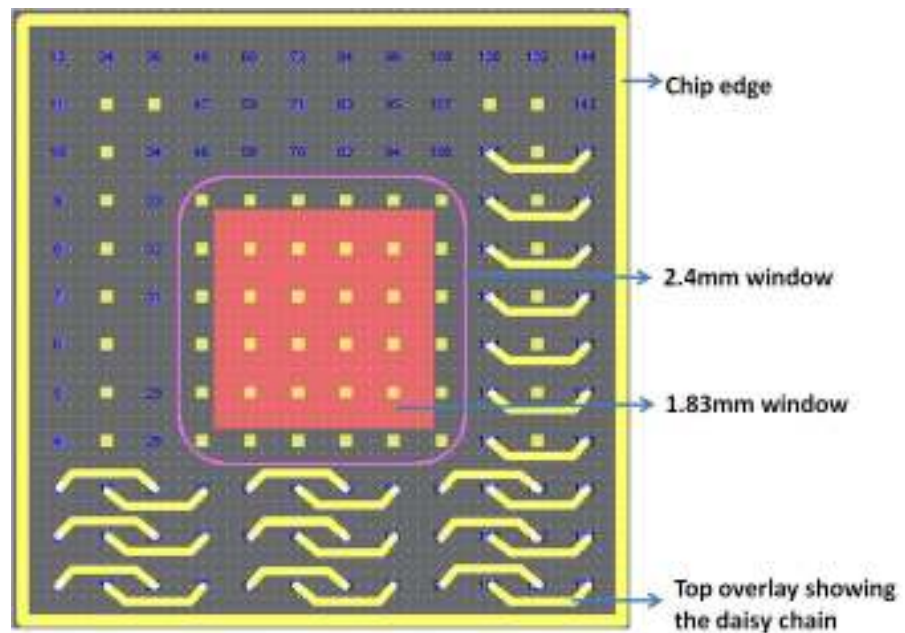


Figure A2.2. 1.83mm window for 5mm x 5mm chip.

The potential issue in choosing such a small window will be routing the electrical connection to the inner most daisy chains. Consequently the 1.83mm window was discarded. And as shown in Figure A2.2, in pink, the 2.4mm was chosen as this will help provide information about the position of the horizontal daisy chains as well as the vertical daisy chain during testing.

References

- [1] M. Ventura, F. Turrone, C. Canchaya, E.E. Vaughan, P.W. O'Toole, and D. van Sinderen, "Microbial diversity in the human intestine and novel insights from metagenomics", *Frontiers in bioscience: a journal and virtual library*, vol. 14, pp. 3214-3863, 2009.
- [2] K. Twomey and J. Marchesi, "Swallowable capsule technology: current perspectives and future directions", *Endoscopy*, vol. 41, pp. 357–362, 2009.
- [3] D.R. Cumming, P.A. Hammond and L. Wang, "Wireless Endoscopy: Technology and Design", *Microengineering in Biotechnology, Methods in Molecular Biology*, M.P. Hughes, and K.F. Hoettges, Ed, vol. 583, New Jersey: Springer Protocols, pp. 221-246, 2008.
- [4] Enchanted Learning, "Human Digestive System", Internet: <http://www.enchantedlearning.com/subjects/anatomy/digestive/index.shtml>, 2010 [Jan. 15, 2011].
- [5] S.I. Fox, *Human Physiology*, vol. 9, New York: McGraw-Hill, 2006.
- [6] J.J. Bray, P.A. Cragg, A.D.C. Macknight, R.G. Mills, and A.D.W. Taylor, *Lecture Notes On Human Physiology*, vol. 2, Oxford: Blackwell Science Ltd, 1990.
- [7] W. Germann, C. Stanfield, and J. Cannon, *Principles of human physiology*, vol. 2, San Francisco: Benjamin Cummings, 2005.
- [8] R. Carola, J. Harley, and C. Noback, *Human anatomy and physiology*, New York: McGraw-Hill, 1990.
- [9] R. Dettmer, "Fantastic voyage [wireless capsule endoscopes]", *IEEE Review*, vol. 51, pp. 28-32, 2005.
- [10] G. Bouma and W. Strober, "The immunological and genetic basis of inflammatory bowel disease", *Nature Reviews Immunology*, vol. 3, pp. 521-533, 2003.
- [11] J. Lennard-Jones, "Classification of inflammatory bowel disease", *Scandinavian Journal of Gastroenterology*, vol. 24, pp. 2-6, 1989.

- [12] R. Sartor, "Mechanisms of disease: pathogenesis of Crohn's disease and ulcerative colitis", *Nature Clinical Practice Gastroenterology and Hepatology*, vol. 3, pp. 390-407, 2006.
- [13] R. Xavier and D. Podolsky, "Unravelling the pathogenesis of inflammatory bowel disease", *Nature*, vol. 448, pp. 427-434, 2007.
- [14] National Digestive Diseases Information Clearinghouse (NDDIC), "A-Z List of Topics and Titles", Internet: <http://digestive.niddk.nih.gov/ddiseases/a-z.asp>, 2011 [Jan. 22, 2011].
- [15] J.O. Hunter, "Crohn's Disease", Internet: <http://www.crohns.org.uk/>, May. 1, 2009 [Jan. 22, 2011].
- [16] E.Á.D. Eulate, "Investigation of an Electronic Tongue Array for Gastro-Intestinal Disease Detection", MSc thesis, University College Cork, Ireland, 2007.
- [17] C. McCaffrey, "Development of Circuitry and Software for a Diagnostic Swallowable Capsule", MEngSc thesis, University College Cork, Ireland, 2008.
- [18] C. McCaffrey, O. Chevalerias, C. O'Mathuna, and K. Twomey, "Swallowable-capsule technology", *IEEE Pervasive Computing*, vol. 7, pp. 23-29, 2008.
- [19] G. Costamagna, S. Shah, M. Riccioni, F. Foschia, M. Mutignani, V. Perri, A. Vecchioli, M. Brizi, A. Picciocchi, and P. Marano, "A prospective trial comparing small bowel radiographs and video capsule endoscopy for suspected small bowel disease", *Gastroenterology*, vol. 123, pp. 999-1005, 2002.
- [20] J.L. Toennies, G. Tortora, M. Simi, P. Valdastrì, and R. Webster, "Swallowable medical devices for diagnosis and surgery: the state of the art", *Proceedings of the Institution of Mechanical Engineers, Part C: Journal of Mechanical Engineering Science*, vol. 224, pp. 1397-1414, 2010.
- [21] Philips, "Philips Intellicap technology", Internet: <http://www.newscenter.philips.com/main/research/news/backgrounders/2008/081111-ipill.wpd>, Nov. 11, 2008 [Jan. 24, 2011].
- [22] R. Allan, "Smart Pill Goes On A Fantastic Voyage", *Electronic Design*, vol. 54, pp. 27-66, 2006.

- [23] L. Wang, E. Johannessen, P. Hammond, L. Cui, S. Reid, J. Cooper, and D. Cumming, "A programmable microsystem using system-on-chip for real-time biotelemetry", *IEEE Transactions on Biomedical Engineering*, vol. 52, pp. 1251-1260, 2005.
- [24] J. Cooper, E. Johannessen, and D. Cumming, "Bridging the gap between micro and nanotechnology: using lab-on-a-chip to enable nanosensors for genomics, proteomics, and diagnostic screening", *Network and Parallel Computing*, vol 3222, pp. 517-521, 2004.
- [25] E.A. Johannessen, W. Lei, C. Li, T. Tong Boon, M. Ahmadian, A. Astaras, S.W.J. Reid, P.S. Yam, A.F. Murray, B.W. Flynn, S.P. Beaumont, D.R.S. Cumming, and J.M. Cooper, "Implementation of multichannel sensors for remote biomedical measurements in a microsystems format", *IEEE Transactions on Biomedical Engineering*, vol. 51, pp. 525-535, 2004.
- [26] E. Johannessen, L. Wang, S. Reid, D. Cumming, and J. Cooper, "Implementation of radiotelemetry in a lab-in-a-pill format", *Lab on a Chip*, vol. 6, pp. 39-45, 2006.
- [27] T. Tang, E. Johannessen, L. Wang, A. Astaras, M. Ahmadian, A. Murray, J. Cooper, S. Beaumont, B. Flynn, and D. Cumming, "Toward a miniature wireless integrated multisensor microsystem for industrial and biomedical applications", *IEEE Sensors Journal*, vol. 2, pp. 628-635, 2002.
- [28] E. Johannessen, L. Wang, C. Wyse, D. Cumming, and J. Cooper, "Biocompatibility of a lab-on-a-pill sensor in artificial gastrointestinal environments", *IEEE Transactions on Biomedical Engineering*, vol. 53, pp. 2333-2340, 2006.
- [29] K. Twomey and K. Murphy, "Investigation into the packaging and operation of an electronic tongue sensor for industrial applications", *Sensor Review*, vol. 26, pp. 218-226, 2006.
- [30] Z. Lai and J.Liu, "The Nordic Electronics Packaging Guideline", Internet: <http://extra.ivf.se/ngl/A-WireBonding/ChapterA.htm>, Sep. 2000 [Feb. 15, 2011].
- [31] C. Xu, "Corrosion in Microelectronics", MSc thesis, San José State University, USA, 2003.

- [32] O.K. Abiola, N.C. Oforika, and S.S. Angaye, "Corrosion behaviour of aluminium in hydrochloric acid (HCl) solution containing mercaptoacetic acid", *Materials Letters*, vol. 58, pp. 3461-3466, 2004.
- [33] G.T.A. Kovacs, *Micromachined Transducers Sourcebook*, Boston: WCB McGraw-Hill, 1998.
- [34] SmartPill Corp, "SmartPill Quick Facts", Internet:
http://www.smartpillcorp.com/index.cfm?pagepath=Products/SmartPill_Quick_Facts&id=17816, [Feb. 15, 2011].
- [35] L.A. Negron, "Ingestible capsule packaging", US Patent 7434691, 2008.
- [36] L. Sudakov-Boreysha, U. Dinnar, and Y. Nemirovsky, "New ISFET catheters encapsulation techniques for brain pH in-vivo monitoring", *11th IEEE International Conference Proceedings on Electronics, Circuits and Systems*, 2004, pp. 424-426.
- [37] R. Ramesham and R. Ghaffarian, "Challenges in interconnection and packaging of microelectromechanical systems (MEMS)", *50th Electronic Components and Technology Conference*, 2000, pp. 666-675.
- [38] M. Shaw, F. Ziglioli, C. Combi, and L. Baldo, "Package design of pressure sensors for high volume consumer applications", *58th Electronic Components and Technology Conference*, 2008, pp. 834-840.
- [39] P. Hammond, D. Ali, and D. Cumming, "Design of a single-chip pH sensor using a conventional 0.6- μ m CMOS process", *IEEE Sensors Journal*, vol. 4, pp. 706-712, 2004.
- [40] L. Chunyan, F.E. Sauser, R. Azizkhan, C.H. Ahn, and I. Papautsky, "Polymer flip-chip bonding of pressure sensors on flexible Kapton film for neonatal catheters", *17th IEEE International Conference on Micro Electro Mechanical Systems*, 2004, pp. 749-752.
- [41] F.E. Sauser, L. Chunyan, R.G. Azizkhan, C.H. Ahn, and I. Papautsky, "Pressure microsensing catheters for neonatal care", *IEEE Sensors Proceedings*, vol.3, pp. 1476-1479, 2004.
- [42] F. Campabadal, J.L. Carreras, and E. Cabruja, "Flip-chip packaging of piezoresistive pressure sensors", *Sensors and Actuators A: Physical*, vol. 132, pp. 415-419, 2006.

- [43] B. Majeed, I. Paul, K.M. Razeeb, J. Barton, and S.C. O'Mathuna, "Effect of Gold Stud Bump Topology on Reliability of Flip Chip on Flex Interconnects", *IEEE Transactions on Advanced Packaging*, vol. 30, pp. 605-615, 2007.
- [44] K. Gilleo, B. Boyes, S. Corbett, G. Larson, and D. Price, "High volume, low cost flip chip assembly on polyester flex", *Circuit World*, vol. 25, pp. 11-17, 1999.
- [45] G.B. Kromann, R.D. Gerke, and W.W.X. Huang, "A hi-density C4/CBGA interconnect technology for a CMOS microprocessor", *IEEE Transactions on Components Packaging and Manufacturing Technology Part B-Advanced Packaging*, vol. 19, pp. 166-173, Feb 1996.
- [46] J. Vähäkangas, O. Rusanen, T. Jaakola, and J. Lenkkeri, "The Nordic Electronics Packaging Guideline", Internet: <http://extra.ivf.se/ngl/B-Flip-Chip/ChapterB.htm>, Sep. 2000 [Feb. 15, 2011].
- [47] S.Y. Kang, and Y.C. Lee, "Yield modeling of MCM assembly with flip-chip thermocompression bondings", *Conference Proceedings of IEEE Multi-Chip Module*, 1992, pp. 68-71.
- [48] X.F. Ang, G.G. Zhang, B.K. Tan, J. Wei, Z. Chen, and C.C. Wong, "Direct metal to metal bonding for microsystems interconnections and integration", *7th Conference Proceedings of Electronic Packaging Technology*, 2005, pp. 390-393.
- [49] L. Cheah, Y. Tan, J. Wei, and C. Wong, "Gold to gold thermosonic flip-chip bonding", *Proceedings HDI*, 2001, pp. 165-175.
- [50] Z. Kun, J. Lei, D. Ji'an, and Z. Jianhua, "Effects of thermosonic bonding parameters on flip chip LEDs", *Conference on High Density Microsystem Design and Packaging and Component Failure Analysis*, 2006, pp. 101-107.
- [51] C. Luk, Y. Chan, and K. Hung, "Development of gold to gold interconnection flip chip bonding for chip on suspension assemblies", *Microelectronics Reliability*, vol. 42, pp. 381-389, 2002.
- [52] R. Windemuth, and T. Ishikawa, "New flipchip technology", *Conference on European Microelectronics and Packaging*, 2009, pp. 1-6.

- [53] S. Tonapi, S. Gopakumar, P. Borgesen, and K. Srihari, "Reliability of lead-free solder interconnects-a review", *Annual Proceedings on Reliability and Maintainability Symposium*, 2002, pp. 423-428.
- [54] Z. Zhong, "Assembly and reliability of flip chip on boards using ACAs or eutectic solder with underfill", *Microelectronics International*, vol. 16, pp. 6-14, 1999.
- [55] H. Shang, J. Goa, P. Nicholson, C. Forrest, and S. Kenny, "Thermal performance of lead-free microelectronic BGA package with defects", *17th World Conference on Nondestructive Testing*, 2008, pp. 1-10.
- [56] J.C.C. Lo, S.W.R. Lee, H.H.L. Wu, and J.K.S. Lam, "Determination of solder bump stand-off height in a flip-chip sub-mount for Micro-Opto-Electro-Mechanical System (MOEMS) packaging applications", *58th Conference on Electronic Components and Technology*, 2008, pp. 1887-1892.
- [57] H.H. Oppermann, M. Hutter, G. Engelmann, and H. Reichl, "Passive alignment flip chip assembly using surface tension of liquid solder and micromechanical stops", *SPIE Proceedings*, 2005, pp. 19-25.
- [58] Z. Zhuqing, and C.P. Wong, "Recent advances in flip-chip underfill: materials, process, and reliability", *IEEE Transactions on Advanced Packaging*, vol. 27, pp. 515-524, 2004.
- [59] N.-C. Lee, *Reflow soldering processes and troubleshooting: SMT, BGA, CSP, and flip chip technologies*, Woburn: Butterworth Heinemann, 2002.
- [60] R. Nagel, "Adhesive Based Flip-Chip Assembly", MEngSc, University College Cork, Ireland, 1996.
- [61] L. Li, and J.E. Morris, "An Introduction To Electrically Conductive Adhesives", *Int J Microelectrocnics Packaging*, vol. 1, pp. 159-175, 1998.
- [62] H. Kristiansen, and J. Liu, "Overview of conductive adhesive interconnection technologies for LCDs", *IEEE Transactions on Components, Packaging, and Manufacturing Technology, Part A*, vol. 21, pp. 208-214, 1998.

- [63] J. Liu, Z. Lai, H. Kristiansen, and C. Khoo, "Overview of conductive adhesive joining technology in electronics packaging applications", *3rd International Conference Proceedings on Adhesive Joining and Coating Technology in Electronics Manufacturing*, Sep 1998, pp. 1-18.
- [64] A. Berduque, "Characterisation of packaged microelectrode devices for sensor applications", MSc thesis, University College Cork, Ireland, 2003.
- [65] J.E. Morris, L. Jeahuck, and J. Liu, "Isotropic Conductive Adhesive Interconnect Technology in Electronics Packaging Applications", *5th International Conference on Polymers and Adhesives in Microelectronics and Photonics, polytronic*, 2005, pp. 45-52.
- [66] Y. Lin and J. Zhong, "A review of the influencing factors on anisotropic conductive adhesives joining technology in electrical applications", *Journal of Materials Science*, vol. 43, pp. 3072-3093, 2008.
- [67] R. Tummala, *Fundamentals of microsystems packaging*, New York: McGraw-Hill Professional, 2001.
- [68] J. Liu, "ACA bonding technology for low cost electronics packaging applications—current status and remaining challenges", *Soldering & Surface Mount Technology*, vol. 13, pp. 39-57, 2001.
- [69] J. Liu, Y. Wang, J. Morris, and H. Kristiansen, "Development of ontology for the anisotropic conductive adhesive interconnect technology in electronics applications", *International Symposium Proceedings on Advanced Packaging Materials: Processes, Properties and Interfaces*, 2005, pp. 193-208.
- [70] M. Yim, and K. Paik, "Design and Understanding of Anisotropic Conductive Films(ACF's) for LCD Packaging", *IEEE Transactions on Components, Packaging, and Manufacturing Technology*, vol. 21, pp. 226-234, 1998.
- [71] L. Frisk, and K. Kokko, "The effects of chip and substrate thickness on the reliability of ACA bonded flip chip joints", *Soldering & Surface Mount Technology*, vol. 18, pp. 28-37, 2006.

- [72] Y. Fu, Y. Wang, X. Wang, J. Liu, Z. Lai, G. Chen, and M. Willander, "Experimental and theoretical characterization of electrical contact in anisotropically conductive adhesive", *IEEE Transactions on Advanced Packaging*, vol. 23, pp. 15-21, 2000.
- [73] Y.C. Chan, and D.Y. Luk, "Effects of bonding parameters on the reliability performance of anisotropic conductive adhesive interconnects for flip-chip-on-flex packages assembly I. Different bonding temperature", *Microelectronics Reliability*, vol. 42, pp. 1185-1194, 2002.
- [74] K. Gustafsson, S. Mannan, J. Liu, Z. Lai, D. Whalley, and D. Williams, "The effect of temperature ramp rate on flip-chip joint quality and reliability using anisotropically conductive adhesive on FR-4 substrate", *47th Electronic Components and Technology Conference*, 1997, pp. 561-566.
- [75] R. Aschenbrenner, R. Miessner, and H. Reichl, "Adhesive flip chip bonding on flexible substrates", *Journal of Electronics Manufacturing*, vol. 7, pp. 245-252, 1997.
- [76] T.A. Min, S.P.S. Lim, A. Yeo, and C. Lee, "Influence of bump geometry, adhesives and pad finishings on the joint resistance of Au bump and A/NCA flip chip interconnection", in *7th Electronic Packaging Technology Conference*, 2005, pp. 797-801.
- [77] C. Wong, Y. Li, and D. Lu, *Electrical Conductive Adhesives with Nanotechnologies*, New York: Springer Verlag, 2009.
- [78] R.D. Pendse, K. Kyung-Moon, and S. Tam, "A new flip chip packaging technology for the mid-range application space", *52nd Conference Proceedings of Electronic Components and Technology*, 2002, pp. 100-104.
- [79] C.L. Chuang, J.N. Aoh, Q.A.Liao, S.J. Liao, and G.S. Huang, "Feasibility and bonding strength for gold stud bumps thermosonic flip-chip onto flex substrates with nonconductive pastes", *International Conference on Electronic Materials and Packaging*, 2008, pp. 208-211.
- [80] Y. Lin, X. Chen, H. Zhang, and Z. Wang, "Effects of hygrothermal aging on epoxy-based anisotropic conductive film", *Materials Letters*, vol. 60, pp. 2958-2963, 2006.

- [81] A. Seppälä, and E. Ristolainen, "Study of adhesive flip chip bonding process and failure mechanisms of ACA joints", *Microelectronics Reliability*, vol. 44, pp. 639-648, 2004.
- [82] A.C. Tan, *Lead Finishing in semiconductor Devices: Soldering*, London: World Scientific Publishing Co. Pte. Ltd, 1989.
- [83] efunda, Inc., "Solders:guidelines", Internet:
<http://www.efunda.com/materials/solders/guidelines.cfm>, 2011 [Jan. 21, 2011].
- [84] T. Korhonen, P. Su, S. Hong, M. Korhonen, and C. Li, "Development of under bump metallizations for flip chip bonding to organic substrates", *Journal of Electronic Materials*, vol. 28, pp. 1146-1149, 1999.
- [85] efunda, Inc., "Solderability", Internet:
http://www.efunda.com/materials/solders/solderability.cfm?search_string=solderability, 2011 [Jan. 21, 2011].
- [86] R.B. Palmer, and S.D. Phillips, "Epoxides and Epoxy Resins", *Medical Toxicology*, Third edition, R.C. Dart, Ed, Philadelphia: Lippincott Williams & Wilkins, pp. 1369-1375, 2003.
- [87] I.B. Kang, M.R. Haskard, and B.K. Ju, "Assembly and interconnection technology for micromechanical structures using anisotropic conductive film", *SPIE Proceedings*, 1996, pp. 280-287.
- [88] Henkel, "Electronic Solutions", Internet:
http://www.loctite.hu/huu/content_data/54816_0802_Electronics.pdf, Jan. 2008 [Aug. 16, 2011].
- [89] C. Connolly, "Adhesives in electronic and electrical assembly", *Assembly Automation*, vol. 28, pp. 289-294, 2008.
- [90] Image J, "Image J, version 1.44h", Internet: <http://rsbweb.nih.gov/ij/download.html>, [Sep. 24, 2010].

- [91] A. West, C. Hinde, C. Messom, R. Harrison, and D. Williams, "Design issues associated with neural network systems applied within the electronics manufacturing domain", *Journal of Electronics Manufacturing*, vol. 10, pp. 19-48, 2000.
- [92] A. West, D. Williams, C. Hinde, and C. Messom, "A Benchmark of Intelligent Control Techniques for Surface Mount Technology (SMT) Adhesive Dispensing: Process Overview and the Application of a Structured Neural Network Controller", *Proceedings of ASME Winter Meeting, Manufacturing Aspects of Electronic Packaging*, vol. 65, pp. 107-118, 1993.
- [93] G. Deng, H. Cui, Q. Peng, and J. Zhong, "Experiment study influences of some process parameters on dispensing dots consistency in contact dispensing process", *Conference on High Density Microsystem Design and Packaging and Component Failure Analysis*, 2005, pp. 1-7.
- [94] D.C. Montgomery, G.C. Runger, and N.F. Hubele, *Engineering Statistics*, New Jersey: John Wiley & Sons Inc., 1997.
- [95] ReliaSoft Corporation, "Reliability Engineering Resources - Experiment Design and Analysis Reference", Internet:
http://www.weibull.com/doewebcontents.htm#Statistical_Background, Jan. 2011, [Jun. 17, 2011].
- [96] M. Levy, "STA 2023 - Basics of Hypothesis Testing - Section 8-2", Internet:
<http://www1.broward.edu/~mlevy/Sta/handouts/Section-8-2-Basics-of-Hypothesis-Testing.pdf>, Jan. 2011 [Jun. 15, 2011].
- [97] Minitab Inc., "Minitab 15", Internet : <http://www.minitab.com/en-IE/products/minitab/default.aspx>, Jan. 2009 [Aug. 21, 2009].
- [98] W.S. Kwon, H.J. Kim, K.W. Paik, S.Y. Jang, and S.M. Hong, "Mechanical Reliability and Bump Degradation of ACF Flip Chip Packages Using BCB (Cyclotene™) Bumping Dielectrics Under Temperature Cycling", *Transaction of ASME Journal of Electronic Packaging*, vol. 126, pp. 202-207, 2004.

- [99] United States of America, Department of Defence, " Test Method Standard Microcircuits", Internet: <http://www.aspentechologies.com/files/rur89tn69a.pdf>, Feb. 2006 [Jan. 15, 2010].
- [100] W.Q. Meeker, and L.A. Escobar, "Pitfalls of accelerated testing", *IEEE Transactions on Reliability*, vol. 47, pp. 114-118, 1998.
- [101] E. Suhir, "Accelerated life testing in microelectronics and photonics, its role, attributes, challenges, pitfalls, and its interaction with qualification tests", *2nd International IEEE Conference on Polymers and Adhesives in Microelectronics and Photonics*, 2002, pp. 44-48.
- [102] R. Islam, Y. Chan, and B. Ralph, "Effect of drop impact energy on contact resistance of anisotropic conductive adhesive film joints", *Journal of Materials Research*, vol. 19, pp. 1662-1668, 2004.
- [103] C. Tan, Y. Chan, and N. Yeung, "Effect of autoclave test on anisotropic conductive joints", *Microelectronics Reliability*, vol. 43, pp. 279-285, 2003.
- [104] G.A. Aitchison, G.S. Walker, I.A. Jones, and C.D. Rudd, "Modeling changes in the modulus of poly(ϵ -caprolactone) due to hydrolysis and plasticization", *Journal of Applied Polymer Science*, vol. 107, pp. 3484-3490, 2008.
- [105] S. Choi, and E.P. Douglas, "Complex Hygrothermal Effects on the Glass Transition of an Epoxy-Amine Thermoset", *ACS Applied Materials & Interfaces*, vol. 2, pp. 934-941, 2010.
- [106] T. Ferguson, and J. Qu, "The Effect of Moisture on the Adhesion and Fracture of Interfaces in Microelectronic Packaging", *Micro- and Opto-Electronic Materials and Structures: Physics, Mechanics, Design, Reliability, Packaging*, E. Suhir, Y.C. Lee, and C.P. Wong, Eds, New York: Springer, 2007, pp. B431-B471.
- [107] G. Xian, and V.M. Karbhari, "DMTA based investigation of hygrothermal ageing of an epoxy system used in rehabilitation", *Journal of Applied Polymer Science*, vol. 104, pp. 1084-1094, 2007.

- [108] Clariant Corporation, "AZ 9200 Thick Film photoresist", Internet:
http://cmi.epfl.ch/photo/photo_process/files/Data_AZ9200.pdf, [Feb. 21, 2009].
- [109] M. Rizvi, Y. Chan, C. Bailey, and H. Lu, "Study of anisotropic conductive adhesive joint behavior under 3-point bending", *Microelectronics and Reliability*, vol. 45, pp. 589-596, 2005.
- [110] M.C. Yip, C.Y.Huang, C.L. Chen, and S.T. Lu, "Bending and Reliability Test of Chip-on-flex (COF) Assembly Using Anisotropic Conductive Films (ACFs)", *8th International Conference on Electronic Packaging Technology*, 2007, pp. 1-3.
- [111] B.I. Noh, J.W. Yoon, J.W. Kim, J. B. Lee, N.C. Park, W.S. Hong, and S.B. Jung, "Reliability of Au bump flip chip packages with adhesive materials using four-point bending test", *International Journal of Adhesion and Adhesives*, vol. 29, pp. 650-655, 2009.
- [112] S.T. Lu, and W.H. Chen, "Reliability of ultra-thin chip-on-flex (UTCOF) with anisotropic conductive adhesive (ACA) joints", *58th Electronic Components and Technology Conference*, 2008, pp. 1287-1293.
- [113] S.T. Lu, and W.H. Chen, "Reliability and Flexibility of Ultra-Thin Chip-on-Flex (UTCOF) Interconnects With Anisotropic Conductive Adhesive (ACA) Joints", *IEEE Transactions on Advanced Packaging*, vol. 33, pp. 702-712, 2010.
- [114] X.H. Cai, B. An, X.W. Lai, Y.P. Wu, and F.S. Wu, "Reliability Evaluation on Flexible RFID Tag Inlay Packaged by Anisotropic Conductive Adhesive", *8th International Conference on Electronic Packaging Technology, ICEPT*, 14-17 Aug 2007, pp. 1-4.
- [115] B. An, X.H. Cai, H.B. Chu, X.W. Lai, F.S. Wu, and Y.P. Wu, "Flex Reliability of RFID Inlays Assembled by Anisotropic Conductive Adhesive", *International Symposium on High Density packaging and Microsystem Integration*, pp. 1-4, 26-28 June 2007.
- [116] Z. Lai, R. Lai, K. Persson, and J. Liu, "Effect of bump height on the reliability of ACA flip chip joining with FR4 rigid and polyimide flexible substrate", *Journal of Electronics Manufacturing*, vol. 8, pp.217-224, 1998.

- [117] D.Y.R. Chong, W.E. Lee, B.K. Lim, J.H.L. Pang, and T.H. Low, "Mechanical characterization in failure strength of silicon dice", *The Ninth Intersociety Conference on Thermal and Thermomechanical Phenomena in Electronic Systems*, 2004, vol.2, pp. 203-210.
- [118] H. Merchant, M. Minor, and Y. Liu, "Mechanical fatigue of thin copper foil", *Journal of Electronic Materials*, vol. 28, pp. 998-1007, 1999.
- [119] A. Hadrboletz, B. Weiss, and G. Khatibi, "Fatigue and fracture properties of thin metallic foils", *International Journal of fracture*, pp. 69-89, 2001.
- [120] Wolfram Alpha LLC – A Wolfram Research Company, "Ni resistivity", Internet: http://www.wolframalpha.com/input/?i=nickel+resistivity&lk=1&a=ClashPrefs_*Element.Nickel.ElementProperty.Resistivity-, Feb. 2010 [Mar. 03, 2011].
- [121] C. Wu, J. Liu, and N. Yeung, "The effects of bump height on the reliability of ACF in flip-chip", *Soldering & Surface Mount Technology*, vol. 13, pp. 25-30, 2001.
- [122] Dupont, "DuPont™ Pyralux® AP flexible circuit materials", Internet: http://www2.dupont.com/Pyralux/en_US/assets/downloads/pdf/APclad_H-73241.pdf, Dec. 2009 [May. 10, 2010].
- [123] N.R. Basavanahally, D.D. Chang, B. Cranston, and S.G. Segar Jr, "Direct chip interconnect with adhesive conductor films", *IEEE Transactions on Components, Hybrids, and Manufacturing Technology*, vol. 15, pp. 972-976, 1992.
- [124] N. Kumbhat, A. Choudhury, M. Raine, G. Mehrotra, P.M. Raj, R. Zhang, K.S. Moon, R. Chatterjee, V. Sundaram, G. Meyer-Berg, C.P. Wong, and R. Tummala, "Highly-reliable, 30µm pitch copper interconnects using nano-ACF/NCF", *Electronic Components and Technology Conference*, 2009, pp. 1479-1485.
- [125] L. Frisk and K. Kokko, "Effect of RCC on the reliability of adhesive flip chip joints", *Journal of Electronic Packaging - Transactions of the ASME*, vol. 129, pp. 260-265, 2007.

- [126] K. Kokko, H. Harjunpää, A.M. Haltia, P. Heino, and M. Kellomäki, "Effects of conformal coating on anisotropically conductive adhesive joints; a medical perspective", *Soldering & Surface Mount Technology*, vol. 21, pp. 4-11, 2009.
- [127] D.D. Chang, J.A. Fulton, H.C. Ling, M.B. Schmidt, R.E. Sinitski, and C.P. Wong, "Accelerated life test of Z-axis conductive adhesives", *IEEE Transactions on Components, Hybrids, and Manufacturing Technology*, vol. 16, pp. 836-842, 1993.
- [128] B. Wunderle, R. Dudek, B. Michel, and H. Reichl, "Thermo-mechanical reliability of power flip-chip cooling concepts", *54th Electronic Components and Technology Conference*, 2004, vol.1, pp. 427-436.
- [129] K. Saarinen, and P. Heino, "Moisture effects on reliability of non-conductive adhesive attachments", *2nd IEEE International Interdisciplinary Conference on Portable Information Devices, and 7th IEEE Conference on Polymers and Adhesives in Microelectronics and Photonics*, 2008, pp. 1-6.
- [130] M. Tsai, C. Wu, C. Huang, and S. Yang, "Transient Stress Distributions in NCF-Bonded COG Packages due to Moisture Diffusion", *IEEE Transactions on Advanced Packaging*, vol. 31, pp. 454-462, 2008.
- [131] A.Teverovsky, "A rapid technique for moisture diffusion characterization of molding compounds in PEMs", *NEPP Report, GSFC*, pp. 1-18, 2002.
- [132] X. J. Fan, S. W. R. Lee, and Q. Han, "Experimental investigations and model study of moisture behaviors in polymeric materials", *Microelectronics Reliability*, vol. 49, pp. 861-871, 2009.
- [133] J.L. Abot, A. Yasmin, and I. M. Daniel, "Hygroscopic behavior of woven fabric carbon-epoxy composites", *Journal of reinforced plastics and Composites*, vol. 24, pp. 195-207, 2005.
- [134] Q. Yuan, C. Shi, G. De Schutter, and K. Audenaert "Effect of temperature on transport of chloride ions in concrete", *2nd International Conference on Concrete Repair, Rehabilitation and Retrofitting (ICCRRR)*, 2008, pp. 150-160.

- [135] C. Yin, H. Lu, C. Bailey, and Y. Chan, "Macro-micro modelling of moisture induced stresses in an ACF flip chip assembly", *Soldering & Surface Mount Technology*, vol. 18, pp. 27-32, 2006.
- [136] Henkel, "Hysol FP5300 technical data sheet", Internet:
[https://tds.us.henkel.com/NA/UT/HNAUTTDS.nsf/web/2C56D8C5F665D652852578680047BF9A/\\$File/FP300-EN.pdf](https://tds.us.henkel.com/NA/UT/HNAUTTDS.nsf/web/2C56D8C5F665D652852578680047BF9A/$File/FP300-EN.pdf), Jun. 2009 [May. 10, 2011].
- [137] A.Teverovsky, "Chlorine contamination diffusion in silicones", *EEE LINKS*, NASA, pp. 1-5, 1999.
- [138] E. Dermitzaki, B. Wunderle, J. Bauer, H. Walter, and B. Michel, "Structure Property Correlation of epoxy resins under the influence of moisture and temperature; and comparison of Diffusion coefficient with MD-simulations", *Electronics System Integration Technology Conferenc, ESTC*, 2008, pp. 897-902.
- [139] M.J. Adamson, "Thermal expansion and swelling of cured epoxy resin used in graphite/epoxy composite materials", *Journal of Materials Science*, vol. 15, pp. 1736-1745, 1980.
- [140] C. Soles and A. Yee, "A discussion of the molecular mechanisms of moisture transport in epoxy resins", *Journal of Polymer Science Part B: Polymer Physics*, vol. 38, pp. 792-802, 2000.
- [141] M. Liu, P. Wu, Y. Ding, and S. Li, "Study on diffusion behavior of water in epoxy resins cured by active ester", *Physical Chemistry Chemical Physics*, vol. 5, pp. 1848-1852, 2003.
- [142] T.K. Lin, "Defect Model and the Current-Voltage Characteristics in Dielectric Thin Films", *Chinese Journal of Physics*, vol. 27, pp. 351-369, 1990.
- [143] S.B.Lyon, L.Philippe, and E.Tsuosoglou, "Direct measurements of ionic diffusion in protective organic coatings", *Transactions-Institute of Metal Finishing*, vol. 84, pp. 23-27, 2006.
- [144] L.Philippe, S.B.Lyon, C.Sammon, and J.Yarwood, "In situ study of phosphate diffusion in epoxy coatings using attenuated total reflection infrared spectroscopy", *Corrosion engineering, science and technology*, vol. 38, pp. 153-156, 2003.

- [145] J.Lizarazo-Marriaga, and P.Claissse, "Determination of the concrete chloride diffusion coefficient based on an electrochemical test and an optimization model", *Materials Chemistry and Physics*, vol. 117, Issues 2-3, pp. 536-543, 2009.
- [146] W.Grover Coors, " Co-Ionic Conduction in Protonic Ceramics of the Solid Solution, $BaCe_{(x)}Zr_{(yx)}Y_{(1-y)}O_{3-\delta}$ Part II: Co-Ionic Conduction", *Advances in Ceramics - Synthesis and Characterization, Processing and Specific Applications*, Prof. Costas Sikalidis (Ed.), ISBN: 978-953-307-505-1, InTech, 2011, pp. 501-521.
- [147] I.Sekine, M.Yuasa, N.Hirose, and T. Tanaki, "Degradation evaluation of corrosion protective coatings by electrochemical, physicochemical and physical measurements", *Progress in Organic Coatings*, vol. 45, Issue 1, pp. 1-13, 2002.
- [148] P.Vanysek, "Ionic conductivity and diffusion at infinite dilution", *CRC Handbook of Chemistry and Physics*, D.R.Lide, 83rd ed., CRC Press, 2003-2004, pp 95-98.
- [149] Faraday Constant, "Faraday Constant value", Internet:
<http://www.avogadro.co.uk/definitions/faraday.htm>, Oct. 2010 [June. 02, 2011].
- [150] P.Halamickova, and R.J.Detwiler, " Water permeability and chloride ion diffusion in Portland cement mortars: relationship to sand content and critical pore diameter", *Cement and Concrete Research*, vol. 25, pp. 790-802, 1995.
- [151] L.L. Mercado, J. White, V. Sarihan, and T.Y.T. Lee, "Failure mechanism study of anisotropic conductive film (ACF) packages", *IEEE Transactions on Components and Packaging Technologies*, vol. 26, pp. 509-516, 2003.
- [152] L.K. Teh, M. Teo, E. Anto, C.C. Wong, S.G. Mhaisalkar, P.S. Teo, and E.H. Wong, "Moisture-induced failures of adhesive flip chip interconnects", *IEEE Transactions on Components and Packaging Technologies*, vol. 28, pp. 506-516, 2005.
- [153] X. Fan, J. Zhou, G. Zhang, and L. Ernst, "A micromechanics-based vapor pressure model in electronic packages", *Journal of Electronic Packaging*, vol. 127, pp. 262-268, 2005.

- [154] J.de Vries, and E. Janssen, "Humidity and reflow resistance of flip chip on foil assemblies with conductive adhesive joints", *IEEE Transactions on Components and Packaging Technologies*, vol. 26, pp. 563-568, 2003.
- [155] J.de Vries, "Failure mechanism of anisotropic conductive adhesive interconnections in flip chip ICs on flexible substrates", *IEEE Transactions on Components and Packaging Technologies*, vol. 27, pp. 161-166, 2004.
- [156] Teledyne Storm Cable, "Coefficient of linear expansion of epoxy", Internet: http://www.stormcable.com/uploads/Thermal_expansion_data_table_tb06.pdf, Feb. 2010 [Apr. 02, 2011].
- [157] J.F.J.M. Caers, X.J. Zhao, J.W.C.de Vries, E.H. Wong, G. Kums, and A.R.C. Engelfriet, "HART: A new highly accelerated robustness test for conductive adhesive interconnects", *58th Electronic Components and Technology Conference*, 2008, pp. 1695-1699.
- [158] J. Liu, X.Z. Lu, and L.Q. Cao, "Reliability aspects of electronics packaging technology using anisotropic conductive adhesives", *Journal of Shanghai University (English Edition)*, vol. 11, pp. 1-16, 2007.
- [159] M. Shirangi, C. Otto, A. Fischer, P.van Staa, W. Muller, and B. Michel, "Advanced virtual testing of structural integrity in microelectronic assemblies", *3rd Electronic System-Integration Technology Conference*, 2010, pp. 1-8.
- [160] C.W. Tan, Y.W. Chiu, and Y.C. Chan, "Corrosion study of anisotropic conductive joints on polyimide flexible circuits", *Materials Science and Engineering B*, vol. 98, pp. 255-264, 2003.
- [161] E. Brun, P. Rain, G. Teissédre, C. Gmllermin, and S. Rowe, "Hygrothermal aging of a filled epoxy resin", *IEEE International Conference on Solid Dielectrics*, 2007, pp. 239-242.
- [162] G.D. Sim, C.K. Chung, K.W. Paik, and S.B. Lee, "Experimental analysis on the mechanism of moisture induced interface weakening in ACF package", *European Microelectronics and Packaging Conference, EMPC*, pp. 1-7, 2009.

- [163] G.D. Sim, C.K. Chung, K.W. Paik, and S.B. Lee, "Moisture induced interface weakening in ACF package", *Materials Science and Engineering: A*, vol. 528, pp. 698-705, 2010.
- [164] C. Jan and K. Grzegorz, "The study of lifetime of polymer and composite bone joint screws under cyclical loads and in vitro conditions", *Journal of Materials Science: Materials in Medicine*, vol. 16, pp. 1051-1060, 2005.
- [165] H.J. Wilke, K. Wenger, and L. Claes, "Testing criteria for spinal implants: recommendations for the standardization of in vitro stability testing of spinal implants", *European Spine Journal*, vol. 7, pp. 148-154, 1998.
- [166] J. Liu, "On the failure mechanism of anisotropically conductive adhesive joints on copper metallisation", *International Journal of Adhesion and Adhesives*, vol. 16, pp. 285-287, 1996.
- [167] D.D. Dylis, " Overview Of Electronic Component Reliability", *Electronic failure analysis handbook: techniques and applications for electronic and electrical packages, components, and assemblies*, P. Martin, Ed, New York: McGraw-Hill Professional, pp. 1-24, 1999.
- [168] J. Łukaszczyk and K. Jaszcz, "Studies on hydrolytic degradation of epoxy-polyester resins cured with glutaric anhydride", *Polymers for Advanced Technologies*, vol. 13, pp. 871-883, 2002.
- [169] Weather Underground, Inc., "History of Cork, Ireland", Internet: <http://www.wunderground.com/history/airport/EICK/2010/8/18/MonthlyHistory.html>, Feb. 2011 [Apr. 03, 2011].
- [170] S. Franssila, "Thin-film Materials and Processes", *Introduction to microfabrication*, West Sussex: John Wiley & Sons Ltd, 2004, pp. 47-64.
- [171] S. Nilsson, M. Svedberg, J. Pettersson, F. Björefors, K. Markides, and L. Nyholm, "Evaluations of the Stability of Sheathless Electrospray Ionization Mass Spectrometry Emitters Using Electrochemical Techniques", *Analytical Chemistry*, vol. 73, pp. 4607-4616, 2001.
- [172] A. Berduque, Y.H. Lanyon, V. Beni, G. Herzog, Y.E. Watson, K. Rodgers, F. Stam, J. Alderman, and D.W.M. Arrigan, "Voltammetric characterisation of silicon-based microelectrode arrays

- and their application to mercury-free stripping voltammetry of copper ions", *Talanta*, vol. 71, pp. 1022-1030, 2007.
- [173] VARTA Microbattery GmbH, "VARTA, CR 1/3N, Lithium Manganese Dioxide", Internet: <http://www.farnell.com/datasheets/416067.pdf>, Dec. 2009 [Mar. 17, 2011].
- [174] RS-Components, "Surface Coating 251-3700", Internet: <http://docs-europe.electrocomponents.com/webdocs/001f/0900766b8001f25d.pdf>, Jun. 2009 [Mar. 17, 2011].
- [175] Polymer Systems Technology Limited, "NuSil Silicone Sheeting Selector Guide", Internet: <http://www.silicone-polymers.com/pdf/Sheeting%20Selector%20Guide%20-%20Customers.pdf>, Nov. 2007 [Apr. 04, 2011].
- [176] P.E.K. Donaldson, "The essential role played by adhesion in the technology of neurological prostheses", *International Journal of Adhesion and Adhesives*, vol. 16, pp. 105-107, 1996.
- [177] Trulon Printed Circuits, "Capability and Design Guidelines", Internet: <http://www.trulon.co.uk/pdf/guidelines.pdf>, Jun. 2008 [Jun. 22, 2011].